



**BLACK HOLE ACCRETION DISC VARIABILITY AND  
THE REQUIREMENTS FOR DISC TRUNCATION**

Submitted in fulfilment of the requirements  
for the degree of Doctor of Philosophy

by

**Charles Field**  
Theoretical Astrophysics Group  
Department of Physics and Astronomy  
University of Leicester

June 2019

# Abstract

The unstable nature that is observed in most X-ray Binaries (XRBs), leads to the disc transitioning between different luminosity states. In the high-soft state, the accretion disc is thought to extend to the inner most stable circular orbit (ISCO), however in the low-hard state the disc is thought to truncate and be replaced by an advection dominated accretion flow. Attempts to identify the point of transition between these two disc geometries has produced conflicting results.

In the first part of this thesis, I analyse close to a decade of *XMM-Newton* observations of the transient XRB system GX 339–4. I outline a new approach to the disc truncation debate, whereby I assume the inner disc radius is fixed at the ISCO, in both the hard and soft states. I highlight a new mass constraint upon the XRB system and present a novel count-rate slicing technique for the spectral analysis. I find only limited evidence to suggest that a fixed inner disc radius is an inadequate assumption, when allowing the emissivity value  $q$  and colour correction factor  $f_{\text{col}}$  to vary. In the final part of this thesis, I consider the steady state XRB LMC X–3, which entered a 3 month period of quiescence in 2012. This period of quiescence was deeper than that previously observed in its 40 year observational history. I investigated this drop into quiescence using a 1D disc instability model, where I examined the variability in the secondary accretion rate required to replicate the observed light-curve. The modelled time to enter quiescence was found to be over an order of magnitude greater than that observed. This appears to result from inadequate cooling in the disc, which may be resolved by solving the vertical disc equations.

# Acknowledgements

I would like to thank my supervisors Graham Wynn and Simon Vaughan for their continuous support and encouragement during my time in Leicester. I could not have asked for two more patient and friendly supervisors to guide me through the field of astrophysics and the practicalities of the scientific method. In this regard, I would also like to thank the theory group academics: Andrew, Walter, Sergei, Mark, Richard, and Chris. The physics department of course would not function without the admin staff Lisa, Kiri, Merry, and Joan. I would also like to thank the RCS support team for fixing all my computing issues and the GO for answering all my queries. I would also like to thank all the students and postdocs that I have had the great pleasure of sharing an office with: Alex, Gillian, Hastyar, Hossam, Pete, Martin, Tom, Claire, Christian, Hasan, Lilian, Mark, Amery, Rob, Seung-Hoon, Kastytis, Alessia, Susan, Stuart, and Stephen.

I have always had great flatmates while in living in Leicester and I would like to thank Andy, Ceciel, Jay, Vivan, Matt, Alex, and Stuart for tolerating both my love of strong smelling cheeses (Époisses de Bourgogne should probably be banned!) and my questionable sense of humour (you know it is a good punch line, when the neighbours complain!). I would also like to thank all of my friends, in particular Paul for his drunken antics and Nishad for her sober antics: your continuous energy and positivity always kept me going. My family have always encouraged me to pursue my interests and have supported me in all my educational pursuits. I might finally leave formal education and get a job: you can but dream!

# Contents

<b>Contents</b>	<b>iv</b>
<b>List of Figures</b>	<b>ix</b>
<b>List of Tables</b>	<b>xiv</b>
<b>SAS tasks</b>	<b>xv</b>
<b>Spectral Models</b>	<b>xvii</b>
<b>1 Introduction</b>	<b>1</b>
1.1 A Short History of Black Holes . . . . .	2
1.2 X-ray Binaries . . . . .	6
1.2.1 Roche lobe overflow . . . . .	7
1.2.2 The Eddington limit . . . . .	10
1.3 Accretion disc theory . . . . .	11
1.3.1 Conservation of mass . . . . .	11
1.3.2 Conservation of angular momentum . . . . .	12
1.3.3 Mass transport . . . . .	13
1.3.4 A steady state disc . . . . .	16
1.3.5 The inner most stable circular orbit . . . . .	17
1.3.6 A turbulent viscosity prescription . . . . .	20
1.4 The thermal-viscous instability . . . . .	21
1.4.1 The outburst decay . . . . .	24

1.4.2	XRB observations and spectral states . . . . .	28
1.5	The inner disc radius . . . . .	30
1.5.1	A multi-temperature blackbody disc . . . . .	30
1.5.2	The reflection slab . . . . .	31
1.5.3	Relativistic and gravitational smearing . . . . .	35
1.6	Thesis overview . . . . .	35
<b>2</b>	<b>An introduction to GX339-4 and the debate on disc truncation</b>	<b>37</b>
2.1	Introduction . . . . .	38
2.2	System Parameters . . . . .	44
2.2.1	Constraining the mass and inclination . . . . .	44
2.2.2	Distance estimates . . . . .	46
2.3	A transient LMXB . . . . .	47
2.3.1	The thermal-viscous instability . . . . .	48
2.3.2	The viscous time . . . . .	52
2.3.3	Duty cycle . . . . .	53
2.4	Observations and data reduction . . . . .	55
2.4.1	<i>XMM-Newton</i> pn-camera observations . . . . .	55
2.4.2	<i>RXTE</i> observations and analysis . . . . .	59
2.5	The interstellar medium . . . . .	59
2.5.1	RGS data reduction . . . . .	61
2.5.2	Modelling the line of sight absorption . . . . .	61
2.6	Broad-band spectral model . . . . .	65
2.6.1	Disc . . . . .	65
2.6.2	Reflection . . . . .	66
2.6.3	Corona . . . . .	67
2.6.4	The core model . . . . .	68
<b>3</b>	<b>A re-analysis of the requirements for disc truncation in GX339-4</b>	<b>69</b>
3.1	Introduction . . . . .	70
3.2	Observations and spectral model . . . . .	71
3.3	Results . . . . .	72

3.3.1	BURST Mode Observations . . . . .	72
3.3.2	TIMING Mode Observations . . . . .	77
3.3.3	An RGS analysis of the soft excess . . . . .	81
3.4	Discussion . . . . .	84
3.4.1	Do we require disc truncation in the bright hard state? . . . .	84
3.4.2	The physicality of the coronal variations . . . . .	88
3.4.3	The ionisation state of the disc . . . . .	91
3.4.4	A variable colour correction factor . . . . .	93
3.5	Conclusions . . . . .	95
<b>4</b>	<b>The varying colour correction factor of GX339-4 in the bright hard state</b>	<b>97</b>
4.1	Introduction . . . . .	98
4.2	Observations and model fitting . . . . .	99
4.3	Results and analysis . . . . .	100
4.3.1	The evolving thermal disc emission . . . . .	100
4.3.2	The geometry of the corona . . . . .	104
4.3.3	Modelling the residual features . . . . .	106
4.4	Discussion and conclusions . . . . .	106
4.4.1	A steady inner disc radius . . . . .	106
4.4.2	An alternative viscosity regime . . . . .	106
<b>5</b>	<b>The variable nature of LMC X-3</b>	<b>110</b>
5.1	Introduction . . . . .	111
5.2	The stability of HMXBs . . . . .	113
5.2.1	LMC X-3 on the Verge of Transience . . . . .	113
5.2.2	Comparisons with other persistent HMXBs . . . . .	115
5.3	A disc instability model . . . . .	117
5.3.1	The disc evolution . . . . .	117
5.3.2	The energy balance . . . . .	119
5.3.3	Numerical Method . . . . .	121
5.3.4	Time Constraints . . . . .	121

5.3.5	Lightcurve Calculations . . . . .	123
5.4	Results and Discussion . . . . .	123
5.4.1	Time Spent in quiescence . . . . .	123
5.4.2	Required reduction factor . . . . .	126
5.4.3	Rise out of quiescence . . . . .	126
5.5	Summary and Conclusions . . . . .	129
5.5.1	Entering quiescence . . . . .	129
5.5.2	Rising out of Quiescence . . . . .	131
5.5.3	Required reduction factor . . . . .	132
5.5.4	Model Assumptions . . . . .	132
5.6	Further work . . . . .	133
<b>6</b>	<b>Conclusions</b>	<b>134</b>
6.1	A novel approach to disc truncation . . . . .	135
6.2	A fixed inner disc radius . . . . .	136
6.3	A variable colour correction factor . . . . .	137
6.4	A steady state drop into quiescence . . . . .	138
6.5	Future work . . . . .	138
	<b>Appendix A The <i>XMM-Newton</i> pn-camera spectral fits</b>	<b>140</b>
A.1	BURST mode results table and spectra . . . . .	141
A.2	TIMING mode results table and spectra . . . . .	147
	<b>Appendix B The count-rate sliced <i>XMM-Newton</i> spectral fits</b>	<b>154</b>
B.1	Count-rate sliced results table . . . . .	155
B.2	Count-rate sliced rev-0782 spectra . . . . .	156
B.3	Count-rate sliced rev-0783 spectra . . . . .	161
B.4	Count-rate sliced rev-1702 spectra . . . . .	166
B.5	Count-rate sliced rev-1886 spectra . . . . .	168
	<b>Appendix C The vertical disc structure</b>	<b>170</b>
C.1	Solving for thermal dynamic equilibrium . . . . .	171



# List of Figures

1.1	The Roche potential . . . . .	8
1.2	Roche Lobe overflow . . . . .	9
1.3	Viscous dissipation of a ring of matter . . . . .	15
1.4	The radius of the inner most stable circular orbit with respect to BH spin . . . . .	20
1.5	S-curve and limit cycle . . . . .	23
1.6	The HLX-1 light curve . . . . .	27
1.7	Multi-temperature blackbody disc . . . . .	31
1.8	Ionisation and power-law signatures upon the reflection spectra . . .	32
1.9	Reflection broadening . . . . .	34
2.1	Determining the BH mass of GX 339–4 . . . . .	45
2.2	The critical accretion rate against the binary period . . . . .	49
2.3	The <i>RXTE</i> long term light curve and hardness intensity diagram for GX 339–4 . . . . .	60
2.4	RGS spectra for GX 339–4 across several spectral states . . . . .	62
2.5	The $N_{\text{H}}$ column density estimates for GX 339–4 . . . . .	64
3.1	The normalised spectra ( $\text{cts s}^{-1}\text{keV}^{-1}$ ) and model ratio verses energy (keV), for the Timing mode observations. . . . .	73
3.2	The normalised spectra ( $\text{cts s}^{-1}\text{keV}^{-1}$ ) and model ratio verses energy (keV), for the Timing mode observations. . . . .	73

3.3	The top and bottom panels show the modelling results for the TIMING mode observation rev-1702. The top panel shows the folded model and spectra, along with the fit ratio. The bottom panel shows the unfolded model and spectrum, along with the respective $\Delta\chi$ values. The solid black line represents the total model emission, with the additive model contributions given as follows: disc and power-law (red), reflection (dark blue), neutral reflection (light blue) . . . . .	80
3.4	The joint fits of the pn-camera BURST mode models to the RGS spectra. The folded models, spectra and the corresponding $\Delta\chi$ values for each of the four observations are given. The gaussian component of the model was removed and the cross correlation parameter is given as $N_{RGS} \sim 0.91$ . The red, green, blue and black line colours correspond to the revolution numbers 1325, 1338, 1318 and 0514 respectively. . . . .	82
3.5	The folded pn-camera model renormalised to the RGS spectra, along with the corresponding $\Delta\chi$ values for observation rev-1886. The top plot is for the full pn-model and required a cross correlation parameter of $N_{RGS} \sim 1.02$ . The bottom plot is the pn-model with the gaussian component removed and with $N_{RGS} \sim 1.14$ . . . . .	83
3.6	The power-law index with respect to the total flux in the 0.01-10keV range. See key for the observation revolution number. . . . .	88
3.7	The scatter fraction and reflection emissivity with total flux in the 0.01-10keV range. See key for the observation revolution number. . . . .	89
3.8	The emissivity parameter with respect to the total flux in the 0.01-10keV range. See key for the observation revolution number. . . . .	92
3.9	The colour correction factor against the total flux obtained in the 0.01-10 keV range. See for the <i>XMM-Newton</i> revolution number for each of the observations. . . . .	94
4.1	The ionisation parameter against total flux in the 0.01-10keV range. See key for the observation revolution number. . . . .	103

4.2	The power-law index against total flux in the 0.01-10keV range. See key for the observation revolution number. . . . .	104
4.3	The scatter fraction and reflection emissivity with total flux in the 0.01-10keV range. See key for the observation revolution number. . .	105
4.4	The variation of the colour correction value with respect to the accretion rate which is given in Eddington units for a Schwarzschild BH. With the spectral fits from both Chapters 3 & 4 used, see plot key for details. . . . .	107
5.1	The bolometric light curve of LMC X-3, as it rises out from quiescence in January 2012. The upper limits upon the luminosity were obtained using <i>XMM-Newton</i> data. This was followed by a <i>Swift</i> monitoring campaign to obtain accurate flux measurements. The 8-day gap in observations is due to the source being located at the satellite orbital pole. Figure obtained from Prof. Chris Done. . . . .	115
5.2	Lightcurves showing the fall and rise of LMC X-3 out of quiescence when $\dot{M}_2$ is dropped by a factor of a hundred for different multiples of the viscous time (different colours on diagram - see key). The upper panels show results for a radiation constant, $\mathcal{C}_x$ of $10^{-5}$ , i.e. minimal radiation, whereas the lower panels show results for a higher radiation constant of $\mathcal{C}_x$ of $10^{-3}$ to compare what happens when radiation is included. The left hand panels assume that mass is injected at $6 \times 10^{10} cm$ the middle, $10 \times 10^{10} cm$ and the righthand panel at $1.5 \times 10^{11} cm$ , close to the disc edge. . . . .	122
5.3	Light curve of LMC X-3 with irradiation on ( $\mathcal{C}_x = 10^{-3}$ ) and an infall radius of ( $R_{\text{circ}} = 1.5 \times 10^{11}$ ) with $f_r$ reduction factors of 2,10,50,300,1000 and $10^6$ over the viscous times multiples, shown by the key. . . . .	124

5.4	The rise out of quiescence for the family of lightcurves from figure 1. With time zero set at the point where $\dot{M}$ returns to its original value. The lower and upper panels show the cases for irradiation on and off respectively. . . . .	128
5.5	The rise out of quiescence for the family of lightcurves from figure 1. With time zero set at the point where $\dot{M}$ returns to its original value. The lower and upper panels show the cases for irradiation on and off respectively. . . . .	130
A.1	BURST mode spectra: rev-0496 . . . . .	142
A.2	BURST mode spectra: rev-0514 . . . . .	143
A.3	BURST mode spectra: rev-1318 . . . . .	144
A.4	BURST mode spectra: rev-1325 . . . . .	145
A.5	BURST mode spectra: rev-1338 . . . . .	146
A.6	TIMING mode spectra: rev-0594 . . . . .	148
A.7	TIMING mode spectra: rev-0600 . . . . .	149
A.8	TIMING mode spectra: rev-0782 . . . . .	150
A.9	TIMING mode spectra: rev-0783 . . . . .	151
A.10	TIMING mode spectra: rev-1702 . . . . .	152
A.11	TIMING mode spectra: rev-1886 . . . . .	153
B.1	Rev-0782 spectral fits for the 1st and 2nd count rate bins . . . . .	156
B.2	Rev-0782 spectral fits for the 3rd and 4th count rate bins . . . . .	157
B.3	Rev-0782 spectral fits for the 5th and 6th count rate bins . . . . .	158
B.4	Rev-0782 spectral fits for the 7th and 8th count rate bins . . . . .	159
B.5	Rev-0782 spectral fits for the 9th and 10th count rate bins . . . . .	160
B.6	Rev-0783 spectral fits for the 1st and 2nd count rate bins . . . . .	161
B.7	Rev-0783 spectral fits for the 3rd and 4th count rate bins . . . . .	162
B.8	Rev-0783 spectral fits for the 5th and 6th count rate bins . . . . .	163
B.9	Rev-0783 spectral fits for the 7th and 8th count rate bins . . . . .	164
B.10	Rev-0783 spectral fits for the 9th and 10th count rate bins . . . . .	165
B.11	Rev-1702 spectral fits for the 1st and 2nd count rate bins . . . . .	166

B.12 Rev-1702 spectral fits for the 3rd count rate bin . . . . . 167  
B.13 Rev-1886 spectral fits for the 1st and 2nd count rate bins . . . . . 168  
B.14 Rev-1886 spectral fits for the 3rd and 4th count rate bins . . . . . 169

# List of Tables

2.1	The primary system parameter constraints for GX 339–4 and the corresponding limits this places upon the expected disc dynamics . . .	49
2.2	An <i>XMM-Newton</i> observation log for the LMXB GX 339–4 . . . . .	57
3.1	The EPIC pn-camera BURST mode parameter and flux tables for GX 339–4 . . . . .	75
3.2	The EPIC pn-camera TIMING mode parameter and flux tables for GX 339–4 . . . . .	78
4.1	The count-rate sliced EPIC pn-camera TIMING mode parameter table for GX 339–4 . . . . .	101
4.2	The count-rate sliced EPIC pn-camera TIMING mode flux table for GX 339–4 . . . . .	102
5.1	HMXB system parameters, viscous times and accretion ratios . . . .	116
A.1	The EPIC pn-camera BURST mode parameter table for GX 339–4, with errors calculated at the 90% confidence level . . . . .	141
A.2	The EPIC pn-camera TIMING mode parameter table for GX 339–4, with errors calculated at the 90% confidence level . . . . .	147
B.1	The count-rate sliced EPIC pn-camera TIMING mode parameter table for GX 339–4, with errors calculated at the 90% confidence level	155

# SAS tasks

The Science Analysis System (SAS) is a collection of scripts for reducing and analysing *XMM-Newton* observations. A practical descriptions of the SAS tasks can be found in Chapter 2, with a full summary of each task available online<sup>1</sup>.

**ARFGEN:**

Generates an Ancillary Response File (ARF).

**EPATPLOT:**

A routine for plotting event pattern statistics to discern pile-up.

**EPFAST:**

Applies a charge transfer correction for Fast mode EPIC pn-camera data.

**EPPROC:**

Processes the EPIC pn-camera data from the *XMM-Newton* observation.

**RGSCOMBINE:**

Allows for RGS spectrum files to be combined.

**RGSPROC:**

Processes the RGS data from the *XMM-Newton* observation.

**RMFGEN:**

Generates a redistribution matrix file (RMF).

---

<sup>1</sup><http://xmm-tools.cosmos.esa.int/external/sas/current/doc/packagelist.html>

SPECGROUP:

A procedure for grouping spectral channels together.

# Spectral Models

A detailed description of all default and publicly released XSPEC models can be found online<sup>2,3</sup>.

## BHSPEC:

A multi-blackbody model for a steady state relativistic accretion disc around a Kerr black hole. The model solves for the vertical structure of the disc to physically calculate the radiative transfer.

## BKNPOW:

A broken photon power-law emission.

## DISKBB:

The spectrum from a multi-blackbody Newtonian disc.

## DISKPN:

The spectrum from a multi-blackbody pseudo-Newtonian disc.

## GABS:

A Gaussian absorption line.

## GAUSS:

A Gaussian emission line.

---

<sup>2</sup><https://heasarc.gsfc.nasa.gov/xanadu/xspec/manual/Models.html>

<sup>3</sup><https://heasarc.gsfc.nasa.gov/xanadu/xspec/newmodels.html>

ISMABS:

A photo-absorption model that takes into account both the neutral and ionised aspects of the interstellar medium.

KDBLUR:

A convolution model that applies a relativistic smoothing correction (with the inner radius  $R_{\text{in}}$  as a variable).

KERRBB:

A multi-blackbody model for a relativistic accretion disc around a Kerr black hole.

PEXRAV/PEXRIV:

The reflection spectrum from a neutral (PEXRAV) and ionised (PEXRIV) material illuminated by a power-law emission with an exponential cut-off. The two models ignore fluorescence line features to allow for piecemeal modelling.

REFLIONX:

The reflection spectrum from a cold disc illuminated by a power-law emission. The model assumes a constant density atmosphere for the disc when computing the radiative transfer.

RELCONV:

A convolution model that applies a relativistic smoothing correction (with spin  $a_*$  as a variable).

RELLINE:

A relativistic fluorescent line model for various illumination geometries of the disc.

SIMPL:

A convolution model that up scatters a fraction of the photons from an input spectrum into a power-law.

TBNEW:

A photo-absorption model for a neutral interstellar medium.

**WARMABS:**

A photo-absorption model for an ionised interstellar medium.

**XILLVER:**

The reflection spectrum from a cold disc illuminated by a power-law emission.

# 1

## Introduction

## 1.1 A Short History of Black Holes

The term black hole was first popularised by the American physicist John Wheeler in 1967, to graphically describe an object with a mass density so great, that even light would be unable to escape from its vicinity (Hawking, 1995). The physical notion of a black hole (BH), in part owes its early conceptualisation to the Danish astronomer Ole Rømer and his study of Io, Jupiter's inner most satellite. In antiquity light had been assumed to travel instantaneously and this remained the prevailing view until 1676 when Rømer announced to the Royal Academy of Sciences in Paris that he had measured a twenty-two minute delay in the orbital period of Io, due to the finite speed of light (Wootton, 2015). He had identified that when Earth was approaching Jupiter, the elapsed time between eclipses would shorten and when Earth was receding from Jupiter, the elapsed time between eclipses would lengthen. Rømer then critically attributed this observed variation in the period of Io, as the time for light to cross the orbital diameter of Earth: which provided the first implicit measurement for the speed of light.

With Newton's law of gravitation and an estimated finite speed for light, John Michell in 1784 published a letter in the *Philosophical Transactions of the Royal Society of London*, identifying that if the radius of the sun was five-hundred times larger and possessed the same mass density, then its escape velocity would exceed that of light (Michell, 1784). This idea of a "Dark star", was also independently developed and published in 1796 by the French mathematician Pierre-Simon Laplace in his book *Exposition du système du Monde*. This mathematical curiosity however was dropped in the 3rd edition of Laplace's book and remained largely ignored during the 19th century, as the massless wave theory for light began to gain traction (Laplace, 1808).

It was not until 1915, with the advent of Einstein's theory of general relativity and the concept of curved spacetime, that black holes would return as a physical solution (Einstein, 1916). In the year 1916, within just a few months of Einstein's publication, the German astrophysicist Karl Schwarzschild was able to produce exact solutions for the spacetime around a non-rotating, spherically symmetric body (Schwarzschild,

1916). In this solution, at a radius now identified as the Schwarzschild radius, several terms tend towards infinity. While this was identified as a coordinate artefact relatively early on, it was not until the second half of the 20th century and through the work of the American physicist David Finkelstein in 1958, that the Schwarzschild radius would be considered a physical event horizon, a boundary where spacetime is contorted in such a manner, as to prohibit the outward propagation of light (Finkelstein, 1958).

This theoretical realisation, eventually lead to the beginning of what the American astrophysicist Kip Thorne, would refer to as "the golden age" of general relativity (Thorne, 2003). This fecund period, was first ignited in 1963 by the New Zealand mathematician, Roy Kerr and his seminal paper, in which he presented a generalised solution of the Schwarzschild metric, for a rotating black hole (Kerr, 1963). In the golden decade to follow, the collective works of Werner Israel, Roger Penrose, Steven Hawkins, Brandon Carter, David Robinson, and James Bardeen, culminated in both the no-hair theorem: that is black holes can be described by just their mass, spin, and charge, which Kip Thorne would later quip as a "two hair" theorem, as astrophysical black holes are believed to possess a minimal charge (Thorne, 2003; Israel, 1967; Carter, 1971; Robinson, 1975); along with the development of black hole thermodynamics: whereby Hawking radiation is emitted at the event horizon via quantum effects (Bardeen et al., 1973).

In 1967 during this period of incredible breakthroughs regarding the theory of black holes, the Cambridge graduate student Susan Jocelyn Bell and her supervisor Antony Hewish would make an extraordinary observational discovery of a repeating 1.337 second radio pulse (Hewish et al., 1968). The short period of the pulse and the fact it followed sidereal time, identified it to be an exotic astrophysical object, possibly from the radial pulsations of a neutron star or white dwarf; though the playful possibility of the pulse originating from an alien civilisation, lead to the source gaining the whimsical contraction of LGM-1, for "little green men" (Hawking, 1995). Several months prior to the discovery of LGM-1, the Italian astrophysicist Franco Pacini, had in fact postulated that a spinning neutron star, with a strong magnetic field, could in theory emit radiation (Pacini, 1967). However it would be

another year, before the two ideas would be linked, with Anglo-Austrian physicist Thomas Gold independently suggesting his own spinning neutron star model for LGM-1 (Gold, 1968). In which the misalignment of the magnetic poles and the spin axis of the neutron star, causes a line of sight precession of the electromagnetic beam and ultimately produces the characteristic radio pulses for which these sources gather the name of Pulsars and the common analogical comparison to that of a light house.

This was the first observational evidence for the existence of a neutron star and an implicit demonstration, that a stellar collapse could form such an extremely dense object. This greatly buoyed the theoretical black hole community and it would be just five years later in 1972, with the firm establishment of X-ray astronomy, that the microquasar Cyg X-1 would come to be considered as a strong black hole candidate (Bowyer et al., 1965; Webster & Murdin, 1972). However during the '50s and early '60s, X-ray astronomy appeared to have a bleak future, with X-ray measurements of the solar corona suggesting that any galactic stellar emission would be below the available instrumental sensitivity (Pounds, 2014). This apparent limitation for X-ray astronomy, was quickly dispelled in 1962, with the launch of the ASE/MIT Aerobee rocket from the New Mexico desert (Giacconi et al., 1962). The mission aim was to measure high energy solar reflection from the lunar surface, to their surprise however they identified several strong X-ray sources from outside of the solar system. This discovery of cosmic X-ray sources, ultimately lead to the birth of modern X-ray astronomy and the awarding of the 2002 physics Nobel prize to the Italian astrophysicist Riccardo Giacconi (Giacconi, 2002).

In the subsequent years, following the discovery of Sco X-1, several additional cosmic X-ray sources would come to be identified, such as Cyg X-1 (Bowyer et al., 1965; Giacconi, 2002). The exact nature of these objects however remained unknown, in part because of the limited spatial resolution of the detectors that were being employed at the time. A limitation that would be over come in the winter of 1970, with launch of NASA's Uhuru X-ray satellite; which improved our knowledge of source locations and also allowed for extended observations, which highlighted their common transient nature (Pounds, 2014). With an improved location for Cyg

X-1, Louise Webster and Paul Murdin at the Royal Greenwich Observatory, were then able to identify the X-ray source's optical companion star and obtain a mass function for Cyg X-1, which heavily suggested the source to be a black hole (Webster & Murdin, 1972).

Just prior to this in the 1960s the combined works of Edwin Salpeter, Yakov Zel'dovich, Igor Novikov, and Donald Lynden-Bell suggested that the gravitational potential energy, released from the the accretion of matter upon a supermassive black hole ( $M_{\text{BH}} \geq 10^6 M_{\odot}$ ), could be responsible for the powering of quasi-stellar radio sources, otherwise known as quasars (Salpeter, 1964; Zel'dovich & Novikov, 1964; Lynden-Bell, 1969; Pounds, 2014). With the discovery of a potential stellar mass black hole in Cyg X-1, the astrophysicists Jim Pringle, Martin Rees, Nikolai Shakura, and Rashid Sunyaev set about expanding the accretion theory, to explain the existence of X-ray binaries: where matter is accreted from a donor star upon a neutron star or black hole, with the transfer of angular momentum resulting in the formation of an X-ray emitting disc (Pringle & Rees, 1972; Shakura & Sunyaev, 1973). Subsequent observations in the intervening decades, have supported the accretion disc theory, for both stellar and supermassive black holes (Done et al., 2007).

In 1971, Donald Lynden-Bell and Martin Rees suggested that a supermassive black hole (SMBH) could reside at the centre of our galaxy, the Milky Way (Lynden-Bell & Rees, 1971). The resolution limits of telescopes at the time however impeded the discovery of Sgr A\* until 1974, when an antenna upgrade at the Green Bank NRAO, allowed Bruce Balick and Robert Brown to identify a synchrotron radio source at the centre of our galaxy (Balick & Brown, 1974; Goss et al., 2003). It was not until 2002, a decade after the start of a campaign to image the central galactic region, using the ESO SHARP camera and later the VLT, that an international team lead by the MPL astrophysicist Rainer Schödel, would be able to analyse the orbit of an inner arc-second star S2. With a decade of data on the proper motion and radial velocity of S2, the team were able to accurately discern its orbital motion and determine a central mass of  $3.7 \pm 1.5 \times 10^6 M_{\odot}$ , within a peri-centre radius of 124 AU, which strongly alluded to the existence of a SMBH (Schödel et al., 2002). This

was further substantiated in 2009, when an orbital study of 28 inner galactic S-stars, calculated the central mass to be approximately  $4.31 \pm 0.36 \times 10^6 M_{\odot}$  (Ghez et al., 2005; Gillessen et al., 2009). These results provided the first concrete observational evidence for the existence of a "dead quasar" and thus lent support to the idea that a SMBH could reside at the centre of every galaxy, a concept that had been first postulated by the CAMK astronomer Andrzej Sołtan in 1982 (Soltan, 1982).

More recently evidence for the existence of stellar mass black holes, received a spectacular boost, following the LIGO collaborations astonishing announcement of the first ever direct gravitational wave detection (Abbott et al., 2016). On the 14th September 2015, two LIGO detectors positioned at Hanford (Washington) and Livingston (Louisiana), simultaneously measured a "transient gravitational-wave signal". This gravitational wave signature was then identified to match the wave form for a  $36 M_{\odot}$  and  $29 M_{\odot}$  black hole merger, with a total gravitational radiative emission of  $3.0 \pm 0.5 M_{\odot} c^2$  (Abbott et al., 2016). It is now 232 years since John Mitchell first suggested the existence of "dark stars", the discovery of gravitational waves adds a final piece for the evidence for the existence of black holes and opens up a whole new window into their study for the 21st century.

## 1.2 X-ray Binaries

The conversion of gravitational potential energy into kinetic energy as an object falls in upon a massive compact body such as a black hole or a neutron star, has the potential to release huge amounts of energy (Salpeter, 1964; Zel'dovich & Novikov, 1964; Lynden-Bell, 1969). If the compact object accretes matter from infinity to its surface, with all kinetic energy converted to electromagnetic radiation, then the maximum accretion luminosity can be calculated as,

$$L = \frac{GM_1\dot{M}}{R_1}, \quad (1.1)$$

where  $M_1$  is the mass of the compact body, which has a radial extension  $R_1$ , and a mass accretion rate  $\dot{M}$ . In the case of an X-ray binary (XRB) the accretion time scale is finite, which naturally limits electromagnetic emissions from the disc

(Pringle & Rees, 1972; Shakura & Sunyaev, 1973). While radiative emissions can continue from the surface of a neutron star, this is not possible for an accreting black hole: whose de facto surface is an event horizon. To account for this discrepancy, a dimensionless value for the accretion efficiency  $\eta$ , is employed for calculating the luminosity  $L = \eta \dot{M} c^2$ ; where the accretion efficiency is typically given as  $\eta \sim 0.15$  for a neutron star and  $\eta \sim 0.1$  for a black hole (Frank et al., 2002a). The accretion efficiency for a black hole is evaluated in more detail in section 1.3.5.

The transfer of mass from the secondary star to its compact primary can occur via Roche-lobe overflow or through stellar wind capture. The exact mechanism is primarily dependant upon the mass of the secondary star  $M_2$ . It is partially for this reason that XRBs are classified by the secondary star mass, as either a low mass X-ray binary (LMXB,  $M_2 \leq 2M_\odot$ ), an intermediate mass X-ray binary<sup>1</sup> (IMXB,  $2M_\odot < M_2 < 10M_\odot$ ), or as a high mass X-ray binary (HMXBs,  $M_2 \geq 10M_\odot$ ). LMXBs generally have short orbital periods with Roche-lobe overflow (RLO) being the dominant secondary accretion mechanism, while HMXBs typically contain a type O/B star that is capable of generating a strong stellar wind. As this thesis is primarily centred around the two XRBs, GX 339–4 and LMC X–3 (both thought to be fed via RLO), further details of the wind accretion process are not covered here.

### 1.2.1 Roche lobe overflow

If the secondary star in a binary system expands beyond its gravitational sphere, matter can be gravitationally stripped from its outer envelope. The geometry of the sphere can be determined by calculating the Roche potential  $\Phi_R$  of the binary system which is given as the sum of the gravitational potentials and the effective potential from the centrifugal force,

$$\Phi_R(\mathbf{r}) = -\frac{GM_1}{|\mathbf{r} - \mathbf{r}_1|} - \frac{GM_2}{|\mathbf{r} - \mathbf{r}_2|} - \frac{1}{2}[\boldsymbol{\omega} \times (\mathbf{r} - \mathbf{r}_3)]^2. \quad (1.2)$$

The mass, and position vectors of the primary and secondary bodies are subscripted

---

<sup>1</sup>IMXBs are thought to transfer a large fraction of their mass on a relatively short time scale. This has resulted in IMXBs remaining largely unobserved at our current epoch.

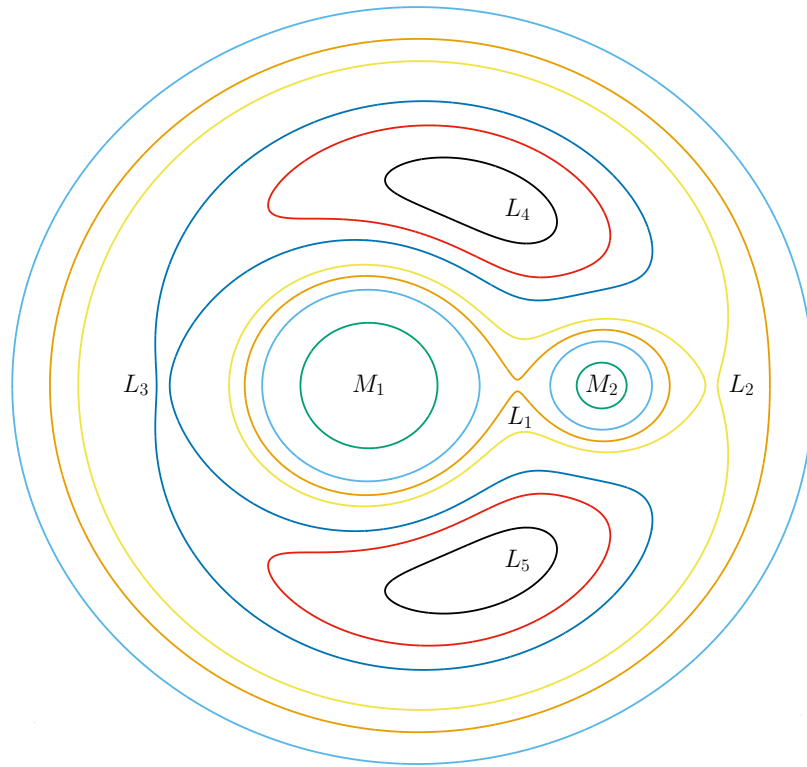


Figure 1.1: The dimensionless Roche potential in the  $x$ - $y$  plane at  $z = 0$ , the coloured contours refer to separate equipotential points. The primary and secondary masses, along with the five Lagrangian points are all labeled in their approximate positions.

1 and 2 respectively, where  $\mathbf{r}_3$  gives the position vector of the centre of mass. The angular velocity is given as  $\omega = 2\pi/P_{\text{orb}}$ , where  $P_{\text{orb}}$  is the orbital period defined by the total mass  $M$  and the orbital separation  $a$ , with

$$P_{\text{orb}}^2 = \frac{4\pi^2 a^3}{G(M_1 + M_2)}. \quad (1.3)$$

In the cartesian co-ordinate frame, the Roche potential can be expressed as

$$\Phi_{\text{R}}(\mathbf{r}) = \frac{GM}{a} \phi_{\text{R}}(\tilde{x}, \tilde{y}, \tilde{z}), \quad (1.4)$$

where the function  $\phi_{\text{R}}$  is the dimensionless Roche potential, with dimensionless units  $\tilde{x} = x/a$ ;  $\tilde{y} = y/a$ ;  $\tilde{z} = z/a$ . If we assume the primary mass resides at the co-ordinate origin, then the dimensionless Roche potential can be defined as

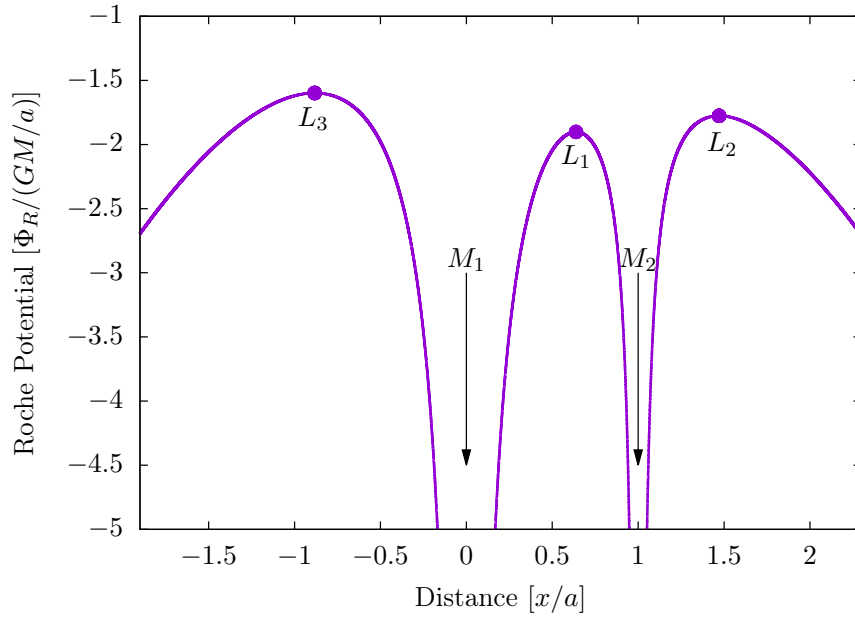


Figure 1.2: The dimensionless Roche potential in the  $x$  direction with  $y = z = 0$ . The primary and secondary masses, along with the three Lagrangian points are shown. Roche lobe overflow occurs when the secondary star's radius exceeds the  $L_1$  point.

$$\phi_R(\tilde{x}, \tilde{y}, \tilde{z}) = -\frac{(1-\mu)}{(\tilde{x}^2 + \tilde{y}^2 + \tilde{z}^2)^{1/2}} - \frac{\mu}{[(\tilde{x}-1)^2 + \tilde{y}^2 + \tilde{z}^2]^{1/2}} - \frac{1}{2}[(\tilde{x}-\mu)^2 + \tilde{y}^2], \quad (1.5)$$

where  $\mu$  is the binary system's centre of mass in the  $x$ -plane, normalised by the separation  $\mu = q/(1+q)$ , where  $q = M_2/M_1$ . Figure 1.1 shows the dimensionless Roche potential in the  $x$ - $y$  plane at  $z = 0$ , the coloured contours refer to equipotential points. The Lagrangian points listed  $L_{1-5}$  are the locations of zero net force upon a test mass (i.e.  $d\Phi/d\mathbf{r} = 0$ ). The smallest equipotential surface that encompasses both of the binary masses is shaped as an hour-glass figure. The two bulbs of this figure are referred to as the Roche Lobes, if the secondary star fills its Roche Lobe then matter will pass through the first Lagrangian point  $L_1$  and become entrapped within the primary star's potential well, see figure 1.2. The Roche lobe of the secondary star can be approximated as a sphere with radius  $R_{L2}$ . Eggleton (1983) provides a parameterisation for  $R_{L2}(q, a)$ , with uncertainty  $\leq 1\%$ ,

$$\frac{R_{L2}}{a} = \frac{0.49q^{2/3}}{0.6q^{2/3} + \ln(1 + q^{1/3})}. \quad (1.6)$$

The Roche lobe radius of the primary  $R_{L1}$  can be calculated by replacing  $q$  with  $q^{-1}$ .

In order for mass transfer to occur, either the secondary star's radius must increase or the binary orbit must decay. While there are transient stellar expansion phases, the long term accretion mechanism is likely to be primarily driven by orbital decay. Orbital decay occurs when angular momentum is lost from the system. Two mechanisms that dominate this process are gravitational radiation: where changes in gravitational quadrupole moment produce gravity waves and magnetic breaking: where the stellar wind is magnetically coupled to the star. The secondary accretion rate  $\dot{M}_2$  for these two orbital decay scenarios has been parameterised by King (1988) in terms of the orbital period, which is taken in units of hours  $P_{\text{orb}}(h)$

$$-\dot{M}_2 \simeq \begin{cases} 10^{-10} \left( \frac{P_{\text{orb}}(h)}{2} \right)^{-2/3} M_{\odot} \text{yr}^{-1} & \text{if } P_{\text{orb}}(h) \leq 2 \\ 6 \times 10^{-10} \left( \frac{P_{\text{orb}}(h)}{3} \right)^{5/3} M_{\odot} \text{yr}^{-1} & \text{if } P_{\text{orb}}(h) \geq 3 \end{cases}$$

This assumes that gravitational radiation dominates the orbital decay at low periods  $P_{\text{orb}}(h) \leq 2$  and that magnetic breaking dominates for  $P_{\text{orb}}(h) \geq 3$ . The star is thought to radially retreat within its Roche lobe in period gap where  $P_{\text{orb}}(h) \sim 2-3$  (Rappaport et al., 1983; Spruit & Ritter, 1983).

### 1.2.2 The Eddington limit

The Eddington limit is the maximum luminosity that a spherical body can achieve while sustaining hydrostatic equilibrium. This occurs when the radiative and gravitational pressures are equal. The steady state Euler equation is given as

$$-\frac{\nabla P_{\text{rad}}}{\rho} = \nabla \Phi, \quad (1.7)$$

where  $\Phi$  is the gravitational potential and  $\nabla P_{\text{rad}}$  is the radiative pressure gradient. With  $\nabla P_{\text{rad}} = \rho \kappa F_{\text{rad}}/c$ , where  $\rho$  is the fluid density,  $\kappa$  the fluid opacity, and  $F_{\text{rad}}$  is

the radiative flux. The luminosity limit at which this occurs can be calculated from the closed surface integral of the radiative flux and applying the gaussian theorem,

$$L_{\text{Edd}} = \int_S F_{\text{rad}} \cdot dS = \frac{c}{\kappa} \int_S \nabla \Phi \cdot dS = \frac{c}{\kappa} \int_V \nabla^2 \Phi dV. \quad (1.8)$$

if we then apply the Poisson's equation, we find

$$L_{\text{Edd}} = \frac{4\pi Gc}{\kappa} \int_V \rho dV = \frac{4\pi GMc}{\kappa}. \quad (1.9)$$

The fluid opacity for ionised hydrogen is given as  $\kappa = \sigma_T/m_p$ , where  $\sigma_T$  is the Thompson scattering cross section for an electron and  $m_p$  is the proton mass. This gives the Eddington luminosity limit of

$$L_{\text{Edd}} = 4\pi GMm_p c/\sigma_T \simeq 1.3 \times 10^{38} (M/M_\odot) \text{ erg s}^{-1}. \quad (1.10)$$

While the Eddington limit is not directly applicable to an accretion disc, due to the lack of spherical symmetry, it does offer a useful unit of measurement:  $\dot{m} = L/L_{\text{Edd}}$ , where  $\dot{m}$  is the Eddington ratio (Abramowicz & Fragile, 2013).

## 1.3 Accretion disc theory

The evolution of an accretion disc is primarily governed by the conservation of mass and the conservation of angular momentum. The accretion disc solutions derived in this section are based on lecture-notes<sup>2</sup> of Prof. Gordon Ogilvie and the works presented in Pringle (1981) and Frank et al. (2002b).

### 1.3.1 Conservation of mass

The continuity equation is dependant upon the fluid density  $\rho$  and its corresponding velocity vector  $\mathbf{u}$ ,

$$\frac{\partial \rho}{\partial t} + \nabla \cdot (\rho \mathbf{u}) = 0. \quad (1.11)$$

<sup>2</sup><http://www.damtp.cam.ac.uk/user/gio10/accretion.html>

In cylindrical coordinates this expands out to give us

$$\frac{\partial \rho}{\partial t} + \frac{1}{R} \frac{\partial}{\partial R} (R \rho u_R) + \frac{1}{R} \frac{\partial}{\partial \phi} (\rho u_\phi) + \frac{\partial u_z}{\partial z} = 0, \quad (1.12)$$

where  $u_r(R, t)$  is the radial drift velocity, which must be negative for accretion to occur. The orbital velocity is given as  $u_\phi = R\Omega_K(R)$ , where  $\Omega_K$  is the Keplerian angular velocity (i.e. the angular velocity of a circular orbit),

$$\Omega_K(R) = \left( \frac{GM_1}{R^3} \right)^{\frac{1}{2}}. \quad (1.13)$$

On the basis that the flow is confined to be close to the orbital plane, the vertical velocity component  $u_z$  is ignored. Based on these assumptions if we then integrate equation 1.12 with respect to  $z$  and  $\phi$ ; with the surface density  $\Sigma(R, t)$  defined as,

$$\Sigma = \int_{-\infty}^{+\infty} \rho \, dz, \quad (1.14)$$

then we obtain the one dimensional mass conservation equation for an accretion disc

$$R \frac{\partial \Sigma}{\partial t} + \frac{\partial}{\partial R} (R \Sigma u_R) = 0. \quad (1.15)$$

The mass conservation equation can some times be presented in terms of the radial mass flux  $\mathcal{F}(r, t)$ , which is defined as

$$\mathcal{F} = \int_0^{2\pi} \int_{-\infty}^{+\infty} R \rho u_R \, dz d\phi. \quad (1.16)$$

### 1.3.2 Conservation of angular momentum

The Euler equation gives the conservation of angular momentum

$$\rho \frac{D\mathbf{u}}{Dt} = -\rho \nabla \Phi - \nabla P + \nabla \cdot \mathbf{T}, \quad (1.17)$$

where the material derivative is defined as

$$\frac{D\mathbf{u}}{Dt} = \frac{\partial \mathbf{u}}{\partial t} + \mathbf{u} \cdot \nabla \mathbf{u}. \quad (1.18)$$

In cylindrical coordinates, the azimuthal component of motion expands out to give us the following cumbersome equation

$$\rho \left( \frac{\partial u_\phi}{\partial t} + u_R \frac{\partial u_\phi}{\partial R} + \frac{u_\phi}{R} \frac{\partial u_\phi}{\partial \phi} + u_z \frac{\partial u_\phi}{\partial z} + \frac{u_R u_\phi}{R} \right) = - \frac{\rho}{R} \frac{\partial \Phi}{\partial \phi} - \frac{1}{R} \frac{\partial P}{\partial \phi} + \frac{\partial T_{R\phi}}{\partial R} + \frac{1}{R} \frac{\partial T_{\phi\phi}}{\partial \phi} + \frac{\partial T_{z\phi}}{\partial z} + \frac{1}{R} (T_{R\phi} + T_{\phi R}). \quad (1.19)$$

If we apply the same assumptions upon the velocity vector as those made in deriving the equation for the conservation of mass (i.e.  $\mathbf{u} = u_R(R, t)\hat{R} + u_\phi(R)\hat{\phi}$ ) and in the case of circular motion the stress tensor reduces to the shear stress component  $T_{R\phi} = T_{\phi R}$ . If we also assume the gravitational potential  $\Phi(R)$  and fluid pressure  $P(z)$  are axisymmetric, then we find the more aesthetically pleasing solution

$$\rho u_R \frac{\partial}{\partial R} (R u_\phi) = \frac{1}{R} \frac{\partial}{\partial R} (R^2 T_{R\phi}). \quad (1.20)$$

The circular shear stress can be defined as  $T_{R\phi} = \rho \nu R \Omega'$ , where  $\nu(R, t)$  is the kinematic viscosity and  $\Omega'$  is the radial derivative of the angular velocity. Integrating equation 1.20 with respect to  $z$  and  $\phi$  gives us

$$\Sigma u_R \frac{\partial}{\partial R} (R u_\phi) = \frac{1}{R} \frac{\partial}{\partial R} (R^3 \Sigma \nu \Omega'). \quad (1.21)$$

The equation for the conservation of angular momentum can some times be presented in terms of the viscous torque  $\mathcal{G}(r, t)$ , which is defined as

$$\mathcal{G} = - \int_0^{2\pi} \int_{-\infty}^{+\infty} R^2 T_{R\phi} dz d\phi. \quad (1.22)$$

### 1.3.3 Mass transport

The diffusion equation for the surface density can be obtained by combining the two conservation equations 1.15 and 1.21, to eliminate the radial velocity component  $u_R$ , so that

$$\frac{\partial \Sigma}{\partial t} = \frac{3}{R} \frac{\partial}{\partial R} \left\{ R^{1/2} \frac{\partial}{\partial R} [\nu \Sigma R^{1/2}] \right\}. \quad (1.23)$$

Substituting in equation 1.15, we can then find the radial velocity

$$u_R = -\frac{3}{\Sigma R^{1/2}} \frac{\partial}{\partial R} [\nu \Sigma R^{1/2}]. \quad (1.24)$$

In order to gain some mathematical insight into the diffusion of matter within the disc, we equate the viscosity term to an averaged value  $\nu = \bar{\nu}$ . If we multiply equation 1.23 by  $R^{1/2}$  and substitute in  $s = 2R^{1/2}$ , we find

$$\frac{\partial}{\partial t} (\Sigma R^{1/2}) = \frac{12\nu}{s} \frac{\partial^2}{\partial s^2} (\Sigma R^{1/2}). \quad (1.25)$$

The terms in the derivatives can be separated into time and radial functions i.e.  $\Sigma R^{1/2} = T(t)S(s)$ , to give us

$$\frac{T'}{T} = \frac{12\nu}{s} \frac{S''}{S} = \lambda^2, \quad (1.26)$$

where  $T(t)$  is an exponential function;  $S(s)$  is a Bessel function, and  $\lambda^2$  is a constant. The Green's function can then be used to solve for  $\Sigma(R, t)$ , to understand the dissipation of matter from when it first enters the disc through the  $L_1$  point. If we take a ring of matter of mass  $m$  at radius  $R_0$ , the initial surface density can be defined using the Dirac delta function  $\delta(R - R_0)$  to be

$$\Sigma(R, 0) = \frac{m}{2\pi R_0} \delta(R - R_0). \quad (1.27)$$

The general solution is then given as

$$\Sigma(x, \tau) = \frac{m}{\pi R_0^2} \tau^{-1} x^{-1/4} \exp\left\{-\frac{1-x^2}{\tau}\right\} I_{1/4}(2x/\tau), \quad (1.28)$$

where  $x = R/R_0$ ,  $\tau = 12\nu t R_0^{-2}$ , and  $I_{1/4}(2x/\tau)$  is the modified Bessel function. A detailed derivation of this solution is given in Lynden-Bell & Pringle (1974). Figure 1.3, shows  $\Sigma(x, \tau)$  as a function of  $x$  for various values of  $\tau$ . The viscous torques within the disc produce a two-way mass transfer: where the majority of the matter is transported inwards (as it loses angular momentum) and a small fraction of the matter is transported outwards (as it gains angular momentum). The nature of this process can be understood by substituting the solution for  $\Sigma(x, \tau)$  into equation 1.24

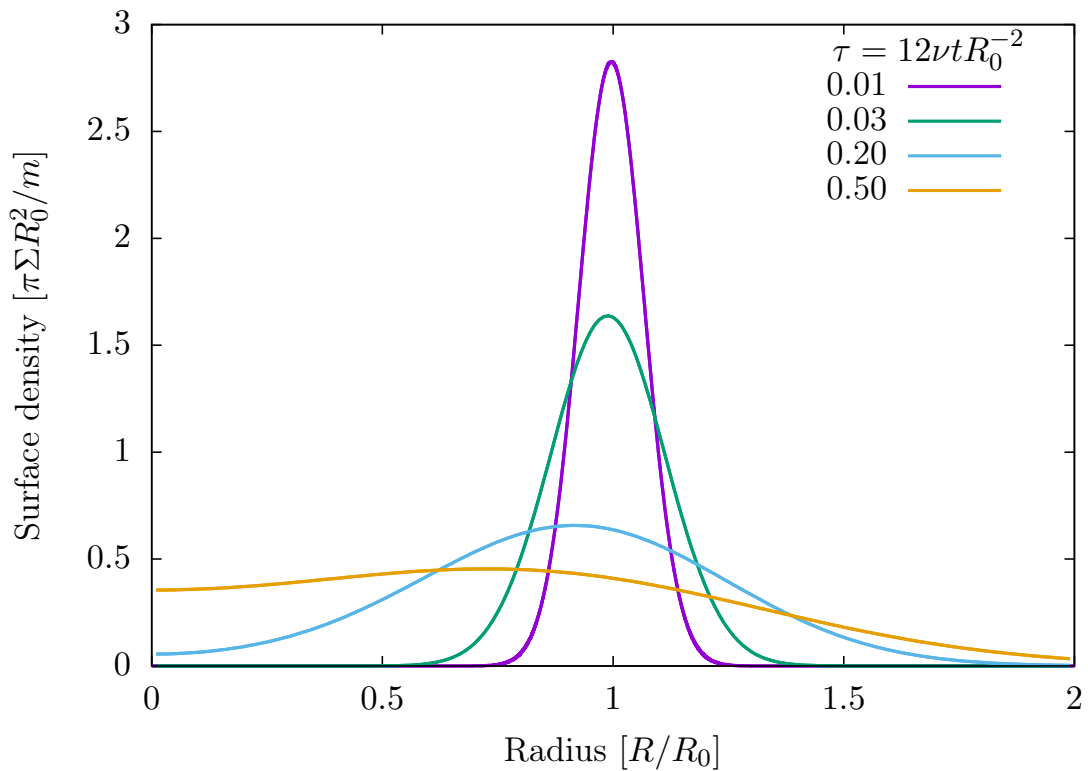


Figure 1.3: The viscous dissipation of a ring of matter with mass  $m$  and initial position  $R_0$ . The surface density  $\Sigma(x, \tau)$  varies with respect to both radius  $x = R/R_0$  and time  $\tau = 12\nu t R_0^{-2}$ . This figure is based on that shown in Frank et al. (2002a).

to find the radial velocity

$$\begin{aligned}
 u_R &= -3\nu \frac{\partial}{\partial R} \ln(\Sigma R^{1/2}) \\
 &= -\frac{3\nu}{R_0} \frac{\partial}{\partial x} \ln(\Sigma x^{1/2}) \\
 &= -\frac{3\nu}{R_0} \frac{\partial}{\partial x} \left\{ \frac{1}{4} \ln(x) - \frac{1-x^2}{\tau} + \ln[I_{1/4}(2x/\tau)] \right\}.
 \end{aligned} \tag{1.29}$$

The asymptotic behaviour of the modified Bessel function,

$$I_{1/4}(z) \propto \begin{cases} z^{1/2} e^z, & \text{if } z \gg 1 \\ z^{1/4}, & \text{if } z \ll 1, \end{cases}$$

produces the following two radial velocity solutions

$$u_R \simeq \begin{cases} \frac{3\nu}{R} \left\{ \frac{1}{4x} + \frac{2x}{\tau} - \frac{2}{\tau} \right\}, & \text{if } 2x \gg \tau \\ -\frac{3\nu}{R} \left\{ \frac{1}{2x} - \frac{2x}{\tau} \right\}, & \text{if } 2x \ll \tau, \end{cases}$$

It is clear to see that as  $\tau$  increases with time, the radius inside of which material moves inwards, must simultaneously expand. This results in the majority of the original mass being accreted at late times  $\tau \gg 1$ .

### 1.3.4 A steady state disc

If we assume a steady state disc where the radial mass flux is constant in time  $d\mathcal{F}/dt = 0$ ; then we can define the mass accretion rate to be constant for the entirety of the disc  $\dot{M} = 2\pi R\Sigma u_R$ , where  $\dot{M} = -\mathcal{F}$ . If we substitute  $\dot{M}$  into the equation for the conservation of angular momentum (i.e. equation 1.21) and integrate with respect to  $R$ , we find

$$\frac{\dot{M}}{2\pi} R^2 \Omega = R^3 \Sigma \nu \Omega' + C, \quad (1.30)$$

The integration constant is determined from the fact that  $T_{R\phi} = 0$  at the inner radius of the disc  $R_{\text{in}}$ . If we assume that  $d\Omega/dR = 0$  occurs at  $\sim R_{\text{in}}$ , then equation 1.30 can be solved to find

$$C \simeq -\frac{\dot{M} R_{\text{in}}^2 \Omega}{2\pi}. \quad (1.31)$$

Substituting this back into equation 1.30 we find

$$\nu \Sigma = \frac{\dot{M}}{2\pi} \left[ 1 - \left( \frac{R_{\text{in}}}{R} \right)^{1/2} \right]. \quad (1.32)$$

The rate of dissipation per unit surface area is given as

$$\begin{aligned}
D(R) &= \frac{1}{2} \int_{-\infty}^{+\infty} T_{R\phi} R \Omega' dz \\
&= \frac{1}{2} \nu \Sigma (R \Omega')^2 \\
&= \frac{9}{8} \nu \Sigma \Omega^2.
\end{aligned} \tag{1.33}$$

If we substitute in equation 1.32 we find

$$D(R) = \frac{3GM\dot{M}}{8\pi R^3} \left[ 1 - \left( \frac{R_{\text{in}}}{R} \right)^{1/2} \right]. \tag{1.34}$$

If we assume that the disc is optically thin and radiates as a blackbody, we can calculate the effective temperature to be,  $\sigma T_{\text{eff}}^4 = D(R)$ . The total bolometric luminosity can then be obtained by integrating the emission across the entirety of the disc

$$\begin{aligned}
L &= 2 \int_{\infty}^{R_{\text{in}}} D(R) 2\pi R dR \\
&= \frac{GM\dot{M}}{2R_{\text{in}}}.
\end{aligned} \tag{1.35}$$

This is only equal to half of the gravitational potential energy that is available from accretion (see equation 1.1). The remainder of the potential energy is then kinetically dispersed upon the accreting body or in the case of a black hole lost beyond the event horizon.

### 1.3.5 The inner most stable circular orbit

In general relativity, the gravitational and centrifugal forces are not able to counterpoise with one another at small radii (i.e., within the close vicinity of a BH or NS). This leads to circular orbits becoming unstable, which has important ramifications upon accretion disc dynamics: as matter beyond the inner most stable circular orbit (ISCO) will free-falling upon the compact object. This truncation of the inner disc, has a significant effect upon the efficiency of BH accretion, owing to matter being lost beyond the event horizon. The ISCO for a non-spinning compact object, can be calculated from the radial solution for a test particle orbiting a Schwarzschild BH,

$$\frac{1}{2} \frac{E^2}{c^2} = \frac{1}{2} \dot{R}^2 + V_{\text{eff}}, \quad (1.36)$$

where  $E$  is the energy per unit rest mass and  $V_{\text{eff}}$  is the effective potential per unit rest mass,

$$V_{\text{eff}} = \frac{1}{2} \left( 1 - \frac{2R_g}{R} \right) \left( c^2 + \frac{h^2}{R^2} \right). \quad (1.37)$$

Here  $R_g$  is the gravitational radius, defined as  $R_g = GM/c^2$  and  $h$  is the specific angular momentum. In a circular orbit the effective force is equal to zero:  $dV_{\text{eff}}/dR = 0$ , as the two attractive forces of gravity, balance with the repulsive centrifugal force. If we differentiate equation 1.37 with respect to radius, we obtain the following quadratic equation,

$$GMR^2 - h^2R + 3R_g h^2 = 0, \quad (1.38)$$

which allows us to obtain the radial and angular momentum solutions for a circular orbit:

$$h^2 = \frac{GMR^2}{(R - 3R_g)} \quad (1.39)$$

and

$$R_{\pm} = \frac{h}{2GM} \left( h \pm \sqrt{h^2 - 12GMR_g} \right). \quad (1.40)$$

It is clear to see from these two equations that the effective potential has a maxima and a minima at  $h^2 > 12GMR_g$ . With the two extrema occurring at  $R_+ > 6R_g$  (which is always a minima:  $V_{\text{eff}}''(R_+) > 0$ , i.e. stable) and  $3R_g < R_- < 6R_g$  (which is always a maxima:  $V_{\text{eff}}''(R_-) < 0$ , i.e. unstable). When  $h^2 = 12GM$ , the effective potential is at a saddle point and the orbital radius is given as  $R_{\pm} = 6R_g$ : which is the inner most stable circular orbit for a Schwarzschild black hole.

The efficiency of an accretion disc can be calculated by solving equation 1.36 for a circular orbit (i.e. the radial velocity is equal to zero  $\dot{R} = 0$  and the angular momentum is given as equation 1.39), which gives us

$$\begin{aligned} \frac{E^2}{c^2} &= c^2 \left( \frac{R - 2R_g}{R} \right) \left( \frac{R - 2R_g}{R - 3R_g} \right) \implies \\ \frac{E}{c^2} &= \frac{R - 2R_g}{R^{\frac{1}{2}}(R - 3R_g)^{\frac{1}{2}}} \end{aligned} \quad (1.41)$$

At the inner disc radius ( $R_{\text{in}} = 6R_g$ ), the orbital energy of a particle with unit mass is given as  $E_{\text{ISCO}} = \sqrt{(8/9)}c^2$ . The binding energy can then be calculated by subtracting this from rest mass energy,  $E_B = 1 - E_{\text{ISCO}} \simeq 0.057c^2$ . If we assume that all of the binding energy is emitted during accretion, then the disc efficiency for a Schwarzschild BH can be given as  $\eta \simeq 5.7\%$ . While this solution provides a basic understanding of the dynamics involved, most compact objects will likely possess angular momentum. Bardeen et al. (1972) provide a solution for the ISCO for a spinning BH, where  $R_{\text{in}}$  is parameterised in terms of the gravitational radius  $R_g = GM/c^2$ , and the dimensionless spin parameter  $a_* = Jc^2/GM^2$ , where  $J$  is the angular momentum of the central body,

$$R_{\text{in}} = R_g \left\{ 3 + Z_2 \mp [(3 - Z_1)(3 + Z_1 + 2Z_2)]^{1/2} \right\} \quad (1.42)$$

with  $Z_1 = 1 + (1 - a_*^2)^{1/3}[(1 + a_*)^{1/3} + (1 - a_*)^{1/3}]$  and  $Z_2 = (3a_*^2 + Z_1^2)^{1/2}$ . The sign  $\mp$  refers to prograde and retrograde spins. At the inner disc radius  $R_{\text{in}}$ , the accretion efficiency is given as

$$\eta = 1 - \sqrt{1 - (2R_g/3R_{\text{in}})} \quad (1.43)$$

The ISCO for a prograde BH can vary between  $6 - 1.23R_g$  where the BH spin is limited to  $a_* = 0.998$  due to counter acting torques (Thorne, 1974). This means that the accretion efficiency can vary between  $5.7 - 31.8\%$ . Figure 1.4 shows how the inner radius and accretion efficiency varies with respect to the BH spin.

The inner disc radius however may not solely depend upon the mass and spin of a black hole. In the case of a thick disc ( $H/R > 0.1$ ), Fragile (2009) found that a moderate inclination of  $15^\circ$  between the accretion disc and the symmetry plane of the black hole, could result in the disc truncating away from the ISCO: possibly due to shocks (Fragile & Blaes, 2008). They suggest however that this effect is unlikely

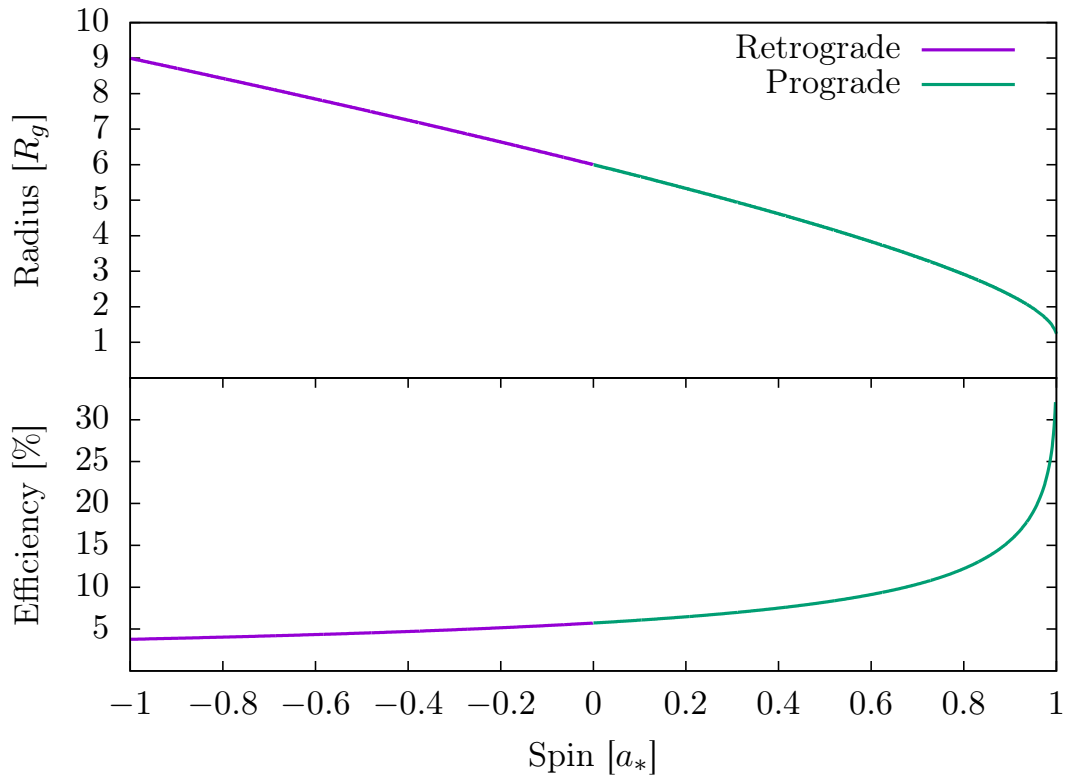


Figure 1.4: The radius of the inner most stable circular orbit,  $R_{\text{ISCO}}$  (top panel) and accretion efficiency as a percentage,  $\eta$  (bottom panel), with respect to the dimensionless spin parameter,  $a_*$ . The retrograde and prograde spins are denoted in purple and green respectively.

to apply in the case of a thin disc ( $H/R < 0.01$ ), as the Bardeen-Petterson effect should align the inner disc region with the spin of the BH, owing to the competing effects of precession and viscosity (Bardeen & Petterson, 1975; Kumar & Pringle, 1985).

### 1.3.6 A turbulent viscosity prescription

If we assume that viscosity arises due to turbulent motion within the disc, then we can parameterise the viscosity as  $\nu \sim \lambda_{\text{turb}} u_{\text{turb}}$ , where  $\lambda_{\text{turb}}$  is the length scale, and  $u_{\text{turb}}$  the velocity, of the turbulent eddies. A simple solution for calculating the viscosity is the  $\alpha$ -parameterisation of Shakura & Sunyaev (1973) which assumes that the disc scale height  $H$ , is the maximum size of the eddies  $\lambda_{\text{turb}} < H$  and that the eddies are operating at subsonic speeds, as shocks would likely dissipate the turbulent motion  $u_{\text{turb}} < c_s$ , where  $c_s$  is the sound speed. This solution does not invoke

any particular mechanism for the viscosity and merely assumes the dimensionless normalisation constant  $\alpha < 1$ . The viscosity is parameterised as,

$$\nu = \alpha H c_s. \quad (1.44)$$

The current favoured mechanism for generating turbulent motion within the disc is the magneto-rotational instability (MRI). This occurs when ionised elements within the disc are connected by magnetic field lines. If one of the elements is inwardly displaced then its greater angular velocity will transfer kinetic energy to the outer element through the stretching of the magnetic field line that is connecting them. This leads to the inner element losing angular momentum and moving to a shorter orbit (transferring potential energy into kinetic energy), while the outer element gains momentum and moves to a greater orbit (transfers its kinetic energy into gravitational potential energy). This process further stretches the magnetic field line that connects the elements, which leads to the instability.

## 1.4 The thermal-viscous instability

The steady state accretion disc solution, requires  $\dot{M}$  to be radially independent however this assumption can break down due to local thermal and viscous instabilities. A local thermal instability can arise when the heating and cooling mechanisms within the disc are no longer balanced. If the radiative heating term  $Q_+$  varies faster with temperature than the local surface cooling term  $Q_-$  then the disc can become thermally unstable. The heating and cooling terms for a half disc are defined as,

$$Q_+ = \frac{9}{8} \nu \Sigma \Omega^2 \quad (1.45)$$

and

$$Q_- = \sigma T_{\text{eff}}^4, \quad (1.46)$$

where the criterion for the disc to become thermally unstable from a perturbation in the central temperature  $T_c$ , is given as

$$\frac{dQ_-}{dT_c} < \frac{dQ_+}{dT_c}. \quad (1.47)$$

As the surface heating varies on the viscous time scale  $t_{\text{visc}} \sim R^2/\nu$ , the viscous mechanism is unable to adjust for instances of inadequate cooling which varies on the shorter thermal time scale  $t_{\text{th}} \sim (H/R)^2 t_{\text{visc}}$  (the thermal time scale is defined as the heat contentment per unit disc area divided by the dissipation rate per unit disc area). In a gas pressure dominated accretion disc, the viscous heating is proportional to the central temperature  $Q_+ \propto T_c$ , while the radiative cooling is dependant upon the disc opacity  $Q_- \propto \kappa^{-1}$ . This means that an instability is instigated when there is a rapid rise in the opacity with temperature. Such a rise occurs when neutral hydrogen becomes semi-ionised at temperatures  $10^4$ - $10^5 K$ . The opacity change is due to high energy photons, ionising the hydrogen within the disc rather than simply escaping through its atmosphere, which leads to run-away heating effect. This rapid rise in the disc temperature can then lead a viscous instability. The criterion for the disc to become viscously unstable from a perturbation in the surface density is given as

$$\frac{\partial \dot{M}}{\partial \Sigma} < 0 \quad (1.48)$$

As the mass accretion rate is dependant upon the disc viscosity, which in turn is proportional to temperature  $\nu \propto T_c$ , any thermal increase will see an equivalent rise in the accretion rate. This means that when the disc is thermally unstable, the viscosity increases despite a diminishing surface density. These two instabilities in tandem are what lead to an S-curve in  $T_{\text{eff}}-\Sigma$  plane when solving for thermodynamic equilibrium. If we assume a one zone steady state model and solve for  $Q_+ = Q_-$ , we can find an analytic relation between the central temperature  $T_c$  and the disc density  $\rho$ ,

$$T_c^2 = \frac{27}{32} \frac{\alpha \kappa \rho^2 \mathcal{R}^2}{\sigma \Omega \mu^2} \quad (1.49)$$

where  $\kappa(T_c, \rho)$  is the frequency averaged Rosseland mean opacity;  $\mu(T_c, \rho)$  is the mean molecular weight, and  $\mathcal{R}$  is the gas constant. The surface density can be

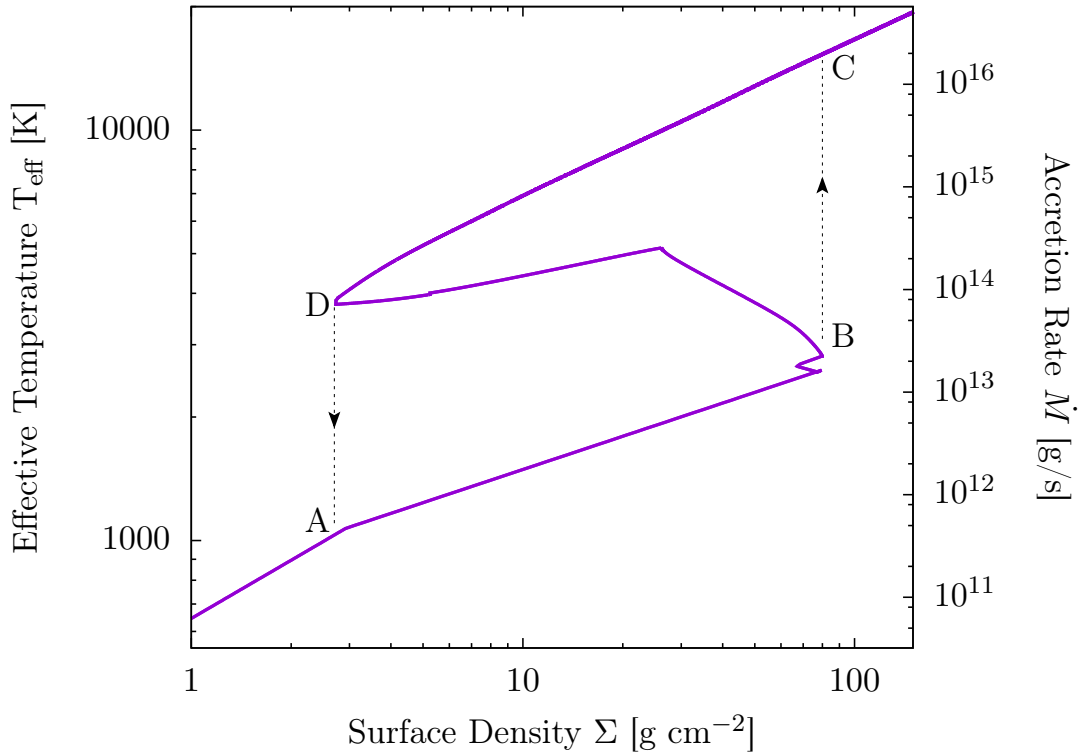


Figure 1.5: The S-curve relation for a  $10M_{\odot}$  BH at  $R = 10^{10}$ cm. The numerical fits of Huré (2000a), and Zhu et al. (2007) were used to calculate  $\mu$ , and  $\kappa$  respectively. The temperature dependant viscosity prescription of Alexander et al. (2011) was adopted. Where label B corresponds to the lower critical point,  $\dot{M}_{\text{crit}}^-$  and label D corresponds to the upper critical point,  $\dot{M}_{\text{crit}}^+$ . If accretion equilibrium rests within the instability region, a limit cycle will ensue as labeled A-B-C-D.

approximated with  $\Sigma \simeq 2\rho H$ , where the pressure scale-height is given as  $H = c_s/\Omega$  and the sound speed is equal to  $c_s^2 \simeq T_c \mathcal{R}/\mu$ , with the effective temperature given as  $T_{\text{eff}}^4 = 8T_c^4/3\tau$ , where the optical depth is equal to  $\tau = \Sigma\kappa/2$  (Hubeny, 1990). This allows us to produce a simplistic S-curve in the  $T_{\text{eff}} - \Sigma$  plane by iterating through values of  $\rho$  and  $T_c$  where thermodynamic equilibrium holds. Figure 1.5 shows the S-curve relation at a fixed radius while assuming a temperature dependant viscosity prescription. The negative gradient in the middle of the S-curve denotes the point of thermal-viscous instability. If the point of accretion equilibrium resides at this location, then local stability is unobtainable and a limit cycle behaviour will ensue. This cyclic behaviour can be thought to begin on the stable cool branch, where the annulus accretes matter as it evolves from A-B, until reaching the lower critical accretion rate  $\dot{M}_{\text{crit}}^-$ . This is the transition point at which the temperature of the

annulus will rapidly rise as atomic hydrogen becomes ionised. Once on the stable hot branch C-D the annulus begins to lose matter until the accretion rate decreases to the upper critical value  $\dot{M}_{\text{crit}}^+$ , where hydrogen transitions from an ionised state to an atomic state.

While the thermal-viscous instability is only local in nature, it thought to globally manifest via the propagation of heating/cooling waves and is used as an explanation for the transient nature of many XRBs, which are seen to undergo luminous outbursts of a periodic nature. In order to reproduce these XRB outburst duty cycles, the viscosity normalisation is required to vary by an order of magnitude between the cold  $\alpha_c = 0.01$  (A-B) and hot  $\alpha_h = 0.1$  (C-D) branches of the S-curve. An ad-hoc temperature dependant alpha function is generally incorporated into models for the transition region between the hot and cold states in order to smooth the transition.

The current set of radiative-magnetohydrodynamic (RMHD) shearing box simulations of the MRI phenomenon have yielded only small values for the viscous normalisation  $\alpha \sim 10^{-3}$ , however Hirose et al. (2014) identified a sharp increase in  $\alpha \sim 0.1$  at the lower end of the hot branch. This is thought to originate from the strong thermal convection which occurs from the rapid opacity changes in the semi-ionised regime. The inclusion of this new alpha variation in the disc instability model (DIM) leads to excess mass within the disc, which impedes the propagation of the cooling wave and leads to re-brightening episodes during the outburst decay (Coleman et al., 2016). It thus still remains to be seen if the shearing box viscosity prescription identified in Hirose et al. (2014) is agreeable with duty cycle observations and whether the same phenomena occurs in global 3D simulations (Lasota, 2016).

### 1.4.1 The outburst decay

The light curve decay of XRBs from outburst typically show an exponential to linear transition. King & Ritter (1998) analytically demonstrated this to arise from the inclusion of self-irradiation in the DIM. The inclusion of irradiation from the highly luminous inner disc region can prevent the immediate onset of a cooling wave, this naturally produces two solutions which are outlined below in sections §1.4.1.1 and

§1.4.1.2.

### 1.4.1.1 A steady hot disc

On the assumption that irradiation maintains the disc in a steady ionised state, we can derive a time dependant solution for the central mass accretion rate  $\dot{M}_c(t)$ . If we use a mean value for the viscosity  $\nu(R) = \bar{\nu}$  and assume that the majority of the mass resides in the outer disc ( $R \gg R_{\text{in}}$ ), then the surface density can be defined as

$$\Sigma \simeq \frac{\dot{M}_c}{3\pi\nu}. \quad (1.50)$$

The mass of the hot zone (i.e. the mass of the disc that is ionised,  $R \leq R_h$ , where  $R_h$  is the outer radius of the hot zone), can then be found through shell integration of the surface density,

$$M_h = 2\pi \int_0^{R_h} \Sigma R \, dR \simeq \frac{\dot{M}_c R_h^2}{3\nu}, \quad (1.51)$$

The total mass can only change through central accretion thus  $-\dot{M}_h = \dot{M}_c$ . If we insert this relation into equation 1.51 and solve for the differential  $\dot{M}_h$  we obtain the solution

$$M_h = M_D \exp(-3\nu t/R_h^2), \quad (1.52)$$

where  $M_D$  is the mass of the disc at the start of the outburst decay, where time  $t$  is equal to zero. The accretion rate in the hot zone  $\dot{M}_h$  can be found by differentiating equation 1.52 with respect to time to find

$$\dot{M}_h = -\frac{3\nu}{R_h^2} M_D \exp(-3\nu t/R_h^2). \quad (1.53)$$

The initial mass in the disc can be estimated from the lower critical accretion rate  $\dot{M}_{\text{crit}}^-$ , however current estimates for this value fail to take account of irradiation. An alternative rough approximation gives the peak accretion rate as  $\sim 3\dot{M}_{\text{irr}}^+$  (Lasota, 2001a), where  $\dot{M}_{\text{irr}}^+$  is the critical accretion rate for an irradiated disc to remain in outburst. This gives the approximate solution

$$\dot{M}_c(t) \simeq 3\dot{M}_{\text{irr}}^+ \exp(-3\nu t/R_h^2). \quad (1.54)$$

As long as the inner disc remains stable, the XRB light curve will decay exponentially until  $\dot{M}_c < \dot{M}_{\text{irr}}^+$ , at which point the hot disc will begin to contract.

#### 1.4.1.2 A contracting hot disc

The hot disc contraction is dependant upon the irradiation temperature of the disc

$$\sigma T_{\text{irr}}^4 = \mathcal{C}_x \frac{\dot{M}_c c^2}{4\pi R^2}, \quad (1.55)$$

where  $\mathcal{C}_x$  is a parameterisation that encapsulates the geometry of the disc and is defined as,

$$\mathcal{C}_x = \eta(1 - \beta) \left( \frac{H_{\text{irr}}}{R} \right) \left[ \frac{d \ln(H_{\text{irr}})}{d \ln(R)} - 1 \right]. \quad (1.56)$$

Here  $\beta$  is the surface albedo and  $H_{\text{irr}}$  is the irradiation photospheric height, which differs from the local scale-height  $H$  (Dubus et al., 1999). If we equate the irradiation temperature to the critical value for the disc to be thermally stable  $T_h$  and assume that is radially independent, then equation 1.55 can be re-arranged to give,

$$R_h^2 = \mathcal{C}_x \frac{\dot{M}_c c^2}{4\pi\sigma T_h^4} = B_x \dot{M}_c, \quad (1.57)$$

where  $B_x$  is a simplifying constant that is dependant upon the geometry of the disc and the critical temperature. If we insert this solution into equation 1.51, then we obtain the central accretion rate

$$\dot{M}_c = \left( \frac{3\nu}{B_x} \right)^{1/2} M_h^{1/2}. \quad (1.58)$$

Once the accretion rate is below the critical value (i.e.  $\dot{M}_c < \dot{M}_{\text{irr}}^+$ ) the ionisation radius begins to contract from the outer disc,

$$\dot{R}_h = \frac{B_x \ddot{M}_c}{2R_h}. \quad (1.59)$$

The mass of the hot zone is thus dependant on the central accretion rate  $\dot{M}_c$  and the velocity of the hot zone contraction  $\dot{R}_h$

$$\dot{M}_h = -\dot{M}_c + 2\pi\Sigma R_h \dot{R}_h. \quad (1.60)$$

Substituting in equations 1.50 and 1.59 gives

$$\dot{M}_h = -\dot{M}_c + \frac{B_x \dot{M}_c}{3\nu} \ddot{M}_c. \quad (1.61)$$

If we then differentiate equation 1.58 and substitute the resulting solution into the above equation we find  $\dot{M}_h = -2\dot{M}_c$ . From equation 1.58 we then find

$$\dot{M}_h = -2 \left( \frac{3\nu}{B_x} \right)^{1/2} M_h^{1/2}. \quad (1.62)$$

Integrating this solution we can then find the time dependent mass of the accretion

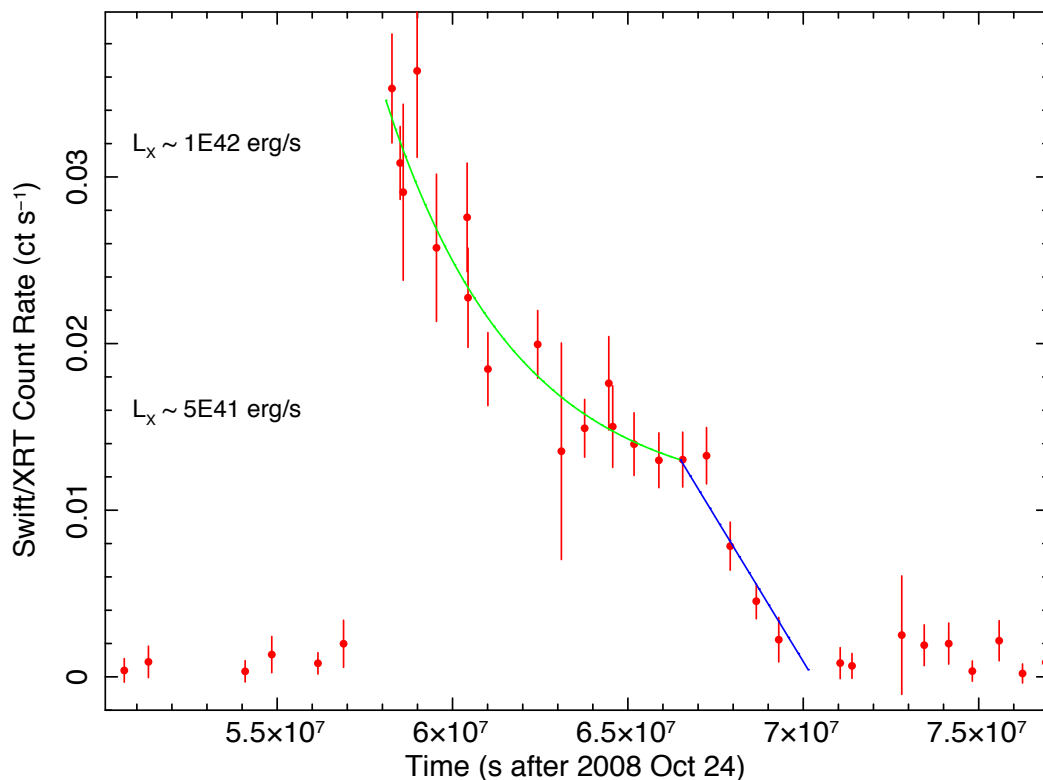


Figure 1.6: The 2010 HLX-1 outburst taken with the *Swift*-XRT camera. The light curve decay is fitted with the standard exponential (green line) to linear (blue line) scenarios. This figure is adapted from (Soria, 2013).

disc to be

$$M_h(t) = \left[ M_h^{1/2}(T) - \left( \frac{3\nu}{B_x} \right)^{1/2} (t - T) \right]^2. \quad (1.63)$$

This gives us the following central accretion rate,

$$\dot{M}_c(t) = \left( \frac{3\nu}{B_x} \right)^{1/2} \left[ M_h^{1/2}(T) - \left( \frac{3\nu}{B_x} \right)^{1/2} (t - T) \right], \quad (1.64)$$

where the linear decay phase begins at time  $T \sim \frac{1}{3}t_{\text{visc}}$  and the initial mass of the hot zone is given as  $M_h(T) \simeq \frac{1}{3}t_{\text{visc}}\dot{M}_{\text{irr}}^+$ . The viscous time is given as  $t_{\text{visc}} = R_{\text{out}}^2/\nu$ , where  $R_{\text{out}}$  is the outer disc radius.

### 1.4.1.3 Decay observations

The outburst decay equations outlined above can be modelled to light curve observations to obtain approximate values for  $M_h$ ,  $R_h$ , and  $\nu$  (Shahbaz et al., 1998; Powell et al., 2007; Soria, 2013); as well as test the general theory behind the DIM, such as the stability criteria and the outburst re-occurrence rates (Coriat et al., 2012a). Figure 1.6 shows the light curve from the 2010 HLX-1 outburst, which exhibits the standard exponential (green line) to linear (blue line) decay. It should be noted that HLX-1 is believed to be an ultra-luminous X-ray (ULX) source (i.e.  $L > 10^{39}$ ); this would imply that HLX-1 either contains an intermediate mass BH ( $10^2 - 10^5 M_\odot$ ) or that the system is accreting above the Eddington accretion rate (Farrell et al., 2009; King & Lasota, 2014; Koliopanos et al., 2017). The nature of HLX-1 may therefore be atypical of XRBs and is merely presented here to demonstrate the practical applications of the decay calculations. A more detailed discussion of these calculations is given in section §2.3.

## 1.4.2 XRB observations and spectral states

The total emission from X-ray binaries is not merely dependant upon the optically thick, geometrically thin, accretion disc, that has been outlined thus far in in this chapter. With observations requiring an additional hot coronal component, where Compton up-scatter accretion photons are used to explain the power-law like spectral

emission  $F_x \propto E^{-\Gamma}$ , where  $F_x$  is the coronal X-ray flux,  $E$  is the photon energy, and  $\Gamma$  is the photon index. These high energy photons are in turn thought to irradiate and excite atoms and ions within the disc, which produces an independent reflection emission. The relative strengths of these three components determines the broad spectral characterisation of XRBs, as either in a high-soft or low-hard state (Nowak, 1995). The soft state occurs at high accretion rates  $\dot{m} \geq 0.01$ , with the majority of the emission occurring in the soft X-ray band from the thermal disc  $\geq 75\%$  (Esin et al., 1997; Remillard & McClintock, 2006). The hard state in comparison occurs at low accretion rates with the flux emission dominated by the hard power-law tail ( $1.4 < \Gamma < 2.1$ ) and in several systems the formation of a jet (Gallo et al., 2014). The transition between these two states is often referred to as a hard or soft intermediate phase, depending on the observed variability: with changes in luminosity of several magnitudes in the hard state compared to a few percent while in the soft state (Belloni et al., 2005; Gierliński & Newton, 2006; Remillard & McClintock, 2006; Done et al., 2007). The disc evolution between these two states is thought to involve the evaporation and replacement of the inner accretion disc by an optically thin, geometrically thick, advection dominated accretion flow<sup>3</sup> (ADAF). At very low accretion rates the disc is believed to be truncated with the ADAF up-scattering disc photons producing a hard spectra. As the accretion rate increases the flow Compton cools and the thin disc expands inwards. At high accretion rates the disc extends to the ISCO, producing a soft spectra. The point of this transition remains uncertain and is the focus of this thesis, an in depth review of this topic is given in §2.1.

---

<sup>3</sup>ADAFs are one of a class of disc models for low accretion rates: with the radiatively inefficient accretion flow (RIAF), convection dominated accretion flow (CDAF), and the advection dominated inflow-outflow solutions (ADIOS), the most commonly referred to alternatives (see reviews by, Done et al., 2007; Narayan & McClintock, 2008; Yuan & Narayan, 2014). The terms ADAF and RIAF however are generally used in a more broader sense to describe these hot accretion flows (Narayan & McClintock, 2008; Yuan & Narayan, 2014).

## 1.5 The inner disc radius

The inner disc radius  $R_{\text{in}}$  can be spectrally determined from independent modelling of the disc, and the reflection features. A brief summary of the main principles underpinning these two models is presented here.

### 1.5.1 A multi-temperature blackbody disc

The accretion disc emission can be treated as a multi-temperature blackbody i.e. a summation of the thermal emission each disc annulus, where the radial temperature distribution can be obtained from equation 1.34, using the the substitution  $\sigma T_{\text{eff}}^4 = D(R)$  to find

$$T_{\text{eff}}^4 = \frac{3GM\dot{M}}{8\pi\sigma R^3} \left[ 1 - \left( \frac{R_{\text{in}}}{R} \right)^{1/2} \right]. \quad (1.65)$$

This temperature profile can then be used to calculate the frequency dependant intensity  $I_\nu$  assuming a blackbody emission

$$I_\nu(R) = \frac{2h\nu^3}{c^2} (e^{h\nu/k_B T} - 1)^{-1}, \quad (1.66)$$

where  $\nu$  is the photon frequency,  $k_B$  is the Boltzmann constant, and  $h$  is the Planck constant. The frequency flux  $F_\nu$  can then be obtained from integrating the intensity across the radial extension of the disc

$$F_\nu = \frac{2\pi \cos i}{D^2} \int_{R_{\text{in}}}^{R_{\text{out}}} I_\nu dR. \quad (1.67)$$

Figure 1.7 shows the spectral emission contribution from various annuli, where the photon energy is defined as  $E = h\nu$ . The emitted disc spectrum (purple line) is a summation of the blackbody emission across the radial extension of the disc. The majority of the disc flux is produced in the inner disc region  $6-20R_g$  (green line), with the peak blackbody emission decreasing at greater radii (blue and amber lines). If the central mass, distance to the system, and inclination of the binary orbit, are known (see section § 2.2 for details), then the spectral modelling of the disc emission can be used to determine the inner disc radius. While this spectral model provides

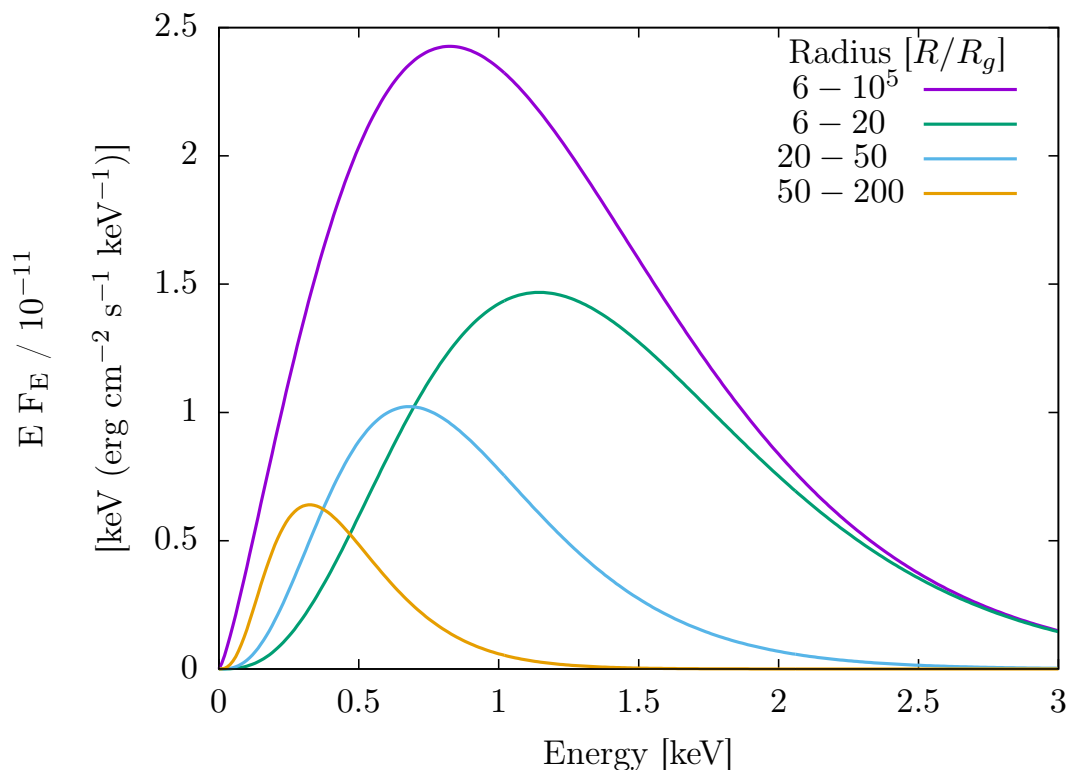


Figure 1.7: The spectral emission from various annuli around a  $10M_{\odot}$  Schwarzschild BH, accreting at  $\dot{M} = 10^{18} \text{g s}^{-1}$ . The inclination and distance were set at  $i = 0$ , and  $D = 8 \text{ kpc}$ .

an adequate approximation for the disc emission, incomplete thermalisation will lead to spectral hardening. A correction factor to the effective temperature to account for this is given as  $T = f_{\text{col}} T_{\text{eff}}$ , where  $f_{\text{col}} \sim 1.8$ , this is discussed in more detail in § 2.1. In addition to the colour correction, general relativistic effects will also impact upon the observed emission, see § 1.5.3.

## 1.5.2 The reflection slab

The upper layers of an accretion disc are thought to be irradiated by high energy photons from an optically thick corona which leads to an additional reflection emission. The physics of this process are typically approximated as an incident power-law, upon a cold disc slab. As photons enter the cold disc slab they ionise the disc resulting in electron scattering or photoelectric absorption. In the case of absorption this can lead to either fluorescent line emission or Auger de-excitation. This combination of electron scattering, fluorescent emission, and Auger de-excitation are what

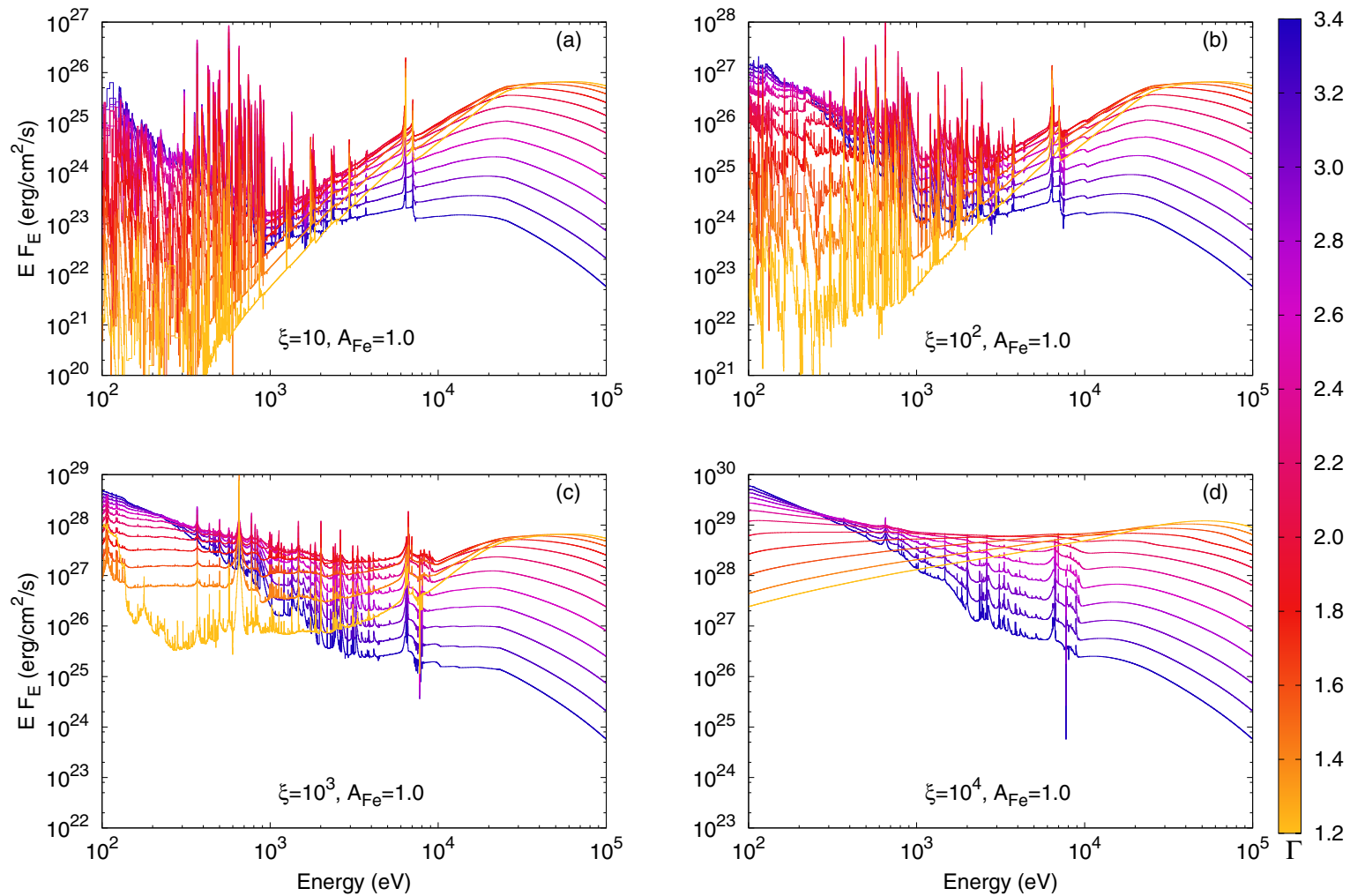


Figure 1.8: The reflection spectra produced from the *Xillver* model. The panels from (a)-(d) correspond to different ionisation values  $10 - 10^4 \text{ erg cm s}^{-1}$ . The colour coding corresponds to different power-law values, see the key on the right hand side. This figure was adapted from García et al. (2013a).

produce the reflection features. The relative strength of these processes with respect to one-another is primarily determined by the level of flux from the corona, which is encapsulated in the reflection models by the ionisation parameter  $\xi$ , which defined as

$$\xi = \frac{4\pi F_x}{n_e} \text{ erg cm s}^{-1}, \quad (1.68)$$

where  $F_x$  is the irradiation flux from the corona and  $n_e$  is the electron density. Figure 1.8 shows how the spectral shape of the reflection emission varies for different incident flux values  $F_x \propto E^{-\Gamma}$ , and across the four ionisation regimes. At low ionisation values ( $\xi < 100$ ) the iron within the disc is in the form Fe<sub>I</sub>-Fe<sub>XVII</sub>. This produces prominent Fe-K lines at  $\sim 6.4\text{keV}$  ( $\alpha$ ) and  $\sim 7.1\text{keV}$  ( $\beta$ ) and the strong absorption features below 10keV from neutral atoms. Higher incident fluxes ( $100 < \xi < 500$ ) further ionise the disc Fe<sub>XVII</sub>-Fe<sub>XXIII</sub>, which in turn weakens the Fe-K $\beta$  emission. Gradually as the disc becomes more and more ionised ( $500 < \xi < 5000$ ), the Auger effect ceases to be effective. This allows for hot iron emission from the helium and hydrogen like iron ions such as Fe<sub>XXV</sub> (6.7keV) and Fe<sub>XXVI</sub> (6.9keV). When the disc becomes highly ionised ( $\xi > 5000$ ), no lines or edges are produced and the emission is similar to the incident power-law.

The ionisation parameter obtained from current reflection models, assumes a cold slab (i.e. zero internal emission from the disc). While this is a reasonable assumption for the modelling of AGN (super-massive BHs), it fails to be the case when modelling XRBs (stellar mass BHs). This results from the fact that the ISCO is proportional to the mass of the BH, this then produces the radial temperature proportionality  $T_{\text{eff}}^4 \propto M^{-2}$ , see equations 1.42 & 1.65. The inclusion of the viscous flux would naturally lead to higher ionisation levels, with lower levels of absorption the fluorescent iron line would then strengthen (Ross & Fabian, 2007). This means that we would expect a larger value for ionisation parameter irrespective of the coronal flux, this was found to be the case in soft state analysis of Plant et al. (2014). The inner radius of the accretion disc can then be calculated from measuring the relativistic and the gravitational broadening of the reflection features, as described in the next section § 1.5.3.

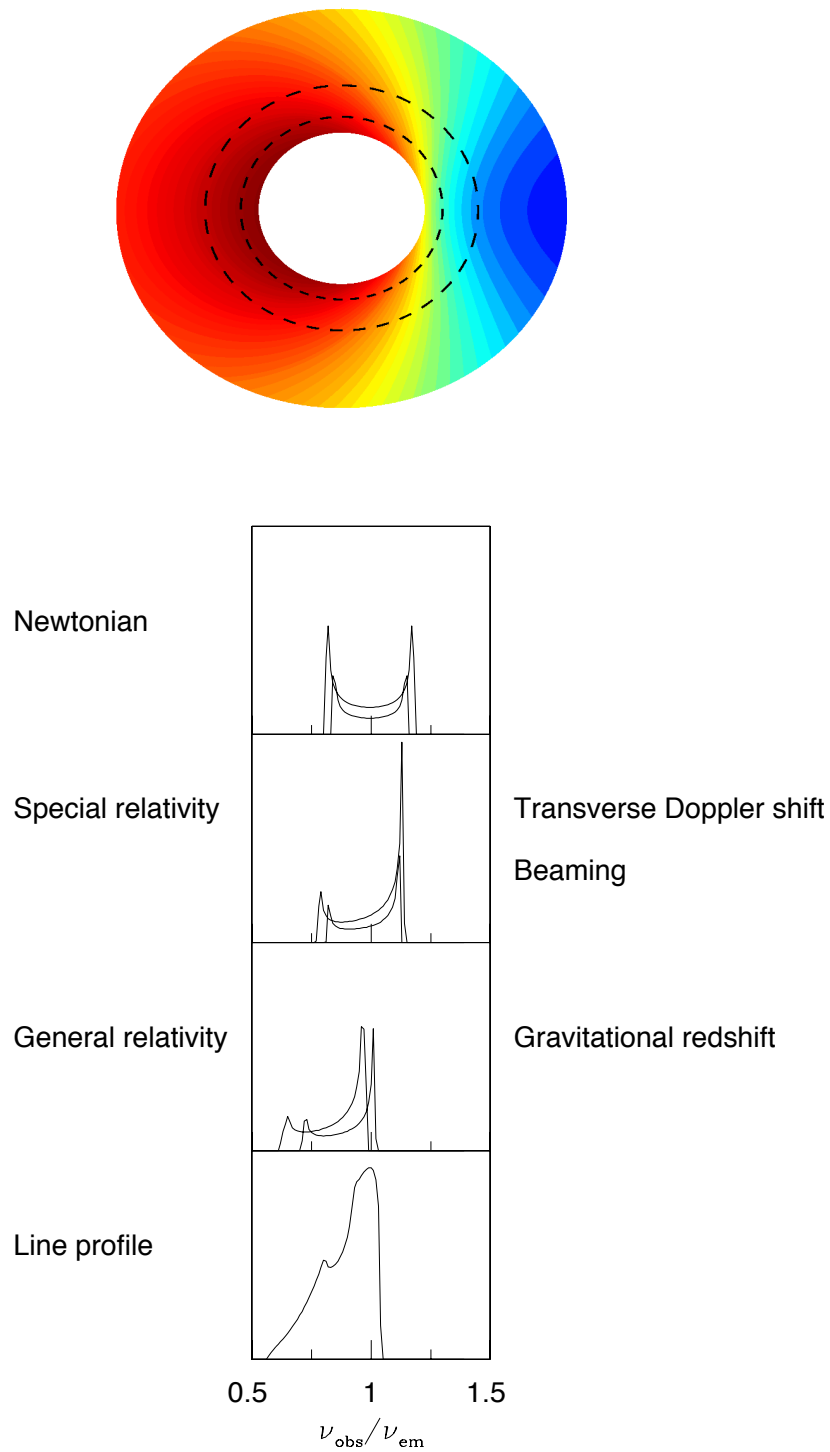


Figure 1.9: The top image shows the red and blue shift distributions for a general relativistic disc rotating in a clockwise fashion. The Fe- $K\alpha$  line profiles in the panel sections correspond to the two radii depicted as dashed lines in the top image and show the broadening effects from varying levels of increased model physicality. This figure was adapted from (Fabian et al., 2000).

### 1.5.3 Relativistic and gravitational smearing

The spectral profiles from the disc and reflection models outlined in § 1.5.1 and § 1.5.2, represent the intrinsic Newtonian emission. This ignores the rotation of the disc and the relativistic effects which are expected to feature prominently due to the extreme environment of the inner accretion disc. These physical modifications to the spectral model can be best visualised when considering the narrow Fe-K $\alpha$  line. Figure 1.9 shows the Fe-K $\alpha$  line for two separate radii and the broadening contributions from increasing the model physicality. In the top panel doppler broadening from the rotation of the disc produces red and blue broadening, with the location of the two peaks dependant upon the radial proximity of emission to the BH. The second panel shows the relativistic corrections for doppler beaming: where light aberration strengthens the emission in the direction of the observer (i.e. a strengthening of the blue wing with a weakening the red wing) and the transverse doppler effect of time dilation which reddens the total emission. The third panel shows the general relativistic effect of gravitational reddening and light bending. The final panel demonstrates the broad resultant Fe-K $\alpha$  fluorescence expected from the entire disc. While the disc and reflection broadening is dependant upon the inclination (blue shifted) and proximity of the disc to the BH (red shifted), the reflection emission is also dependant upon the emissivity: which characterises the geometry of both the corona and accretion disc (Wilkins & Fabian, 2012; Dauser et al., 2013). The emissivity radial profile is modelled as  $\epsilon \propto R^{-q}$  and typical coronal and disc geometries give  $q \sim 3$ . This means that reflection broadening is strongly dependant upon the disc emissivity as well as the extension of the disc, this is discussed in more detail in § 2.1.

## 1.6 Thesis overview

In this introduction I have explored the scientific history leading to the discovery of BHs and summarised the principle theoretical and observational knowledge of accretion discs around stellar mass BHs. In Chapter 2, I give an in-depth summary of the current debate surrounding the requirements for disc truncation which is the

---

focus of this thesis. I then outline a new approach to the truncation debate which has centred around the archetypal LMXB GX 339–4. In addition to this I highlight new constraints upon the GX 339–4 system and present a novel count rate slicing technique for the spectral analysis of the *XMM-Newton* data set. In Chapter 3, I present the results from the spectral fitting of 11 *XMM-Newton* observations using a single model grouping across both the hard and soft states. I identify only limited evidence to suggest that a fixed inner disc radius is an inadequate assumption, however several prominent residuals of unknown origin remain in the fits. In Chapter 4, I expand upon this work by analysing the spectral variations of 27 count rate sliced *XMM-Newton* hard-state spectra and I discuss the physical implication of a varying emissivity value  $q$  and the possibility of an accretion dependant colour correction factor  $f_{\text{col}}$ . In Chapter 5, I move on to consider the disc instability model, whereby I implement a simple 1D vertically averaged accretion model to investigate the HMXB LMC X-3 and its limited fall into quiescence from a long term steady state. I then consider the future work required to investigate this problem in more detail. Chapter 6 concluded my thesis, to which I summarise my main results and discuss possible avenues for future research.

# 2

An introduction to GX339-4 and the  
debate on disc truncation

In this chapter, I provide a detailed introduction to the ongoing disc truncation debate, regarding the LMXB GX 339–4 and I outline an Ockham’s razor style of approach to the issue of disc truncation. I then go on to describe the *XMM-Newton* data extraction for 11 archival observations of GX 339–4 and present a novel count rate slicing technique to extend the observational flux coverage. In the final section, I present a single collection of spectral models to be fitted across the entire spectral range, with the aim of maximising the physical consistency between each model. In order to limit the number of free variables when fitting, I re-analyse past system parameter constraints on GX 339–4 and use a set ISM values calculated by Dr. Simon Vaughan from the simultaneous *XMM-Newton* RGS data. The subsequent results and analysis of these spectral fits are presented in chapters 3 and 4.

## 2.1 Introduction

A black hole X-ray binary spectrum is typically thought to consist of three primary components (Done et al., 2007): (1) a multi-blackbody thermal component from a geometrically thin, optically thick accretion disc; (2) a hard component, thought to be from Compton up scattering of disc photons by a hot  $\sim 10^9\text{K}$ , optically thin, geometrically thick corona or possibly synchrotron radiation in cases of a jet and (3) a reflection component from the coronal irradiation of the disc. The relative strengths of these three components, are what determine the spectral characterisation of an BHXRB, as residing in a high-soft, low-hard, intermediate or quiescent state (Nowak, 1995). When in the high-soft state, the interior edge of the accretion disc is thought to reside at the inner most stable circular orbit, which is dependant upon a black hole’s mass and spin (Gierliński & Done, 2004), with the ISCO equal to  $6R_g$  for a non-rotating ( $a_* = 0$ ) Schwarzschild BH and  $1.23R_g$  for a maximally rotating ( $a_* = 0.998$ ) Kerr BH (Thorne, 1974). In the quiescent state however, our current theoretical understanding indicates that the inner accretion disc is truncated, with the inner region replaced by an optically thin, advection dominated accretion flow (ADAF), possibly through the evaporation of the accretion disc (Narayan & Yi, 1994, 1995; Chen et al., 1995; Esin et al., 1997; McClintock et al., 2001; Kub-

ota & Done, 2004; Mayer & Pringle, 2007a). This picture of a two flow (optically thin-thick) accretion disc, has also been observationally argued to be the case in the low-hard state (Esin et al., 2001; Salvo et al., 2001; Done & Diaz Trigo, 2010b; Kolehmainen et al., 2014; Plant et al., 2015, 2014a) where it is used to qualitatively explain both jet formation, which is thought to require a large disc scale-height (Meier, 2001) and also to explain the power law softening, that is observed with increased luminosity, during an outburst: where the disc’s expansion back to the ISCO, is thought to increase the Compton cooling of the ADAF (Esin et al., 1997). However in the past decade, several measurements of the inner disc radius of the LMXB GX 339–4, have lead to a questioning of this two flow model in the low-hard state (Miller et al., 2006; Tomsick et al., 2008; Reis et al., 2008, 2010; Salvesen et al., 2013).

In the following paragraphs, I present a short chronological summary of this decade long debate on the requirements of disc truncation in the low-hard state, which have primarily focused around the single XRB source GX 339–4. While little is known of this system’s fundamental parameters (see §2.2), its short duty cycle does provides an ideal platform for the study of accretion disc dynamics, across all spectral states (Coriat et al., 2012b). Where measurements of the inner disc radius, obtained either from the spectral model fitting of the Fe-K line (where doppler broadening, relativistic beaming and gravitational redshifting, all determine the emission proximity to the BH) or from the thermal disc emission (where the maximum inner disc temperature is similarly dependent upon the gravitational radius), can be used to determine both the BH spin and the level of disc truncation.

In the early months of 2004, GX 339–4 was captured undergoing an outburst while in the low-hard state, by both the *RXTE* and *XMM-Newton* X-ray telescopes. The spectral fitting of both the Fe-K line and the thermal disc component, suggested a high BH spin value of  $a_* \sim 0.9$ . This offered the first credible challenging of the two flow model in the low-hard state (Miller et al., 2006; Reis et al., 2008); however both of the fits required a disc inclination, in relation to the line of sight of  $i \simeq 18 - 20^\circ$ . With a mass function  $m = 5.8 \pm 0.5$  (Hynes et al., 2003), this would indicate either an implausible BH spin misalignment with the binary plane (Kolehmainen & Done,

2010) or an extremely large BH mass (Muñoz-Darias et al., 2008).

This result was further cast into doubt, when Done & Diaz Trigo (2010b) re-analysed the EPIC MOS data of Miller et al. (2006) and found it to suffer from heavy pile-up: this occurs when multiple photons register as a single high energy event upon a CCD. As a solution to this Done & Diaz Trigo (2010b) opted to analyse data from the *XMM-Newton* pn-camera: as the pn CCD exhibits superior read-out times over its MOS counterpart, which significantly reduces the occurrence of pile-up when observing bright sources. The analysis of Done & Diaz Trigo (2010b) resolved a more narrow Fe-K line ( $R_{\text{in}} > 6R_g$ ) and also a less problematic disc inclination,  $i \sim 45^\circ$ , than that previously obtained in the Miller et al. (2006) analysis. This allowed Done & Diaz Trigo (2010b) to suggest that pile-up in the MOS data had been artificially broadening the modelled Fe-K line and masking disc truncation, however the thermal component of their model still required a thin disc within close proximity of the ISCO. This same model inconsistency between the Fe-K line and the thermal disc component is also apparent in the Plant et al. (2015) study; which analysed archival *Suzaku*, and *XMM-Newton* observations of GX 339–4, in the low-hard state. In that analysis, Plant et al. (2015) identified a gradual broadening of the Fe-K line with increasing flux, across each of the outburst-rising observations: consistent with a heavily truncated disc expanding back to the ISCO. The thermal disc component however remained stationary within the ISCO region across each of these observations.

This contradiction in the measurements of the inner disc radius, between the reflection and thermal components, can not be easily reconciled as a truncated disc: as the strength of the thermal flux contribution in the bright hard-state is incompatible with the observed re-occurrence times (Steiner et al., 2017). This is clearly demonstrated in the Plant et al. (2014) analysis of the *RXTE* data set for GX 339–4, where the high disc flux obtained in several of the fits, correspond to a super Eddington accretion rate based on the Fe-K line measurements of the inner disc. This implies either a considerable over estimation of the thermal disc component or an artificial narrowing of the Fe-K line, when modelling the spectra of GX 339–4. This inconstancy in measuring the inner disc radius was first highlighted

in Kolehmainen et al. (2014), which analysed the *XMM-Newton* data of several XRBs including GX 339–4. In the Kolehmainen et al. (2014) analysis they identified no apparent correlation in the difference between the two methods, which may arise for a multiple reasons: model assumptions breaking down, parameter degeneracies within the fit, instrument calibration issues or a poor capture of the disc-coronal continuum.

The hard state reflection component in GX 339–4 may also be more complex than previously thought, as several studies have identified an additional reflection component, with narrow neutral features (Kolehmainen et al., 2014; Fürst et al., 2015; García et al., 2015). In addition to this, the GX 339–4 reflection modelling of Fürst et al. (2015) and García et al. (2015) required a super solar abundance of iron in the disc  $A_{\text{Fe}} \gg 1$ , to fit both the Fe-K line and the Compton-hump<sup>1</sup>. The García et al. (2015) study of *RXTE* data identified  $R_{\text{in}} < 6R_{\text{g}}$  across a large range of luminosities  $1.6 - 17\%L_{\text{Edd}}$ . Neither of the study however required a disc component owing the lower sensitivity of the XRT instrument (Fürst et al., 2015) and the hard X-ray band coverage ( $> 3$  keV) of the Nustar (García et al., 2015).

In a re-analysis of the hard state *XMM-Newton* data, Basak & Zdziarski (2016) found the disc inner edge to truncate with increasing flux when tying the inner disc radius of the multi-blackbody and reflection components to one another. With no obvious physical explanation for such a variation, Basak & Zdziarski (2016) re-fitted the spectra while ignoring the soft X-ray emission  $< 2.35$  keV in which they identify a heavily truncated disc which would require a super Eddington accretion rate (Steiner et al., 2017).

An alternative possibility to consider, is the basic assumptions concerning the geometry of both the corona and the disc in the reflection fitting. This is primarily determined by the inverse radial emissivity value  $q$ , which is typically assumed to be equal to 3, with the emissivity decaying as  $\epsilon \propto R^{-3}$ . If the geometry of the disc or corona differ from this standard picture however and  $q$  is allowed to vary or if the emissivity is represented by a broken power law instead, then the obtained

---

<sup>1</sup>García et al. (2015) highlight that the requirement for  $A_{\text{Fe}} \gg 1$  is predominantly driven by the model fitting of the Compton-hump as opposed to the Fe-K line.

value for  $R_{\text{in}}$  could be substantially different from that obtain with a canonical value fit. A similar assumption, which is made when considering the thermal disc emission, is the colour-correction/hardening factor  $f_{\text{col}}$ . The colour correction factor is defined as  $f_{\text{col}} = T_c/T_{\text{eff}}$ , where  $T_c$  and  $T_{\text{eff}}$  are the colour and effective temperatures respectively. This corrects for the hardening of the blackbody thermal emission due to incomplete Comptonisation within the disc. The colour correction factor has generally been assumed to be constant at  $f_{\text{col}} \sim 1.7 - 2$  based on theoretical and high state observational studies (Shimura & Takahara, 1995; Davis et al., 2005; Dunn et al., 2011). The inverse proportionality between the colour correction factor and the inner disc radius ( $f_{\text{col}}^{-2} \propto R_{\text{in}}$ ) (Kubota et al., 1998), allows for disc truncation in the low-hard state to be explained by a variation in  $f_{\text{col}}$  (Merloni et al., 2000; Salvesen et al., 2013). Salvesen et al. (2013) using XRTE data on GX339-4, found that a change in  $f_{\text{col}}$  by a factor of 2.0 – 3.5, could be used to explain the spectral changes usually attributed to disc truncation. These variation in  $f_{\text{col}}$  could be due to the increased fractional emission from the corona in the hard-state, where coronal irradiation of the disc fails to thermalise, causing a hardening in the disc emission (Merloni et al., 2000).

The majority of results suggesting a truncated disc based on the Fe-K line, appear to come with the caveat of requiring a thermal disc component close to the ISCO. However if we relax our assumptions about both the reflection and thermal components regarding the priori values for  $q$  and  $f_{\text{col}}$ , then we can attempt to consistently fit the inner radius and resolve the previous discrepant findings.

In this study we utilise all available *XMM-Newton* observations of GX 339–4 made with the EPIC-pn camera, in both 'burst' and 'timing' modes, expanding upon previous studies which have either limited themselves in terms of the spectral states considered (Done & Diaz Trigo, 2010b; Kolehmainen & Done, 2010; Plant et al., 2015, 2014a) or to the sole fitting of the Fe-K component (García et al., 2015; Fürst et al., 2015). In the low-hard state, the flux variability is typically much higher and so for this reason we have binned the data based on the count rate, allowing us to achieve unprecedentedly low flux values for GX 339–4.

We aim in this reanalysis of the *XMM-Newton* data, to use the most physically

motivated and consistent grouping of relativistic models to date for both the high-soft and low-hard state observations. In order to better evaluate the requirement for disc truncation in the bright hard state, we crucially fix the inner radius at the ISCO for a Schwarzschild BH, while allowing both  $q$  and  $f_{\text{col}}$  to be free and retroactively consider the physicality of these parameter variations and the quality of the fits obtained.

The two major sources of uncertainty in previous have been the disc inclination and interstellar absorption (ISM). The first of these is due to the limited detection of the secondary star in GX 339–4, which has led to a wide range of fundamental parameters for the BH mass, inclination and distance, being taken or spectrally obtained. To address this we use Muñoz-Darias et al. (2005) fourth order K2 correction function, on Hynes et al. (2003) Bowen fluorescence observations, in order to obtain the best possible constraints on both the BH mass and inclination, that can currently be made.

The value taken for the ISM hydrogen column density to GX 339–4, has similarly taken a wide range of values ( $N_{\text{H}} \simeq 0.4\text{--}0.7 \times 10^{22} \text{cm}^{-2}$ ). In order to better estimate the line of sight absorption, we uniquely make use of the simultaneously taken RGS soft X-ray observations across all our observations where possible, while using the highest resolution absorption model currently available. This has allowed us to test claims of  $N_{\text{H}}$  variability with flux (Cabanac et al., 2009a) and also obtain the most accurate ISM column density to GX 339–4 to date.

Several studies based on the spectral fitting of soft state observations have suggested that GX 339–4 contains a high spinning BH ( $a_* \sim 0.9$ ) (Miller et al., 2004, 2008; Reis et al., 2008). Individual measurements of the inner disc even in the high state remain extremely uncertain, despite the statistical model errors appearing reasonably small; this is owing to the limited knowledge of GX 339–4 fundamental parameters and uncertain model degeneracies. We thus caution on the side of simplicity, with the assumption of a Schwarzschild BH. While this assumption is unlikely to be correct, it should provide a close approximation for  $R_{\text{in}}$  while in the soft state and break down in the hard state if large disc truncation occurs (Done & Diaz Trigo, 2010b; Kolehmainen & Done, 2010; Plant et al., 2015, 2014a).

## 2.2 System Parameters

The three primary system parameters: mass, inclination, and distance, have only ever been weakly constrained in the LMXB GX 339–4, primarily due to the difficulty of detecting, the system’s donor star (Hynes et al., 2004). This has naturally resulted, in past studies, employing a wide range of free and fixed values, in their spectral model fittings. In order to overcome this and limit possible model degeneracies or inconsistencies, all primary system parameters are fixed to the chosen values discussed in this chapter, in which I re-analyse the current mass and inclination constraints and present a summary of the available distance estimates.

### 2.2.1 Constraining the mass and inclination

In GX 339–4, the continuum emission from the donor star can not be detected, even when the system is in a quiescent state (Hynes et al., 2004). Hynes et al. (2003), however were able to detect, a series of sharp  $N_{III}$  emission components traveling at over  $\sim 300 \text{ km s}^{-1}$  from the system and attributed this to be Bowen fluorescence from the irradiated donor star. Combining all their velocities measurements and fitting sinusoidal velocity curves, they obtained the orbital velocity  $K_{\text{em}} = 317 \pm 10 \text{ km s}^{-1}$  and orbital period  $P = 1.7557 \pm 0.0004 \text{ d}$ . This  $K_{\text{em}}$  measurement however is only a lower limit to the true orbital velocity, as the Bowen emission should originate from the inner irradiated face of the donor star and thus requires a correction factor.

$$K_2 = \frac{K_{\text{em}}}{1 - f(1 + q)}, \quad (2.1)$$

where  $K_2$  is the corrected radially velocity and  $q$  the mass ratio of the system. The correction factor  $f$  can be crudely estimated by assuming the emission line originates at L1, however this ignores irradiation across the Roche lobe photosphere. To correct for this Muñoz-Darias et al. (2005), simulated an isotropic irradiation of a Roche lobe geometry divided into  $10^5$  triangular tiles, for which they provide a 4th order polynomial fit,

$$f_{\text{max}} = 0.116 + 0.946q + 1.947q^2 + 2.245q^3 + 1.002q^4. \quad (2.2)$$

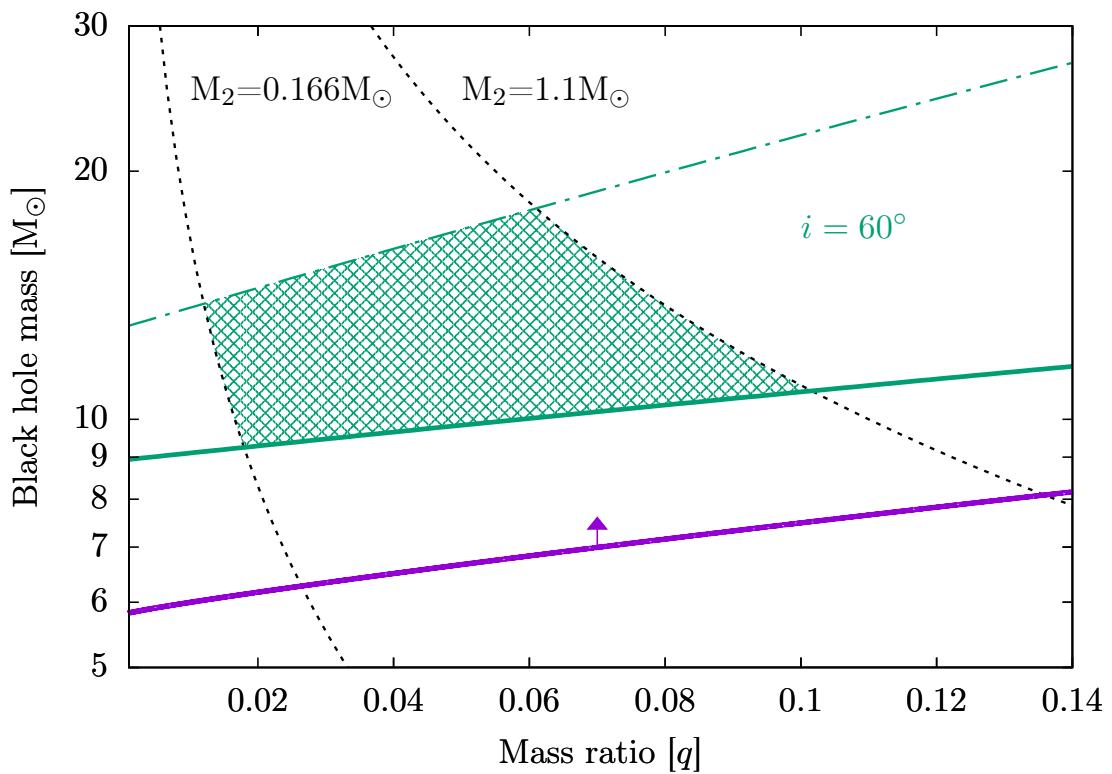


Figure 2.1: The BH mass determination. The two vertical black dashed lines are the limits on the donor star mass. The solid horizontal lines correspond to different inclinations: an upper limit on  $i$  from the absence of eclipses (purple) and  $i = 60^\circ$  (green). The solid lines assume no  $K_2$  correction, the dashed line uses  $f_{\text{max}}$ ; with the green hash region covering all plausible mass values at  $i = 60^\circ$ .

This  $K_2$  correction, however only allow for a tighter range on the mass function, in order to obtain a BH mass estimate, constraints must also be placed upon the donor star mass. While little is known of GX 339–4 companion star, Muñoz-Darias et al. (2008) were able to speculate on its nature due to its short orbital period, and non detection, which identified it as a likely helium sub-giant with a mass of  $0.166M_\odot \leq M_2 \leq 1.1M_\odot$ . Muñoz-Darias et al. (2008) also went on to estimate a lower mass limit for the BH using Muñoz-Darias et al. (2005) minimum correction factor  $f_{\min} \cong R_2^2/a^2$ , which takes account of disc screening of the donor star. However this  $f_{\min}$  correction, is merely an artefact from the use of the small angle approximation and thus should not be applied. A re-analysis of the  $M_{\text{BH}}$  verses  $q$ , using the the  $K_2$  correction factor of equation 2.2, is presented in figure 2.1 (see caption for details).

As is the case for most XRBs, the inclination angle of GX 339–4 is relatively unknown, though with little evidence of a disc wind (Ponti et al., 2012) and no signs of an eclipsing companion star (Cowley et al., 2002), an upper limit for the inclination, is commonly proposed at  $i \leq 60^\circ$ . As disc shielding of the companion is likely to be weak, the  $K_2$  correction should be close to  $f_{\max}$ , which would give a BH mass range of  $13.80\text{-}18.02M_\odot$  ( $i = 60^\circ$ ) and  $68.00\text{-}72.95M_\odot$  ( $i = 30^\circ$ ). On the assumption that the BH spin axis, is not misaligned with the binary plane, this would appear to rule out a low inclination source (Kolehmainen & Done, 2010), indicating  $i \sim 60^\circ$ ; with the low duty cycle of GX 339–4 suggesting a BH mass of  $M_{\text{BH}} = 18.021_{-1.344}^{+1.324}M_\odot$  (Muñoz-Darias et al., 2008).

### 2.2.2 Distance estimates

Constraints on the distance to GX 339–4 have been made using several different techniques and early estimates suggested a distance in the region of  $\sim 4\text{kpc}$ , though more recently measurements have suggested this could be much larger. The most robust method of determining the distance to GX 339–4 to date, has been achieved through the spectral fitting of the line of sight velocity structure. This technique however, has failed to converge on a standard result, with Buxton & Vennes (2003) obtaining  $D \sim 4 \pm 1\text{kpc}$  from the equivalent width measurements of Ca II-K and  $D \sim 7 \pm 2\text{kpc}$  for the two measured Na-D lines. In Hynes et al. (2004) improved

high resolution fits of the Na-D absorption lines established a distance beyond the tangent point  $D \geq 6$  and that GX 339–4 could even possibly reside on the other side of the galaxy  $D \sim 15\text{kpc}$ . A larger distance is also supported by the small systemic velocity measurements reported in Hynes et al. (2003) for the He II wings (Hynes et al., 2004).

The majority of alternative techniques, have similarly proposed large distances to GX 339–4, with Zdziarski et al. (2004) constraining the non-detection of the donor star, to an apparent diameter of  $s_\star \lesssim 3.2\mu\text{as}$ , allowing them to obtain a inclination dependant distance value of  $D > 6.7 \sin^{-1}i \text{ kpc}$ . However uncertainty over the distance to GX 339–4 continues to persist, with Gallo et al. (2004) identifying the March 2003 radio jet head at approximately  $s_j \sim 12\text{as}$  away from the core and tentatively suggested that the emission may have originated from the May 2002 radio flare observed in GX 339–4; in order for the jet to be sub-luminal an upper distance constraint of  $D \lesssim 4.3\text{kpc}$  would be required, though in contradiction of the majority of distance estimates, this is unlikely to be the case.

An additional, though significantly less robust technique, to those outlined above is the observationally derived, statical-distance relation of Maccarone (2003). In which Maccarone, investigated several well constrained XRBs and found the soft to hard state transition, to occur at a fixed fraction of the Eddington Luminosity and thus as a standard candle. With this relation, Maccarone (2003) were able to place a lower limit on the distance to GX 339–4 of  $D \geq 7.6\text{kpc}$  (With a higher mass estimate, such as that reported in §2.2, this lower limit would rise to  $D \sim 11.7\text{kpc}$ ). While this is a crude estimate, combined with fits of the Na-D absorption lines (Buxton & Vennes, 2003; Hynes et al., 2004), it does support the notion of  $D > 4\text{kpc}$ , with Zdziarski et al. (2004) suggesting that the most likely distance is close to  $\sim 8\text{kpc}$ .

## 2.3 A transient LMXB

Analytical solutions and parameterisations, can offer invaluable insight into accretion disc dynamics and provide a useful tool in the analysis of spectral fitting results.

In this section, I provide order of magnitude estimates of the expected accretion rates at S-curve transitions from the cold and hot states; the viscous time requirements for disc truncation, and an evaluation of the BH mass estimates from §2.2, based on the duty cycle rates.

### 2.3.1 The thermal-viscous instability

XRBs are generally observed to be transient in nature, spending the majority of their existence in a quiescent state, while semi-periodically entering an outburst phase (Coriat et al., 2012a). This transient nature has been qualitatively explained by the thermal-viscous instability, in which an incremental increase in the accretion rate of a cold disc, can lead to the partially ionisation of hydrogen and a subsequent run-away in the opacity and disc temperature (thermal instability), which in turn is thought to trigger a sharp rise in the viscosity (viscous instability) (Meyer & Meyer-Hofmeister, 1981; Dubus et al., 1999; Lasota, 2001b). These two instabilities combine, to produce an S-curve in the  $\Sigma - \dot{M}$  diagram; where at the instability, the mass accretion rate  $\dot{M}$  is found to increase, with a decreasing surface density  $\Sigma$ , which naturally leads to a limit cycle behaviour for any secondary accretion rate that resides in this region. While the thermal-viscous instability is only a local phenomenon, it is thought to globally manifest via the propagation of heating or cooling waves and thus acts as a switch for the accretion of matter from the outer disc (King & Ritter, 1998; Frank et al., 2002a). The critical mass accretion rates for a solar composition disc, to enter ( $\dot{M}_{\text{crit}}^-$ ) and remain ( $\dot{M}_{\text{crit}}^+$ ) in outburst, have been parameterised by Lasota et al. (2008); the subscripts (- & +) respectively refer to the cold-lower and hot-upper branches of the S-curve,

$$\dot{M}_{\text{crit}}^- = 2.64 \times 10^{15} \alpha_{0.1}^{0.01} R_{10}^{2.58} M_1^{-0.85} \text{ g s}^{-1} \quad (2.3)$$

and

$$\dot{M}_{\text{crit}}^+ = 8.07 \times 10^{15} \alpha_{0.1}^{-0.01} R_{10}^{2.64} M_1^{-0.89} \text{ g s}^{-1}, \quad (2.4)$$

Table 2.1: Primary and secondary mass constraints for GX 339–4 and the corresponding critical accretion rates; viscous times; quiescence and outburst times, and duty cycle rates.

mass [ $M_\odot$ ]		critical rate [ $10^{-2}$ ]			$t_{\text{visc}}$ [ks]			time [yrs] [ $10^{-2}$ ]		
$M_2$	$M_1$	$\dot{m}_{\text{crit}}^-$	$\dot{m}_{\text{crit}}^+$	$\dot{m}_{\text{irr}}^+$	$50R_g$	$100R_g$	$200R_g$	$t_q$	$t_b$	$\tau_c$
1.1	18.02	22.7	81.4	7.0	2.4	6.1	15.5	6.85	1.93	22.0
0.166	13.80	32.1	116	9.4	1.6	4.0	10.1	92.2	1.64	1.75

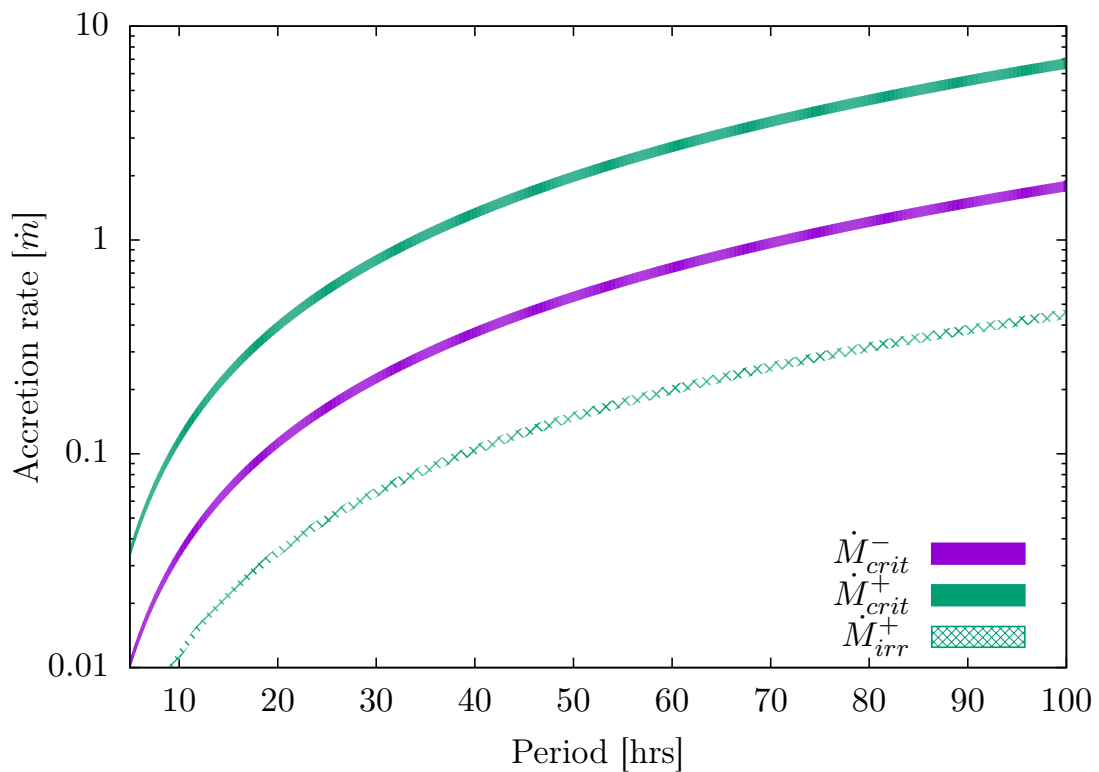


Figure 2.2: The critical accretion rate in Eddington units against the binary period in hrs for a  $10M_\odot$  BH. The solid green area covers  $\dot{M}_{\text{crit}}^+$ ; the solid purple area is for  $\dot{M}_{\text{crit}}^-$ , and the dashed green area is for  $\dot{M}_{\text{irr}}^+$ .

where the alpha-viscosity term is normalised as  $\alpha_{0.1} = \alpha/0.1$ ; the radius term is given as  $R_{10} = R/10^{10}$  cm and  $M_1$  is the mass of the BH, in solar masses. In order to facilitate the accretion of the cool outer disc mass reserves, the region must first transition to an ionised state. If we assume that the outer annulus is self ionising, then an estimation of the outer disc radius,  $R_{\text{out}}$ , can be used calculate the critical mass accretion rates.

The outer disc is deterred by the strength the tidal torques from the secondary star, which removes angular momentum from the outer disc. Paczyński (1977) provides an estimate of the outer disc radius, by modelling the maximum non-intersecting particle orbits, in which he parameterises the results in terms of  $a$ , the binary separation given by Kepler's law and  $q = M_2/M_1$ , the mass ratio, with

$$\frac{R_{\text{out}}}{a} = \frac{0.60}{1+q} \quad 0.03 < q < 1 \quad (2.5)$$

and

$$a = 3.53 \times 10^{10} M_1^{1/3} (1+q)^{1/3} P_{\text{orb}}^{2/3} (\text{h}) \text{ cm}, \quad (2.6)$$

as this solution assumes a cold disc, the outer accretion edge may in fact be larger than this. The critical accretion rates given in equations 2.3 and 2.4 are for a non-irradiated disc. While this is argued to be the case during quiescence, it is unlikely to remain true at the higher accretion rates, where self-irradiation is thought to significantly alter the vertical disc structure (Dubus et al., 1999). To account for this, Lasota et al. (2008) have parameterised the critical accretion rate, for a self-irradiated, ionised disc.

$$\begin{aligned} \dot{M}_{\text{irr}}^+ &= 9.5 \times 10^{14} \mathcal{C}_{-3}^{-0.36} \alpha_{0.1}^{0.04-0.01 \log \mathcal{C}_{-3}} R_{10}^{2.39-0.10 \log \mathcal{C}_{-3}} \\ &\times M_1^{-0.64+0.08 \log \mathcal{C}_{-3}} \text{g s}^{-1}, \end{aligned} \quad (2.7)$$

where  $\mathcal{C}_{-3} = \mathcal{C}_x / 10^{-3}$ , is the X-ray heating coefficient; which is primarily dependant upon the albedo, and irradiation height of the disc and is typically taken as

$\mathcal{C}_x \simeq 10^{-3}$  (Gierliński et al., 2009). The observational physicality of the transition estimations that are present in Lasota et al. (2008), can be loosely evaluated by considering an archetypal LMXB system. In figure 2.2, the critical accretion rates, which are normalised to the Eddington luminosity, are plotted against the orbital period, assuming a  $10M_\odot$  Schwarzschild BH and a mass ratio of  $q = 0.03 - 0.1$ . With the Eddington units defined as  $\dot{m}_{\text{crit}} = \eta \dot{M}_{\text{crit}} c^2 / L_{\text{Edd}}$ ; where  $L_{\text{Edd}}$  is the Eddington luminosity (Frank et al., 2002b) and  $\eta$  the accretion efficiency (Bardeen et al., 1972), see equations 2.8 and 2.9 respectively. The dimensionless alpha-viscosity term is assumed to transition by one dex between the hot ( $\alpha_h = 0.1$ ) and cold ( $\alpha_c = 0.01$ ) branches,

$$L_{\text{Edd}} = 4\pi GMm_p C / \sigma_T \simeq 1.3 \times 10^{38} (M/M_\odot) \text{ erg s}^{-1} \quad (2.8)$$

and

$$\eta = 1 - \sqrt{1 - (2R_g/3R_{in})}. \quad (2.9)$$

In the non-irradiated disc scenario, we can see from figure 2.2: that LMXB systems with periods greater than 20 days, would require an  $\dot{m} \geq 0.1$ , just to enter in to outburst. A quiescent accretion rate this high, would require an unfeasible donor star mass transfer to the disc and a super Eddington accretion rate while in outburst, with  $\dot{m}_{\text{crit}}^+ \geq 0.37$ . This is clearly not supported by observations (Done et al., 2007; Coriat et al., 2012a) and demonstrates the importance of self-irradiation even in the quiescent state. The original proportionality argument that suggested that self-irradiation was inconsequential in the quiescent state, was put forward by Dubus et al. (1999), in which they assumed  $\dot{M}_{\text{crit}}^- \propto R^{2.65}$  (Hameury et al., 1998) and subsequently found viscous heating to dominate in the outer disc  $D_{\text{vis}}/D_{\text{irr}} \propto R^{1.65}$ : where  $D_{\text{vis}}$  and  $D_{\text{irr}}$  correspond to the viscous and irradiation energy fluxes, see equations 2.10 and 2.11 respectively. However this appears to ignore the dependency of  $D_{\text{irr}}$  upon  $\dot{M}$  and the result should in fact closer resemble  $D_{\text{vis}}/D_{\text{irr}} \propto R^{-1}$ .

The radius at which the irradiative energy density dominates the accretion power ( $D_{\text{irr}} \geq D_{\text{vis}}$ ), is not synchronous with the irradiation flux dominating the radiative

transfer equations, as this would only occur if  $D_{\text{irr}} \geq \tau_{\text{tot}} D_{\text{vis}}$ ; where  $\tau_{\text{tot}}$  is the total optical depth of the disc, with typical values of  $10^2 - 10^3$  at large radii (Dubus et al., 1999). Irradiation however does modify the disc instability properties and can significantly reduce the effective temperature at which point the disc becomes unstable (Hameury et al., 1998; Dubus et al., 1999; Lasota et al., 2008).

$$D_{\text{vis}} \simeq \frac{3GM\dot{M}}{8\pi R^3} \quad (2.10)$$

and

$$D_{\text{irr}} = \mathcal{C}_x \frac{\dot{M}c^2}{4\pi R^2}. \quad (2.11)$$

In the case of an irradiated disc, the critical accretion rate required to remain in outburst reduces to  $\dot{m} \geq 0.033$  for an orbital period of  $P \geq 20$  days, which is inline with observational constraints (MacCarone, 2003); the self contradicting relation  $\dot{M}_{\text{crit}}^- > \dot{M}_{\text{irr}}^+$  also holds for all orbital periods, further highlighting the effects that irradiation must have upon a non-ionised disc. In table 2.1, I present the critical accretion rates, normalised in Eddington units for GX 339–4, assuming the system parameter ranges calculated in §2.2. On the assumption that the non-irradiated values are unphysical, we can expect the transition from outburst to occur at an accretion rate of  $\dot{m} = 6.96 - 9.40 \times 10^{-2}$  (this this can treated as an upper limit, as an outburst is likely to originate from the circularisation radius: where the initial angular momentum of the accreting matter is equal to that of a circular orbit).

### 2.3.2 The viscous time

The viscous time is the theoretical timescale for the re-distribution of angular momentum within a disc annulus: defined as  $t_{\text{visc}} \sim R^2/\nu$ , where  $\nu$  is the viscosity term. A lower constraint for the truncation or expansion of a thin disc, can be calculated from estimating the viscous time; here I consider three typical truncation radius values: 50, 100, and  $200R_g$  (see: Esin et al., 2001; Salvo et al., 2001; Done & Diaz Trigo, 2010b; Kolehmainen et al., 2014; Plant et al., 2015, 2014a). At these

relatively short radii, the disc is likely to be highly ionised, with electron scattering dominating the opacity  $\kappa_R \simeq 0.4 \text{ cm}^2 \text{ g}^{-1}$  (Frank et al., 2002b). As radiation pressure dominated alpha-viscous discs are unstable (Lightman & Eardley, 1974), I choose to assume an ad-hoc ideal-gas equation of state, in deriving the viscosity parameterisation shown in equation 2.12.

$$\nu = 1.1 \times 10^{14} \alpha_h^{4/5} \dot{M}_{16}^{2/5} M_1^{-1/5} R_{10}^{3/5} f^{8/5} \text{ cm}^2 \text{ s}^{-1} \quad (2.12)$$

Where the zero torque inner boundary correction parameter  $f = [1 - (R_{\text{in}}/R)^{1/2}]^{1/4}$ ; acts as an approximation for the reduced viscous energy generation, that occurs in the vicinity of the ISCO region. The accretion rate can then be estimated from the upper *RXTE* hard state flux limit,  $F_{\text{peak}} \leq 10^{-7.5} \text{ erg cm}^{-2} \text{ s}^{-1}$  (Plant et al., 2015), on the assumption that the disc is isotropically emitting, around a Schwarzschild BH. While this assumes the entire flux emission originates from the disc, it does provide an order of magnitude lower limit for the viscous time; which suggests that disc variations occur on kilo-second time scales and indicates that significant changes in  $R_{\text{in}}$  are unlikely to occur between the *XMM-Newton* count rate sliced observations presented in this work, see table 2.1 and §2.4.1.

### 2.3.3 Duty cycle

Analytical estimates of the duty cycle can be used to both evaluate the ad-hoc alpha-viscosity prescription, and to place further constraints upon a systems fundamental mass values. The duty cycle is typically defined as:  $\tau_c = t_b/(t_b + t_q)$ ; in the case GX 339–4 the quiescent time span  $t_q$ , and outburst time span  $t_b$  are roughly equal at approximately 2 years, with a high LMXB duty rate of  $\tau_c \sim 50\%$  (Coriat et al., 2012a). The time spent in quiescence can be approximated as  $t_q \simeq M_D/|\dot{M}_2|$ ; where the complete mass replenishment of the disc, via the secondary accretion rate is assumed. With the total mass of the disc prior to outburst, calculated as  $M_D = \pi R_{\text{out}}^2 \Sigma_d$ ; where the outer disc surface density is taken as equal to the critical density  $\Sigma_{\text{crit}}^-$ , parameterised by Lasota et al. (2008),

$$\Sigma_{\text{crit}}^- = 74.6 \alpha_{0.1}^{-0.83} R_{10}^{1.18} M_1^{-0.40} \text{ g cm}^{-2}, \quad (2.13)$$

and the secondary accretion rate is assumed to be equal to that from a helium sub-giant, parameterised by King (1988),

$$-\dot{M}_2/m_2 = 5.4 \times 10^{-9} (m_c/0.25)^{7.11} M_\odot \text{ yr}^{-1}. \quad (2.14)$$

The donor stars total mass  $m_2$  ( $0.166 - 1.1 M_\odot$ ) and core mass  $m_c$  ( $0.166 - 0.187 M_\odot$ ) are given in solar mass units (Muñoz-Darias et al., 2008). This estimate however gives an unfeasibly large quiescent time span of  $19 - 272 \times 10^3$  years, which again highlights the issues of neglecting the effects of irradiation in the cold disc state. With no parameterisation for the critical irradiated surface density  $\Sigma_{\text{irr}}^-$ , a lower based estimate for the outer disc density is calculated assuming  $\Sigma_d \simeq \dot{M}/3\pi\nu$ . The accretion rate is estimated from the minimum hard state flux value obtain from *RXTE* data, with  $F_{\text{min}} \geq 10^{-10.5} \text{ erg cm}^{-2} \text{ s}^{-1}$  (Plant et al., 2015) and the viscosity term is given by equation 5.49 of Frank et al. (2002b): in which they assume a steady state gas pressure dominated disc, with Kramers' opacity  $\kappa_R \simeq 5 \times 10^{25} \rho T_c^{-7/2} \text{ cm}^2 \text{ g}^{-1}$ . It should also be noted that the normalisation of equation 2.15 is corrected from Frank et al. (2002b),

$$\nu = 2.88 \times 10^{14} \alpha^{4/5} \dot{M}_{16}^{3/10} M_1^{-1/4} R_{10}^{3/4} f^{6/5} \text{ cm}^2 \text{ s}^{-1}. \quad (2.15)$$

This estimation gives a more reasonable quiescent time span of  $6.9 - 92$  years and favours the high donor star mass values, as identified in Muñoz-Darias et al. (2008). To accompany this and calculate the expected duty cycle rate, the outburst time,  $t_b$  is estimated from the standard exponential to linear decay scenario, as outlined in King & Ritter (1998),

$$t_b \simeq \frac{R_{\text{out}}^2}{3\nu} \left[ 1 + \ln \frac{\dot{M}_{\text{max}}}{\dot{M}_{\text{irr}}^+} \right], \quad (2.16)$$

where  $\dot{M}_{\text{irr}}^+$  is given by equation 2.7 and  $\dot{M}_{\text{max}}$  is calculated from the peak *RXTE* hard state flux,  $F_{\text{peak}} \leq 10^{-7.5} \text{ erg cm}^{-2} \text{ s}^{-1}$  (Plant et al., 2015). This gives an outburst

time of between 1.6 – 1.9 years, which is in reasonable agreement with observations (Coriat et al., 2012a) and provides a duty cycle of  $\tau_c \simeq 1.7 - 22\%$ , which clearly favours the higher mass BH and donor star, see table 2.1.

## 2.4 Observations and data reduction

Since its discovery in 1971, GX 339–4 has been a significant target for all major X-ray missions: owing to its high luminosity, and short duty cycle (Markert et al., 1973; Smith et al., 1999; Miller et al., 2004; Miller et al., 2008; Tomsick et al., 2008; Coriat et al., 2012a). The free availability of these extensive archival data sets can now be exploited, in the study of accretion disc dynamics across the spectral states (Plant et al., 2015). In this section, I present a spectral reduction of close to a decade of *XMM-Newton* observations, taken with the pn-camera in both the TIMING, and BURST modes. In conjunction with this, I discuss the issues pile-up, exhibited in several of the TIMING mode observations and summarise a new count rate slicing technique. Finally I give a brief summary of the *RXTE* data extraction performed by Mr. Alexander Eckersall and highlight how the *XMM-Newton* observations fit into the long term outburst cycle of GX 339–4.

### 2.4.1 *XMM-Newton* pn-camera observations

The *XMM-Newton* observatory was launched in December 1999 and has been fundamental in furthering our understanding of XRBs; galaxy clusters; stellar formation, and the nature of supernova remnants (Schartel et al., 2010). The *XMM-Newton* observatory consists of three co-aligned  $\sim 1500 \text{ cm}^{-2}$  X-ray telescopes (Jansen et al., 2001) and each telescope contains a European Photon Imaging Camera EPIC sensitive over 0.3 – 10 keV (consisting of two MOS and one pn CCD array) (Turner et al., 2001; Strüder et al., 2001), along with two Reflection Grating Spectrometers RGS', which cover the band pass 3.3 – 20.2 keV (den Herder et al., 2001). In the 17 years that the *XMM-Newton* observatory has been operational, GX 339–4 has been monitored on 27 occasions; which offers an unparalleled wealth of archival data from which to analyse the requirements of disc truncation when in the bright hard

state.

In the course of an outburst the high luminosity of GX 339–4 can lead to pile-up issues within the observation data set. This occurs when multiple incident photons register as a single event upon a CCD, due to photons striking the pixels faster than the read-out time (Ballet, 2003); which is referred to as either photon pile-up (effects a single pixel) or pattern pile up (effects neighbouring pixels). In the case of *XMM-Newton*, the MOS camera is intrinsically more susceptible to pile-up than that of the pn, which has a significantly quicker read-out time; the fast observing modes of the pn-camera, in which the source is one dimensionally imaged across the CCD array and then charge transferred along the chips, allows for photon rates as high as 60,000 cts s<sup>-1</sup>.

In this study I make use of all publicly available observations longer than 15 ks, for which the EPIC pn-camera was operated in one of the fast observing modes (TIMING or BURST), this excludes the 2015 observations (revs 2879-2886), which only became publicly available on the 20th November 2016. A lists the 27 *XMM-Newton* observations of GX 339–4, of which 11 are considered in this analysis (6 hard state and 5 soft state) are presented in table 2.2. The six hard state observations were all made while in the TIMING mode (a frame time of 30 ms and a nominal observing efficiency of 99.5 per cent); with the five soft state observations taken using the BURST mode (a frame time of 7  $\mu$ s, and efficiency of 3 per cent). Several of the hard state observation (e.g. revs 0782, and 0783), were found to suffer from frequent telemetry losses due to the high count rate of GX 339–4, which acts to limit piled-up data (Done & Diaz Trigo, 2010a).

The raw Observation Data Files (ODFs) were processed using standard processing chains of the *XMM-Newton* Science Analysis Software (SAS V15.0.0). Source events were extracted from a rectangular region 15 columns wide (e.g. RAWXin31 : 45) to produce light curves and spectra; background spectra were also extracted from off-source regions to check for background-related problems, but as there is no true source-free region in the images (see e.g. Done & Diaz Trigo, 2010a; Kolehmainen et al., 2011), they were not subtracted from the source spectra. Pile-up analysis with the SAS task EPATPLOT, of the three brightest TIMING mode observations

Table 2.2: An observation log of GX 339–4. The observations analysed in this paper are numbered in column 1. Columns 2, 3, and 4 give the unique observation ID number, the *XMM-Newton* revolution number and the duration of each observation; columns 5, and 6 display the sources state, and the observation date; with column 7 showing the EPIC pn observing mode (B=burst, T=timing, FFM=full frame masked, SW = small window).

no.	Obs ID	rev	duration (ks)	source state	observation date	pn mode
(1)	(2)	(3)	(4)	(5)	(6)	(7)
–	112900201	139	6.9	hard	2000-09-11	T
–	85680501	223	8.2	hard	2001-02-26	T
–	85680601	223	12.2	hard	2001-02-26	T
1	93562701	496	61.4	soft	2002-08-24	B
–	111360201	509	10.9	soft	2002-09-19	FFM
2	156760101	514	76.3	soft	2002-09-29	B
3	148220201	594	20.5	hard	2003-03-08	T
4	148220301	600	16.3	hard	2003-03-20	T
–	111360401	691	2.6	hard	2003-09-17	–
–	111360501	768	7.9	hard	2004-02-18	FFM
5a	204730201	782	137.9	hard	2004-03-16	T
5b	204730301	783	138.5	hard	2004-03-18	T
6	410581201	1318	15.8	soft	2007-02-19	B
7	410581301	1325	16.7	soft	2007-03-05	B
8	410581701	1338	18.3	soft	2007-03-30	B
–	410581801	1338	3.6	soft	2007-03-30	–
9	605610201	1702	33.5	hard	2009-03-26	T
10	654130401	1886	34.9	hard	2010-03-28	T
–	692341201	2539	13.7	hard	2013-09-29	SW
–	692341301	2529	15.0	hard	2013-09-30	SW
–	692341401	2530	23.0	hard	2013-10-01	SW
–	760646201	2879	20.0	hard	2015-08-28	T
–	760646301	2881	29.2	hard	2015-09-02	T
–	760646401	2884	23.7	hard	2015-09-07	T
–	760646501	2886	22.1	hard	2015-09-12	T
–	760646601	2889	53.8	hard	2015-09-17	SW
–	760646701	2895	42.9	hard	2015-09-30	SW

(rev- 0596, 0600 & 1886), highlighted that the data suffers from heavy pile-up. In order to mitigate the effects of this we exclude the central three rows of the source in RAWX across all three observations.

The high count rates from GX 339–4 can cause problems other than pile-up within the spectrum (Guainazzi et al., 2014). One is X-ray loading (XRL), which occurs for observations of bright sources taken prior to May 2012 and is caused by the offset map (taken prior to the science exposure) being contaminated by source photons. A second effect is charge transfer inefficiency (CTI) which is different for bright sources as charge traps become filled. We treat the data using the latest calibration files, and in particular, we use EPPROC to apply an XRL correction, and EPFAST to apply a count rate dependent<sup>2</sup> CTI correction.

The EPIC pn-camera data files were filtered for only single and double events `PATTERN <= 4`, with bad pixels ignored `FLAG == 0`; periods of very high background noise (e.g. solar flaring events) were also removed. 800 c/s and 60000 c/s respectively

Response matrices were generated using `RMFGEN v2.2.1` and `ARFGEN v1.92`. Spectra were binned using `SPECGROUP v1.6` such that each bin contains no fewer than 25 source counts, and is no wider than 1/3 the instrumental (FWHM) energy resolution. This ensures the data are approximately Normally distributed, allowing the standard  $\chi^2$  fit statistic to be used, and spectrum is not over-resolved. The bandpass was taken to range from 0.7 – 10Kev, with the the exclusion of the energy band 1.75 – 2.35 keV due to a sharp feature, which is thought to be instrumental (Plant et al., 2015).

In the hard state, GX 339–4 is highly variable. In order to exploit and take account of this, we have split each of the longer hard state observations (revs 0782, 0783, 1702 and 1886) into multiple spectra based on count rate. First, broad-band light curves were extracted with 1 second time resolution. Partially exposed time bins were corrected for lost exposure. The count rate distribution was then divided into ten intervals spanning the full range such that each interval contains approximately the same number of counts. In this manner, more time was accumulated

---

<sup>2</sup>We used EPFAST with the parameter `TIMEBINWIDTH` set to 1 second as the source count rate varies significantly on short timescales, and the correction is a function of the count rate.

at low count rates, and narrower rate intervals were used near the peak of the rate distribution, in order to achieve comparable signal-to-noise spectra at each flux level.

### 2.4.2 *RXTE* observations and analysis

The launch of *RXTE* in December 1995, has been pivotal in our understanding of the long term evolution of XRBs, and their respective outburst cycles. In this section, I consider the long term evolution of GX 339–4 and highlight the outburst cycle stages of the *XMM-Newton* observations covered in this study. The *RXTE* data extraction was carried out by Mr. Alexander Eckersall, inline with the standard data reduction cookbook.

The pointed *RXTE* observations of GX 339–4, were obtained from the HEASARC archive and represented more than a decade of monitoring (2000-2012). The extraction used only STANDARD2 mode data from the Proportional Counter Array (PCA), which covers the energy band 3 – 20 keV in a 129 channels and with a time resolution of 16s. The only Proportional Counter Unit (PCU), used in this study was the PCU2, as it was the sole unit to be operational across all observations. The source and background spectra, along with the spectral response files, were created for each pointing using the standard *RXTE* software (HEASOFT v6.15.1). The light curve, hardness ratio curve and a hardness-intensity diagram (HID) of this source was produced by following the example of Belloni et al. (2005), in which the accumulated background corrected PCU2 rates are split three bands  $A = 3.3 - 20.2$  keV,  $B = 3.3 - 6.1$  keV and  $C = 6.1 - 10.2$  keV. Fig. 2.3 shows the long term light curve produced from energy band  $A$ , and the corresponding hardness ratio curve and HID produced from hardness ratio defined as  $C/B$  (the times and HID positions of the *XMM-Newton* observations are indicated).

## 2.5 The interstellar medium

The interstellar line of sight absorption has always been a major source of uncertainty when modelling X-ray binaries. In previous studies of GX 339–4, the absorption has generally been modelled as a neutral ISM with photoelectric edges (e.g. the PHABS

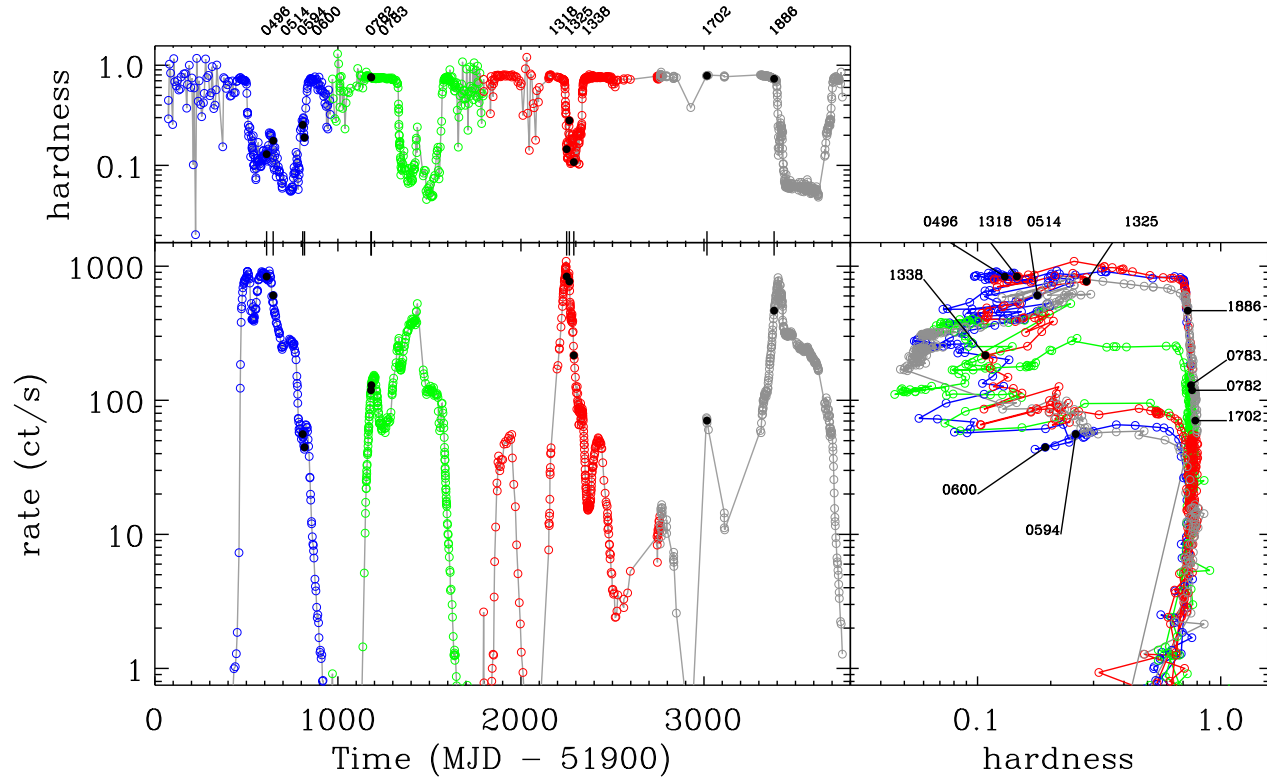


Figure 2.3: The main panel is the long term light curve of GX 339–4 in the 3 – 20 keV range, produced from *RXTE* observations between 2000 to 2012. The top panel corresponds is the hardness ratio curve 6 – 10/3 – 6 keV and the right panel is the hardness-intensity diagram. Each of the four full outbursts is plotted with a different colour, and the nearest times of the *XMM-Newton* observations are labelled.

or WABS models in XSPEC); where the absorption is solely characterised by the total hydrogen column density, which has yielded a broad range of values  $N_{\text{H}} = 2-8 \times 10^{21} \text{ cm}^{-2}$  (Cabanac et al., 2009b; Allured et al., 2013; Plant et al., 2015). An alternative approach to this is to fix the ISM absorption, based on external measurements from either 21cm radio or soft X-ray observations; with simultaneous RGS and pn-camera data from *XMM-Newton*, this later option in principle allows for individual absorption profiles for each of the observation outlined in §2.4.1 and is the approach taken in this study. In the rest of this section, I present a summary of Dr. Simon Vaughan’s RGS data reduction and his ISM analysis for the source GX 339–4.

### 2.5.1 RGS data reduction

The RGS spectra were extracted from all observations considered in §2.4.1; excluding the revolutions 0594, and 0600 due to their short exposure times. The source and background spectral files, along with the instrument response files were generated with RGSPROC v1.31.1. The data from RGS1, and RGS2 were combined using RGS COMBINE v1.3.4; as were the separate exposures within each observation. The revolutions 0782, and 0783 were also combined due to their close time proximity to one another. Each of the spectra were then grouped using SPECGRUP, with a maximum bin width, equal to a third of the instrumental energy resolution. All of the RGS fit were carried out in the 7 – 28 Å range, though issues of pile-up affected several of the observations, particularly at higher energies (7 – 12 Å i.e.  $E > 1 \text{ keV}$ ); this meant that the spectrum, rev 0496 which has the highest RGS count rate had to be excluded from the ISM analysis.

### 2.5.2 Modelling the line of sight absorption

In the case of GX 339–4, measuring the line of sight absorption is complicated by the suggestion that the hydrogen column density, appears to be dependant upon the sources state or luminosity (Cabanac et al., 2009b); which would rule out a single ISM model for all observations. In this analysis seven RGS observations, covering a wide range of spectral states are modelled, to investigate this claim, and obtain an

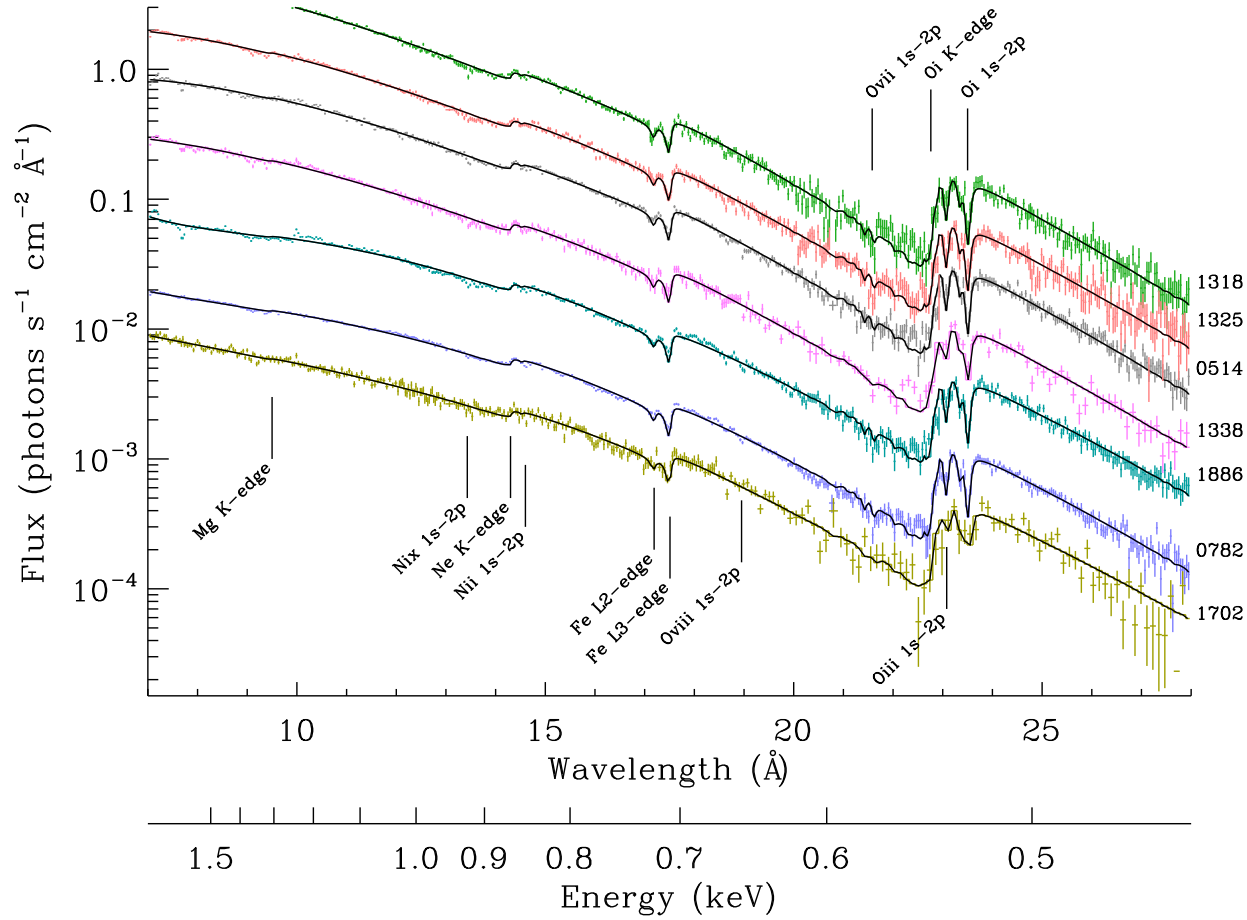


Figure 2.4: RGS spectra for GX 339–4 in different states. The revolution numbers of each observation are given on the right. The data are shown in brightness order, but the brightest spectra have been offset vertically for clarity. Some of positions of spectral features expected for neutral and ionised absorption are indicated. The model is a multi-temperature blackbody plus broken power law continuum, modified by neutral and ionised absorption.

independent ISM absorption model for the EPIC pn-camera data outlined in §2.4.1. The main goal of this analysis was not to reproduce every individual feature within the detailed spectra considered but to accurately capture the broad absorption profile across the spectral states; the results of this analysis are primarily contrasted with the column densities obtained, from the more detailed RGS modelling performed by Pinto et al. (2013), who solely considered the revolutions 0782 and 0783.

The absorption model fitting of this analysis, consisted of both a neutral and ionised phase for the ISM. The neutral component was modelled with TBNEW (Wilms et al., 2000): using the photoelectric cross-sections of Verner & Yakovlev (1995) and the ISM elemental abundances of Wilms et al. (2000); with ionised absorption modelled using WARMABS: an implementation of the XSTAR photoionisation code of Bautista & Kallman (2001), with abundances fixed to that of the neutral absorber. The continuum was modelled assuming a thermal disc contribution DISKBB (Mitsuda et al., 1984) and an up-scattered coronal component which was treated as a broken power-law to account for the scattering drop off at low energies BKNPOW, with energy break fixed at  $E_{br} = 0.7$  keV. With the final model given as: TBNEW \* WARMABS \* (DISKBB + BKNPOW ); where the inner disc temperature and normalisation of DISKBB, along with the normalisation and two photon indices of the BKNPOW, were free across each spectra; for the neutral ISM model TBNEW, the O, Ne and Fe abundances were free parameters (the O-K, Fe-L and Ne-K edges are the strongest features in the RGS spectra) but tied together between the seven spectra; in the ionised absorption model WARMABS, the ionisation parameter ( $\xi$ ) and  $N_{\text{H}}$  were free to vary but tied together between the seven spectra, and the velocity width was fixed to  $10 \text{ km s}^{-1}$ . The seven RGS spectra were simultaneously fitted, over the wavelength range  $7 - 28 \text{ \AA}$  ( $E \sim 0.44 - 1.7$ ), using XSPEC and the maximum likelihood method (Cash, 1979).

Figure 2.4 shows the best fitting model across the seven spectra; while the vast majority of spectral features were well captured, several residuals at the O edge at  $\approx 23 \text{ \AA}$  remained, which are likely due to an incomplete capture of the ISM dust grain structure; for a more detailed treatment see figures 5, and 6 of Pinto et al. (2013). This appears to have little effect upon the column densities which

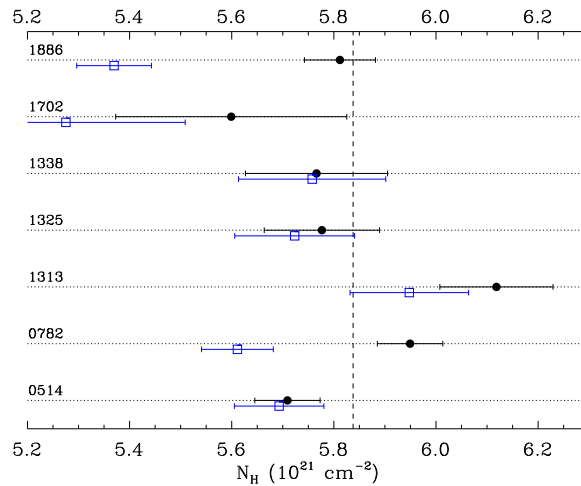


Figure 2.5: The  $N_{\text{H}}$  column density estimates for seven RGS spectra. The black points are the best-fitting values using a model with only neutral absorption. The blue (slightly offset) points are those estimated using a model that includes additional ionised absorption. The vertical line marks the weighted mean value.

appear consistent with those of Pinto et al. (2013)<sup>3</sup>; with a neutral ISM column densities of  $N_{\text{H}} = 5.6 \pm 0.02 \text{ cm}^{-2}$ ,  $N_{\text{O}} = 3.8 \times 10^{18} \text{ cm}^{-2}$ ,  $N_{\text{Ne}} = 6.5 \times 10^{17} \text{ cm}^{-2}$ , and  $N_{\text{Fe}} = 1.9 \times 10^{17} \text{ cm}^{-2}$ , with the ionised model giving  $\log \xi = -1.67$  and  $N_{\text{H}} = 1.0 \times 10^{21} \text{ cm}^{-2}$ . The overall  $N_{\text{H}}$  value differs from Pinto et al. (2013) but this is mostly due to the use of different photoelectric cross-sections and elemental abundances.

While this model does account for the detailed structure seen in the RGS data, the complexity of the model makes it slow to compute, which is impractical for the purpose of modelling the broad-band EPIC data, which only requires the absorption model to be accurate above 0.7 keV and thus ignore the ionisation component. While this leaves the OII and OIII features around 22 – 23 Å ( $E \sim 0.54 \text{ keV}$ ) features unmodelled, it does still reproduce the overall depths of the O, Ne and Fe edges, with the two models almost identical at short of 17 Å ( $E > 0.7 \text{ keV}$ ). Figure 2.5 shows the hydrogen column density estimates from the neutral absorber for each observation, excluding the ionisation component (black points) and including it (blue points). The  $N_{\text{H}}$  estimates increased from  $5.3 - 5.9 \times 10^{21} \text{ cm}^{-2}$  to  $5.6 - 6.1 \times 10^{21} \text{ cm}^{-2}$  when

<sup>3</sup>Including both gas and dust components, Pinto et al. (2013) reported  $N_{\text{H}} = 5.1 \times 10^{21} \text{ cm}^{-2}$ ,  $N_{\text{O}} = 4.0 \times 10^{18} \text{ cm}^{-2}$ ,  $N_{\text{Ne}} = 6.8 \times 10^{17} \text{ cm}^{-2}$  and  $N_{\text{Fe}} = 2.1 \times 10^{17} \text{ cm}^{-2}$  for the revolutions 0782, and 0783.

ignoring ionisation; the the relative abundances also change slightly from 1.37, 1.34, and 1.27 for O, Ne, and Fe, respectively to 1.44, 1.21, and 1.22 when ignoring the ionisation component. Assuming the contribution from the ISM ionisation phase is minimal, the later values are used for all EPIC spectral fittings, using the wighted mean of the seven  $N_H$  estimates of  $5.83 \times 10^{21} \text{ cm}^{-2}$ .

Since this analysis, the more comprehensive model *ISMABS* which includes both the neutral and ionised phases of the ISM has become available (Gatuzz et al., 2015). An analysis of a single RGS observation gave a significantly different results outside of that expected from the change in model and cross sections and also in conflict with previous 21cm and Pinto results (Gatuzz et al., 2016). This is mostly likely due to the fits neglecting a blackbody disc component which can be significant even in the hard state.

## 2.6 Broad-band spectral model

The main motivation of this study is to investigate the requirements of disc truncation in the low-hard state of GX 339–4. While this system has been extensively studied over the past decade, it has never been spectrally fitted using a single model-grouping for both the hard and soft states. An archetypal XRB spectrum consists of four primary components: the ISM absorption; a thermal accretion disc emission; an approximate power-law component, which we assume to come from Compton up-scattering of disc photons by a hot corona, and a reflection component from coronal irradiation of the disc. The majority of previous studies have analysed individual observations of GX 339–4 which has resulted in a wide range of conflicting values for the systems fundamental parameters (see discussion in Plant et al., 2015). In this analysis I have aimed to assemble the most physically accurate and self consistent model-grouping possible.

### 2.6.1 Disc

The accretion disc is typically modelled as a multi-temperature blackbody, in either a Newtonian potential (model: *DISKBB*), a pseudo-Newtonian potential (*DISKPN*),

or a general relativistic potential (KERRBB and BHSPEC). The simplicity of the model DISKBB allows for quick spectral fits, however it assumes a non-zero torque upon the inner disc edge i.e.  $T \propto R^{-3/4}$  (Shakura & Sunyaev, 1973; Novikov & Thorne, 1973; Gierliński et al., 1999); this renders the model inadequate for discs which extend to the ISCO: beyond which matter chaotically free-falls into the BH (Zimmerman et al., 2005). While the model DISKPN offers a good approximation of a GR disc, it intrinsically assumes a significantly greater accretion efficiency and fails to take account of relativistic smearing (see section 1.5.3). The GR models KERRBB and BHSPEC avoid all of these drawbacks, but at the expense of requiring increased computational time: as the two models rely upon interpolation between parameter tables (Li et al., 2005; Davis & Hubeny, 2006). The greatest difference between these two models is in their treatment of the disc’s atmosphere: where BHSPEC self-consistently solves the vertical disc structure and radiative transfer equations, while KERRBB approximates the disc emission to be a multi-temperature blackbody and corrects for the incomplete thermalisation of high energy photons by implementing a colour correction factor. The model KERRBB thus offers a more phenomenological approach that may better capture the underlying physics.

## 2.6.2 Reflection

Currently the most commonly used reflection models are: PEXRAV/PEXRIV, REFLIONX and XILLVER. The PEXRAV/PEXRIV models include both Compton reflection and bound-free absorption from a completely neutral and ionised slab, respectively (Magdziarz & Zdziarski, 1995). Neither of the two models include fluorescence line emissions and thus require additional models for the S, Ar, Ca and Fe lines. Further to this PEXRIV also assumes the slab to be isothermal with a maximum temperature of  $T = 10^6$  K, which leads to a much higher level of absorption and a deeper Fe-K edge, when compared to both REFLIONX and XILLVER, which solve the ionisation balance of the slab (Ross & Fabian, 2005; García et al., 2013b; Eggen et al., 2013).

REFLIONX and XILLVER are much more complex models, but they have several differences; the primary of which being that XILLVER resolves the radiation

transfer equations treating the disc as a plane-parallel slab which is thought to represent the disc more accurately than the constant density approximation of REFLIONX (Nayakshin et al., 2000). XILLVER's use of XSTAR a photo-ionisation code to solve the ionisation balance (Kallman & Bautista, 2001), means that the more recent solar abundances of Grevesse & Sauval (1998) are used instead of Morrison & McCammon (1983) for REFLIONX, with the difference quite large in the cases for O, Fe and Ne, though if corrected for this should play little difference (García et al., 2013b). Calculations include the most recent and complete atomic data for K-shell transitions equivalent widths of Fe K line REFLIONX does not include Fe K $\beta$  lines and does not include most of the second row Ge K $\alpha$  ions under the assumption of Auger resonant destruction, though XILLVER predicts emission at these energies (García et al., 2013b).

Neither of these models take account of relativistic effects such as gravitational red-shifting, beaming, light bending/self-irradiation, frame dragging or the effect of Doppler broadening and thus must be convolved with a relativistic smoothing model such as KDBLUR or RELCONV (Li et al., 2005; Dauser et al., 2010). This means that photon emission is angle averaged across the disc. The recently released model RELXILL however links the reflection code XILLVER to the relativistic smearing kernel of RELCONV, which allows it to correctly treat the angular distribution of the reflected X-rays (García et al., 2014).

### 2.6.3 Corona

The corona is typically modelled as a power-law emission. The reflection model XILLVER includes a self consistent power-law component, however the disc-convolution model SIMPL offers several advantages over the standard power-law prescription, as it self-consistently converts a fraction of the disc emission into an up-scattered power-law. This better mimics the underlying physics, as it avoids both over predicting soft photons and artificially suppressing the disc emission.

### 2.6.4 The core model

Here I present a summary of the core model and its parameters. The accretion disc is modelled using KERRBB, where we assume a self irradiated isotropic disc around a Schwarzschild BH with a zero torque inner boundary. The mass, inclination and distance are all fixed, with the normalisation equal to unity. This is then convolved with the model SIMPL, which self consistently steals photons from the disc and up scatters them into a power-law, in order mimic the effects of coronal Compton up scattering better than a standard power-law which over predicts soft X-rays.

The relativistic reflection component is modelled using RELXILL, which is the first reflection model to treat the angular distribution of the reflected X-rays, compared to the angle averaging which is obtained from the convolution between RELLINE and XILLVER. This gives us the final model TBNEW(SIMPL(KERRBB) + RELXILL), which contains eight free variables, all of which are listed in respective order:  $\Gamma$  and  $f_{\text{scat}}$ , is the energy powerlaw and scatter fraction of the disc photons;  $\dot{M}$  and  $f_{\text{col}}$  are the accretion rate and colour correction factor for the disc;  $q_1$  and  $q_2$  are the broken emissivity powerlaw values;  $\log(\xi)$  &  $N_{\text{Ref}}$ , cover the disc ionisation parameter and the reflection normalisation.

# 3

A re-analysis of the requirements for  
disc truncation in GX339-4

In this chapter, I present the results and analysis for the spectral model fitting of 11 archival *XMM-Newton* observations of GX 339–4, in the BURST and TIMING modes of the pn-camera. Where I investigate the physicality of assuming a fixed inner disc radius across all spectral states, in order to review the requirements for disc truncation.

### 3.1 Introduction

An XRBs inner disc region is thought to be truncated at low accretion rates where it is replaced by an optically thin, geometrically thick, advection dominated flow (Narayan & Yi, 1994, 1995; Chen et al., 1995). In the course of an outburst, as the accretion rate rises the advection dominated flow is thought to evaporate and be replaced by the standard optically thick, geometrically thin disc (Shakura & Sunyaev, 1973; Esin et al., 1997; McClintock et al., 2001; Kubota & Done, 2004; Mayer & Pringle, 2007a). The critical accretion rate for the transition between these two accretion regimes remains uncertain as their theoretical stability regions overlay with one another (Chen et al., 1995; Abramowicz & Fragile, 2013). The radiative inefficiency of ADAFs currently limit possible direct observations however the truncation radius of the thin accretion disc can be spectrally constrained from the modelling of either the thermal disc component or the Fe-K line broadening (Davis et al., 2005; McClintock et al., 2006). Studies of the archetypal LMXB GX 339–4 have produced conflicting measurements for the inner disc radius. This has lead to opposing views on the requirements for disc truncation in the low-hard states of transient XRBs (Reis et al., 2008; Done & Diaz Trigo, 2010b; Kolehmainen et al., 2014; Plant et al., 2014a; García et al., 2015).

An alternative approach to the disc truncation debate is to assume a fixed inner disc radius across both the hard, and soft states; while relaxing the commonly taken constraints upon the radial emissivity value  $q$ , and the colour correction factor  $f_{\text{col}}$ . In this multi-state analysis of the *XMM-Newton* EPIC-pn camera observations of GX 339–4, I review the feasibility of such a model and whether an apagogical argument can be made based on the  $q$  and  $f_{\text{col}}$  values.

## 3.2 Observations and spectral model

In this analysis, I consider 11 archival *XMM-Newton* observations of GX 339–4 taken in fast observing modes of the EPIC pn-camera: 6 hard-state observations (TIMING mode) and 5 soft-state observations (BURST mode). The data was extracted using the standard processing chains of the *XMM-Newton* Science Analysis Software (SAS V15.0.0). The three brightest TIMING mode observations (revs 0594, 0600 & 1886) were all found to suffer from heavy pile-up when analysed with the SAS task EPATPLOT; the pixel event distribution was subsequently found to improve with the removal of the central three RAWX columns. Several of the longer exposure ( $>30$ ks) EPIC pn-camera TIMING mode observations were count rate sliced in to multiple spectra in order to broaden the flux range of the observations: revolution-0782 (10 spectra), 0783 (10), 1702 (3) & 1886 (4). In this chapter only the lowest ranged count rate sliced spectra were utilised from each of the four observations, with the remaining spectral slices considered in chapter 4.

In this re-analysis the same core model is fitted across both the hard and soft states, with the inner disc fixed at the ISCO and all duplicated parameters tied: TBNEW(SIMPL(KERRBB) + RELXILL) for which there are 7 free parameters:  $\Gamma$  (energy power-law),  $f_{\text{scat}}$  (power-law scatter fraction),  $\dot{M}$  (accretion rate),  $f_{\text{col}}$  (colour correction factor),  $q$  (inverse radial emissivity value),  $\xi$  (ionisation parameter), and  $N_{\text{ref}}$  (reflection normalisation). The preliminary fits highlighted a strong residual in the  $\sim 1$  keV region of up to 30% in both the soft and hard state spectra. This was found to be best approximated by the addition a gaussian component. Such a strong soft excess has been acknowledge in several previous XRBs studies including those of GX 339–4, however its origin remain unknown (see studies: Kolehmainen et al., 2014; Done & Diaz Trigo, 2010b; Boirin et al., 2004, 2005; Díaz Trigo et al., 2006, 2009; Hiemstra et al., 2011; Papitto et al., 2013). The addition of the model GAUSS was required for all observations apart from rev-1702. This expanded the core model to TBNEW(SIMPL(KERRBB) + RELXILL + GAUSS), with an additional three variables:  $E_{\text{gs}}$  (line energy),  $\sigma_{\text{gs}}$  (line width), and  $N_{\text{gs}}$  (gaussian normalisation); with the line energy & width constrained as follows:  $0.8 \leq E_{\text{gs}} \leq 1.2$  keV and  $\sigma_{\text{gs}} \leq 0.2$  keV.

In order to investigate the physicality of this soft residual, several of the pn-model fits were applied to the RGS data: this data was extracted using the standard processing chains of the *XMM-Newton* Science Analysis Software (SAS V13.5.0). Several of the observations also exhibited a non-blurred neutral Fe-K line. This was fitted using the reflection model **XILLVER**, with  $\xi = 0$  and all parameters tied to the core model, apart from the normalisation parameter  $N_{\text{Fe}}$ . A detailed description of the GX 339-4 parameter constraints, data reduction, count rate slicing technique, ISM analysis, and the rationale behind the chosen models, is presented in §2.2-2.6.

### 3.3 Results

The spectral modelling was carried out using **XSPEC** (V12.9.0i) within the energy bandpass: 0.7 – 10 keV. The energy range 1.75 – 2.35 keV was excluded as it is thought to contain instrumental edges (Done & Diaz Trigo, 2010a; Plant et al., 2015). An energy gain correction was found to be required for several of the observations: this provides a linear shift in the energy of the the response matrix and the energy slope of the effective area, which should correct for any CTI anomalies. The energy gain correction was applied to all observations, adding two extra variables to the model: the energy *offset* and the energy *slope*.

#### 3.3.1 BURST Mode Observations

The *XMM-Newton* BURST mode observations, capture GX 339–4 across the systems soft state evolution, see HID from figure 2.3. The five soft state observations are split across the the 2002 (rev-0496 & 0514) and the 2007 (rev-1318, 1325 & 1338) outbursts. The observations rev-0496 & 1318 capture GX 339–4 close to its peak luminosity before the outburst decay phase. In the decay phase the flux of the source decreases and the spectral hardness ratio is found to sporadically change. This can lead to spectral hardening episodes within the decay as seen in observations rev-0514 & 1325, with the emission softening again as seen in observation rev-1338.

At low energies  $\leq 1\text{keV}$  each of the observations show pronounced residuals despite the inclusion of the soft gaussian component, see figure 3.2. The modelling

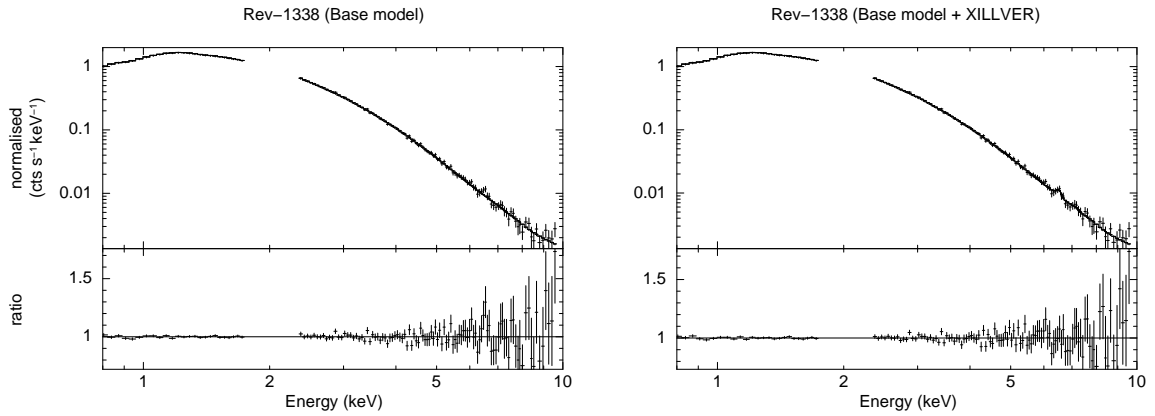


Figure 3.1: The normalised spectra ( $\text{cts s}^{-1}\text{keV}^{-1}$ ) and model ratio verses energy (keV), for the Timing mode observations.

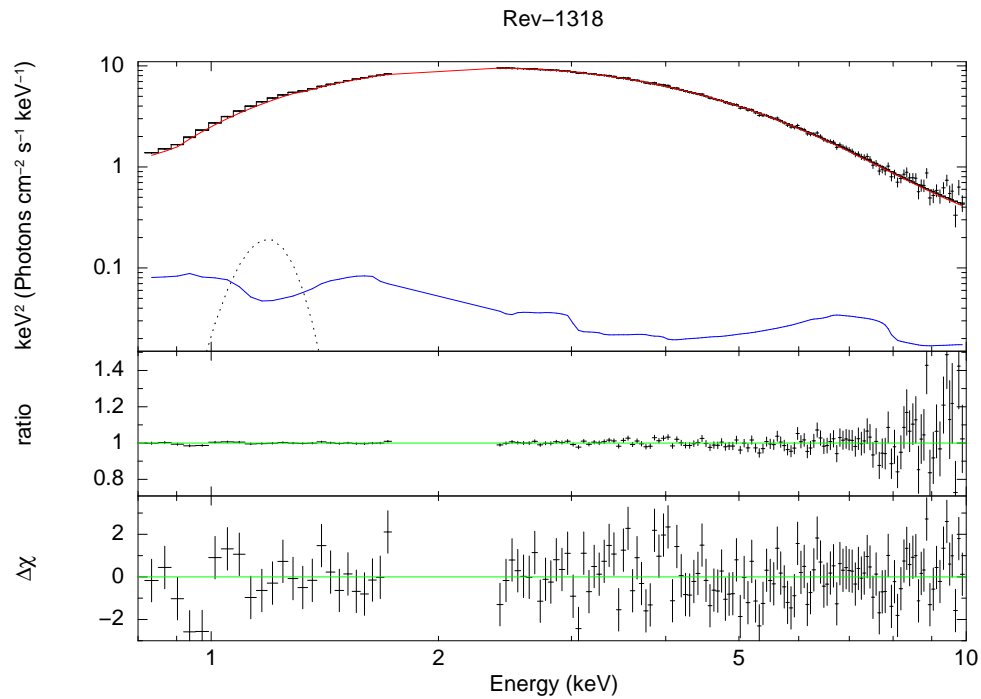


Figure 3.2: The normalised spectra ( $\text{cts s}^{-1}\text{keV}^{-1}$ ) and model ratio verses energy (keV), for the Timing mode observations.

of these features as either an additional gaussian line at  $\sim 0.6\text{keV}$  (**GAUSS**) or as an absorption feature at  $\sim 0.8\text{keV}$  (**GABS**) was found to significantly improve the fits, however neither model appears to be favoured. The addition of a 1% systematic error was found to dramatically decrease the goodness of fit across each of the observations  $\chi^2/\nu < 1.05$ , suggesting that these soft residuals are well within the instrumental calibration range. While the core model captured the majority of the spectral features, the lowest luminosity soft state observation rev-1338, was found to show a strong residual in the neutral Fe-K line region, see figure 3.1. The existence of a neutral reflection feature has been identified in several previous studies of GX 339–4 and is thought to originate from the illumination of the outer disc. As the residual was relatively large  $\sim 50\%$  and could affect the broad Fe-K line fitting, the non-blurred neutral reflection model **XILLVER** was incorporated into the modelling for this single BURST mode observation.

The parameter and component flux values for each of the modelled BURST mode observations are shown in table 3.1, in order of total flux (highest to lowest). A parameter table which includes errors calculated at the 90% confidence level, along with plots of the spectra fits, are presented in Appendix A.1.

### 3.3.1.1 The 2002 outburst

The spectral modelling of observations rev-0496 and rev-0514 produced statistically weak fits:  $\chi^2/\nu < 2.3$ . This is primarily due to the high statistical significance of the low energy residuals, which results from the extremely high signal to noise ratio of these two observations. The model struggles to fully capture the spectral shape of highly luminous soft state observation rev-0496, with residuals around the Fe-K line and an under estimation of photons above 8 keV. The residuals around the Fe-K are dominated by a broad absorption feature which was modelled with **GABS** centred at  $\mu = 5.42_{-0.05}^{+0.04}\text{keV}$ , with the variance  $\sigma = 0.2_{-0.07}^{+0.11}\text{keV}$ . This could be a neutral Cr-K $\alpha$  absorption line from a transient structure. The abundance ratio of Cr to Fe is around  $\sim 1\%$  for a solar composition disc and even with the higher photon count rate at lower energies, we would still expect to see a similar magnitude Fe line feature. The alternative possibility is that the feature is a highly redshifted Fe-K $\alpha$

Table 3.1: The EPIC pn-camera BURST mode parameter and flux tables. In the parameter table, all eight variables are listed, along with the gain values and fit statistic. The flux table gives the total flux in cgs units ( $\text{erg s}^{-1} \text{cm}^{-2}$ ) across two flux ranges. The relative flux contribution from each component is listed as a percentage of the total (due to the photon up-scattering from the convolution model SIMPL, the total flux percentage is greater 100% ).

Model	Parameters	<i>XMM-Newton</i> Revolution				
		0496	1318	1325	0514	1338
SIMPL	$\Gamma$	3.40	3.13	2.21	2.20	2.95
	$f_{\text{scat}}$	0.02	0.04	0.09	0.01	0.02
KERBB	$\dot{M}/10^{18}$ [ $\text{gs}^{-1}$ ]	5.39	5.38	3.45	3.50	2.40
	$f_{\text{col}}$	2.57	2.58	2.78	2.71	2.45
RELXILL	$q$	2.87	2.53	2.20	1.50	2.78
	$\xi$ [ $\log_{10}$ ]	2.82	2.71	3.13	3.62	2.48
	$N_R$ [ $\log_{10}$ ]	-1.42	-1.54	-1.60	-1.82	-1.68
GAUSS	$E_{gs}$ [keV]	1.16	1.16	1.18	1.18	1.15
	$\sigma_{gs}$ [keV]	0.08	0.09	0.12	0.10	0.11
	$N_{gs}$ [ $\log_{10}$ ]	-1.14	-1.14	-1.09	-1.36	-1.14
XILLVER	$N_{Fe}$ [ $\log_{10}$ ]	-	-	-	-	-1.50
GAIN	slope	1.01	1.01	0.98	1.00	1.02
	offset [keV]	0.00	0.00	0.03	0.02	0.00
	$\chi^2$	355	186	182	325	95
	dof	140	136	140	141	118

Model Components		<i>XMM-Newton</i> Revolution				
		0496	1318	1325	0514	1338
		Flux Range (0.7 – 10 keV)				
Total	[ $\log_{10}$ ]	-7.53	-7.53	-7.61	-7.66	-7.91
Disc	[%]	96.6	95.1	73.5	82.8	91.9
Power-law	[%]	3.7	6.6	15.1	1.4	4.4
Reflection	[%]	1.3	1.4	17.1	16.0	4.1
Gaussian	[%]	0.5	0.5	0.6	0.4	1.1
Neutral	[%]	-	-	-	-	0.5

emission from a disc wind. The underestimation of photons above 8 keV is partially driven by the Gaussian fitting of the soft excess, which favours a softer power-law ( $\Delta\Gamma = -0.4$  when including the spectral emission between 0.75-1.5 keV), however a hard excess with residual snaking remains. The intermediate state observation rev-0514 shows no major residuals, other than those at low energies.

In the course of the 14 days between rev-0496 and rev-0514, the emission dramatically hardens  $\Delta\Gamma = -1.2$ , despite the scatter fraction remaining insignificant. The radial emissivity shows a significant drop from 2.84 to the lower limit 1.5 and the ionisation parameter was found to significantly increase, this is tentatively consistent with an increase in the coronal coverage however the change in the scatter fraction fails to fit this picture. The colour correction factor increases mildly between the soft and intermediate state observations, in a similar fashion to the 2007 outburst fits  $f_{\text{col}} = 2.57 - 2.71$ . The unknown soft gaussian component remains fairly stable across the two observations.

### 3.3.1.2 The 2007 outburst

The spectral modelling produced reasonable fits across each of the observations: rev-1318, 1325, and 1338, with  $\chi^2_{\nu} < 1.37$ . The fits identified few major residuals other than an the apparent neutral Fe-K line in rev-1338 which was subsequently fitted with the XILLVER model. In addition to this a narrow high energy absorption feature in rev-1325 was well fitted using the model GABS centred at  $\mu = 8.19^{+0.16}_{-0.11}$  keV, with the variance fixed at  $\sigma = 10^{-2}$  keV. As no absorption edges or atomic lines are known to reside within this energy range, the most probable physical explanation is for the residual to be a doppler shifted absorption line. This would indicate an accretion disc wind however with no evidence of any wind absorption features in the RGS data and owing to the low statical importance of the residual, it is not considered in further detail here.

In the course of the three observation, GX 339–4 is seen to transition from a high luminosity disc dominated state, into a harder intermediate phase, before returning to the soft state. This all occurs within a 25 day period, over which the power-law index and scatter fraction are seen to significantly vary: in the 14 day

period between rev-1318 & 1325 we see a significantly harder emission  $\Delta\Gamma = -0.92$  and a doubling in the scatter coverage  $\Delta f_{\text{scat}} = +0.05$ , with similar magnitude changes in the opposite direction following this in the 11 days between rev-1325 & 1338, with a softening in the emission  $\Delta\Gamma = +0.74$  and a reducing scatter fraction  $\Delta f_{\text{scat}} = -0.07$ . These dynamical and thermal variations of the corona emission are well above the estimated timescales of the inner disc region. These coronal variations can also be seen in the reflection modelling. The radial emissivity is below the canonical value for all observations where it ranges between 2.53 – 2.78 in the soft state observations but drops to 2.2 in the SIM state. This is broadly in keeping with an increase in the coronal coverage for the scatter fraction. The unknown GAUSS component remain fairly stable across each of the observations.

### 3.3.2 TIMING Mode Observations

The six *XMM-Newton* TIMING mode observations capture GX 339–4 in both the hard and intermediate states. The two brightest observations rev-0594 & 0600 were made as GX 339–4 returned to quiescence from the 2002/03 outburst; the other four observations rev-0782 & 0783 and rev-1702 & 1886 respectively track the systems rise from quiescence during the 2004 and 2009/10 outbursts, see the HID in figure 2.3 for better contextual placement. All of the outburst rise observations showed a non-blurred, neutral Fe-K $\alpha$  line, as before with the BURST mode observation rev-1338, an additional neutral reflection model was used in the fitting XILLVER. The parameter values and flux contributions from each model component are shown in table 3.2 in order of total flux (highest to lowest). A parameter table which includes errors calculated at the 90% confidence level, along with plots of the spectra fits, are presented in Appendix A.2.

#### 3.3.2.1 The 2002/03 outburst

The spectral model fittings for the two intermediate state observations rev-0594 & 0600, show strong statistical residuals both close to the Fe-K line, with a particularly poor capture of the spectral decay above 8 keV. A relaxation of the power-law coupling between the models SIMPL and REXILL was found to significantly im-

Table 3.2: The EPIC pn-camera TIMING mode parameter and flux tables. In the parameter table, all eight variables are listed, along with the gain values and fit statistic. The flux table gives the total flux in cgs units ( $\text{erg s}^{-1} \text{cm}^{-2}$ ) across two flux ranges. The relative flux contribution from each component is listed as a percentage of the total (due to the photon up-scattering from the convolution model SIMPL, the total flux percentage is greater 100% ).

Model	Parameters	<i>XMM-Newton</i> Revolution					
		0600	0594	1886	0783	0782	1702
SIMPL	$\Gamma$	2.95	2.90	1.65	1.61	1.60	1.51
	$f_{\text{scat}}$	0.08	0.18	0.45	0.30	0.32	0.43
KERBB	$\dot{M}/10^{18}$ [ $\text{gs}^{-1}$ ]	0.74	0.55	0.17	0.10	0.08	0.04
	$f_{\text{col}}$	2.56	2.48	1.81	1.41	1.51	2.07
RELXILL	$q$	2.03	2.21	1.59	2.16	2.24	1.88
	$\xi$ [ $\log_{10}$ ]	2.70	2.70	3.17	2.29	2.30	2.46
	$N_K$ [ $\log_{10}$ ]	-1.74	-1.74	-1.73	-2.59	-2.58	-3.11
GAUSS	$E_{gs}$ [keV]	1.17	1.17	0.89	1.01	1.06	-
	$\sigma_{gs}$ [keV]	0.10	0.11	0.20	0.16	0.12	-
	$N_{gs}$ [ $\log_{10}$ ]	-1.55	-1.52	-0.85	-2.34	-2.63	-
XILLVER	$N_{Fe}$ [ $\log_{10}$ ]	-	-	-3.15	-3.45	-3.24	-3.24
GAIN	slope	0.99	0.98	0.99	1.01	1.00	1.01
	offset [keV]	0.02	0.03	0.03	0.01	0.01	0.00
	$\chi^2$	142	277	188	153	155	142
	dof	129	139	140	140	140	143

Model Components		<i>XMM-Newton</i> Revolution					
		0600	0594	1886	0783	0782	1702
Flux Range (0.7 – 10 keV)							
Total	[ $\log_{10}$ ]	-8.43	-8.50	-8.34	-9.00	-9.04	-9.22
Disc	[%]	79.2	64.1	6.5	6.9	6.9	7.2
Power-law	[%]	14.7	31.0	43.2	88.7	88.6	92.0
Reflection	[%]	10.7	14.8	49.4	5.3	5.6	3.0
Gaussian	[%]	1.4	1.8	3.7	0.7	0.4	-
Neutral	[%]	-	-	0.2	0.4	0.6	0.8

prove the fitting around the Fe-K line and goes some way to addressing model over estimation that occurs above 8 keV, however this required an un-physical difference between the parameters  $|\Delta\Gamma| > 0.8$ . This is primarily due to a degeneracy between the two power-law components and the ionisation parameter. Where a decrease in the ionisation parameter leads to an increase in low energy absorption features, this then compensates for any hardening in the reflection power-law. This in turn leads to an over abundance of low energy photons which can be compensated for by having an extremely soft power-law component. In the case of these observations this leads to an extremely large difference between the two values  $|\Delta\Gamma| > 0.8$ . While residuals still remain the addition of a 1% systematic error was found to dramatically reduce the fit statistics: rev-0594( $\chi^2/\nu = 1.31$ ) and 0600( $\chi^2/\nu = 0.84$ ).

### 3.3.2.2 The 2004 & 2009/10 outburst

The four outburst rising models all yielded reasonable statistical fits  $\chi^2/\nu \leq 1.35$ , with few residuals other than a neutral Fe-K feature at  $\sim 6.4$  keV which was fitted using the XILLVER model across all four spectra. This was found to significantly improve the fit statistics for an additional single degree of freedom, while minimising the Fe-K line residual: rev-0782 ( $\Delta\chi^2 = 14$ ), 0783 ( $\Delta\chi^2 = 6$ ), 1702 ( $\Delta\chi^2 = 20$ ), and 1886 ( $\Delta\chi^2 = 2$ ). Figure 3.3 highlights the significance of the neutral Fe-K line for the lowest luminosity observation rev-1702. While the XILLVER normalisation is relatively steady across the four observations at the 90% confidence level, the relative flux contribution is seen to steadily decrease with increasing flux from 0.8% to 0.2%. This means that the most luminous of the four observations rev-1886 is consistent with no neutral component, despite having the largest normalisation value  $N_{\text{Fe}} = -3.15_{-\text{inf}}^{+0.38}$ . If the source of this emission is from the illumination of the outer disc as speculated, the diminishing relative flux contribution may stem from an increase in the ionisation level of the cool disc region.

The observations in order of flux rev-1702, 0782, 0783 & 1886, neatly track the outburst rise along the right hand stem of the HID see fig 2.3. The photon index is seen to gradually soften from 1.51 to 1.65, which is consistent with a cooling corona. The scatter fraction however appear to decrease before rising again, this

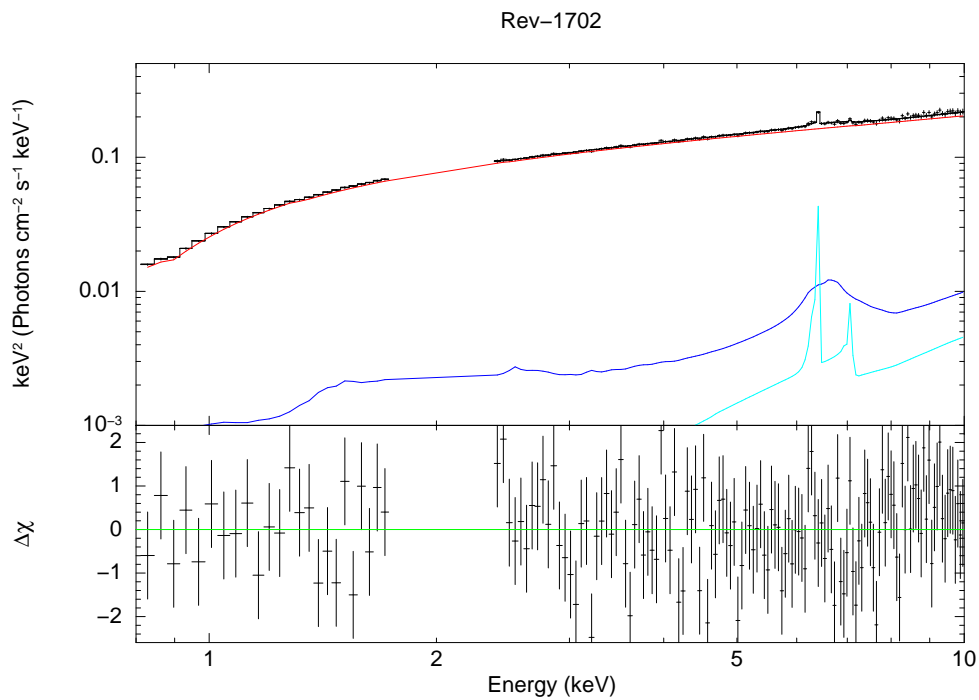


Figure 3.3: The top and bottom panels show the modelling results for the TIMING mode observation rev-1702. The top panel shows the folded model and spectra, along with the fit ratio. The bottom panel shows the unfolded model and spectrum, along with the respective  $\Delta\chi$  values. The solid black line represents the total model emission, with the additive model contributions given as follows: disc and power-law (red), reflection (dark blue), neutral reflection (light blue)

may just signify a different coronal coverage between the two outburst observations, with the 2004 outburst  $f_{\text{scat}} = 0.30 - 0.32$ , while the the 2009/10 outburst shows  $f_{\text{scat}} = 0.43 - 0.45$ . This is similarly seen in the radial emissivity variations with the 2004 outburst  $\log(\xi) = 2.16 - 2.24$ , while the the 2009/10 outburst shows  $\log(\xi) = 1.59 - 1.88$ . The larger 90% confidence intervals of rev-1886 do place its scatter fraction value  $f_{\text{scat}} = 0.45^{+0.09}_{-0.10}$  with the range of the 2004 outburst scatter fraction values. The radial emissivity values are consistent with a constant value within the region of  $q \sim 2$ , below the canonical value.

### 3.3.3 An RGS analysis of the soft excess

A statistically significant residual at  $\sim 1\text{keV}$  was identified in all of the pn-camera observations that were analysed here; with the only exception being rev-1702, the observation with the lowest total flux. The existence of this soft excess has been highlighted in several studies concerning various XRBs, however they all primarily analysed *XMM-Newton* data (Boirin et al., 2004, 2005; Díaz Trigo et al., 2006, 2009; Done & Diaz Trigo, 2010b; Hiemstra et al., 2011; Papitto et al., 2013; Kolehmainen et al., 2014; Yoneyama et al., 2017). It currently remains unclear as to whether the soft residual features are merely confined to the EPIC instrument or if they are also exhibited in the RGS spectra (Papitto et al., 2013). In order to qualitatively assess the physical existence of the soft excess and to evaluate the pn-models at low energies ( $\leq 0.7\text{ keV}$ ); I simultaneously fit all of the BURST mode pn-camera fits to their respective RGS spectra (except for rev-0496, as the RGS data suffers from heavy pile-up). All of the model parameters were fixed, with only a single cross-calibration constant  $N_{\text{RGS}}$ , allowed to vary across the four observations.

The modelling achieved a goodness of fit of  $\chi^2_{\nu} = 10190/2080$  (with  $N_{\text{RGS}} \sim 0.90$ ) and showed few residuals other than those around the O-K edge  $\sim 0.54\text{ keV}$ . This likely stems from the OII and OIII ionisation features not being included in the ISM model TBNEW, though it could also possibly be due to the incomplete capture of the dust grain structure. When removing the model GAUSS and re-fitting, both the fit statistic and the calibration constant were found to marginally increase to  $\chi^2_{\nu} = 10215/2080$  and  $N_{\text{RGS}} \sim 0.91$ , see figure 3.4. The lower effective area of

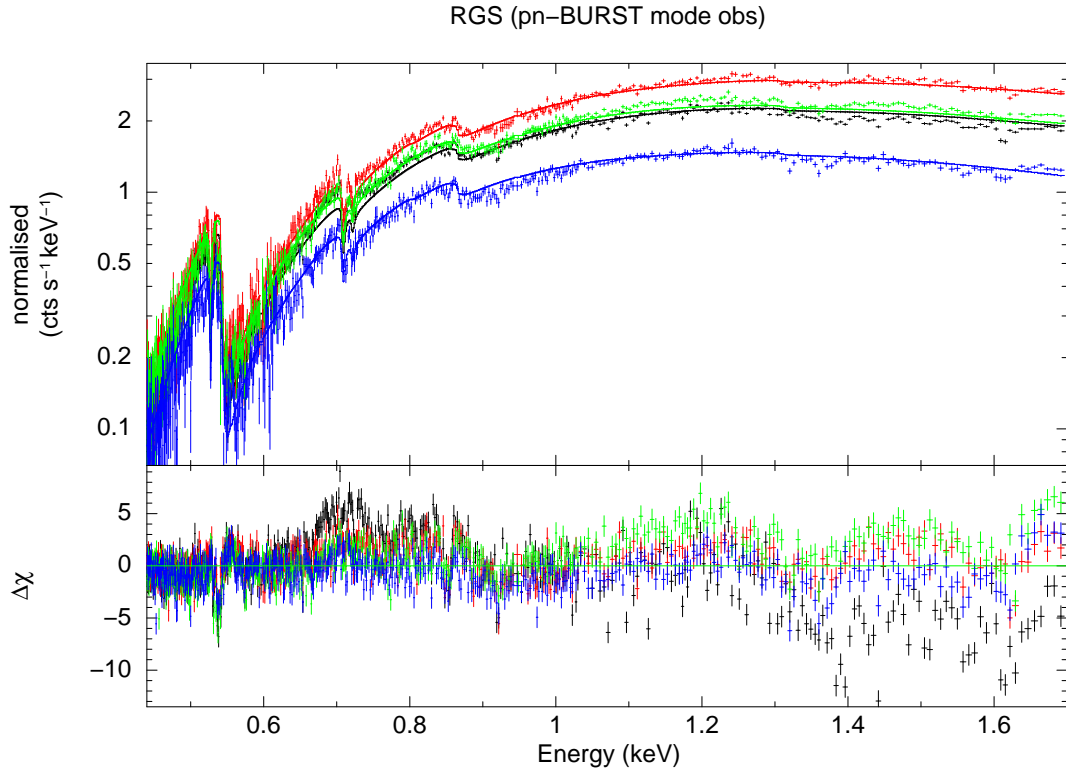


Figure 3.4: The joint fits of the pn-camera BURST mode models to the RGS spectra. The folded models, spectra and the corresponding  $\Delta\chi$  values for each of the four observations are given. The gaussian component of the model was removed and the cross correlation parameter is given as  $N_{RGS} \sim 0.91$ . The red, green, blue and black line colours correspond to the revolution numbers 1325, 1338, 1318 and 0514 respectively.

the RGS CCDs in comparison to the pn-camera however reduces the statistical significance of any residuals and this in part makes detection of a potential soft excess problematic within the RGS data. The only observation to show a soft residual was rev-1325, where the removal of the model `GAUSS` weakened the fit from  $\chi^2_\nu = 1948/520$  to  $\chi^2_\nu = 2136/520$ .

The gaussian component across all of the BURST mode observations only contributes 0.4 – 1.1% of the total flux in the 0.7 – 10 keV energy band but contributes  $\sim 3.7\%$  to the total flux for the TIMING mode observation rev-1886. On this basis I fit the model grouping: `TBNEW(SIMPL(KERRBB) + RELXILL + GAUSS + XILLVER)` to the non-count rate sliced pn-camera spectra, in order to make a fit comparison to

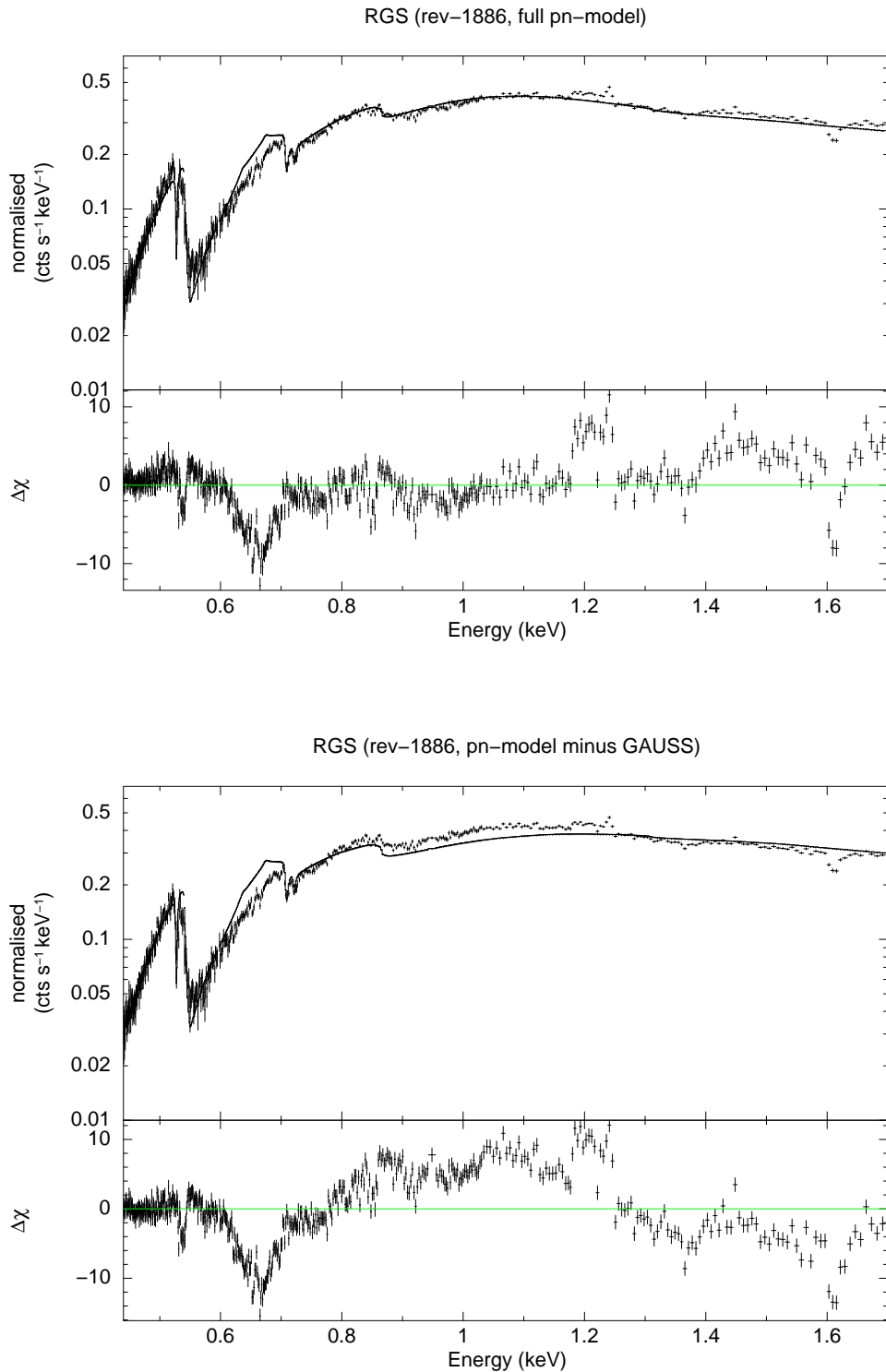


Figure 3.5: The folded pn-camera model renormalised to the RGS spectra, along with the corresponding  $\Delta\chi$  values for observation rev-1886. The top plot is for the full pn-model and required a cross correlation parameter of  $N_{RGS} \sim 1.02$ . The bottom plot is the pn-model with the gaussian component removed and with  $N_{RGS} \sim 1.14$ .

the RGS data. The subsequent RGS modelling exhibited several broad residuals and achieved a goodness of fit of  $\chi^2_\nu = 5262.36/519$  (with  $N_{\text{RGS}} \sim 1.02$ ), see top plot of figure 3.5. While the majority of these residuals are present in the ISM analysis, the negative residual at  $\sim 0.7$  keV appears to result from the energy gain correction and may be an artefact arising from an over correction for the CTI effects in the rev-1886 pn-camera data. When removing the model `GAUSS` the goodness of fit dramatically weakens to  $\chi^2_\nu = 11624/519$  (with  $N_{\text{RGS}} \sim 1.14$ ) and a clear residual can be seen at  $\sim 1$  keV, see bottom plot of figure 3.5. This would appear to indicate that the soft excess is independent of the pn-camera and thus not an instrumentation issue.

The physical source of the residual is not clear and has thus far been modelled either as an emission line (Díaz Trigo et al., 2006, 2009) or as an absorption edge (Boirin et al., 2004). While the feature is at an energy range comparable to the Fe-L emission, the disc ionisation parameter required to fit the Fe-K line is too high for reflection to be the source (Kolehmainen et al., 2014). The residual could be due to an  $\alpha$ -element over abundance in the secondary star, which could lead to stronger emission lines from elements such as Ne or O in the disc (Papitto et al., 2013), however it is not fully clear that this would be the case for the low/intermediate stellar mass companion in GX339-4. If an over abundance of Ne or O was the source of the excess, the plateauing in the emission size at higher luminosities could be due to fluorescence saturation. While the source of the soft excess remains uncertain, it is unlikely to effect our broader results, as the emission contributes less than 2% of the total observed flux for all observations bar rev-1886. Once reflection models allow for the variation of elemental abundances, the plausibility of an  $\alpha$ -element over abundance in the disc could be assessed.

## 3.4 Discussion

### 3.4.1 Do we require disc truncation in the bright hard state?

The main aim of this re-analysis was to evaluate the requirement of disc truncation in the low-hard state. While previous studies have always allowed the inner disc radius to be a free parameter, the primary premise of this study was to model all

spectral states with a fixed inner disc radius. This was built on the assumption that while  $R_{\text{in}} = 6R_g$  would provide an adequate approximation in the soft state and break down in the hard state, should truncation occur (Done & Diaz Trigo, 2010b; Kolehmainen & Done, 2010; Plant et al., 2015, 2014a). The fit statistics however shows the opposite trend to this, with  $\chi^2/\nu$  seen to gradually increase with total flux from  $\sim 1 - 1.4$ , with several outlying fits regarding the observation rev-1886. This could be due to the increasing S/N ratio with increasing flux, where physics which has not been encapsulated into the models leads to degrading in the fit quality. The main source of this, is likely the misuse of the reflection model RELXILL which is designed for the cool discs found in active galactic nuclei (García et al., 2014). In the case for XRBs however the disc is much brighter due to the closer proximity of the inner disc edge to the BH. This hotter disc leads to an additional illumination component from below the atmosphere and also increases the ionisation level of the disc (Ross & Fabian, 2007).

The goodness of fits we obtain for the hard state observations give no suggestion of a truncated disc and compare favourably with previous studies which have analysed the same EPIC pn-camera data, with the conclusion of a recessed disc (Done & Diaz Trigo, 2010b; Kolehmainen et al., 2014; Plant et al., 2015). The first of these previous studies Done & Diaz Trigo (2010b), analysed the two observations rev-0782/0783, identifying the MOS data, which required a broadened Fe-K line (Miller et al., 2006; Reis et al., 2008), to have suffered from heavy pile-up and suggested that while the pn-camera suffers from telemetry drop-outs, the effects of this while in TIMING mode should be lessened any issues regarding pile-up.

The subsequent fitting of the pn-camera data with the central three columns excluded using REFLIONX revealed a marginally more narrow Fe-K line than Miller et al. (2006) and highlighted the dependence of  $R_{\text{in}}$  upon inclination and the fit requirement for GX 339–4 to be a low inclination source. The inner radius was found to change from  $11 - 100R_g$  for an inclination of  $25^\circ$  (free) and  $60^\circ$  (fixed) respectively, with the goodness of fit  $\chi^2/\nu$  worsening from 1.81 to 2.20. This narrow Fe-K line, thus suggested that pile-up effects had caused broadening observed in the MOS data. This conclusion however was strongly rebuked by Miller et al. (2010), who illustrated

that photon pile-up should in theory narrow the Fe-K line. The fit requirement for GX 339–4 to be a low inclination would also require either an extremely large BH mass (Muñoz-Darias et al., 2008) or an implausible BH spin misalignment with the binary plane (Kolehmainen & Done, 2010) and is suggestive of a break down in the model fitting, which highlighted further due to the thermal disc component extending close to the ISCO, in contradiction with the reflection emission.

Kolehmainen & Done (2010) who conducted joint fits with the *XMM-Newton* pn-camera and *RXTE* PCA, across the the soft state observations, similarly required a Kerr BH thermal disc emission, while simultaneously fitting a narrow Fe-K line. Irrespective of this, they were however able to ascertain that phenomenological disc models yield a significantly improved goodness of fit in comparison to more physical motivated relativistic models. With the relativistic model BHSPEC obtaining a  $\chi^2/\nu$  range of 5.2 – 2.29 corresponding to the observations rev-1325 and rev-1318 respectively; in comparison with the simpler DISKBB model, with goodness of fit range of 2.3-1.15 for the observations rev-0514 and rev-1318 respectively.

While Kolehmainen & Done (2010) conclude that the disc is unlikely to be truncated due to the strong disc emission  $\sim 75\%$  of the total flux, it does highlight the innate difficulty in modelling spectra. Kolehmainen et al. (2014) investigated this further with hard state *XMM-Newton* observations of GX 339–4 using the models DISKBB for the disc and RFXCONV for reflection, while assuming a fixed inclination of  $60^\circ$ . Identifying that the two methods for measuring  $R_{\text{in}}$ , the thermal disc and Fe-K line are not consistent with one another, with no no apparent correlation in the difference between the two values. The fit values they obtain were predominately weaker than ours, achieving  $\chi^2/\nu$  of 2.26, 3.49, 0.98 and 2.411 for observations rev- 0782, 0783, 1702 and 1886 respectively; though this is impart due to not modelling the soft  $\sim 1\text{Kev}$  residual and also the weaker S/N of our count rate sliced spectra.

Plant et al. (2015) using the same *XMM-Newton* data as Kolehmainen et al. (2014), with the addition of two *Suzaku* observation identified the Fe-K to narrow with increasing flux. Their use of the more advanced reflection model XILLVER, while fitting the inclination across all the observations allowed them to obtain vastly

improved goodness of fits, with  $\chi^2/\nu$  of 1.81, 1.10, 1.04 for the observations rev - 0782/0783, 1702 and 1886 respectively, though this will also be down to ignoring the soft state data  $< 1.3\text{Kev}$ , which contains the soft residual.

In comparison to this study and Kolehmainen et al. (2014), they allow the inclination to vary, obtaining  $i = 42^\circ$ . While such a low inclination would suggest a BH spin misalignment with the binary plane and also require an extremely large BH mass, it is markedly less challenging to understand than the inclination values obtained in previous studies for GX 339–4,  $i \sim 20^\circ$  (Miller et al., 2006; Done & Diaz Trigo, 2010b). The large disc truncation identified in Plant et al. (2015) and Plant et al. (2014a) who considered *RXTE* data, however requires a super or close to Eddington accretion rate for a Schwarzschild BH, with no offered rationale of why the disc would remain truncated at such distances at high accretion rates.

While statistical comparisons with previous studies is an inadequate measure of the quality of the fits, due to the possibility that goodness of fit improvements could be down to inconsistent or phenomenological approaches to the modelling. We have to the contrary shown that if both the emissivity and colour correction are allowed to vary, it is possible to obtain equal, if not improved fits while using a consistent grouping of relativistic models with the inner disc edge parameters from the thermal disc component and the Fe-K line tied. While taking non-fiducial values for GX 339–4’s fundamental parameters:  $i, M_1, D$  and also crucially fixing the interstellar absorption. If a 1% systematic error is also introduced, as in Done & Diaz Trigo (2010b); Kolehmainen & Done (2010); Kolehmainen et al. (2014), then the fit statistic drastically improves even further, due to the 1Kev, soft residual heavily driving the fit statistics.

The balance between producing a good fit with minimal residuals, while maintaining a physically plausible grouping of models is an extremely precarious act owing to the current uncertainty over the state of the corona in terms of the geometrical coverage and whether the photon thermalisation in the disc is flux dependant. This subsequently effects both the degree of up-scattering, the measured reflection emissivity and also the colour correction factor in the fittings. The 1Kev residual and also the reflection residuals identified by Fürst et al. (2015) and (García et al.,

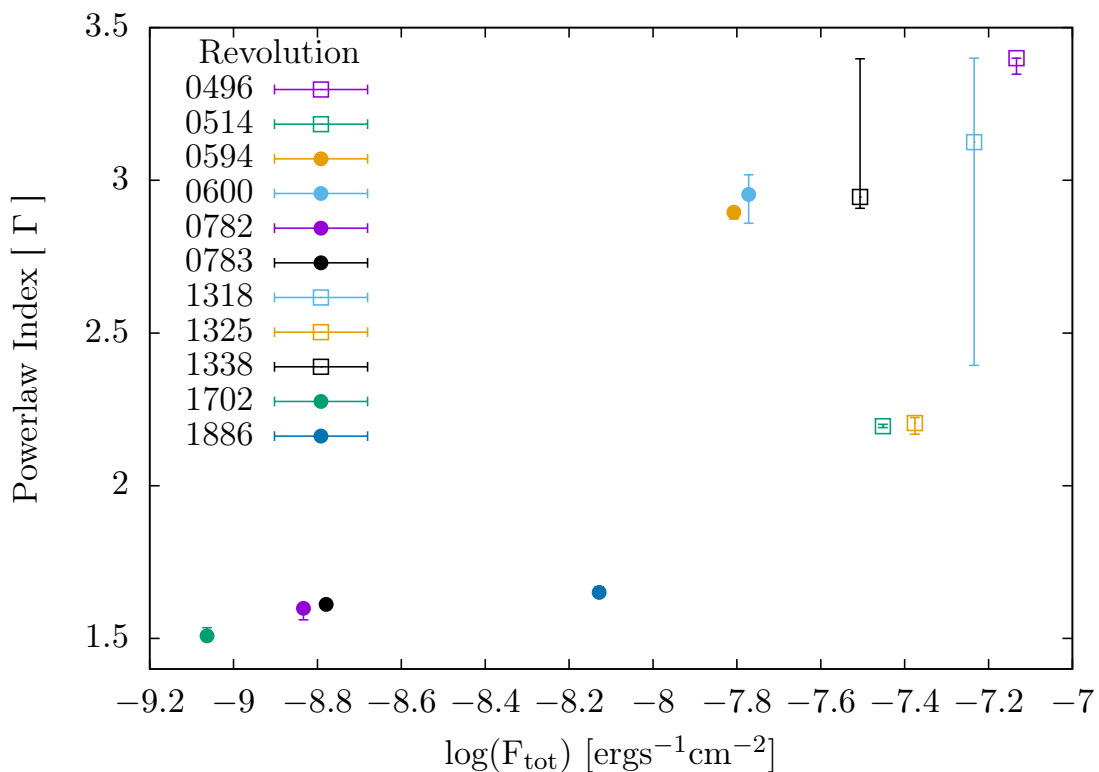


Figure 3.6: The power-law index with respect to the total flux in the 0.01-10keV range. See key for the observation revolution number.

2015) could merely be indicative of the limitation in the current reflection models due to the high computational costs. While attempting to fit these features, we should remain sceptical to their physicality and effects upon the accretion parameters. With this in mind however we find no evidence that the disc is required to truncate, on the allocation that  $q$  and  $f_{\text{col}}$  are allowed to vary, with the results in agreement with (García et al., 2015), with the main sole caveat of our fits in the form of a gain correction to the several of the TIMING mode observations for rev-0600, 0594, 0782, 0783 and 1886. Though these variations are extremely small they will have a significant effect on the goodness of fit comparisons.

### 3.4.2 The physicality of the coronal variations

There are currently three prominent theories for describing the geometry of the corona in the hard state (Esin et al., 1997; Nayakshin & Kallman, 2001; Miniutti & Fabian, 2004; Done et al., 2007): the first assumes an extended corona which is

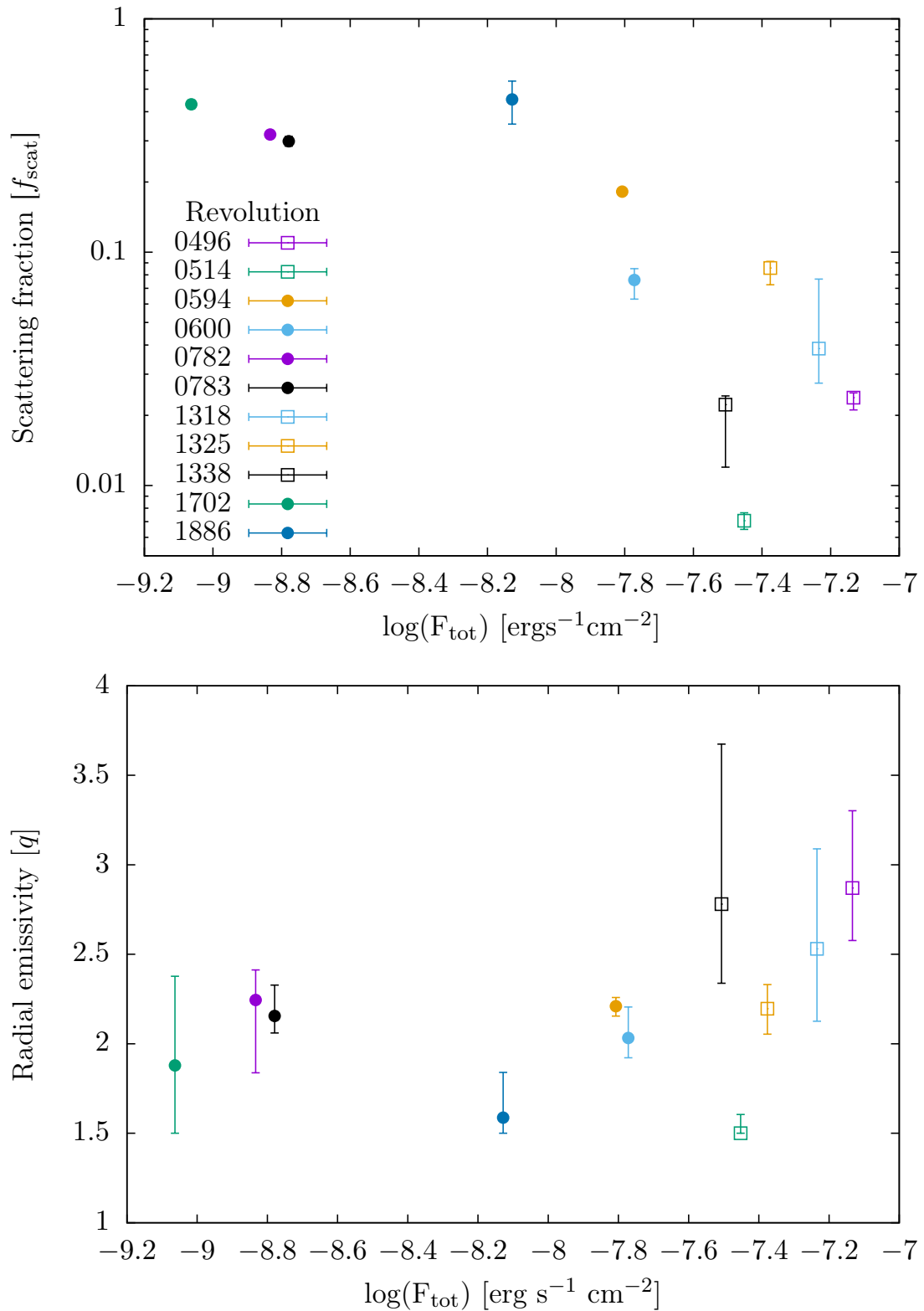


Figure 3.7: The scatter fraction and reflection emissivity with total flux in the 0.01-10keV range. See key for the observation revolution number.

treated as an expansion of the disc atmosphere; the second assumes a lamp-post geometry where the corona is positioned on the BH  $z$ -axis, perpendicular to the disc plane and at the base of a jet, and the final geometry assumes a truncated disc with an ADAF region. In this study I have chosen to use the empirical model SIMPL, which broadly mimics the physical Compton up-scattering models in regards to conserving seed photon loss from the disc component. In order to achieve this, the model assumes that all photons have the same probability of being scattered and that the degree of up-scattering is energy independent (Steiner et al., 2009). This means that the model SIMPL, does not specifically assume a geometry for the corona, however Barnard (2010) highlight that the energy independent up-scattering is likely to favour a compact coronal geometry.

The power-law photon index  $\Gamma$  was found to marginally increase with flux while in the hard state  $\sim 1.51 - 1.65$ , in agreement with the findings of Plant et al. (2015). This incremental softening of the powerlaw, is followed by a jump to  $\sim 3.5$  as the disc entered the soft intermediate state. While the model SIMPL does not assume a geometry for the corona, the scattering-fraction does provide a crude picture of the coronal coverage of the disc and thus modest information of the geometry. The hard state observations rev-0782, 0783, 1702 & 1886 give a scatter fraction range of  $0.3 - 0.45$  and this appear to be independent of the total flux.  $f_{\text{scat}}$  sharply declines in the soft state observations. This apparent coronal contraction in the soft state, is generally attributed to the rising coronal cooling levels expected from the increased photon density in the soft state (Poutanen et al., 1997). The gradual increase in the scatter fraction observed in the hard state however can only be explained in a concise manner by invoking disc truncation, where the cool disc coalesces into the ADAF region (Esin et al., 1998), any alternative would likely require variations in the coronal height or opacity during the cooling process. The reflection emissivity, can also be used as an indication of coronal geometry (Wilkins & Fabian, 2012). The steep  $q_1$  emissivity in the low-hard state is likely due to the disc extending within  $6R_g$ , where a large emissivity is expected for high spinning BHs  $a_* > 0.8$ , due to gravitational light bending (Wilkins & Fabian, 2012).  $q_2$  is extremely flat in the low-hard state and

The recent analysis of García et al. (2015) using the *RXTE* decade long data set and also that of Fürst et al. (2015) who conducted joint fits of the *Suzaku* and *NuSTAR* data, have suggested a much more complex form for the reflection features from GX 339–4. Requiring both a super-solar  $A_{\text{Fe}}$  and also a neutral Fe-K line to accompany the standard blurred reflection model, which was previously identified in Kolehmainen & Done (2010). In conjunction with this, Fürst et al. (2015) also found a statistically significant gain from untying the photon indexes of the power-law and reflection models. We subsequently examined the variation of the  $A_{\text{Fe}}$  and the decoupling of the reflection and power-law photon indexes from one another, across the three observations with the largest iron line residuals. In allowing  $A_{\text{Fe}}$  to vary I found no improvement to the fits. This is possibly due to the super-solar iron abundance primarily being driven by the Compton hump, which Fürst et al. (2015) suggested is the reason that studies below 10Kev have not previously required this. When the  $\Gamma_{\text{ref}}$  was also allowed to vary freely from  $\Gamma_{\text{PL}}$ , this again lead to only narrow improvements in the fitting of the two observations rev-0594 and rev-0782, though significant gains were made to the fitting of the observation rev-1886 with a total  $\Delta\chi^2$  improvement of -30. As before the observation rev-0782 appears to not require a super-solar iron abundance, though both rev-0594 and rev-1886 obtain an  $A_{\text{Fe}}$  value of 2.00 and 3.28 respectively. The small statistical improvement for the observation rev-0594 however would suggest that the iron abundance is relatively degenerate with the photon indexes and while the spectral fitting greatly improved for the observation rev-1886, there is however a large disparity between the two photon index values of  $\Delta\Gamma = 0.86$ . In each of the three fits and also in Fürst et al. (2015) analysis the reflection power-law was always found to be steeper than the coronal power-law emission. While the feasibility is ambiguous, this could be due to the softer coronal X-rays thermalising in the disc, which is not considered in current reflection models and thus could manifest itself as a hardening in the input PL.

### 3.4.3 The ionisation state of the disc

The ionisation parameter is defined as  $\xi = 4\pi F_x/n$ , where  $F_x$  is the illuminating flux and  $n$  is the gas number density. When the ionisation parameter is low  $\xi <$

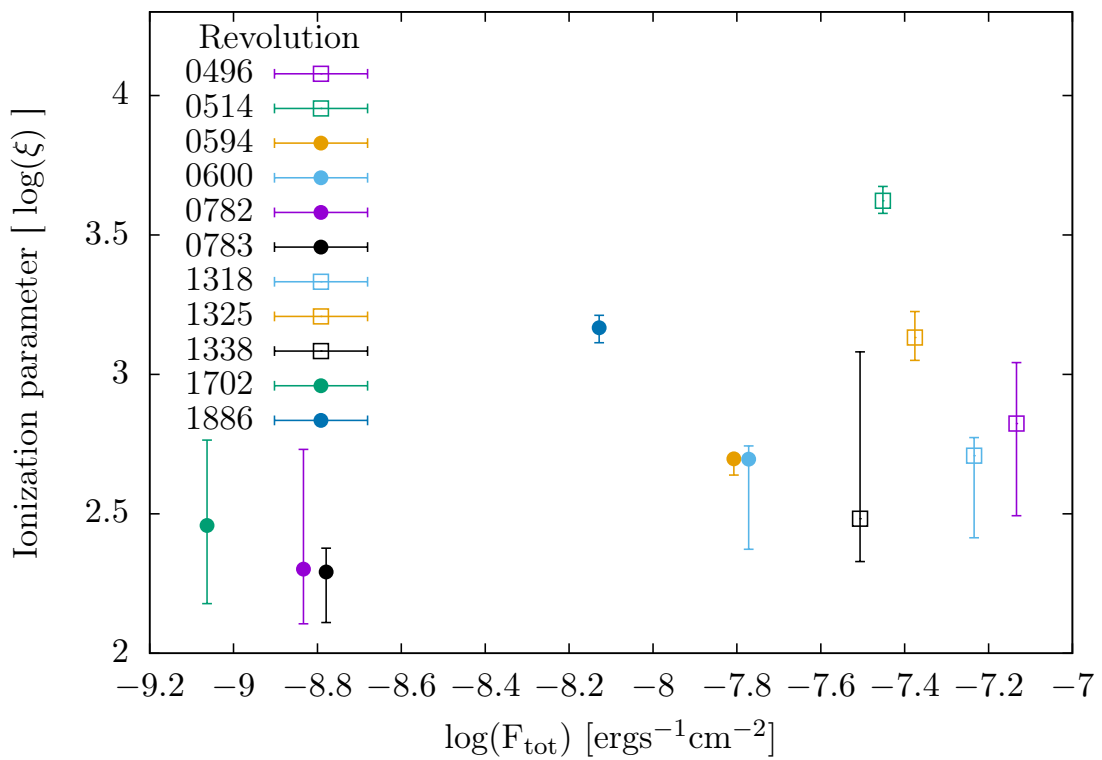


Figure 3.8: The emissivity parameter with respect to the total flux in the 0.01-10keV range. See key for the observation revolution number.

100, the reflection model produces a complex set of emission line profiles, with heavy absorption features. As the ionisation parameter increases the fluorescent emission lines broaden and the disc absorption weakens. This is due to the increased flux increasing the temperatures of the disc, while simultaneously broadening the ionisation range. At very high ionisation rates  $\xi > 500$  the emission lines, which originate primarily from ionised species narrow and the disc absorption to decrease to the point that the base continuum resembles the incident power-law (García & Kallman, 2010; García et al., 2014).

In the low-hard state, the ionisation parameter was found to be approximately constant at  $\sim 200$ , despite an increase in both the power-law and disc flux. Without count rate slicing the data however, all three of the hard state observations rev-0782/0783 and 1702 reside in the equivalent region of the HID, with previous values in this region of  $\xi \sim 250 - 400$  (Plant et al., 2015, 2014a; García et al., 2015).

In the brighter soft state observations however the ionisation parameter returns to a value inline with that expected from the previous observational studies  $\xi \sim 10^3$ , with the general trend, other than the intermediate state observations of an increasing ionisation parameter with flux.

### 3.4.4 A variable colour correction factor

The incomplete thermalisation of the accretion disc emission is parameterised through the frequency independent hardness correction factor, which is generally assumed to be constant with respect to the accretion rate  $f_{col} \sim 1.7 - 2.0$  (Shimura & Takahara, 1995; Gierliński & Done, 2004; Davis et al., 2005; Dunn et al., 2011). The most comprehensive and self consistent study of the colour correction factor to date is the 1D radiative transfer analysis of Davis et al. (2005), however this study ignored to take account of the effects magnetic pressure which may increase the vertical density profile and increasing hardening of the emission (Merloni et al., 2000; Turner, 2004; Begelman & Pringle, 2007; Salvesen et al., 2013; Narayan et al., 2016). The direct proportionality between the colour correction factor and the inner disc radius  $f_{col}^2 \propto R_{in}$ , makes the respective variations indiscernible from one another (Kubota et al., 1998; Salvesen et al., 2013).

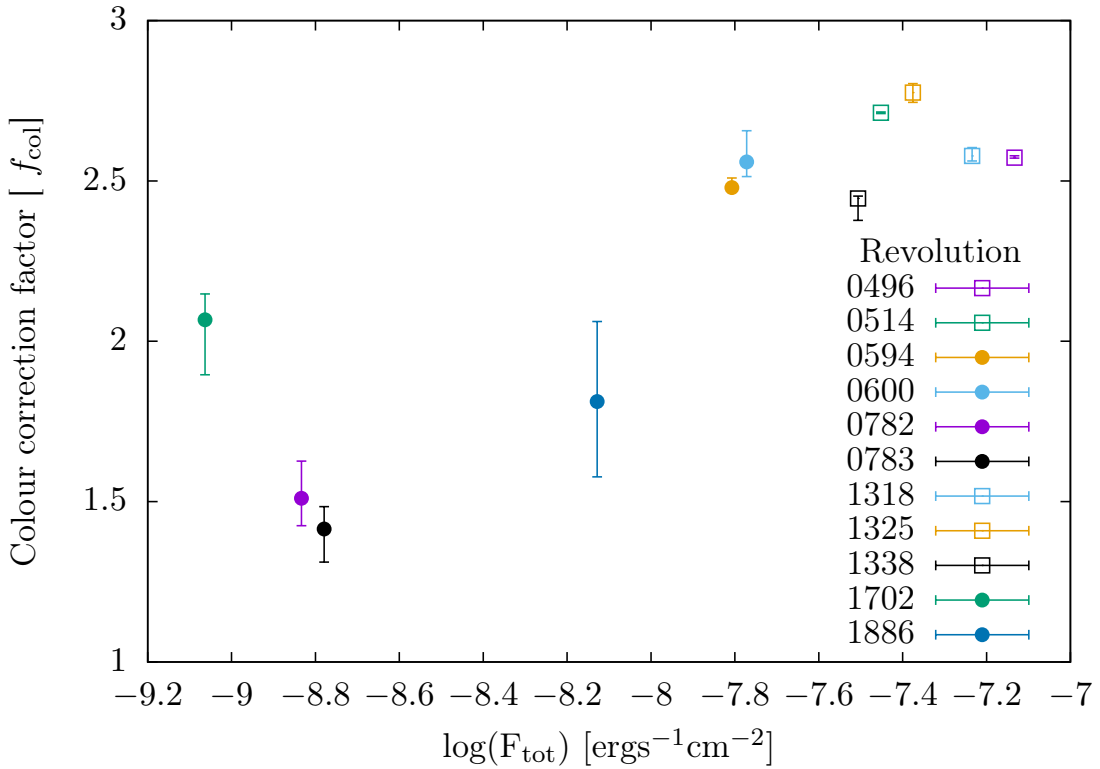


Figure 3.9: The colour correction factor against the total flux obtained in the 0.01-10 keV range. See for the *XMM-Newton* revolution number for each of the observations.

The colour correction factor measured in this re-analysis suggests there exists two quasi-stable values for  $f_{\text{col}}$  dependant upon the accretion state. With the hardening factor approximately equal to  $\sim 2.5-2.8$  while in the soft state and  $\sim 1.5-2.1$  in the hard state, see figure 3.9. This soft state hardness correction is considerably larger than the canonical value of  $\sim 1.7$ , this is probably caused by the assumption of a Schwarzschild BH breaking down and  $f_{\text{col}}$  having to increase to compensate for the disc residing within  $6R_g$  (Salvesen et al., 2013). The decrease in the colour correction factor from the high-soft to the low-hard state, conflicts with the expectations of a truncating disc where  $f_{\text{col}}$  would be expected to increase.

This softened  $f_{\text{col}}$  in the hard state could be due to the disc appearing more optically thick, with the cooler electrons reducing the non-thermal emission, as well as more limited viscous mixing (Shimura & Takahara, 1995). In the lowest flux observation rev-1702, the colour correction factor increases from  $\sim 1.51$  to  $\sim 2.07$  in contrast to the other hard state observations. This may be due to the much weaker disc contribution to the spectral emission or could indicate a truncating disc.

### 3.5 Conclusions

In this study we have re-analysed all available *XMM-Newton* observations of GX 339–4, which have been carried out with the EPIC-pn camera, while in the BURST or TIMING modes. This has allowed us to consider as wide a range of spectra states as currently possible with the *XMM-Newton* telescope. We further expand this flux range, with the application of the novel technique of count rate slicing the highly variable hard-low state data with approximately equal S/N, allowing us to achieve unprecedented low flux spectra of GX 339–4.

Several studies based on the spectral fitting of soft state observations have suggested that GX 339–4 contains a high spinning BH ( $a_* \sim 0.9$ ) (Miller et al., 2004, 2008; Reis et al., 2008), though there remains debate over whether the disc truncates as it enters the bright hard state (Miller et al., 2006; Done & Diaz Trigo, 2010b). Recent analysis has suggesting a truncated disc in the hard state based on a narrow Fe-K line, though conflictingly requires a thermal disc component extending close to the ISCO (Kolehmainen et al., 2014; Plant et al., 2015). This highlights how the limited knowledge of GX 339–4 fundamental parameters and uncertain model/parameter degeneracies, have lead to measurements of  $R_{\text{in}}$  to remain extremely uncertain, despite relatively small statistical model errors.

To address some of the issues regarding the conflicting results and the model inconsistencies of previous studies, we have assumed  $R_{\text{in}}$  is fixed at the ISCO for a Schwarzschild BH, while relaxing the priori requirements for constant values of  $q$  and  $f_{\text{col}}$ . This has been made on the premise that  $a_*$  can not be confidently constrained with current spectral fitting and while the assumption of  $a_* = 0$  is unlikely to be the case, it should at least provide a close approximation for  $R_{\text{in}}$  while in the soft state and be seen to break down in the hard state if large disc truncation occurs (Done & Diaz Trigo, 2010b; Kolehmainen & Done, 2010; Plant et al., 2015, 2014a). Similarly the requirement of constant value for  $q$  based on analytical Newtonian assumptions and  $f_{\text{col}}$  on a steady non-irradiated disc are unlikely to hold and could well explain the inconstancy in the measurements of  $R_{\text{in}}$  between the Fe-K line and thermal disc component (Wilkins & Fabian, 2012; Salvesen et al., 2013).

The goodness of fits here suggested no presence of a truncated disc, however a neutral reflection component was needed for several of the hard state observations in addition to the broad reflection model. This may be the result of irradiation upon the outer disc, however it would also be consistent with a truncated disc. In addition to the neutral reflection feature, a soft excess around  $\sim 1\text{keV}$  was identified across both the hard and soft state observations. This excess appeared to increase with the total flux of the observation and was also present in the RGS data. The goodness of the fits compare favourably with previous studies and the parameters vary inline with typical expectations for the hard and soft states.

The modelling struggled with the low-luminosity intermediate state observations of the 2002/03 outburst: rev-0594 & rev-0600. These observation capture GX 339–4 in a late outburst decay phase, as the coronal emission begins to harden. The Plant et al. (2014b) spectral study of GX 339–4 during its failed outburst in 2013, identified a mildly truncated disc ( $R_{\text{in}} \sim 20R_g$ ) with good agreement between the measurement of  $R_{\text{in}}$  from the disc and reflection components. This mild truncation however was obtained from the use of canonical values for  $f_{\text{col}}$  and  $q$ , a small variation in these values could return the disc to the ISCO. The truncation of the disc also reduces the accretion efficiency, where even with mild truncation the accretion rate would have to be greater than the level required at the peak of the outburst (assuming the disc was at ISCO during the peak). The Plant et al. (2014b) analysis was of observations in the hardening late phase of an outburst, it may be the case that the disc truncates at different luminosity depending on whether the disc is rising or decaying during the outburst.

# 4

The varying colour correction factor  
of GX339-4 in the bright hard state

In this chapter, I present the results and analysis from the spectral model fitting of four archival *XMM-Newton* observations of GX 339–4, while in the hard state. On the assumption of a steady inner disc, I consider the physicality of both the colour correction factor and emissivity variations seen with flux. With the use of a novel count rate slicing technique, I am able to expand the number of fitted spectra to 27, maximising the flux coverage of the *XMM-Newton* observations.

## 4.1 Introduction

The spectral modelling uncertainties in measuring the inner disc radius of XRBs, has lead to a charged debate over the requirements for disc truncation in the low-hard state of GX 339–4 (Esin et al., 2001; Salvo et al., 2001; Tomsick et al., 2008; Reis et al., 2008; Done & Diaz Trigo, 2010b; Salvesen et al., 2013; Kolehmainen et al., 2014; Plant et al., 2015, 2014a). In the last few years it has become apparent that the inner disc measurements obtained from the Fe-K line broadening, can often fail to correlate with those obtained from the thermal disc emission (Kolehmainen et al., 2014). This issue could be further compounded when considering the possibility of parameter variations from their typically priori values such the radial emissivity parameter  $q \sim 3$  or the colour correction factor  $f_{\text{col}} \sim 1.8$ .

An alternative approach the issue of disc truncation is to assume a fixed inner disc radius across all spectral states while allowing the both  $q$  and  $f_{\text{col}}$  to vary. In Chapter 3, I applied such a model to 11 *XMM-Newton* observations covering both the hard and soft states of GX 339–4 and identify no discernible reason to posit the disc truncation model. The results of modelling yielded a significantly more shallow emissivity value with  $q \sim 2$  but perhaps more interestingly the colour correction factor showed a dichotomy between the hard  $f_{\text{col}} \sim 1.5$  and soft  $f_{\text{col}} \sim 2.7$  states. Such a transition in  $f_{\text{col}}$  was tentatively proposed by Gierliński & Done (2004) as suggestive of a beta accretion disc where gas pressure rather than total pressure drives the disc torque.

The concept of a beta accretion disc was first proposed as a solution to the radiation pressure instability that is exhibited in alpha accretion discs. When ra-

radiation pressure dominates the viscous heating term becomes strongly dependant upon temperature  $Q_+ \propto T^4$ , this leads to a thermal runaway independent of the thermal-viscous instability generated from the ionisation of hydrogen. With little observational evidence for such an instability, the beta viscosity prescription offers a simple ad-hoc solution for the modelling of accretion discs.

In this chapter I present the results and analysis from the spectral model fitting of four archival *XMM-Newton* observations of GX 339–4, while in the hard state. With a novel count rate slicing technique I expand this number of fitted spectra to 27, thus expanding the explored flux range in order to better identify the colour correction factor and emissivity parameter variations.

## 4.2 Observations and model fitting

In this chapter I analyse 4 archival *XMM-Newton* observations of GX 339–4 taken in the hard-state, using the fast observing mode of the EPIC pn-camera. The data was extracted using the standard processing chains of the *XMM-Newton* Science Analysis Software (SAS V15.0.0). The brightest observation rev-1886 was found to suffer from heavy pile-up when analysed with the SAS task EPATPLOT. The pixel event distribution was subsequently found to improve with removal of the central three RAWX columns. These four observations were count rate sliced in to multiple spectra (rev 0782 [10 spectra], 0783 [10], 1702 [3] & 1886 [4]), in order to broaden the flux range of the observations. The single model TBNEW(SIMPL(KERRBB) + RELXILL+ GAUSS + XILLVER) was fitted across each of the 27 spectra, with 7 free parameters:  $\Gamma$  (energy powerlaw),  $f_{\text{scat}}$  (powerlaw scatter fraction),  $\dot{M}$  (accretion rate),  $f_{\text{col}}$  (colour correction),  $q$  (inverse radial emissivity),  $\xi$  (ionisation parameter),  $N_{\text{ref}}$  (reflection normalisation),  $E_{\text{gs}}$  (gaussian line energy),  $\sigma_{\text{gs}}$  (line width),  $N_{\text{gs}}$  (gaussian normalisation), and  $N_{\text{Fe}}$  (neutral reflection normalisation). A detailed description of the GX 339-4 parameter constraints, data reduction, count rate slicing technique, ISM analysis, and the rationale behind the chosen spectral model is presented in §2.2-2.6.

## 4.3 Results and analysis

The spectral modelling was carried out using XSPEC (V12.9.0i) within the energy bandpass 0.7–10 keV. The energy range 1.75–2.35 keV was excluded as it is thought to contain instrumental edges (Done & Diaz Trigo, 2010a; Plant et al., 2015). An energy gain correction was found to be required for several of the observations, which provides a linear shift in the energy of the the response matrix and the energy slope of the effective area, which should correct for any CTI anomalies. The energy gain correction was thus applied to all observations, adding two extra variables to the model: the energy *offset* and the energy *slope*. The model parameter values for all of the spectral fits are listed in table 4.1 and the flux values for each component of the model are listed in table 4.2. A parameter table which includes errors, along with spectral plots of each of the fits are presented in appendix B. The quality of the fits, across all of the observations is relatively high ( $\chi^2/\nu \leq 1.6$ ), with the goodness of fit primarily driven by the soft residuals close to the  $\sim 1$ keV feature, which is due to the limitations of the ad-hoc gaussian approximation. If a systematic error of 1% is included, then over-fitting occurs for all the observations.

### 4.3.1 The evolving thermal disc emission

The thermal disc emission is dependant upon both the accretion rate and the colour correction factor, thus changes in these parameters subsequently effect the resulting ionisation state of the disc and the respective reflection features, formed from the coronal irradiation of the disc. The colour correction factor is simply a crude measure of the thermalisation of the disc emission, where poor thermalisation leads to a considerable Compton component, which subsequently hardens the disc emission. The colour correction factor is generally assumed to be constant  $f_{col} \sim 1.7 - 2$ , based on theoretical and high state observational studies (Shimura & Takahara, 1995; Davis et al., 2005; Dunn et al., 2011). The colour correction factor has a negative correlation with the total flux for observations rev-1702, 0782 & 0783, where it decreases from 1.61-1.32, there are two significant outlier  $f_{col} > 2$  this includes the observation with the lowest luminosity and the slight erroneous fit for

Table 4.1: The count-rate sliced parameter table for GX 339–4. The *XMM-Newton* revolution and the spectral slice number are given in columns 1 & 2; columns 3-13 give the model values; 14 & 15 give the gain corrections, and 16 & 17 give the fit statistics.

Spectrum		SIMPL		KERRBB		RELXILL			GAUSSIAN			XILL	GAIN		$\chi^2$	dof
Rev	No	$\Gamma$	$f_{\text{scat}}$	$\dot{M}_{18}$ gs $^{-1}$	$f_{\text{col}}$	$q$	$\xi$ log $_{10}$	$N_R$ log $_{10}$	$E_{gs}$ keV	$\sigma_{gs}$ keV	$N_{gs}$ log $_{10}$	$N_{Fe}$ log $_{10}$	slope	offset keV		
0782	1	1.60	0.32	0.08	1.51	2.24	2.30	-2.58	1.06	0.12	-2.63	-3.24	1.00	0.01	155	140
0782	2	1.58	0.50	0.07	2.17	2.15	2.89	-2.78	0.80	0.19	-1.50	-3.23	1.01	0.00	215	140
0782	3	1.61	0.33	0.13	1.52	1.74	2.30	-2.58	1.01	0.10	-2.31	-3.47	1.01	0.00	207	140
0782	4	1.62	0.33	0.14	1.47	2.07	2.29	-2.41	0.98	0.15	-2.01	-3.21	1.00	0.01	142	140
0782	5	1.63	0.32	0.15	1.41	1.93	2.29	-2.35	1.00	0.15	-1.91	-3.32	1.00	0.01	166	140
0782	6	1.64	0.38	0.15	1.52	1.95	2.30	-2.27	0.96	0.17	-1.67	-7.77	1.00	0.00	171	140
0782	7	1.65	0.39	0.17	1.49	2.01	2.30	-2.31	0.98	0.17	-1.63	-3.37	1.00	0.00	149	140
0782	8	1.66	0.38	0.19	1.45	2.05	2.29	-2.24	0.99	0.16	-1.62	-2.91	1.00	0.01	185	140
0782	9	1.67	0.34	0.23	1.32	2.04	2.28	-2.12	1.01	0.15	-1.55	-4.73	0.99	0.02	124	140
0782	10	1.67	0.38	0.29	1.39	2.05	2.29	-2.04	1.02	0.15	-1.45	-3.13	0.99	0.02	193	140
0783	1	1.61	0.30	0.10	1.41	2.16	2.29	-2.59	1.01	0.16	-2.34	-3.45	1.01	0.01	153	140
0783	2	1.62	0.34	0.11	1.48	2.19	2.29	-2.44	0.98	0.17	-2.06	-3.35	1.00	0.01	178	140
0783	3	1.63	0.36	0.13	1.50	2.02	2.29	-2.55	1.00	0.13	-2.02	-3.08	1.01	0.00	183	140
0783	4	1.63	0.37	0.14	1.55	1.82	2.33	-2.46	0.98	0.15	-1.93	-3.60	1.01	0.00	163	140
0783	5	1.62	0.30	0.18	1.40	1.50	2.31	-2.51	1.01	0.11	-2.06	-9.59	1.01	0.01	173	140
0783	6	1.66	0.36	0.17	1.44	1.97	2.30	-2.39	0.97	0.16	-1.68	-3.04	1.01	0.01	163	140
0783	7	1.66	0.33	0.20	1.36	1.83	2.29	-2.24	1.00	0.15	-1.70	-4.27	1.00	0.02	187	140
0783	8	1.66	0.32	0.23	1.32	1.96	2.30	-2.25	1.01	0.14	-1.72	-3.31	1.00	0.03	204	140
0783	9	1.67	0.38	0.24	1.45	1.92	2.28	-2.19	1.00	0.14	-1.55	-3.12	1.00	0.01	208	140
0783	10	1.68	0.37	0.30	1.37	2.23	2.30	-2.00	1.01	0.16	-1.39	-3.31	0.98	0.04	181	140
1702	1	1.51	0.43	0.04	2.07	1.88	2.46	-3.11	-	-	-	-3.24	1.01	0.00	142	143
1702	2	1.58	0.38	0.08	1.45	2.59	2.31	-2.61	1.03	0.20	-2.27	-3.00	1.01	0.00	160	140
1702	3	1.61	0.46	0.12	1.61	2.11	2.30	-2.30	0.94	0.19	-1.73	-3.03	1.00	0.00	158	140
1886	1	1.65	0.45	0.17	1.81	1.59	3.17	-1.73	0.89	0.20	-0.85	-3.15	0.99	0.03	188	140
1886	2	1.63	0.34	0.26	1.63	1.50	3.19	-1.58	0.93	0.18	-0.89	-2.88	0.97	0.05	208	140
1886	3	1.63	0.40	0.25	1.80	1.50	3.20	-1.47	0.94	0.19	-0.78	-2.89	0.97	0.04	223	140
1886	4	1.63	0.40	0.27	1.74	1.50	3.21	-1.34	0.94	0.18	-0.68	-3.87	0.97	0.05	206	140

Table 4.2: The count-rate sliced flux table for GX 339–4. The total flux is given in cgs units ( $\text{erg s}^{-1} \text{cm}^{-2}$ ), for the range (0.7–10 keV). The *XMM-Newton* revolution and the spectral slice number are given in columns 1 & 2; column 3 gives the total flux; columns 4-8 respectively give the percentage flux from the disc, power-law, reflection, gaussian & neutral, components of the spectral modelling.

Spectrum		Flux Range (0.7 – 10 keV)					
Rev	No	Total	$F_{\text{Disc}}$	$F_{\text{PL}}$	$F_{\text{Ref}}$	$F_{\text{Gau}}$	$F_{\text{Neu}}$
		[ $\log_{10}$ ]	[%]	[%]	[%]	[%]	[%]
0782	1	-9.04	6.9	88.6	5.6	0.4	0.6
0782	2	-8.93	9.7	83.8	8.5	2.4	0.5
0782	3	-8.85	9.6	89.1	3.6	0.6	0.2
0782	4	-8.82	9.3	87.1	5.3	1.0	0.4
0782	5	-8.78	9.1	86.7	5.7	1.1	0.3
0782	6	-8.73	9.3	86.2	6.4	1.6	0.0
0782	7	-8.68	9.5	86.8	5.5	1.6	0.2
0782	8	-8.64	10.0	85.3	6.2	1.6	0.6
0782	9	-8.59	9.7	84.4	7.5	1.7	0.0
0782	10	-8.47	11.5	84.0	6.9	1.7	0.2
0783	1	-9.00	7.0	88.9	5.2	0.7	0.4
0783	2	-8.89	8.0	87.4	6.0	1.0	0.4
0783	3	-8.82	8.9	88.7	4.0	1.0	0.6
0783	4	-8.78	9.7	87.5	5.1	1.1	0.2
0783	5	-8.74	10.9	88.1	3.5	0.8	0.0
0783	6	-8.70	9.7	86.8	4.9	1.6	0.5
0783	7	-8.67	9.8	85.6	6.4	1.4	0.0
0783	8	-8.63	10.6	85.4	5.9	1.3	0.2
0783	9	-8.56	11.4	85.3	5.8	1.6	0.3
0783	10	-8.46	11.5	83.0	7.7	1.9	0.2
1702	1	-9.22	7.2	92.0	3.0	0.0	0.8
1702	2	-8.96	5.1	90.7	4.4	0.8	0.9
1702	3	-8.74	7.7	88.2	5.7	1.4	0.5
1886	1	-8.34	6.5	43.1	49.4	3.7	0.2
1886	2	-8.23	7.6	38.7	53.0	2.9	0.2
1886	3	-8.15	7.1	35.0	57.4	3.2	0.2
1886	4	-8.05	6.1	30.4	62.7	3.2	0.0

rev-0782 obs-2. The colour correction factor for the brighter observation rev-1886 span 1.63-1.81, with the range of the canonical value. This could signify that the disc is recessed from the ISCO and the  $f_{\text{col}}$  value has decreased to compensate, how the truncation would be very minor  $R_{\text{in}} \sim 10R_g$ .

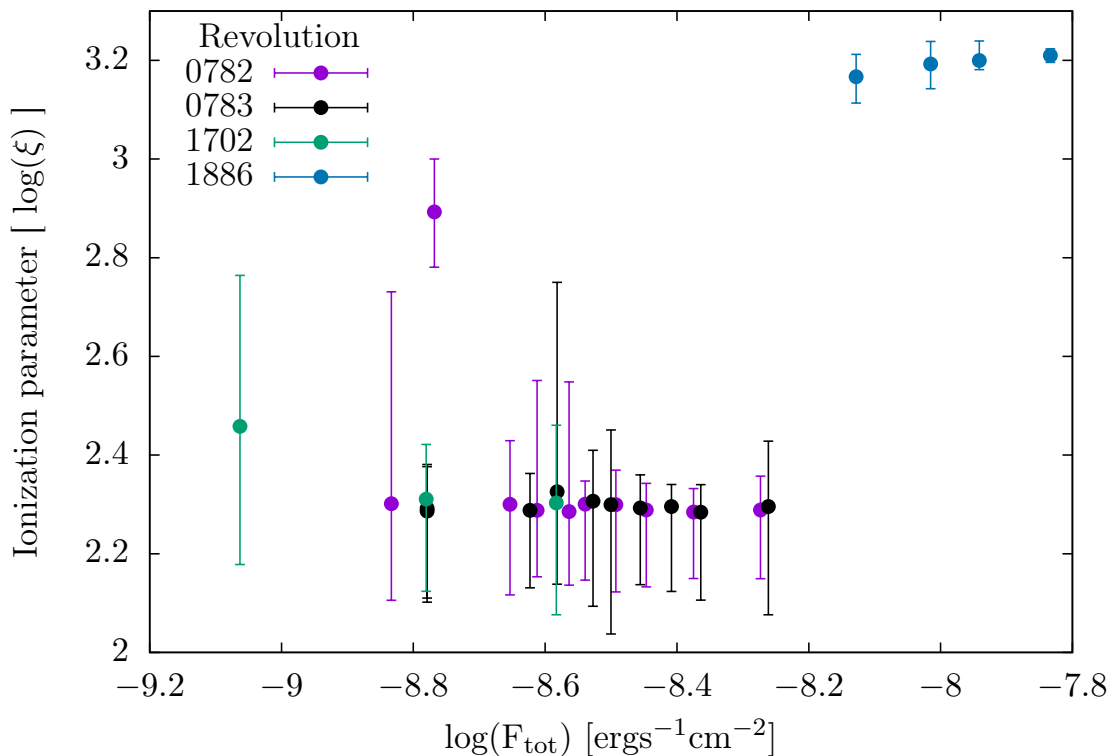


Figure 4.1: The ionisation parameter against total flux in the 0.01-10keV range. See key for the observation revolution number.

The ionisation parameter is defined as  $\xi = 4\pi F_x/n$ , where  $F_x$  is the illuminating flux and  $n$  is the gas number density. If the gas number density is assumed to be approximately constant, then  $\xi$  should just track the illuminating flux, which is dependant upon both the coronal irradiation of the disc, as well as the internal disc emission. However this is unlikely to be the case as  $n$  prior to saturation is dependant upon  $F_x$ . Figure 4.1 shows the log of the ionisation parameter with disc flux. The ionisation parameter is fairly stable across the observations rev-1702, 0782 & 0783, at  $\log(\xi) \sim 2.28 - 2.46$ , with the rev-0782 obs-2 as the only outlier at  $\log(\xi) = 2.89$ . These are fairly typical values for the hard state. The ionisation level for rev-1886 is closer to that expected for a soft state disc  $\log(\xi) \sim 3.17 - 3.21$ .

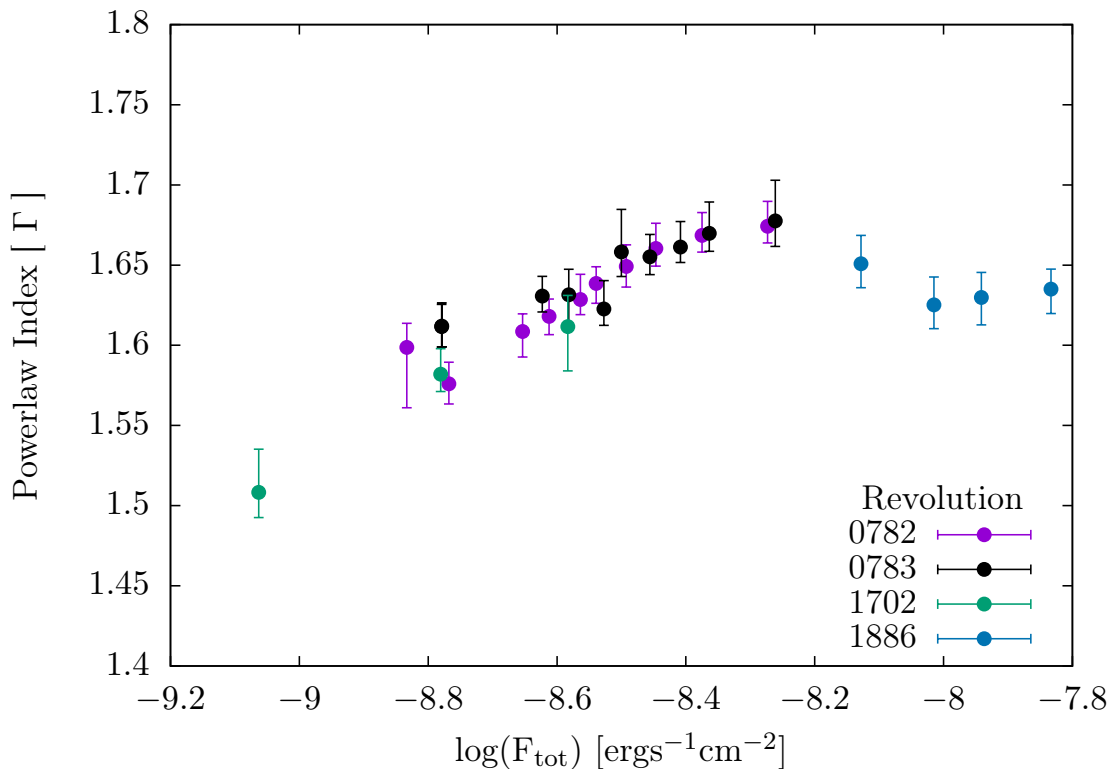


Figure 4.2: The power-law index against total flux in the 0.01-10keV range. See key for the observation revolution number.

### 4.3.2 The geometry of the corona

The power-law photon index, scatter fraction and reflection emissivities values, all allude to the geometry of the corona. Figure 4.2 shows how the power-law photon index varies with total flux. The photon index can be seen to incrementally steepen from  $\sim 1.51 - 1.68$ , before mildly decreasing and levelling out at 1.63 for the observation rev-1886. This is likely driven by the disproportionately large soft residual.

Figure 4.3 shows the evolution of the scatter fraction and radial emissivity with total flux. The scatter fraction shows a general broad range of values 0.32–0.50 with no obvious correlation with the total flux, though a general increase in the coverage can be seen in rev-0782 & 0783. The reflection emissivity values in a similar fashion show no strong correlation with the typical value close to  $\sim 2$ , this significantly lower than the typical value of  $q = 3$ .

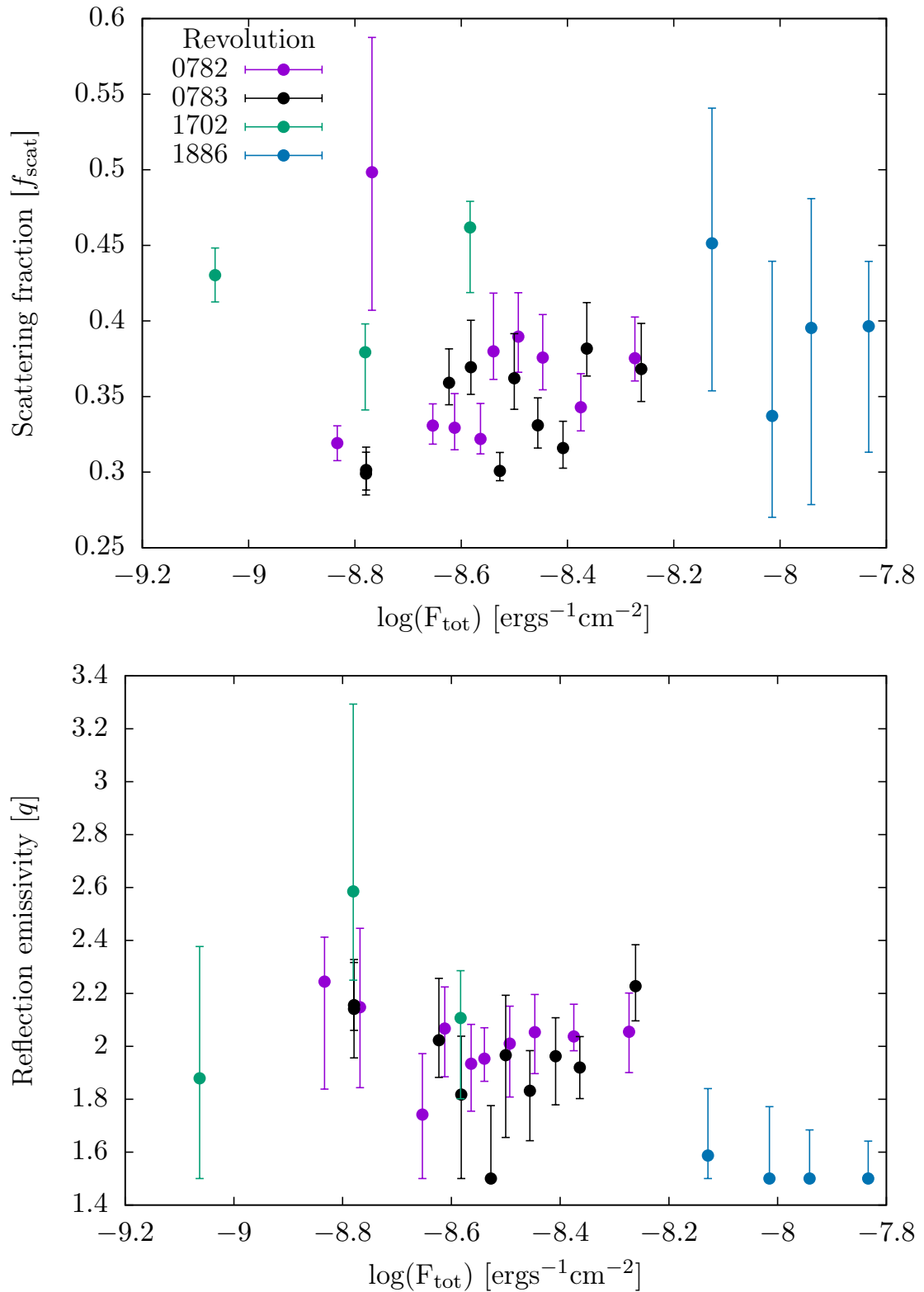


Figure 4.3: The scatter fraction and reflection emissivity with total flux in the 0.01-10keV range. See key for the observation revolution number.

### 4.3.3 Modelling the residual features

In chapter 3, two prominent residual features required the core model to be expanded: a soft excess at  $\sim 1\text{keV}$ , which was modelled with gaussian component (GAUSS) and a neutral Fe-K line, which was modelled with a neutral reflection component (XILLVER). With the count rate sliced spectra, the variation in these components can be tracked across a broad flux range. The gaussian component is seen to significantly increase as a percentage of the total flux. The flux from the neutral reflection component is relatively constant and so diminish with increases in the total flux. The neutral Fe-K line feature however is not seen in all observations, which may suggest that it is a transient emission.

## 4.4 Discussion and conclusions

### 4.4.1 A steady inner disc radius

In this chapter, I have analysed the spectral model fitting of four archival *XMM-Newton* observations of GX 339–4, while in the hard state. With the use of a novel count rate slicing technique, I was able to expand the number of fitted spectra to 27, maximising the flux coverage of the *XMM-Newton* observations. On the assumption of a steady inner disc radius, I find that if the colour correction factor and emissivity are allowed to deviate from their canonical values then there is no evidence for a truncated disc, with  $f_{\text{col}} \sim 1.4$  and  $q \sim 2$ . The soft residual at  $\sim 1\text{keV}$  that was identified in chapter 3, appears to increase with flux across the spectrally sliced observations, while the emission from the neutral Fe-K line appears to remain constant.

### 4.4.2 An alternative viscosity regime

The inner accretion disc is thought to be radiation pressure dominated at accretion rates a few percent of the Eddington ratio  $\dot{m} \geq 0.05$ . In this radiative pressure dominated regime the viscous heating term is strongly dependant upon the disc temperature  $Q_+ \propto T^4$ , which leads to a thermal runaway independent of the thermal-viscous

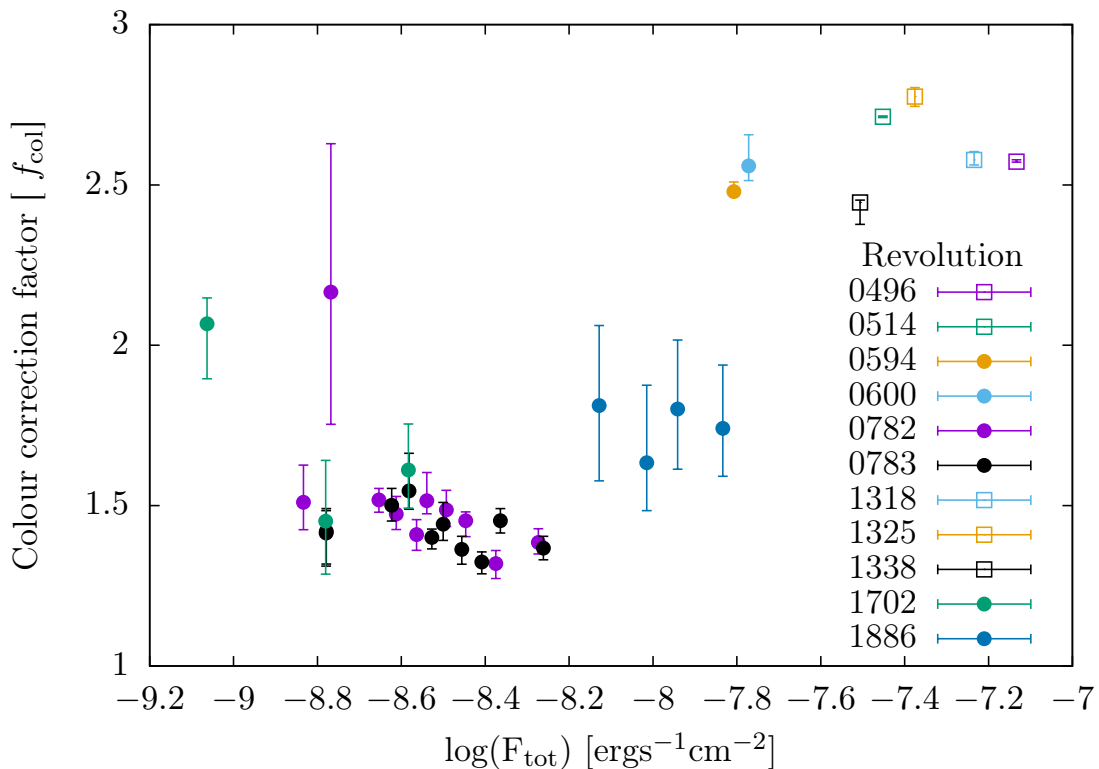


Figure 4.4: The variation of the colour correction value with respect to the accretion rate which is given in Eddington units for a Schwarzschild BH. With the spectral fits from both Chapters 3 & 4 used, see plot key for details.

instability that is generated from the ionisation of hydrogen. With no observational evidence for any such limit cycle behaviour, alternative ad-hoc viscosity prescriptions have been proposed, such as the beta accretion disc model whereby the viscosity is dependant upon the gas pressure not the total pressure. This viscosity scenario has been shown to remain thermally stable at moderate accretion rates, while still exhibiting the standard ionisation instability that is required to explain the XRB outburst cycle (Huré et al., 2001).

The spectral emission from a beta accretion disc may produce a distinctive colour correction signature with respect to the disc flux (Gierliński & Done, 2004). The first detailed investigation of the spectral hardening factor for an  $\alpha$ -disc was performed by Shimura & Takahara (1995), in which they identified a near constant correction value across a range of accretion rates  $f_{\text{col}} \sim 1.7 - 2.0$ . In the Shimura & Takahara (1995) study however the effect of metals upon the total opacity is ignored: this simplifying assumption likely leads to an underestimation of the total absorption within the disc,

particularly at low luminosities (Gierliński & Done, 2004). A later study of  $f_{\text{col}}$  by Merloni et al. (2000) included heavy element absorption but assumed a constant vertical disc density, which is at odds with expected vertical structure of an  $\alpha$ -disc. In the Merloni et al. (2000) study they found the colour correction factor to vary from  $f_{\text{col}} \sim 1.8$  at high accretion rates to  $f_{\text{col}} \sim 2.7$  at low accretion rates, with the transition point defined as  $\dot{m} = 0.1$ . This disagreement between the Shimura & Takahara (1995) and Merloni et al. (2000) colour correction results at low accretion rates stems from the flawed assumption of a constant disc density (Gierliński & Done, 2004; Davis et al., 2005), however both studies found that Compton down scattering has no discernible effect at low accretion rates. With this last point in mind Gierliński & Done (2004) tentatively suggested that the correction factor would likely vary from  $f_{\text{col}} \sim 2.7$  at high accretion rates to  $f_{\text{col}} \sim 1.8$  at low accretion rates for a  $\beta$ -disc: on the basis that the two viscosity prescriptions are indiscernible in the gas pressure dominated regime but differ at high accretion rates where the greater density of the  $\beta$ -disc would likely impede Compton down scattering, which would be consistent with the lower luminosity result of Merloni et al. (2000). This is close to the colour correction factor dichotomy that was identified in chapter 3 and which has been further substantiated in this chapter with the inclusion of the spectrally sliced spectra. Figure 4.4 shows how  $f_{\text{col}} \sim 1.4 - 1.5$  at low accretion rates but drastically increases to  $f_{\text{col}} \sim 2.4 - 2.8$  at  $\dot{m} > 0.01$ .

The assumption that Compton down scaling is inconsequential in a  $\beta$ -disc is far from clear. The Davis et al. (2005) analysis, which uses the 1D radiative transfer code TLUSTY (Hubeny & Lanz, 1995); found the effective photosphere of a  $\beta$ -disc to form in the low density surface layers and thus no discernible difference in the hardening factor would exist between an  $\alpha$  &  $\beta$  viscosity disc. The results from recent 3D MHD radiative transfer simulations however have backed up previous suggestions that magnetic pressure tends to increasing the vertical density profile (Narayan et al., 2016; Turner, 2004), which may have a greater effect upon the vertical structure than previously identified from ad-hoc modifications to the dissipation profile that were presented in Davis et al. (2005).

The actual physical existence of this radiative driven instability however has

been pulled into question in recent years. The alpha accretion disc is an ad-hoc viscosity prescription and thus likely fails to capture the true viscosity. Hirose et al. (2009), using a MHD local shearing box with flux limited diffusion (FLD) found radiation pressure dominated discs to be thermally stable. This result however has been questioned by (Jiang et al., 2013) who ran global MHD simulations and found the disc to eventually undergo thermal runaway. When working with the (Hirose et al., 2009) team, (Jiang et al., 2013) they were only able to reproduce the radiative stability result when using the same box size and the FLD prescription. When using a more accurate radiation transfer algorithm or expanding the shearing box size by one scale height, the thermal runaway would return. Suggesting that alpha accretion discs are unstable in the radiatively dominated regime.

The observational findings here offer a potential degree of credence to the Gierliński & Done (2004) hypothesis and the alternative beta viscosity regime. However a thorough theoretical investigation of the colour correction factor for a  $\beta$ -disc is required before such a model could even be considered as a physical robust explanation for the hardness variations that were exhibit in this study.

# 5

## The variable nature of LMC X-3

## 5.1 Introduction

LMC X-3 was first observed as a bright X-ray source in 1971, with the *Uhuru* satellite (Leong et al., 1971). In 1983 after successive optical studies, the system was identified as a High Mass X-ray Binary (HMXB): consisting of a  $\sim 4-8M_{\odot}$  B-type star and  $\sim 9-10M_{\odot}$  black hole, in a 1.7 day orbit with each other (Cowley et al., 1983).

LMC X-3 is one of the few HMXBs to have been extensively studied for over 40 years, owing to its persistently high X-ray luminosity:  $L_X \simeq 1.8 \times 10^{38}$  erg/s (Leong et al., 1971; Cowley et al., 1983; Soria et al., 2001; Wilms et al., 2001; Steiner et al., 2010). When in the high-soft state, LMC X-3 has been observed to be highly variable (Nowak et al., 2001). This variability was investigated by Wilms et al. (2001) who used archival Rossi X-ray Timing Explorer (*RXTE*) data to produce a periodogram for LMC X-3, from which they identified four semi-periodic peaks at 100, 160, 190 & 250 days.

The mechanism behind the semi-periodic nature of LMC X-3 has long been speculated upon and could be the results of a wind driven limit cycle (Shields et al., 1986; Cowley et al., 1991); a precession of the disc about the black hole (Foulkes et al., 2010; Ogilvie & Dubus, 2001; Montgomery & Martin, 2010; Larwood, 1998; Schandl, 1996), or the result of novel accretion modes such as the evaporation-condensation mechanism (Cambier & Smith, 2013; Mayer & Pringle, 2007b).

Coronal winds are thought to be generated from the irradiation of the disc photosphere at large radii, leading to the formation of a tentative corona. If the coronal density is below a critical value, radiative cooling will dominate. This can lead to a rapid increase in the coronal temperature until the sound speed exceeds the escape velocity a wind will form and mass will be lost from the disc forming a limit cycle.

A precession of the disc about the black hole can be driven by irradiation from the inner disc (Foulkes et al., 2010; Ogilvie & Dubus, 2001) or from tidal torques from the companion star (Montgomery & Martin, 2010; Larwood, 1998; Schandl, 1996). A warped disc can affect the accretion rate by changing the disc density and subsequent inflow rates. The disc tilted from the orbital plane can also effect line of

sight observations of the inner disc and can also lead to shadowing of the companion star.

The evaporation-condensation mechanism, involves the transport of matter from the outer to the inner disc via the corona (Mayer & Pringle, 2007b; Cambier & Smith, 2013). At large radii matter can evaporate from the disc and form a corona, this matter can then be transported through the corona towards the BH, where it condenses upon the inner regions via radiative cooling (Liu et al., 2007; Meyer et al., 2007).

Cambier & Smith (2013) numerically explored all three of these mechanisms in relation to LMC X-3, but they were unable to reproduce the same depth and short periodicity seen in observations. In addition to this, the lack of strong variability in the hydrogen column density  $N_H$  during high and low states, likely rules out any significant coronal wind or disc precession (Wilms et al., 2001). The evaporation-condensation mechanism however could offer a possible solution, but current models transport excessive levels of matter to the inner disc region (Cambier & Smith, 2013).

There are currently only three known persistent HMXBs: LMC X-1, LMC X-3, and Cyg X-1; with all three of these systems producing significant different light-curves (see figure 5 of Done et al., 2007). LMC X-1 and Cyg X-1 are both believed to be powered by the stellar winds of O-type stars, while LMC X-3 is likely to be fed via Roche lobe overflow (RLO) from a B5 IV type star (Soria et al., 2001). LMC X-1 shows comparatively little variability in comparison to LMC X-3,

The similarities and differences of these systems along with extensive observational data, allows for detailed testing of accretion disc models. Despite the large number of observations, the system has only been observed to drop into a prolonged state of quiescence once. This took place in January 2012 and lasted nearly 3 months, before the source rapidly rose back to its high-luminosity state. In order to better understand this unusual activity, a 1D disc model as described in Alexander et al. (2011) is presented here to explain the main features of the LMC X-3's light curve.

Through estimating the average mass transfer rate,  $\dot{M}_2$ , we can show that LMC X-3 is on the verge of transience/persistence. This means a change in  $\dot{M}_2$  by a

single order of magnitude, over a suitable length of time, could send the system into quiescence, as observed. While we cannot measure the mass transfer rate of LMC X-3 directly, nor its variation, we can infer from systems such as AM Herculis stars, in which material flows directly onto the compact object (in this case a white dwarf) via magnetic field lines, that  $\dot{M}_2$  may vary by approximately 2 orders of magnitude on time scales of a month or less (Hessman et al., 2000). We suggest that a random fluctuation such as this is suitable to explain the observed light-curve.

## 5.2 The stability of HMXBs

### 5.2.1 LMC X-3 on the Verge of Transience

As a persistent source, LMC X-3's accretion disc must be kept at a sufficiently high surface density and temperature at all radii, in order to be stable to the thermal-viscous instability. The rate at which the disc is fed material from the secondary star must therefore be greater than a critical value,  $\dot{M}_{\text{crit}}^+$  which has been parametrised by Lasota et al. (2008) for a solar composition disc;

$$\begin{aligned} \dot{M}_{\text{crit}}^+ &= 9.5 \times 10^{14} \mathcal{C}_{-3}^{-0.36} \alpha_{0.1}^{0.04-0.01 \log \mathcal{C}_{-3}} R_{10}^{2.39-0.10 \log \mathcal{C}_{-3}} \\ &\times M_1^{-0.64+0.08 \log \mathcal{C}_{-3}} \text{g s}^{-1}, \end{aligned} \quad (5.1)$$

where  $R_{10}$  is the radius of the disc,  $R_{\text{out}}/10^{10}$  cm,  $M_1$  is the mass of the central object in solar masses and  $\alpha_{0.1} = \alpha/0.1$ , is the viscosity parameter.  $\mathcal{C}_{-3} = \mathcal{C}_x/10^{-3}$  is the X-ray heating coefficient which takes account of disc irradiation and is defined by the irradiation flux (Dubus et al., 1999);

$$\sigma T_{\text{irr}}^4 = C_x \frac{\dot{M} c^2}{4\pi R^2}. \quad (5.2)$$

Since equation 5.1 is an increasing function of radius, we can best test this condition on the outer edge of the disc. Paczyński (1977) computed maximum disc radii by following single particle orbits and tabulating the maximum radius vector of the

last non-intersecting orbit. His results can be parametrised in terms of  $a$ , the binary separation, and  $q$  the mass ratio,  $M_2/M_1$ , as;

$$\frac{R_{\text{out}}}{a} = \frac{0.60}{1+q} \quad 0.03 < q < 1, \quad (5.3)$$

where,  $a$  is the binary separation given by Kepler's law;

$$a = 3.53 \times 10^{10} M_1^{1/3} (1+q)^{1/3} P_{\text{orb}}^{2/3} (\text{h}) \text{ cm}, \quad (5.4)$$

Taking typical values for LMC X-3's orbital period of  $\sim 40.8$  hours, a primary mass of  $\sim 9M_\odot$ , a mass ratio  $q \sim 0.6$  (Cowley et al., 1983) and assuming the disc to be in a hot irradiated state,  $\alpha = 0.1$  and  $\mathcal{C} = 10^{-3}$ . We calculate  $M_{\text{crit}}^+$  to be approximately  $2.2 \times 10^{-8} M_\odot/\text{yr}$ . A comparison of this value with the secondary accretion rate, allows for the stability of the system to be known. As LMC X-3 is typically in a steady state, the secondary accretion rate can be assumed to be equal in magnitude to the primary accretion rate  $-\dot{M}_2 = \dot{M}_1$ . The primary accretion rate can be established from the X-ray luminosity:  $L_X = \eta \dot{M}_1 c^2$ , where  $c$  is the speed of light and  $\eta$  the accretion efficiency, taken to be 0.1 for a black hole. The mean luminosity is taken as  $\sim 1.8 \text{ erg/s}$  (White & Marshall, 1984), which gives an accretion rate of  $\dot{M}_2 \simeq 10^{-7.5} M_\odot/\text{yr}$  and confirming that LMC X-3 is a persistent X-ray source with  $\dot{M} > \dot{M}_{\text{crit}}$ . However, fluctuations in the mass infall rate by  $\sim 29\%$  could cause this system to drop below this critical value, suggesting it is on the verge of transience.

Fluctuations in the mass accretion rate which take place on shorter timescales than the viscous time scale,  $t_{\text{visc}}$ , do not give the disc sufficient time to react and so will not produce any observable change in disc structure. Consequently the change in  $\dot{M}_2$ , which produced the drop into quiescence for LMC X-3, must have lasted  $\mathcal{O}(t_{\text{visc}})$  or longer. If the source had spent too long in quiescence, we would have observed outbursts from the low state, since the disc would now be unstable to the thermal-viscous instability (reviewed in Lasota, 2001). Instead, the lightcurve of Figure 5.1 shows a smooth fall into, and rise out of quiescence. This places an upper limit for time that  $\dot{M}_2$  drops to a lowered state, which will depend on various factors such as the radius the wind is injected and also the magnitude of its drop, both of

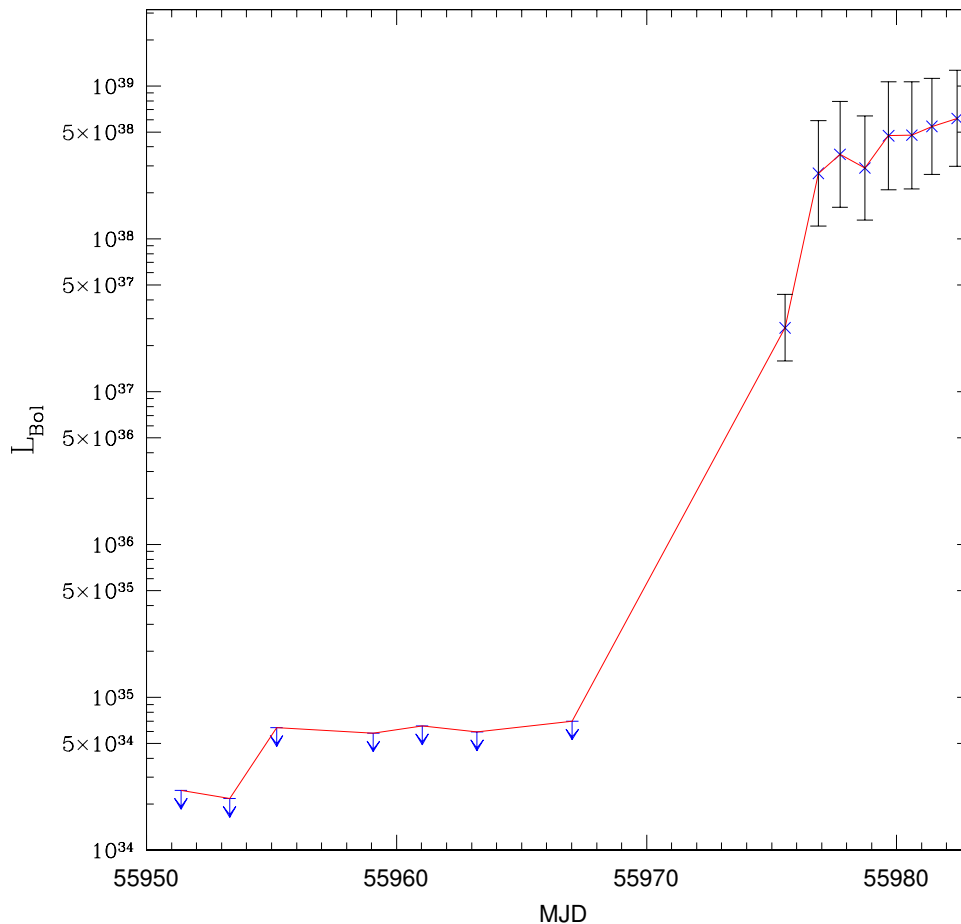


Figure 5.1: The bolometric light curve of LMC X-3, as it rises out from quiescence in January 2012. The upper limits upon the luminosity were obtained using *XMM-Newton* data. This was followed by a *Swift* monitoring campaign to obtain accurate flux measurements. The 8-day gap in observations is due to the source being located at the satellite orbital pole. Figure obtained from Prof. Chris Done.

which are numerically investigated.

### 5.2.2 Comparisons with other persistent HMXBs

Other persistent HMXB systems such as LMC X-1 and Cyg X-1 have a more stable light curve compared to that of LMC X-3 and have yet to be observed entering quiescence. An analytical approximation of  $t_{\text{visc}}$  and  $\dot{M}/\dot{M}_{\text{crit}}^+$  is calculated for these following three systems to identify LMC X-3's relative variability and fall into quiescence, see table 5.1.

Table 5.1: HMXB system parameters, viscous times and accretion ratios.

HMXB	$M_1$	$M_2$	$L_X(10^{37}\text{erg/s})$	$P(h)$	$T_{\text{visc}}(\text{days})$	$\dot{M}/\dot{M}_{\text{crit}}^+$
LMC X-3	$\sim 10^{[1,2]}$	$\sim 6^{[1,2]}$	$\sim 18^{[1,3]}$	$40.8^{[4]}$	787.9	1.4
LMC X-1	$10.9^{[5]}$	$31.8^{[5]}$	$23^{[5]}$	$93.6^{[5]}$	1437.7	0.54
Cyg X-1	$14.8^{[6]}$	$19.2^{[6]}$	$2.1^{[6]}$	$134.4^{[7]}$	5039	0.025

[1]Cowley et al. (1983), [2]Soria et al. (2001), [3]White & Marshall (1984), [4]van der Klis et al. (1983), [5]Orosz et al. (2009), [6]Orosz et al. (2011), and [7]Brocksopp et al. (1999).

The values for  $M_1, M_2$  and  $L_X$  given in table 5.1 are taken from observations, referenced in the table caption.  $\dot{M}$  is calculated from the luminosity as before, while  $\dot{M}_{\text{crit}}^+$  and  $t_{\text{visc}}$  is calculated for the outer radius of the disc using equations 5.1 and 5.6 respectively. As  $q > 1$  for Cyg X-1 and LMC X-1, equation 5.3 can not be used to calculate  $R_{\text{out}}$ . Instead an approximation is taken that the outer disc radius is determined solely by tidal forces and thus can be given by  $R_{\text{out}} \simeq 0.9R_1$  (Frank et al., 2002b), where  $R_1$  is the primary stars Roche lobe radius,

$$\frac{R_1}{a} \simeq \frac{0.49q^{-2/3}}{0.6q^{-2/3} + \ln(1 + q^{-1/3})} \text{cm}. \quad (5.5)$$

An  $\alpha$  disc parameterisation from Frank et al. (2002b) is used to estimate  $t_{\text{visc}}$ . The outer radius is assumed to be in a hot state state  $\alpha = 0.1$  and the disc to be irradiated  $C = 10^{-3}$ . The vicious time can parameterised in terms of the radius of the disc  $R_{10} = R_{\text{out}}/10^{10}\text{cm}$  and the accretion rate  $\dot{M}_{16} = \dot{M}/10^{16} \text{ g/s}$ ,

$$t_{\text{visc}} \simeq 3 \times 10^5 \alpha^{-4/5} \dot{M}_{16}^{-3/10} m_1^{1/4} R_{10}^{5/4} \text{ s}. \quad (5.6)$$

The values for  $\dot{M}/\dot{M}_{\text{crit}}^+$  and  $t_{\text{visc}}$  given in table 5.1, show that LMC X-3's calculated viscous time is appreciably less than the other two persistent systems. This allows for variations in the donors accretion rate, to more readily effect LMC X-3's lightcurve. The viscous time calculated here is greater then the time spent in quiescence, which is a problem considered in Section (5.3.4). This means that a variations on time scales shorter than the vicious time may be required such as thermal or even irradiative warping effects of the disc.

Unlike LMC X-3, the observed luminosity of both LMC X-1 and Cyg X-1 suggest that they should be in the thermal-viscous instability range  $\dot{M}_{crit}^- < \dot{M} < \dot{M}_{crit}^+$ . Both systems though are observed to be persistent, one possible reason for this an over estimation of the outer disc radius (Coriat et al., 2012a), though this would require a reduction of approximately 28% and 78% respectively from our outer radius estimates. An alternative explanation could be due to high levels of irradiation, from both the inner disc and the secondary star. This would lower the accretion rate for disc instability and could even lead to a straightened S-curve with no instability region.

## 5.3 A disc instability model

We use a one-dimensional parallelised time dependent disc model which includes viscous heating, radiative cooling, disc irradiation and a temperature dependant  $\alpha$  prescription, allowing for thermal-viscous instabilities. A full description of the numerical method can be found in Alexander et al. (2011), with only a summary provided here.

### 5.3.1 The disc evolution

The time dependant surface density of the disc  $\Sigma(R, t)$ , is governed by the secondary accretion rate and the diffusion of matter resulting from the viscous and tidal forces acting within and upon the disc respectively (Lynden-Bell & Pringle, 1974);

$$\frac{\partial \Sigma}{\partial t} = \frac{1}{R} \frac{\partial}{\partial R} \left[ 3R^{1/2} \frac{\partial}{\partial R} (\nu \Sigma R^{1/2}) - \frac{2\Lambda \Sigma R^{3/2}}{(GM_1)^{1/2}} \right] + \dot{\Sigma}_{infall}(R, t).$$

Here  $t$  is time,  $R$  is cylindrical radius,  $\nu$  is the kinematic viscosity,  $M_1$  is the mass of the primary, and  $\dot{\Sigma}_{infall}(R, t)$  is the mass infall rate from the secondary star. The two terms which are bracketed on the right-hand side respectively represent the viscous and tidal contributions to the diffusion of matter within the disc. The rate of specific angular momentum transfer from the secondary star to the disc  $\Lambda(R, a)$ , is given by Lin & Papaloizou (1986);

$$\Lambda(R, a) = -\frac{q^2 GM_1}{2R} \left( \frac{R}{\Delta_p} \right)^4, \quad (5.7)$$

with  $q = M_2/M_1$  as the binary mass ratio and  $\Delta_p = \max(H, |R - a|)$  the pressure gradient of the disc; where  $a$  is the binary separation and  $H = c_s/\Omega$  is the disc scale-height. The standard Shakura & Sunyaev (1973) viscosity parameterisation is employed;

$$\nu = \alpha c_s^2/\Omega, \quad (5.8)$$

where  $c_s$  is the radial sound speed,  $\Omega = \sqrt{GM/R^3}$  is the Keplerian angular frequency, and the dimensionless parameter  $\alpha$  specifies the efficiency of angular momentum transport.

The radial sound speed provides a de facto means of keeping track of the local gas and radiation pressure;

$$c_s^2 = \frac{\mathcal{R}T_c}{\mu} + \frac{4\sigma_{\text{SB}}T_c^4}{3c\rho_c}. \quad (5.9)$$

Here  $\mathcal{R}$  is the gas constant,  $\mu$  is the mean molecular weight and  $c$  is the speed of light. We adopt standard numerical fits for the mean molecular weight  $\mu(T, \rho)$  from (Huré, 2000a). In practice, radiation pressure is only significant at high temperatures, with the gas pressure being predominant. The mid-plane density  $\rho_c$  is evaluated from the surface density by assuming that the disc is vertically isothermal,

$$\rho_c = \frac{\Sigma}{\sqrt{2\pi}(c_s/\Omega)}. \quad (5.10)$$

The efficiency of angular momentum transport is thought to dramatically increase as hydrogen within the disc becomes ionised. This behaviour is incorporated into the model by assuming a rapid transition between the cold and hot states at the point that hydrogen ionises  $T_{\text{crit}}=5000\text{K}$ ;

$$\alpha(T) = \frac{\alpha_{\text{hot}} - \alpha_{\text{cold}}}{1 + \exp\left(\frac{T_{\text{crit}} - T}{\Delta T}\right)} + \alpha_{\text{cold}}, \quad (5.11)$$

where  $\alpha_{\text{cold}} = 0.01$ ,  $\alpha_{\text{hot}} = 0.1$ , and  $\Delta T = 250\text{K}$ .

### 5.3.2 The energy balance

The thermal evolution of the central temperature of the accretion disc  $T_c(R, t)$  was calculated using the simplified energy equation of Cannizzo (1993);

$$\frac{\partial T_c}{\partial t} = \frac{2(Q_+ - Q_-)}{c_P \Sigma} - u_R \frac{\partial T_c}{\partial R}, \quad (5.12)$$

where  $Q_+$  and  $Q_-$  are the instantaneous heating and cooling rates per unit surface. The radial velocity  $u_R$  in the advective term, is taken to be the vertically averaged value and is computed as;

$$u_R = -\frac{3}{\Sigma R^{1/2}} \frac{\partial}{\partial R} (\nu \Sigma R^{1/2}). \quad (5.13)$$

The specific heat capacity  $c_P$  is approximately constant for most temperatures of interest, but rises dramatically at  $\sim 10^4$  K, due to the ionisation of atomic hydrogen. We adopt the functional form for  $c_P$  from (Cannizzo, 1993). The surface rate heating term  $Q_+$  is evaluated as,

$$Q_+ = Q_\nu + Q_{\text{tid}} + Q_{\text{hs}} + Q_{\text{irr}}. \quad (5.14)$$

$Q_\nu$  is the heating from viscous dissipation given by,

$$Q_\nu = \frac{9}{8} \nu \Sigma \Omega^2. \quad (5.15)$$

The heating due to the tidal torque from the secondary is evaluated as that in (Lodato et al., 2009);

$$Q_{\text{tid}} = [\Omega_2 - \Omega] \Lambda \Sigma, \quad (5.16)$$

where  $\Omega_2$  is the orbital frequency of the secondary. The heat input at the hotspot where the accretion stream lands on the disc is given by (Lasota, 2001a);

$$Q_{\text{hs}} = \eta \frac{GM_1 \dot{M}_{\text{infall}}}{2R_{\text{out}}} \frac{1}{2\pi \Delta R_{\text{hs}}^2} \exp\left(\frac{R - R_{\text{out}}}{\Delta R_{\text{hs}}}\right), \quad (5.17)$$

here  $\eta = 1$  is an (arbitrary) efficiency factor,  $\dot{M}_{\text{infall}} = \int 2\pi R \dot{\Sigma}_{\text{infall}} dR$  is the accretion rate from the secondary.  $R_{\text{out}}$  is the outer disc radius (computed as the radius where  $\Sigma$  falls below  $1 \text{ g cm}^{-2}$ ) and  $\Delta R_{\text{hs}} = 0.1 R_{\text{out}}$  is the width of the heated region.

$Q_{\text{irr}}$  is an additional heating term which is included to take account of irradiative heating from the inner accretion disc,

$$Q_{\text{irr}} = \mathcal{C}_x \frac{\dot{M} c^2}{4\pi R^2}. \quad (5.18)$$

Here  $\mathcal{C}_x$  is a geometric parameter, giving the fraction of accreted energy that irradiates the disc. Typical values for BH primaries are  $\mathcal{C}_x \sim 1 \times 10^{-4}$  with an upper limit of  $\mathcal{C}_x < 0.01$ . In our model the heating parameter is taken to be  $10^{-3}$  for an irradiated disc and  $10^{-5}$  for a non irradiated disc.

In practice viscous heating and irradiation dominate, with hotspot heating almost completely negligible and tidal heating only significant very close to the outer edge of the disc and even then is not dominant. We adopt a *one-zone* model for cooling as used by (Johnson & Gammie, 2003);

$$Q_- = \frac{8}{3} \frac{\tau}{1 + \tau^2} \sigma_{\text{SB}} (T_c^4 - T_{\text{min}}^4) \quad (5.19)$$

Here, the second term allows for a smooth transition between the limits of optically thick and optically thin cooling.  $\sigma_{\text{SB}}$  is the Stefan-Boltzmann constant and the last term is prescribed in a manner that enforces a minimum disc temperature  $T_{\text{min}} = 10 \text{ K}$ . The vertical optical depth  $\tau$  is computed as;

$$\tau = \frac{1}{2} \kappa(T_c, \rho_c) \Sigma. \quad (5.20)$$

We adopt standard numerical fits for the opacity  $\kappa(T, \rho)$  as that of Zhu et al. (2007).

### 5.3.3 Numerical Method

These equations were solved using an explicit finite-difference method on a grid that is equispaced in  $R^{1/2}$  with 500 cells from  $\sim 1000R_g$  to  $1 \times 10^{12}$  cm. The disc model was in convergence for models with 130, 350 and 500 grid cells. In the staggered grid, scalar quantities were evaluated at cell centres and vectors at cell edges. Adopting zero-torque boundary conditions at both the inner and outer boundaries by setting  $\Sigma = 0$  in the boundary cells.

Using the parameters for the LMC X-3 system shown in table 5.1. We produce initial conditions by allowing the system to evolve for  $\sim 2000$  days, generating a steady state surface density profile of the disc. In order to replicate the drop into quiescence, we drop the system into a low state by reducing the mass infall by a reduction factor ( $f_r$ );  $\dot{M}_{\text{infall}} = \dot{M}_{\text{infall}}^{\text{int}}/f_r$ . After a time  $t_{\text{low}}$  we allow the mass infall rate to return to its initial value for  $\sim 1000$  days, in order to observe the rise out.

### 5.3.4 Time Constraints

The 3 months that LMC X-3 spent in quiescence and approximate 80 days to enter and less than 8 days to rise out from observations, places difficult time constraints on our simulations. In the steady high state produced for our initial conditions, we estimate a viscous time of 250 – 400 days close to the edge of the disc; this of course depends on our choice of  $\mathcal{C}_x$ , the irradiation constant. If the disc requires times scales on these durations to respond to external changes, it becomes very difficult to ratify our simulations with the observational constraints.

A reduced viscous time could either be due to a shorter infall radius or high irradiation effects. A shorter infall radius could be due to extremely high wind velocities from the secondary star, while irradiation effects predominately dependant upon the geometry of the disc. Combining both of these two alternatives for example, by including a reasonable choice for the irradiation constant  $\mathcal{C}_x = 10^{-3}$  and considering a small infall radius  $R_{\text{out}} = 6 \times 10^{10}$  cm, the viscous time of the disc reduces to  $\sim 80$  days, approximately inline with observations.

We therefore run our models for a wide range of parameter values. With  $t_{\text{low}}$

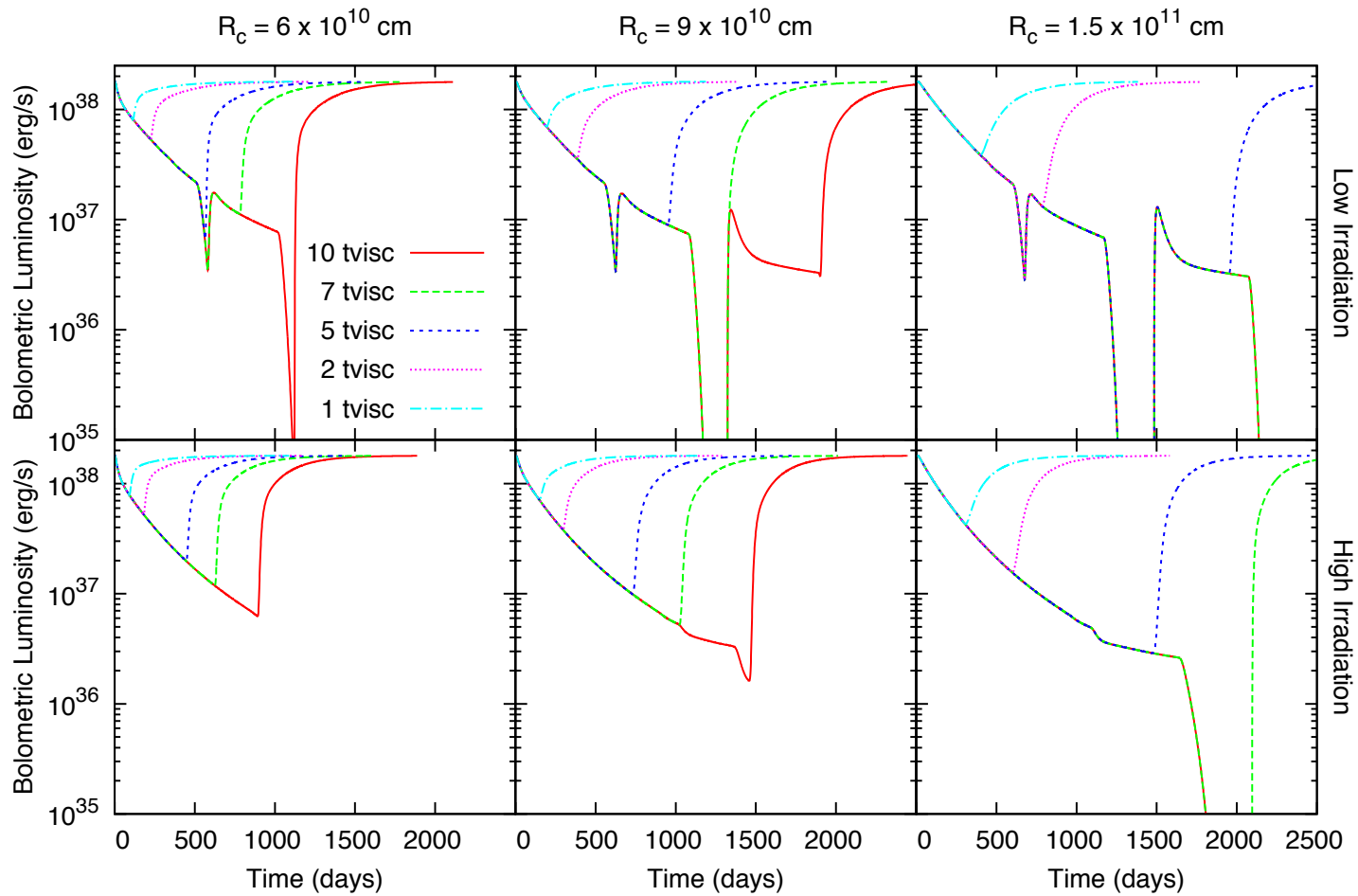


Figure 5.2: Lightcurves showing the fall and rise of LMC X-3 out of quiescence when  $\dot{M}_2$  is dropped by a factor of a hundred for different multiples of the viscous time (different colours on diagram - see key). The upper panels show results for a radiation constant,  $\mathcal{C}_x$  of  $10^{-5}$ , i.e. minimal radiation, whereas the lower panels show results for a higher radiation constant of  $\mathcal{C}_x$  of  $10^{-3}$  to compare what happens when radiation is included. The left hand panels assume that mass is injected at  $6 \times 10^{10} \text{ cm}$  the middle,  $10 \times 10^{10} \text{ cm}$  and the righthand panel at  $1.5 \times 10^{11} \text{ cm}$ , close to the disc edge.

ranging from 1 to  $10 t_{\text{visc}}$  at three different infall radii,  $R_{\text{circ}} = 6 \times 10^{10} \text{cm}$ ,  $9 \times 10^{10} \text{cm}$  and  $1.5 \times 10^{11} \text{cm}$ , with the later of these approximately at the discs outer radius. These runs are then considered for high and low levels of irradiation of the disc,  $\mathcal{C}_x = 10^{-3}$  and  $10^{-5}$  respectively. the magnitude of the reduction factor will affect the surface density of the disc and may subsequently alter the time to enter and rise out of quiescence and is investigated for the following values,  $f_r = 2, 10, 50, 300, 1000$  and  $10^6$ .

### 5.3.5 Lightcurve Calculations

The luminosity calculations in our model of LMC X-3 have two contributions. The contribution from accretion on to the BH primary and also the blackbody emission of the disc. Luminosity from accretion is calculated in the usual form of;  $L = \eta \dot{M}_1 c^2$ . The blackbody contribution from the disc is found by taking the effective temperature of the photosphere ( $T_{\text{eff}}$ ) at the centre of each annulus and using the Stefan-Boltzmann law for a flat disc;  $L_{\text{disc}} = \pi R^2 \sigma_{\text{SB}} T_{\text{eff}}^4$  to find the luminosity of each annulus which values are summed across the entire grid. The effective temperature of the optically thick photosphere is taken as  $T_{\text{eff}} = T_c \tau^{-1/4}$ . The total luminosity is then binned into one day time intervals before plotting. This value will be referred to as the bolometric luminosity from here on in.

## 5.4 Results and Discussion

### 5.4.1 Time Spent in quiescence

Figure 5.2 shows the light curve produced from reducing  $\dot{M}_2$  by a reduction factor of  $f_r = 100$  for three different mass infall radii  $R_{\text{circ}}$ ;  $6 \times 10^{10} \text{cm}$ ,  $9 \times 10^{10} \text{cm}$  and  $1.5 \times 10^{11} \text{cm}$  with low levels of irradiation  $\mathcal{C}_x = 10^{-5}$  (Upper panel) and high levels  $\mathcal{C}_x = 10^{-3}$  (Lower panel).

In the upper panels for the low-irradiated case all infall radii take  $\sim 500$  days for  $\dot{M}$  to drop by one order of magnitude and thus fall below the critical value  $\dot{M}_{\text{crit}}$ . Once accretion is below this value a cooling wave is generated. As the cooling

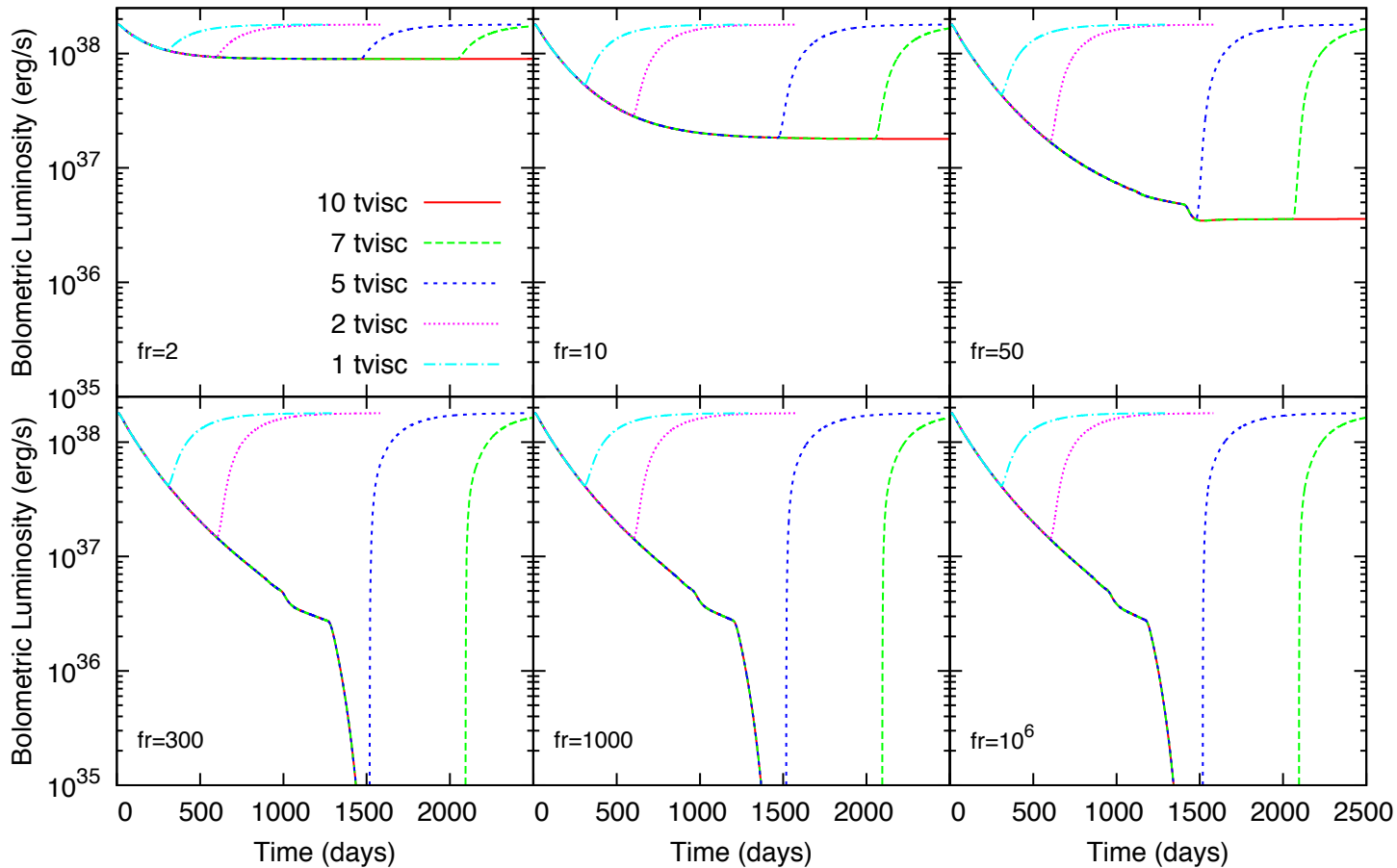


Figure 5.3: Light curve of LMC X-3 with irradiation on ( $C_x = 10^{-3}$ ) and an infall radius of ( $R_{\text{circ}} = 1.5 \times 10^{11}$ ) with  $f_r$  reduction factors of 2,10,50,300,1000 and  $10^6$  over the viscous times multiples, shown by the key.

wave propagates, viscous mixing decreases, leading to a build up of matter behind the wave front. If enough matter builds up i.e  $\Sigma \geq \Sigma_{crit}^+$ , a heating wave begins propagating out (Menou et al., 1999). The hot gas in the outer regions then soon moves inwards and the cooling front stops. The reason for this process occurring so rapidly could be due to a very narrow S-curve (i.e  $\Sigma_{crit}^+/\Sigma_{crit}^-$  is very small), though after this outburst phase the surface density is low enough for quiescence to occur. The total time required for quiescence is  $\sim 1100$  days for all radii, regardless of the lower viscous times for shorter  $R_{circ}$ . This is due to viscous mixing further out from  $R_{circ}$  maintaining the disc's stability. This means the accretion rate decline is based upon the global properties of the disc and not a reduced accretion rate at a single annulus. The cooling wave that takes the disc into quiescence is outside in and thus its travel time is approximately equal for all infall radii.

In the lower panel of figure 5.2, the extra heating from irradiation exacerbates this effect by reducing the viscous times whilst also delaying the drop into quiescence, leading to discs with shorter infall radii e.g  $R_{circ} = 6$  and  $9 \times 10^{10}$  cm failing to drop into quiescence within  $t_{low} \leq 10t_{visc}$ . The reduced viscous time of the disc leads to a faster rate of decrease in  $\dot{M}$  and also lowers  $\dot{M}_{crit}^+$  by maintaining the disc at a higher temperature, as discussed before. After  $\sim 1100$  days a slight kink in the accretion rate is observed. This is due to the inner disc  $\Sigma$  reaching the critical  $\Sigma_{crit}^+$ . At this phase matter in the outer disc is at a high enough surface density to stop any cooling wave from forming and so dictates the rate of accretion as the disc begins to contract. This produces an outburst like profile before dropping into quiescence after  $\sim 1700$  days.

For both upper and lower panels the quiescent luminosity is in the region of  $\sim 2.7 \times 10^{32}$  erg/s, with inside-out type outbursts steadily decreasing in magnitude and duration during this short time period. The time spent in quiescence before an outburst in the non-irradiated model is  $\sim 100 - 250$  days, while for high irradiation only  $R_{circ}; 1.5 \times 10^{11}$  cm entered quiescence and this lasted  $\sim 950$  days before the first outburst. The extra delay is likely due to a lower surface density in the irradiated case from prolonged accretion in the higher state before entering quiescence.

### 5.4.2 Required reduction factor

Figure 5.3, shows the light curves produced by varying the reduction factor of the secondary mass transfer rate  $\dot{M}_2$  by factors of 2, 10, 50, 300, 1000 and  $10^6$  for a highly irradiated disc. A mass infall radius of  $1.5 \times 10^{11}$  cm was chosen as LMC X-3 companion star is thought to possess a very weak stellar wind due to its type B5 V classification (Soria et al., 2001).

Small mass reduction factors of 2 and 10 are lower than that required for disc accretion to be in the thermal-viscous instability regime and cause the system to drop into a lower steady state. A reduction factor of 50 does however cause the accretion rate to fall below  $\dot{M}_{crit}^+$ , though the high surface density and irradiation levels mean the cooling wave is immediately shut off producing a kink in the light curve as seen before in figure 5.2. The system then remains on the cusp of entering quiescence and fails to fall within  $t_{low} \leq 10t_{visc}$ .

Reduction values of  $f_r \geq 300$  only subtly affect the time to enter quiescence, as the secondary accretion rate is low enough to not substantially affect the surface density of the disc. This means the time to enter is predominately dependant on the initial density of the disc, with a maximum reduction of  $\sim 400$  days to enter quiescence compared to  $f_r = 100$ .

### 5.4.3 Rise out of quiescence

Figure 5.5 shows the rise out of quiescence for the family of light curves from figure 5.2, with time zero set at the point where  $\dot{M}$  returns to its original value. The light curves from depleted discs (i.e viscous time multiples of 5, 7 and  $10 t_{visc}$ ), show a similar rise out curve for all radii and irradiation levels, regardless if from quiescence or outburst. This is due to there being a lower surface density in the disc, which subsequently affects the propagation of the ionization waves.

These waves form when  $\dot{M}_2$  is returned to the systems original accretion rate which leads to a surge in density at  $R_{circ}$ . This surge in density leads to a jump in viscosity and temperature causing outward and inward bound heating waves to propagate out from the infall annulus. The greater distance for the inner bound wave

to cover, means the total travel time of this wave determines the approximate delay time for the disc to rise out of quiescence, see equation (5.21). This means that small infall radii have shorter delay time and the inner and outer bound ionization waves simultaneously propagate for a longer period. This leads to a larger mass buildup at the heating front and a higher immediate accretion rate once the wave reaches the inner disc. So not only do we see a quicker rise time but also a higher luminosity rises compared to larger  $R_{\text{circ}}$  values. There is relatively little difference between high and low irradiation because the sound speed and viscosity are approximately equal in the heating wave when returning from quiescence.

The delay time for the disc to respond to an increase in the secondary accretion can be estimated from figure 5.5. This gives delay times of  $\simeq 16, 44$  and  $60$  days for  $R_{\text{circ}} = 6, 9$  and  $15 \times 10^{10}$  cm, respectively. All rises out of quiescence after this period see a four magnitude increase in the luminosity occurring in under a day before forming a gentle gradient back to the systems high accretion state. As most of the modelled returns from quiescence occur from a semi-outburst state, an analytical estimate of the ionisation wave propagation time is calculated as a comparison. If the inward propagating ionisation wave is treated as a temperature and mass movement from the point  $R_{\text{circ}}$ , then the following equation can be used;

$$t_r(R) \simeq \frac{R}{\alpha_h C_s} = t_{\text{visc}}(R) \frac{H}{R}, \quad (5.21)$$

where  $R$  is  $R_{\text{circ}}$  and  $\alpha_h C_s$  determines the velocity of the heating wave.  $t_{\text{visc}}$  is calculated as before in equation (5.6). An analytical approximation for the relative disc scale height with radius ( $H/R$ ) for a steady thin disc is given below, from Frank et al. (2002b);

$$H/R = 1.7 \times 10^{-2} \alpha^{-1/10} \dot{M}_{16}^{3/20} m_1^{-3/8} R_{10}^{1/8} f^{3/5}. \quad (5.22)$$

The heating front will be in the hot state giving an  $\alpha = 0.1$  while the accretion rate will still be in quiescence, which is assumed to be approximately  $\dot{M} = 2 \times 10^{12} \text{gs}^{-1}$  from the simulations. As before  $\dot{M}_{16} = \dot{M}/10^{-16} \text{gs}^{-1}$ , where  $m_1$  is the primary star's mass in  $M_{\odot}$ ,  $R_{10} = R_{\text{circ}}/10^{10}$  cm and  $f^4 = (1 - (R_*/R_{\text{circ}})^{1/2}) \simeq 1$  with

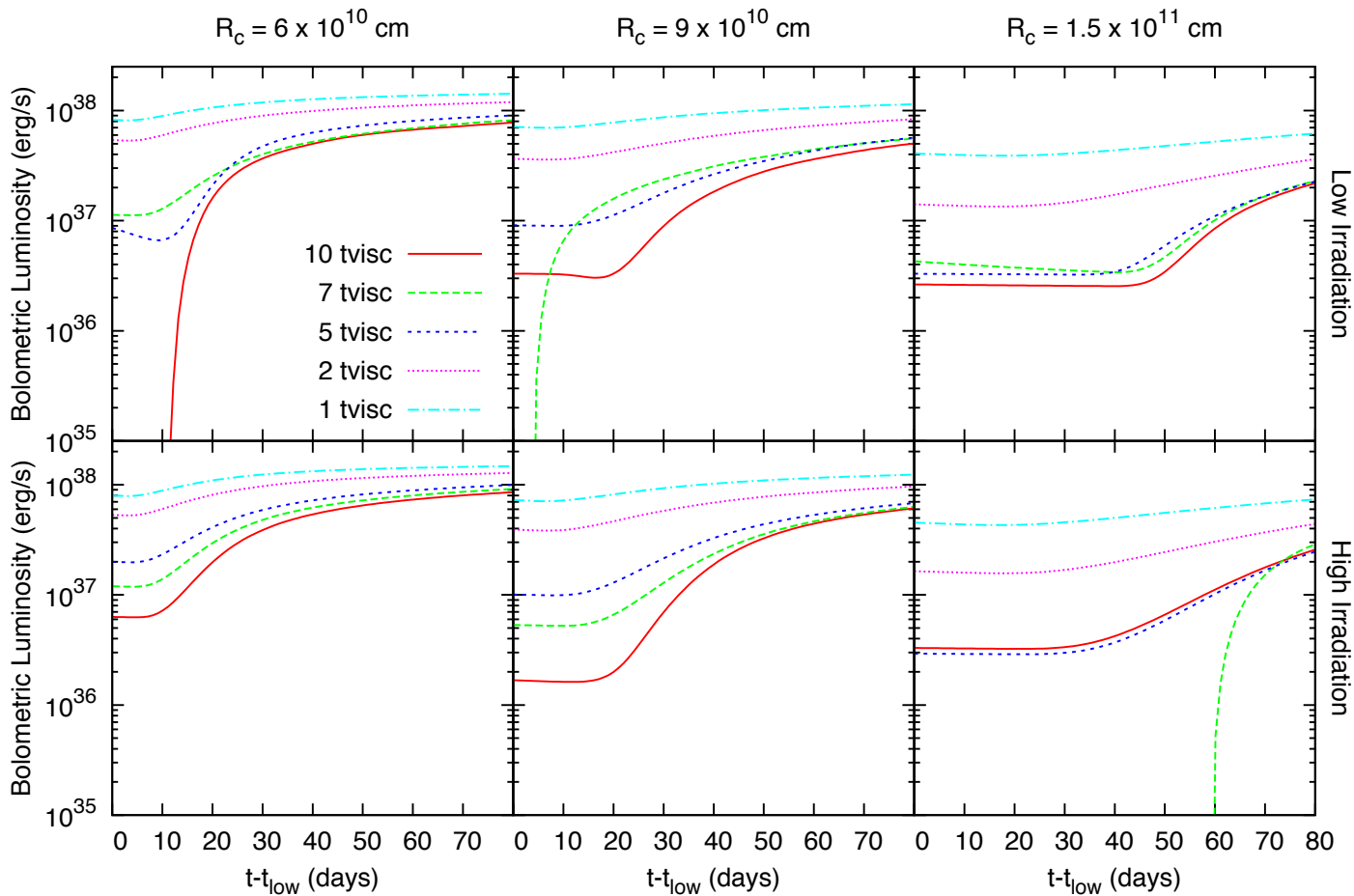


Figure 5.4: The rise out of quiescence for the family of lightcurves from figure 1. With time zero set at the point where  $\dot{M}$  returns to its original value. The lower and upper panels show the cases for irradiation on and off respectively.

$R_* = 3R_{sw}$  as the inner most stable circular orbit.

- $t_r \simeq 52.1$  days for  $R_{\text{circ}} = 1.5 \times 10^{11}$  cm
- $t_r \simeq 25.8$  days for  $R_{\text{circ}} = 9 \times 10^{10}$  cm
- $t_r \simeq 14.8$  days for  $R_{\text{circ}} = 6 \times 10^{10}$  cm

Equation (5.21) yields similar values for  $t_r$  as our model even though the total delay time also depend on how long it takes for an annulus to meet the relation ( $\Sigma > \Sigma_{\text{crit}}^+$ ) in order for a heating wave to form, though this does appear to be minimal in our model due to the large viscous times while in quiescence. The differences in the delay times may not just be determined by the infall radius but also by the sound speed which is predominately temperature and density dependant. This could possibly be why the inner infall radius  $R_{\text{circ}} = 6 \times 10^{10}$  cm is disproportionately quicker to rise. LMC X-3 spent 3 months in quiescence, similar to the delay time for  $R_{\text{circ}} = 1.5 \times 10^{11}$  cm, which would mean the secondary accretion rate would have to return to its maximum level immediately as the disc enters quiescence.

## 5.5 Summary and Conclusions

The 1D disc model described here has placed approximate time scales and magnitude reductions required in the secondary accretion rate for LMC X-3 to enter and rise out of quiescence. The simulations demonstrated that the decline time was dependant on the surface density of the disc while the rise out profile is dependent upon the infall radius. The time to enter quiescence was found to be over an order of magnitude greater than that observed, with high levels of irradiation shown to compound this problem. The rise out profiles favoured a small infall radii with a larger immediate luminosity increase. This extended time to enter suggests a truncated disc, which would also explain the favoured small infall radius.

### 5.5.1 Entering quiescence

The time to enter quiescence was calculated for three different infall radii, with high and low levels of irradiation from the central source, see figure 5.2. The accretion

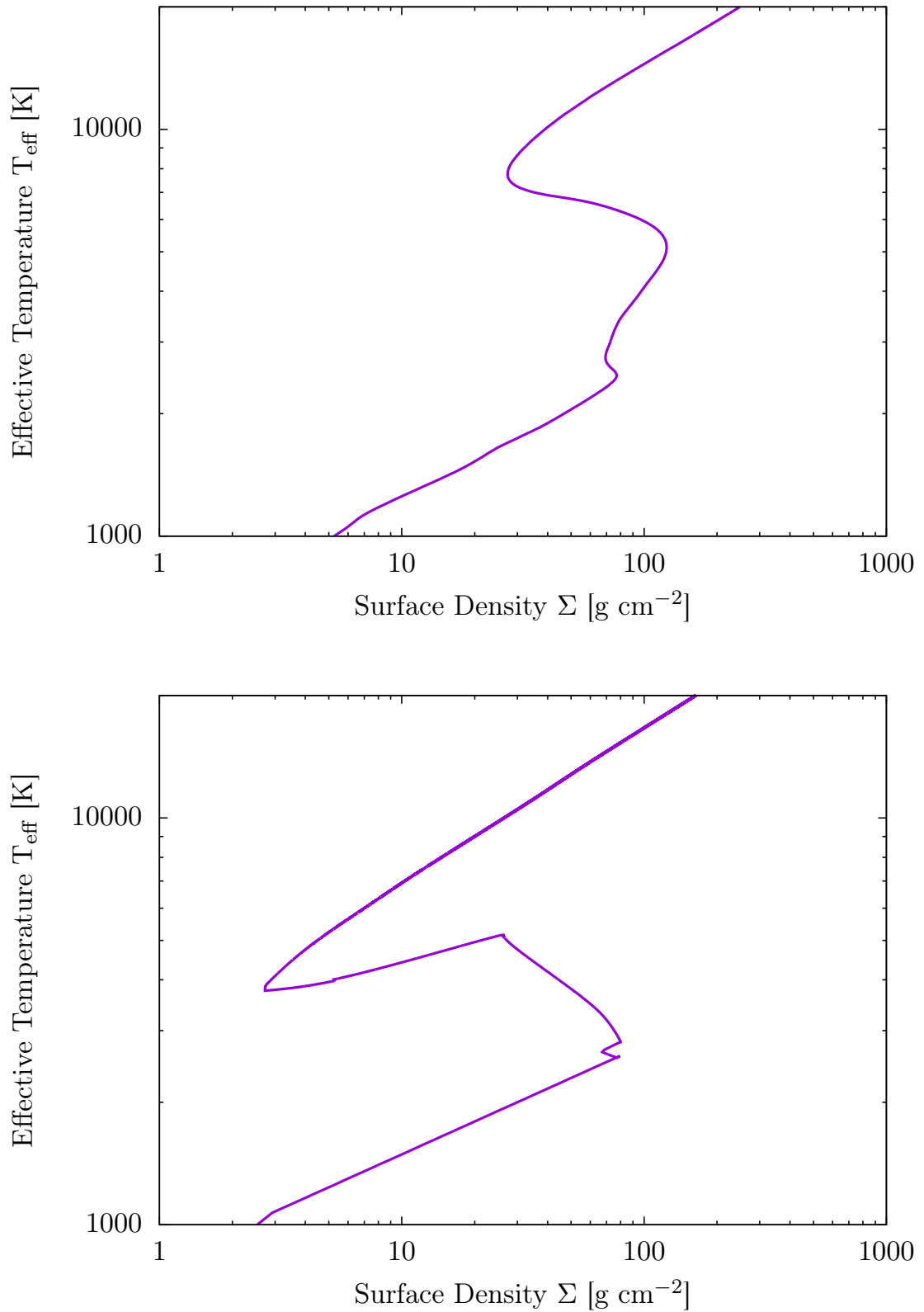


Figure 5.5: The rise out of quiescence for the family of lightcurves from figure 1. With time zero set at the point where  $\dot{M}$  returns to its original value. The lower and upper panels show the cases for irradiation on and off respectively.

rate decline was found to be dependant on the outer disc radius and not the infall radius, with heating from irradiation accelerating the fall in  $\dot{M}$ . This more rapid decline in accretion from irradiation is compensated by the disc remaining stable at low  $\dot{M}$  values, with the time to enter quiescence extend by  $\sim 450$  days.

The time to enter for both high and low irradiation levels are approximately an order of magnitude greater than that observed, suggesting an outer disc radius of  $\sim 6 \times 10^{10}$  cm. This truncated disc could simply be due to an over estimation of the surface density in the initial conditions, where we assumed the disc to be accreting at LMC X-3's typical mean luminosity, with observations showing a slightly lower than average value just prior to quiescence.

Analytical estimates of the stable hot state accretion ratio for the other known persistent HMXB's, LMC X-1 and Cyg X-1, previously calculated by Coriat et al. (2012a), suggested that they should be prone to outburst contrary to observations, see table 5.1. In order to explain this Coriat proposed an over estimation of the disc radius from the analytical values, though it is possible that another mechanism not considered in either the analytical approximation or our simple modeling of LMC X-3 could be causing this reduction.

### 5.5.2 Rising out of Quiescence

Observations of the rise out of quiescence showed a several magnitude increase in luminosity occurring in under 8 days, though due to upper boundaries while in quiescence this could be a conservative estimate for the total time to rise. All simulations were able to reproduce this, with only slight variations in the delay time and magnitude of the luminosity jump. The delay time was found to increase with infall radius, which places an upper bound estimate of  $R_{\text{infall}} \leq 2.0 \times 10^{11}$  cm, due to the time spent in quiescence. This favours a small infall radius which is also support by a larger luminosity jump, seen at shorter infall radii.

The way in which the accretion rate was step increased may alter these results, as a more gradual change in  $\dot{M}$ , would not only delay the time before a heating wave forms but also change the waves origin to the outer regions, as matter is accreted across the disc. This is thought unlikely though as the large vicious times

in quiescence should minimalist any redistribution of matter.

### 5.5.3 Required reduction factor

In order to place constraints on the required reduction factor in the secondary accretion rate for LMC X-3's drop into quiescence, runs for an irradiated disc with an infall radii  $R_{\text{circ}} = 1.5 \times 10^{11}$  cm and reduction ( $f_r = 2, 10, 50, 300, 1000, 10^6$ ), produce the following requirements;

- $f_r \lesssim 10$  A lower steady state is reached.
- $f_r \sim 50$  Prolonged outburst state
- $f_r \gtrsim 100$  Quiescence
- $f_r \gtrsim 300$  Little difference in infall time

A drop in LMC X-3's infall matter by a factor of a hundred is need for quiescence, though as discussed before a reduction of 50 and possibly less, also leads to the system falling into the thermal-viscous instability regime but due to high surface densities a cooling wave fails to propagate and the system remain in a long duration outburst. This phase could be shortened if the density of the disc just prior to quiescence is less than that assumed in the initial conditions of our model. This would allow for a lower reduction factor and also a quicker drop into quiescence, as discussed before.

### 5.5.4 Model Assumptions

Due to the one dimensional nature of this model a number of simplifying assumptions were made. These should only have very limiting effects on the the disc structure and subsequent light-curve. Most notable would be primarily from disc scale height and opacity calculations of the vertical structure, which heavily depend on the functions  $\kappa(T_c, \rho_c)$  and  $\mu(T_c, \rho_c)$ . The thin disc approximation can break down here, where there is large variation in  $T_c$  and  $\rho_c$ , such as drops into quiescence and outbursts.

Though both functions chosen show flexibility in this and a temperature dependant  $\alpha$  aids in reproducing the appropriate S-curves to minimise this.

Non-axisymmetric effects such as hotspot heating and tidal torques are azimuthally averaged. With the hotspot and tidal heating far less than that from viscous or irradiative effects and thus unlikely to alter the disc evolution considerably. The secondary accretion rate was also step decreased and increased. This may not be unphysical as the exact nature of the reduced accretion rate is unknown and the step increase as already discussed, should have no effect due to the high viscous times in quiescence.

## 5.6 Further work

Our current simulations point towards LMC X-3 having a shortened disc with low levels of irradiation from the central source. This is likely the result of the *one-zone* assumption for the vertical disc structure breaking down, with cooling underestimated. If we solve for the vertical structure of the disc, see Appendix C, then the S-curve significantly narrows, see figure 5.5. This reduces both the time to drop into quiescence and also the time for the disc to return to the hot state. This should better resolve the observed light-curve, however previous studies of the variability in LMC X-3 have required novel accretion mechanisms, such as the evaporation-condensation mechanism described by Mayer & Pringle (2007b), with matter transportation from the outer to the inner disc via the corona.

# 6

## Conclusions

This thesis has focused on the disc variability of two XRBs: GX 339–4 and LMC X–3. The regular outbursts in GX 339–4 lends it self to studying the transition point between the hard and soft state, allowing us to review the requirements of disc truncation. The steady state nature of LMC X–3 and its very short lived drop into quiescence in 2012, poses a stern test of the disc instability model. Here I summarise the main conclusions from each chapter.

## 6.1 A novel approach to disc truncation

In Chapter 2, I summarised the disc truncation debate which has centred around the LMXB: GX 339–4 and I presented a fresh approach to tackling the problem. In the low-hard state, the inner disc is thought to be truncated: where the geometrically thin, optically thick disc is replaced by a geometrically thick, optically thin ADAF. The point of transition between these two states however is a contentious issue, with several studies of GX 339–4 reporting conflicting measurements for the inner disc radius. This issue is further complicated by the spectral modelling inconsistencies of these studies, where measurements of the inner disc radius from the thermal disc emission, contradict those of the reflection component. In addition to this, as there is a large amount of uncertainty in the fundamental parameters of GX 339–4, the binary inclination and interstellar absorption, are typically left as free parameters, which has resulted in a wide range of values.

In order to better resolve these issues around disc truncation, I proposed to spectrally model close to a decade of *XMM-Newton* observations of GX 339–4, while assuming the inner disc radius remains fixed at the ISCO ( $R_{\text{in}} = 6R_g$ ) in both the soft and hard states; under the assumption, that should truncation occur the model would fail to fit or require unphysical parameters. In order to reduce possible degeneracy in the model, I proposed that the system’s fundamental parameters should be fixed and all duplicated variables across the models should tied. The high variability of XRBs in the hard state allows for count rate slicing of the *XMM-Newton* data, which would increase the flux coverage of the fitted spectra.

In order to better constrain the mass of the black hole and the binary inclina-

tion of the system, I apply a  $K_2$  correction to the orbital velocity measurement to correct for the fact the Bowen fluorescence emission would originate from the inner irradiated face of the donor star. This correction also took account that irradiation occurs across the Roche lobe photosphere. With the knowledge that eclipses are not observed and a higher secondary mass is favoured  $M_{\text{BH}} = 18.0 \pm 1.3 M_{\odot}$  for  $i = 60^\circ$ . I presented Dr. Simon Vaughan's analysis of the RGS spectra and constrains upon the absorption in the ISM. The weighted mean of the seven hydrogen column density estimates gave  $N_H = 5.83 \times 10^{21} \text{cm}^{-2}$ , with a relative abundance of O, Ne, and Fe of 1.44, 1.21, and 1.22 respectively. In order to extend the flux range of the hard state *XMM-Newton* Timing mode observations, I employ a novel technique of count rate slicing the observations in to multiple spectra, with equal signal to noise. I then presented the most physically consistent grouping of models currently possible: TBNEW(SIMPL(KERRBB) + RELXILL).

## 6.2 A fixed inner disc radius

In Chapter 3, I presented the results from the spectral fitting of 11 *XMM-Newton* observations using a single model grouping across both the hard and soft states. I used the most physically consistent grouping of models possible. The results suggested no presence of a truncated disc, however a neutral reflection component was needed for several of the hard state observations in addition to the broad reflection model. This may be the result of irradiation upon the outer disc, however it would also be consistent with a truncated disc. In addition to the neutral reflection feature, a soft excess around  $\sim 1 \text{keV}$  was identified across both the hard and soft state observations. This excess appeared to increase with the total flux of the observation and was also present in the RGS data. The goodness of the fits compare favourably with previous studies and the parameters vary inline with typical expectations for the hard and soft states.

The modelling struggled with the low-luminosity intermediate state observations of the 2002/03 outburst: rev-0594 & rev-0600. These observations capture GX 339-4 in a late outburst decay phase, as the coronal emission begins to harden. The

Plant et al. (2014b) spectral study of GX 339–4 during its failed outburst in 2013, identified a mildly truncated disc ( $R_{\text{in}} \sim 20R_g$ ) with good agreement between the measurement of  $R_{\text{in}}$  from the disc and reflection components. This mild truncation however was obtained from the use of canonical values for  $f_{\text{col}}$  and  $q$ , a small variation in these values could return the disc to the ISCO. The truncation of the disc also reduces the accretion efficiency, where even with mild truncation the accretion rate would have to be greater than the level required at the peak of the outburst (assuming the disc was at ISCO during the peak). The Plant et al. (2014b) analysis was of observations in the hardening late phase of an outburst, it may be the case that the disc truncates at different luminosity depending on whether the disc is rising or decaying during the outburst.

### 6.3 A variable colour correction factor

In Chapter 4, I analysed the spectral model fitting of four archival *XMM-Newton* observations of GX 339–4, while in the hard state. With the use of a novel count rate slicing technique, I am able to expand the number of fitted spectra to 27, maximising the flux coverage of the *XMM-Newton* observations. On the assumption of a steady inner disc radius, I find that if the colour correction factor and emissivity are allowed to deviate from their canonical values then there is no evidence for a truncated disc, with  $f_{\text{col}} \sim 1.4$  and  $q \sim 2$ . The soft residual at  $\sim 1\text{keV}$  that was identified in chapter 3, appears to increase with flux across the spectrally sliced observations, while the emission from the neutral Fe-K line appears to remain constant. When comparing the colour correction results of chapter 4, with chapter 3, a clear dichotomy appears where  $f_{\text{col}} \sim 1.4 - 1.5$  at low accretion rates, but increases to  $f_{\text{col}} \sim 2.4 - 2.8$  at  $\dot{m} > 0.01$ . Such a variation in the colour correction factor was tentatively suggested by Gierliński & Done (2004) to be that expected for a beta accretion disc: where the viscosity is dependant upon the gas pressure, as apposed to the total pressure of an alpha disc. Beta accretion discs were proposed as a possible solution to the radiative instability of alpha discs, which are thought to exhibit thermal runaway in the radiation pressure dominated regime.

## 6.4 A steady state drop into quiescence

In Chapter 5, I investigated the HMXB: LMC X-3 and its short fall into quiescence. LMC X-3 has generally been observed to be a steady high-soft state, however in 2012 the system entered a 3 month period of quiescence, deeper than that previously observed in its 40 year observational history. For the first time, *Swift* observations were able to capture LMC X-3's rise out of quiescence, allowing us to better explore the parameter space of the system. I investigated this fall into quiescent using a 1D disc instability model where I assumed a short period variation in  $\dot{M}_2$  was responsible, such as that seen in AM Herculis stars.

The time to enter quiescence was found to be independent of the infall radius, as the cooling wave originates in the outer disc; the rise out of quiescence however is dependant upon the infall radius, as the surface density locally peaks at this point. Irradiation of the disc significantly extends the time to enter quiescence, but has little effect upon the time in quiescence as the increase in the surface density at the infall radius is so rapid. The time to enter quiescence was over an order of magnitude greater than that observed, suggesting that the outer disc is either truncated or that the *one-zone* model of the vertical disc structure was under estimates cooling in the disc. If we solve for the vertical structure of the disc, then the S-curve significantly narrows, reducing both the time to drop into quiescence and also the time for the disc to return to the hot state. This should better resolve the observed light-curve, however previous studies of the variability in LMC X-3 have required novel accretion mechanisms, such as the evaporation-condensation mechanism.

## 6.5 Future work

The work presented here on the requirements for disc truncation in GX 339-4 has focused on relatively high flux observations where the *XMM-Newton* EPIC pn-camera is in the fast mode. The extension of this work to lower luminosities using the full imaging mode may more clearly highlight if a model with a fixed inner disc radius is a suitable approximation. The expansion of this work to other sources would also test the robustness of the results presented in chapters 3 & 4, beyond

GX 339–4 and if the colour correction variation seen between the hard state and soft state remain. The application of the count rate slicing technique to multiple sources could also provide invaluable knowledge on the spectral residuals identified in this study. In all the studies which have modelled the spectra at higher energies ( $> 10\text{Kev}$ ) they have required super solar abundances of iron to fit the Fe-K line and Compton hump. This may be due to the limitation of current reflection models or it may have a physical basis, which could significantly effect the fitting of the Fe-K line: the spectral modelling of *NuSTAR* data would allow us to explore higher energy ranges.

The modelling of LMC X–3 highlighted that the time to enter quiescence is solely dependent upon the size of the disc. The under estimation of cooling when assuming a *one-zone* model likely extends the time to enter quiescence by over a magnitude. The solving of the vertical disc equations should resolve the under-estimation of cooling and a 1+1D model, where the vertical and radial structure are solved separately would allow us to place constraints upon the variation in the secondary accretion rate  $\dot{M}_2$  required for LMC X–3 to enter quiescence for  $\sim 3$  months.

# A

## The *XMM-Newton* pn-camera spectral fits

This appendix contains the spectral modelling fits of the XRB GX 339–4, as outlined in Chapter 3. All the fitted EPIC pn-camera spectra were taken in the BURST and TIMING modes, which are respectively separated in to §A.1 and §A.2.

## A.1 BURST mode results table and spectra

Model	Parameters	<i>XMM-Newton</i> Revolution				
		0496	1318	1325	0514	1338
SIMPL	$\Gamma$	$3.40^{+0.00}_{-0.05}$	$3.13^{+0.27}_{-0.73}$	$2.21^{+0.02}_{-0.04}$	$2.20^{+0.01}_{-0.00}$	$2.95^{+0.45}_{-0.04}$
	$f_{\text{scat}}$	$0.02^{+0.00}_{-0.00}$	$0.04^{+0.04}_{-0.01}$	$0.09^{+0.01}_{-0.01}$	$0.01^{+0.00}_{-0.00}$	$0.02^{+0.00}_{-0.01}$
KERBB	$\dot{M}/10^{18}$ [gs <sup>-1</sup> ]	$5.39^{+0.01}_{-0.01}$	$5.38^{+0.01}_{-0.02}$	$3.45^{+0.04}_{-0.06}$	$3.50^{+0.03}_{-0.01}$	$2.40^{+0.03}_{-0.01}$
	$f_{\text{col}}$	$2.57^{+0.01}_{-0.00}$	$2.58^{+0.03}_{-0.02}$	$2.78^{+0.03}_{-0.03}$	$2.71^{+0.00}_{-0.00}$	$2.45^{+0.01}_{-0.07}$
RELXILL	$q$	$2.87^{+0.43}_{-0.29}$	$2.53^{+0.56}_{-0.40}$	$2.20^{+0.13}_{-0.14}$	$1.50^{+0.10}_{-0.00}$	$2.78^{+0.89}_{-0.44}$
	$\xi$ [log <sub>10</sub> ]	$2.82^{+0.22}_{-0.32}$	$2.71^{+0.07}_{-0.29}$	$3.13^{+0.09}_{-0.08}$	$3.62^{+0.05}_{-0.05}$	$2.48^{+0.60}_{-0.15}$
	$N_K$ [log <sub>10</sub> ]	$-1.42^{+0.10}_{-0.01}$	$-1.54^{+0.42}_{-0.16}$	$-1.60^{+0.01}_{-0.00}$	$-1.82^{+0.03}_{-0.00}$	$-1.68^{+0.61}_{-0.03}$
GAUSS	$E_{gs}$ [keV]	$1.16^{+0.01}_{-0.00}$	$1.16^{+0.02}_{-0.01}$	$1.18^{+0.01}_{-0.01}$	$1.18^{+0.01}_{-0.01}$	$1.15^{+0.01}_{-0.01}$
	$\sigma_{gs}$ [keV]	$0.08^{+0.01}_{-0.01}$	$0.09^{+0.01}_{-0.01}$	$0.12^{+0.01}_{-0.01}$	$0.10^{+0.01}_{-0.01}$	$0.11^{+0.01}_{-0.01}$
	$N_{gs}$ [log <sub>10</sub> ]	$-1.14^{+0.02}_{-0.05}$	$-1.14^{+0.11}_{-0.09}$	$-1.09^{+0.04}_{-0.04}$	$-1.36^{+0.04}_{-0.02}$	$-1.14^{+0.04}_{-0.05}$
XILLVER	$N_{Fe}$ [log <sub>10</sub> ]	-	-	-	-	$-1.50^{+0.10}_{-0.13}$
GAIN	slope	1.01	1.01	0.98	1.00	1.02
	offset [keV]	0.00	0.00	0.03	0.02	0.00
	$\chi^2$	355	186	182	325	95
	dof	140	136	140	141	118

Table A.1: The EPIC pn-camera BURST mode parameter table for GX 339–4, with errors calculated at the 90% confidence level.

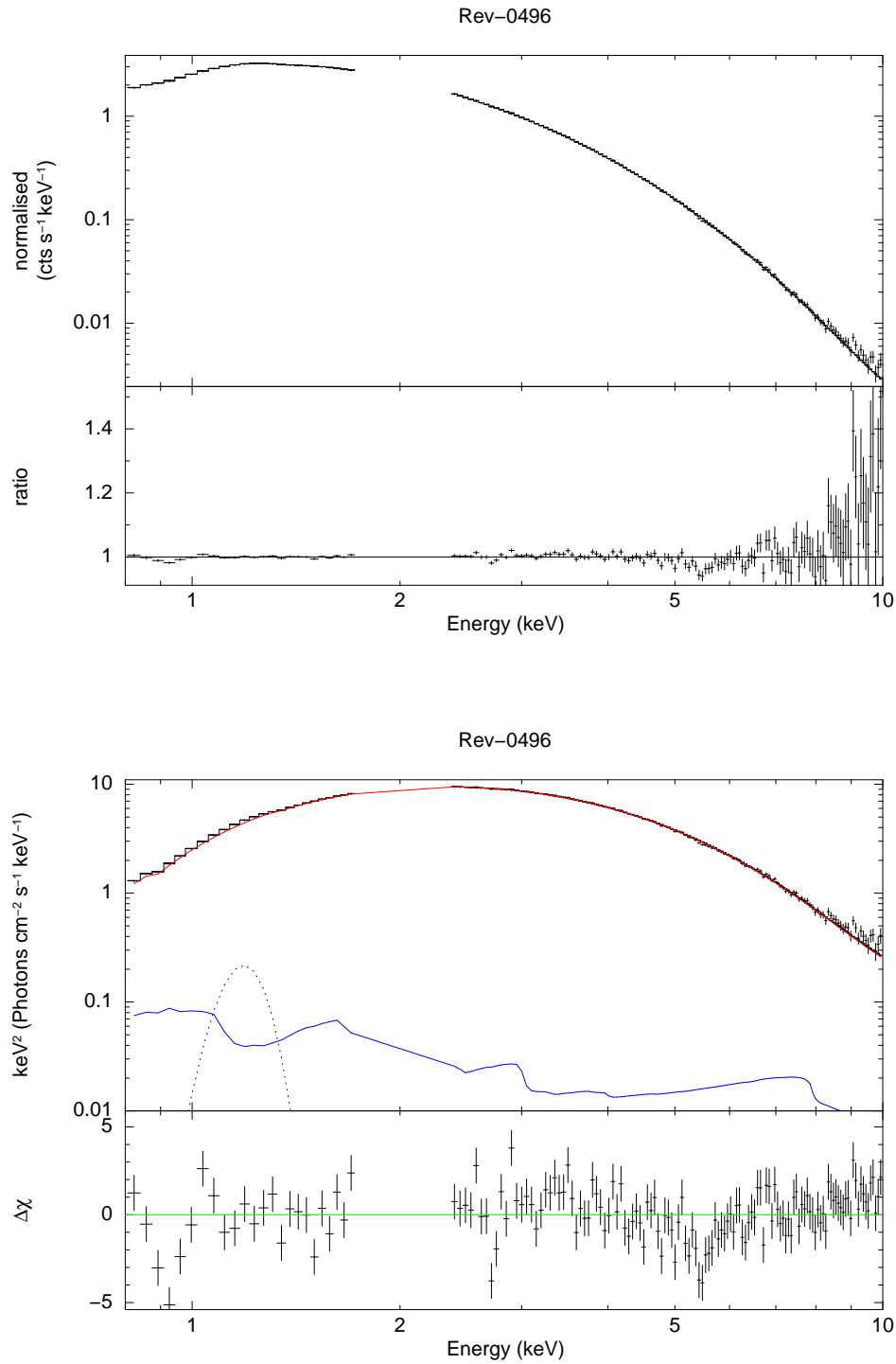


Figure A.1: The top and bottom panels show the modelling results for the BURST mode observation rev-0496. The top panel shows the folded model and spectra, along with the fit ratio. The bottom panel shows the unfolded model and spectrum, along with the respective  $\Delta\chi$  values. The solid black line represents the total model emission, with the additive model contributions given as follows: disc and powerlaw (red), reflection (dark blue) and the soft gaussian (dotted black).

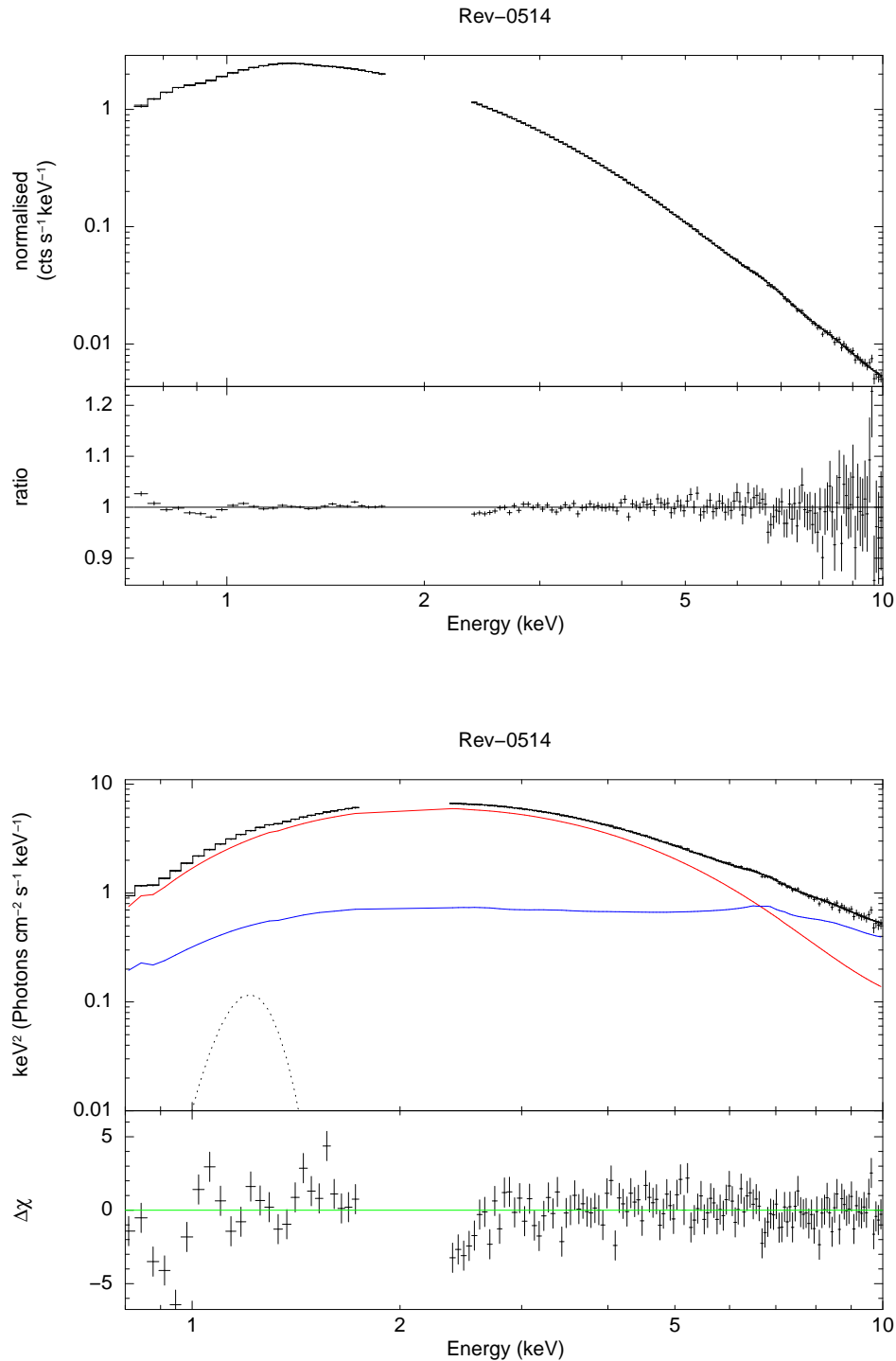


Figure A.2: The top and bottom panels show the modelling results for the BURST mode observation rev-0514. The top panel shows the folded model and spectra, along with the fit ratio. The bottom panel shows the unfolded model and spectrum, along with the respective  $\Delta\chi$  values. The solid black line represents the total model emission, with the additive model contributions given as follows: disc and powerlaw (red), reflection (dark blue) and the soft gaussian (dotted black).

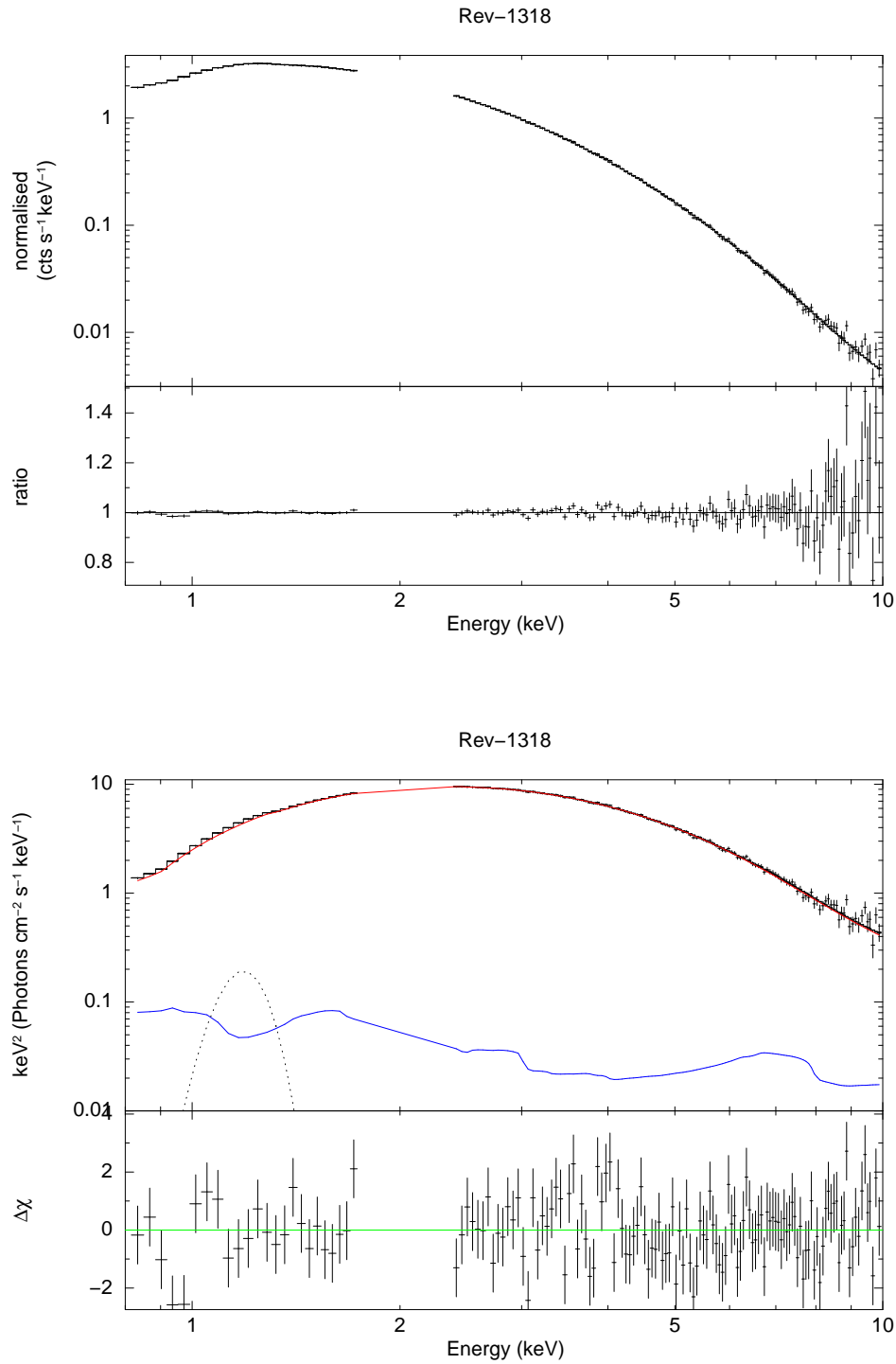


Figure A.3: The top and bottom panels show the modelling results for the BURST mode observation rev-1318. The top panel shows the folded model and spectra, along with the fit ratio. The bottom panel shows the unfolded model and spectrum, along with the respective  $\Delta\chi$  values. The solid black line represents the total model emission, with the additive model contributions given as follows: disc and powerlaw (red), reflection (dark blue) and the soft gaussian (dotted black).

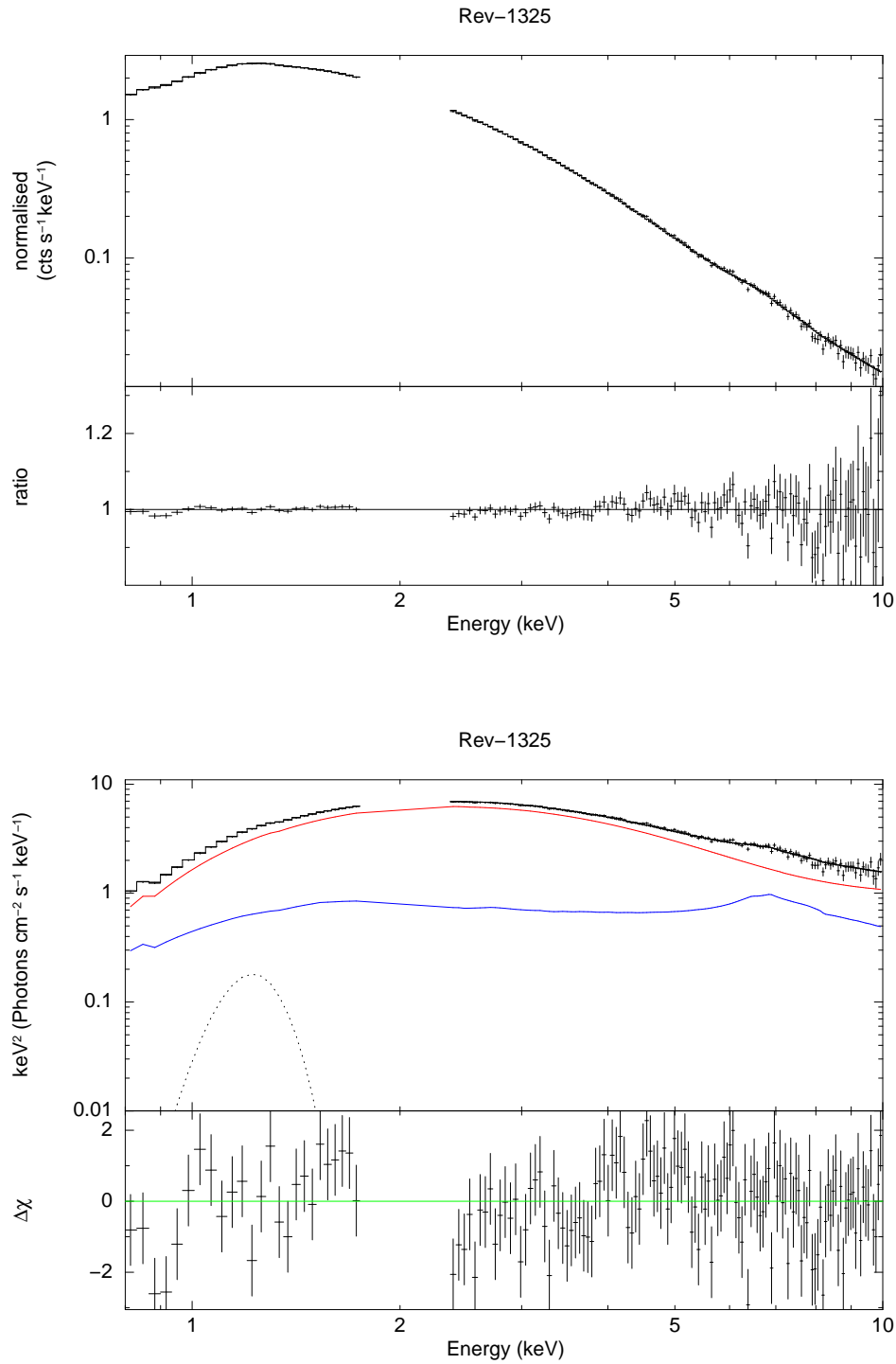


Figure A.4: The top and bottom panels show the modelling results for the BURST mode observation rev-1325. The top panel shows the folded model and spectra, along with the fit ratio. The bottom panel shows the unfolded model and spectrum, along with the respective  $\Delta\chi$  values. The solid black line represents the total model emission, with the additive model contributions given as follows: disc and powerlaw (red), reflection (dark blue) and the soft gaussian (dotted black).

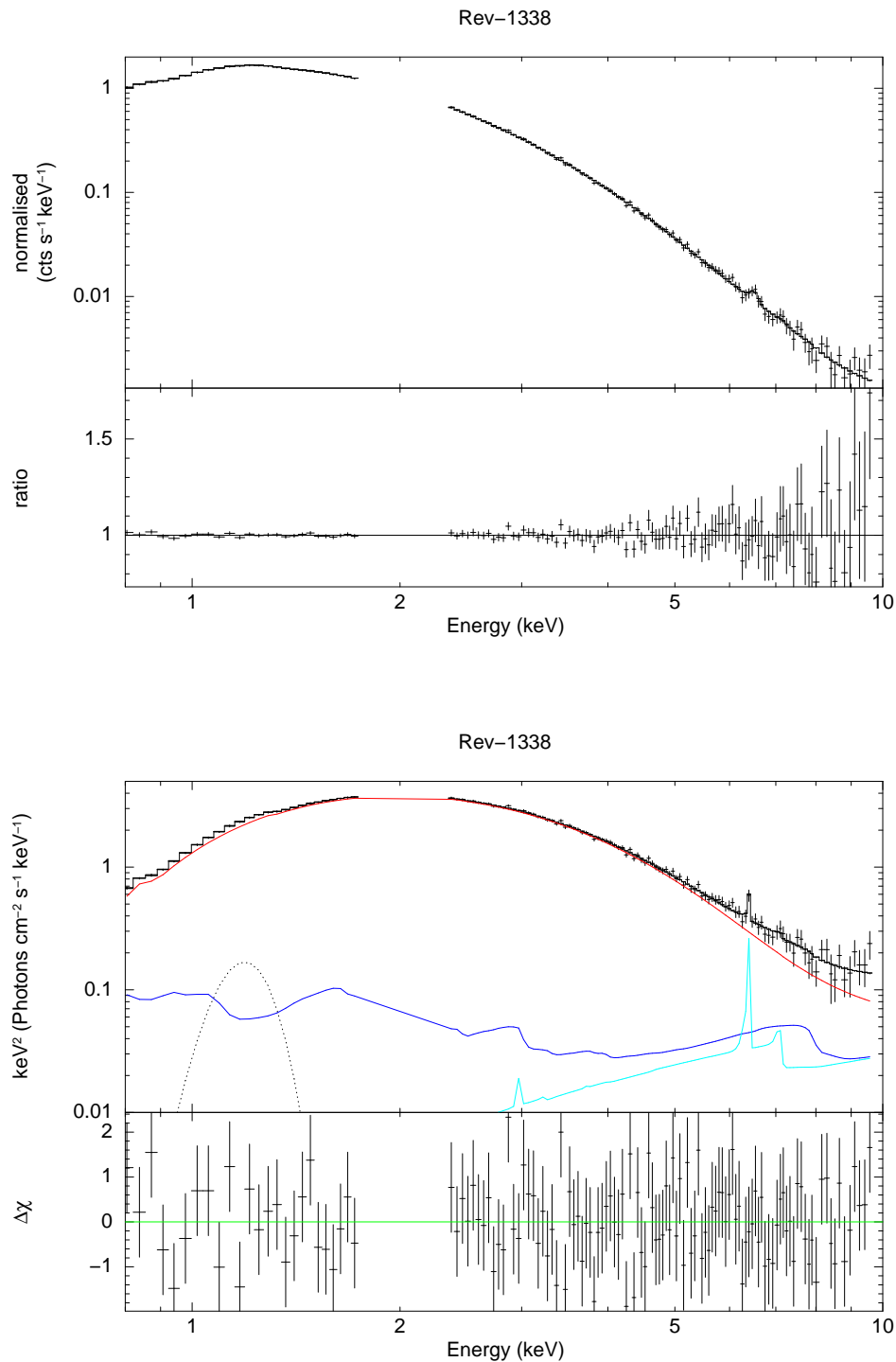


Figure A.5: The top and bottom panels show the modelling results for the BURST mode observation rev-1338. The top panel shows the folded model and spectra, along with the fit ratio. The bottom panel shows the unfolded model and spectrum, along with the respective  $\Delta\chi$  values. The solid black line represents the total model emission, with the additive model contributions given as follows: disc and powerlaw (red), reflection (dark blue), neutral reflection (light blue) and the soft gaussian (dotted black).

## A.2 TIMING mode results table and spectra

		<i>XMM-Newton</i> Revolution					
Model	Parameters	0600	0594	1886	0783	0782	1702
SIMPL	$\Gamma$	$2.95^{+0.06}_{-0.09}$	$2.90^{+0.01}_{-0.02}$	$1.65^{+0.02}_{-0.01}$	$1.61^{+0.01}_{-0.01}$	$1.60^{+0.01}_{-0.04}$	$1.51^{+0.03}_{-0.02}$
	$f_{\text{scat}}$	$0.08^{+0.01}_{-0.01}$	$0.18^{+0.00}_{-0.01}$	$0.45^{+0.09}_{-0.10}$	$0.30^{+0.01}_{-0.01}$	$0.32^{+0.01}_{-0.01}$	$0.43^{+0.02}_{-0.02}$
KERBB	$\dot{M}/10^{18}$ [gs $^{-1}$ ]	$0.74^{+0.02}_{-0.01}$	$0.55^{+0.00}_{-0.01}$	$0.17^{+0.03}_{-0.03}$	$0.10^{+0.00}_{-0.00}$	$0.08^{+0.00}_{-0.01}$	$0.04^{+0.00}_{-0.00}$
	$f_{\text{col}}$	$2.56^{+0.10}_{-0.05}$	$2.48^{+0.03}_{-0.00}$	$1.81^{+0.25}_{-0.23}$	$1.41^{+0.07}_{-0.10}$	$1.51^{+0.12}_{-0.09}$	$2.07^{+0.08}_{-0.17}$
RELXILL	$q$	$2.03^{+0.17}_{-0.11}$	$2.21^{+0.05}_{-0.06}$	$1.59^{+0.25}_{-0.09}$	$2.16^{+0.17}_{-0.10}$	$2.24^{+0.17}_{-0.41}$	$1.88^{+0.50}_{-0.38}$
	$\xi$ [log $_{10}$ ]	$2.70^{+0.05}_{-0.32}$	$2.70^{+0.02}_{-0.06}$	$3.17^{+0.05}_{-0.05}$	$2.29^{+0.08}_{-0.18}$	$2.30^{+0.43}_{-0.20}$	$2.46^{+0.31}_{-0.28}$
	$N_K$ [log $_{10}$ ]	$-1.74^{+0.11}_{-0.08}$	$-1.74^{+0.00}_{-0.00}$	$-1.73^{+0.06}_{-0.06}$	$-2.59^{+0.05}_{-0.10}$	$-2.58^{+0.05}_{-0.23}$	$-3.11^{+0.26}_{-0.17}$
GAUSS	$E_{gs}$ [keV]	$1.17^{+0.01}_{-0.01}$	$1.17^{+0.00}_{-0.01}$	$0.89^{+0.04}_{-0.01}$	$1.01^{+0.03}_{-0.05}$	$1.06^{+0.02}_{-0.10}$	-
	$\sigma_{gs}$ [keV]	$0.10^{+0.01}_{-0.01}$	$0.11^{+0.00}_{-0.00}$	$0.20^{+0.00}_{-0.02}$	$0.16^{+0.04}_{-0.03}$	$0.12^{+0.04}_{-0.05}$	-
	$N_{gs}$ [log $_{10}$ ]	$-1.55^{+0.10}_{-0.10}$	$-1.52^{+0.02}_{-0.01}$	$-0.85^{+0.04}_{-0.15}$	$-2.34^{+0.27}_{-0.21}$	$-2.63^{+0.21}_{-0.33}$	-
XILLVER	$N_{Fe}$ [log $_{10}$ ]	-	-	$-3.15^{+0.38}_{-\text{inf}}$	$-3.45^{+0.21}_{-0.45}$	$-3.24^{+0.13}_{-0.19}$	$-3.24^{+0.13}_{-0.21}$
GAIN	slope	0.99	0.98	0.99	1.01	1.00	1.01
	offset [keV]	0.02	0.03	0.03	0.01	0.01	0.00
$\chi^2$		142	277	188	153	155	142
dof		129	139	140	140	140	143

Table A.2: The EPIC pn-camera TIMING mode parameter table for GX 339–4, with errors calculated at the 90% confidence level.

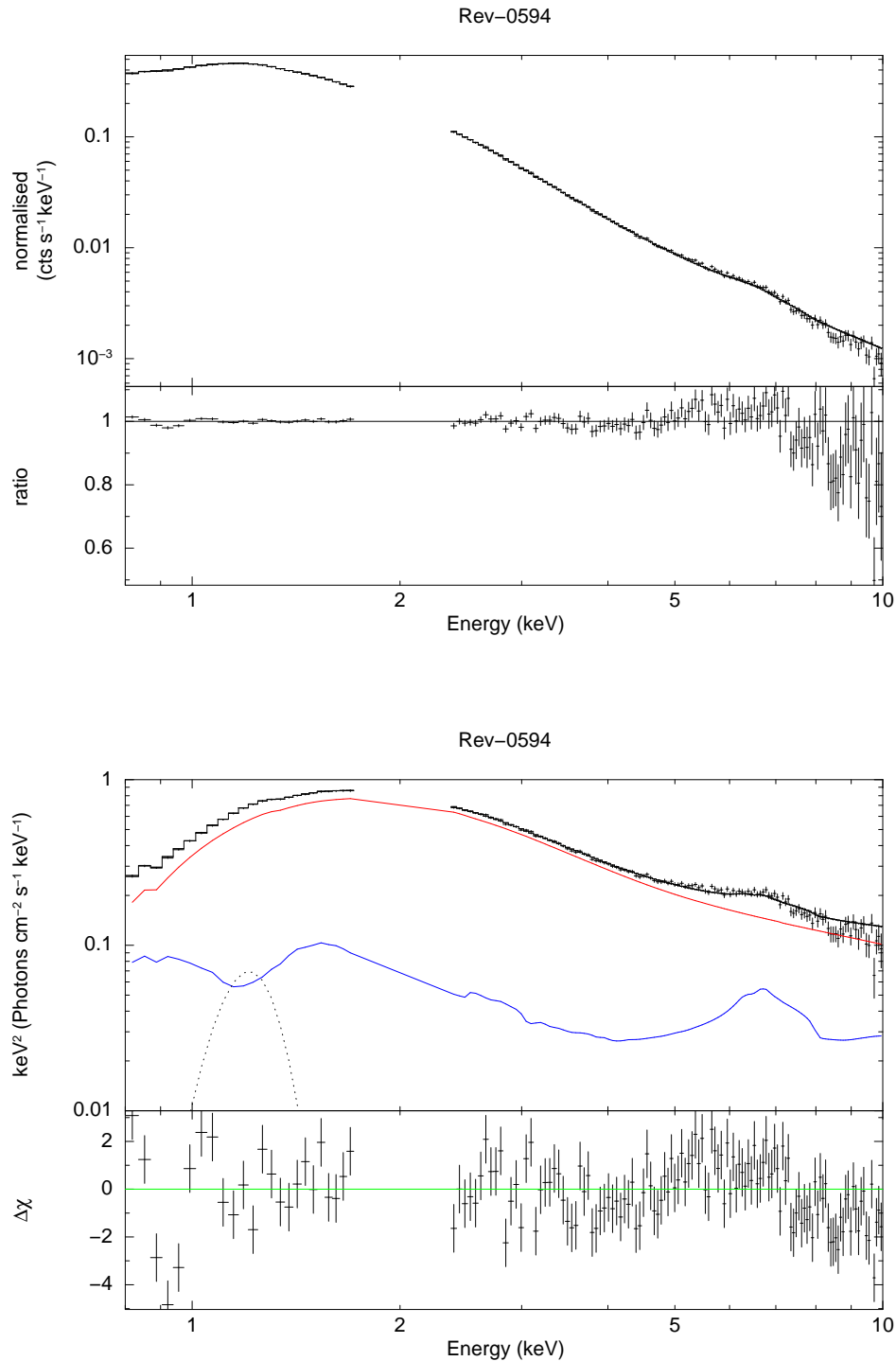


Figure A.6: The top and bottom panels show the modelling results for the TIMING mode observation rev-0594. The top panel shows the folded model and spectra, along with the fit ratio. The bottom panel shows the unfolded model and spectrum, along with the respective  $\Delta\chi$  values. The solid black line represents the total model emission, with the additive model contributions given as follows: disc and powerlaw (red), reflection (dark blue) and the soft gaussian (dotted black).

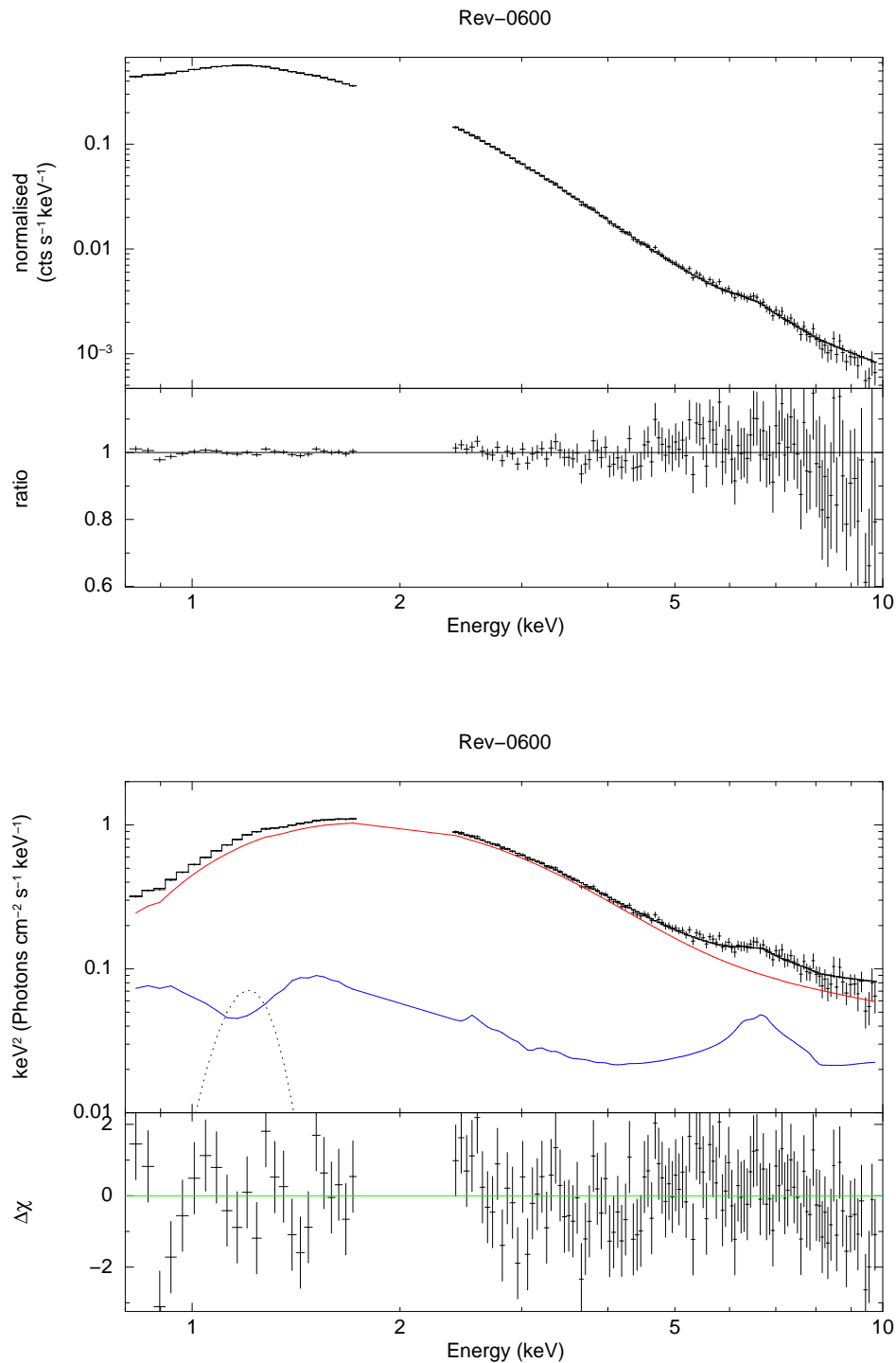


Figure A.7: The top and bottom panels show the modelling results for the TIMING mode observation rev-0600. The top panel shows the folded model and spectra, along with the fit ratio. The bottom panel shows the unfolded model and spectrum, along with the respective  $\Delta\chi$  values. The solid black line represents the total model emission, with the additive model contributions given as follows: disc and powerlaw (red), reflection (dark blue) and the soft gaussian (dotted black)..

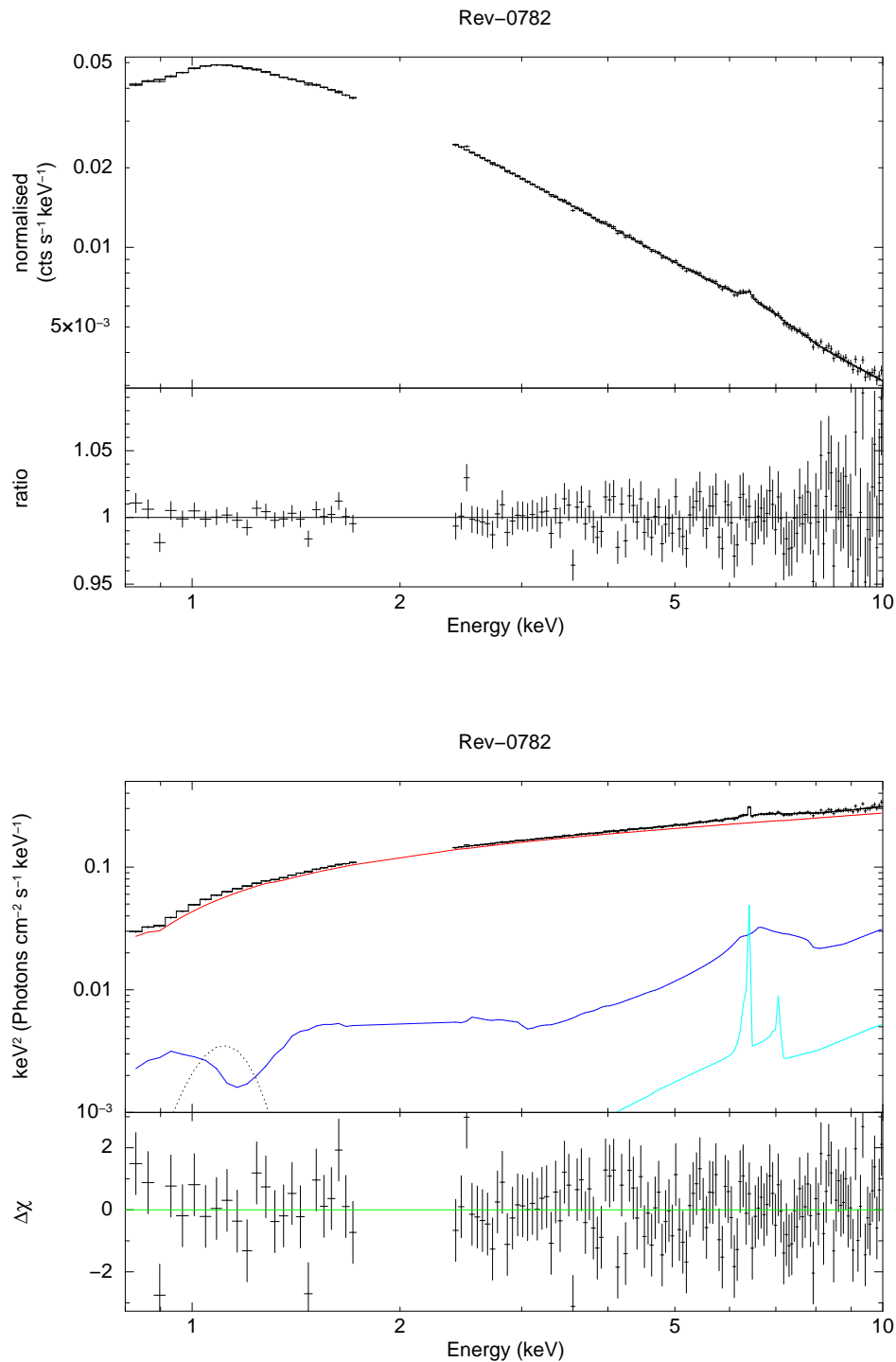


Figure A.8: The top and bottom panels show the modelling results for the TIMING mode observation rev-0782. The top panel shows the folded model and spectra, along with the fit ratio. The bottom panel shows the unfolded model and spectrum, along with the respective  $\Delta\chi$  values. The solid black line represents the total model emission, with the additive model contributions given as follows: disc and powerlaw (red), reflection (dark blue), neutral reflection (light blue) and the soft gaussian (dotted black).

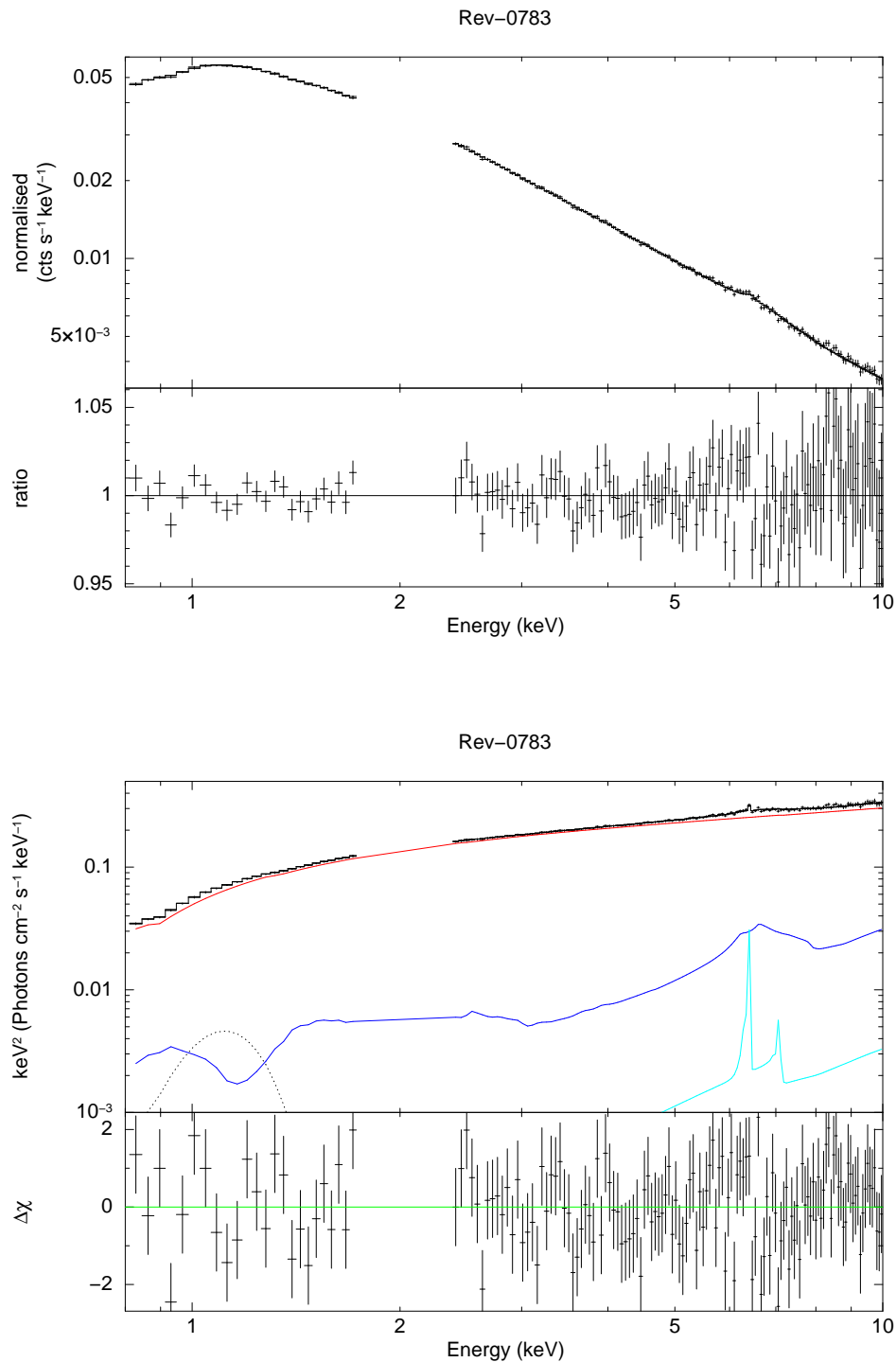


Figure A.9: The top and bottom panels show the modelling results for the TIMING mode observation rev-0783. The top panel shows the folded model and spectra, along with the fit ratio. The bottom panel shows the unfolded model and spectrum, along with the respective  $\Delta\chi$  values. The solid black line represents the total model emission, with the additive model contributions given as follows: disc and powerlaw (red), reflection (dark blue), neutral reflection (light blue) and the soft gaussian (dotted black).

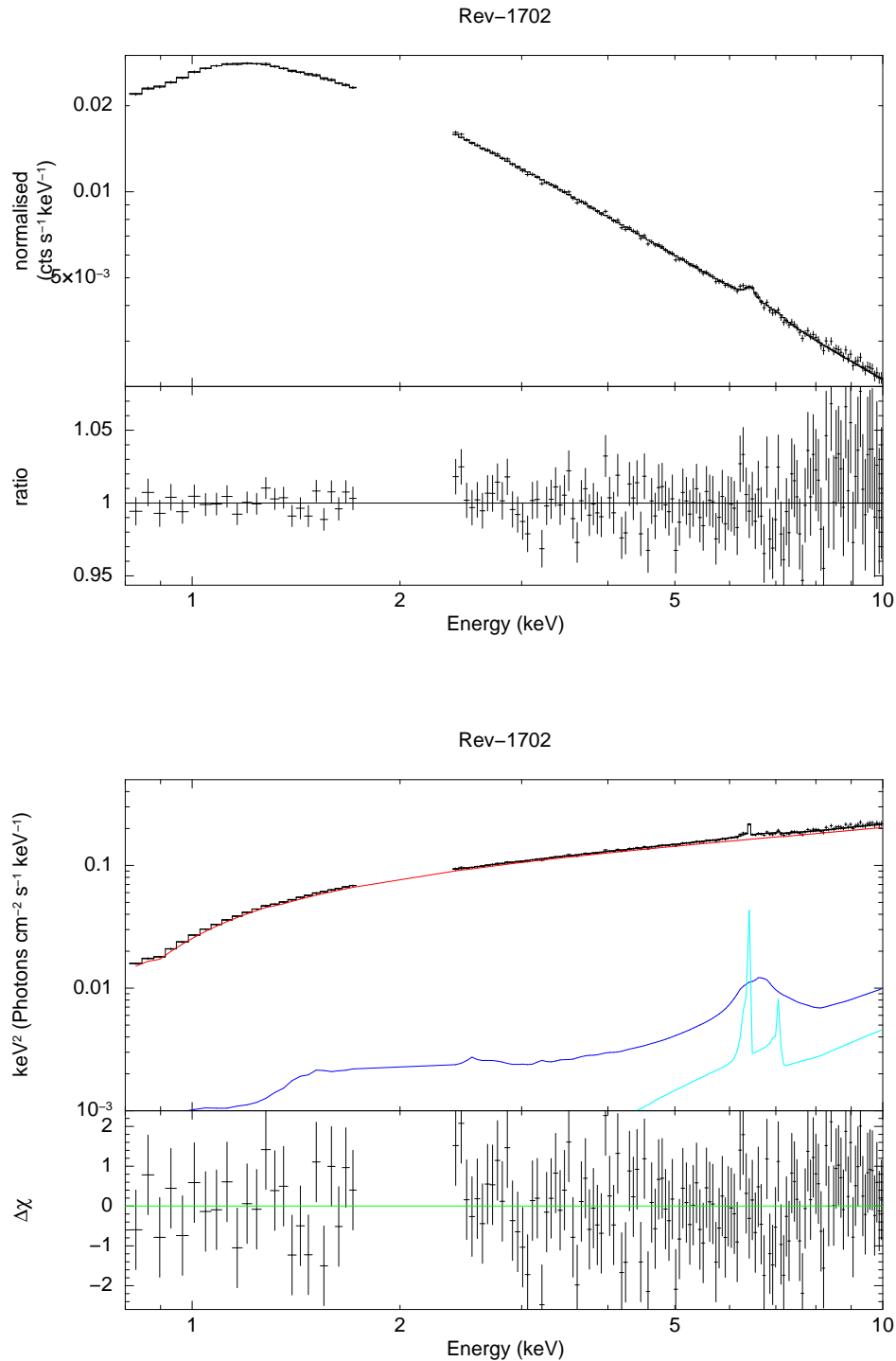


Figure A.10: The top and bottom panels show the modelling results for the TIMING mode observation rev-1702. The top panel shows the folded model and spectra, along with the fit ratio. The bottom panel shows the unfolded model and spectrum, along with the respective  $\Delta\chi$  values. The solid black line represents the total model emission, with the additive model contributions given as follows: disc and powerlaw (red), reflection (dark blue), neutral reflection (light blue).

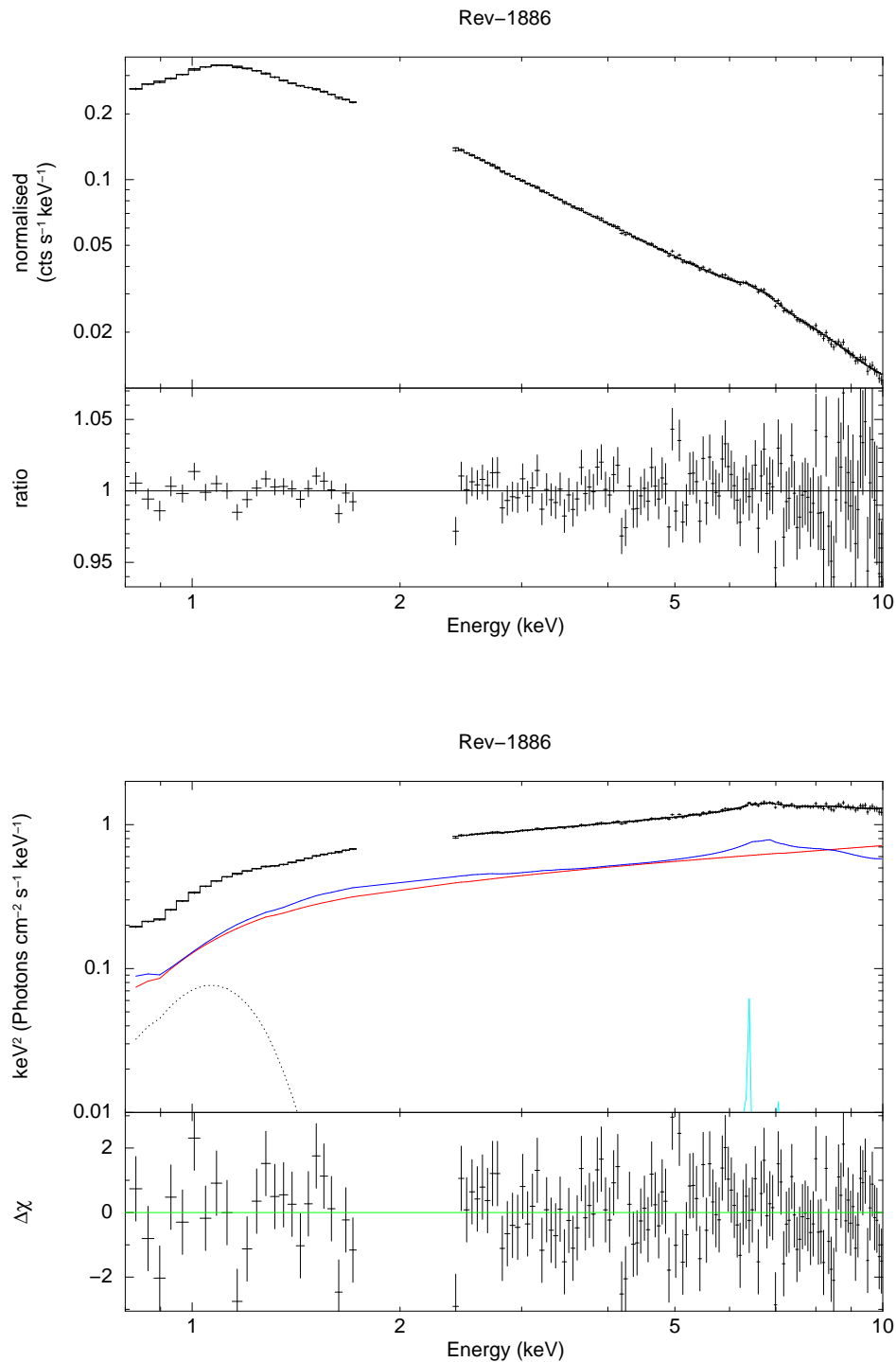


Figure A.11: The top and bottom panels show the modelling results for the TIMING mode observation rev-1886. The top panel shows the folded model and spectra, along with the fit ratio. The bottom panel shows the unfolded model and spectrum, along with the respective  $\Delta\chi$  values. The solid black line represents the total model emission, with the additive model contributions given as follows: disc and powerlaw (red), reflection (dark blue), neutral reflection (light blue) and the soft gaussian (dotted black).

# B

## The count-rate sliced *XMM-Newton* spectral fits

This appendix contains the count-rate sliced spectral fits of the XRB GX 339–4, as outlined in Chapter 4. The EPIC pn-camera observations were count-rate sliced in to multiple spectra (rev-0782 [10 spectra], 0783 [10], 1702 [3] & 1886 [4]). A table containing the parameter fits for all 27 spectra is given in §B.1, with the respective spectral plots listed in to sections according to their *XMM-Newton* revolution number (i.e. rev-0782 in §B.2; rev-0783 in §B.3; rev-1702 in B.4 & rev-1886 in §B.5).

## B.1 Count-rate sliced results table

Spectrum		SIMPL		KERRBB		RELXILL		GAUSSIAN			XILL	GAIN		$\chi^2$	dof	
Rev	No	$\Gamma$	$f_{\text{scat}}$	$\dot{M}_{18}$ gs $^{-1}$	$f_{\text{col}}$	$q$	$\xi$ log $_{10}$	$N_R$ log $_{10}$	$E_{gs}$ keV	$\sigma_{gs}$ keV	$N_{gs}$ log $_{10}$	$N_{Fe}$ log $_{10}$	slope	offset keV		
0782	1	1.60 $^{+0.01}_{-0.04}$	0.32 $^{+0.01}_{-0.01}$	0.08 $^{+0.00}_{-0.01}$	1.51 $^{+0.12}_{-0.09}$	2.24 $^{+0.17}_{-0.41}$	2.30 $^{+0.43}_{-0.20}$	-2.58 $^{+0.05}_{-0.23}$	1.06 $^{+0.02}_{-0.10}$	0.12 $^{+0.04}_{-0.05}$	-2.63 $^{+0.21}_{-0.33}$	-3.24 $^{+0.13}_{-0.19}$	1.00	0.01	155	140
0782	2	1.58 $^{+0.01}_{-0.01}$	0.50 $^{+0.09}_{-0.09}$	0.07 $^{+0.01}_{-0.01}$	2.17 $^{+0.46}_{-0.41}$	2.15 $^{+0.30}_{-0.30}$	2.89 $^{+0.11}_{-0.11}$	-2.78 $^{+0.11}_{-0.09}$	0.80 $^{+0.03}_{-0.00}$	0.19 $^{+0.01}_{-0.01}$	-1.50 $^{+0.19}_{-0.07}$	-3.23 $^{+0.22}_{-0.27}$	1.01	0.00	215	140
0782	3	1.61 $^{+0.01}_{-0.02}$	0.33 $^{+0.01}_{-0.01}$	0.13 $^{+0.00}_{-0.01}$	1.52 $^{+0.04}_{-0.04}$	1.74 $^{+0.23}_{-0.24}$	2.30 $^{+0.13}_{-0.18}$	-2.58 $^{+0.07}_{-0.18}$	1.01 $^{+0.02}_{-0.03}$	0.10 $^{+0.03}_{-0.03}$	-2.31 $^{+0.19}_{-0.18}$	-3.47 $^{+0.28}_{-1.76}$	1.01	0.00	207	140
0782	4	1.62 $^{+0.01}_{-0.01}$	0.33 $^{+0.02}_{-0.01}$	0.14 $^{+0.01}_{-0.01}$	1.47 $^{+0.05}_{-0.05}$	2.07 $^{+0.16}_{-0.18}$	2.29 $^{+0.26}_{-0.13}$	-2.41 $^{+0.05}_{-0.09}$	0.98 $^{+0.03}_{-0.06}$	0.15 $^{+0.02}_{-0.02}$	-2.01 $^{+0.17}_{-0.14}$	-3.21 $^{+0.19}_{-0.39}$	1.00	0.01	142	140
0782	5	1.63 $^{+0.02}_{-0.01}$	0.32 $^{+0.02}_{-0.01}$	0.15 $^{+0.01}_{-0.01}$	1.41 $^{+0.05}_{-0.05}$	1.93 $^{+0.15}_{-0.18}$	2.29 $^{+0.26}_{-0.15}$	-2.35 $^{+0.07}_{-0.07}$	1.00 $^{+0.02}_{-0.05}$	0.15 $^{+0.03}_{-0.02}$	-1.91 $^{+0.15}_{-0.16}$	-3.32 $^{+0.25}_{-0.76}$	1.00	0.01	166	140
0782	6	1.64 $^{+0.01}_{-0.01}$	0.38 $^{+0.04}_{-0.02}$	0.15 $^{+0.01}_{-0.01}$	1.52 $^{+0.09}_{-0.04}$	1.95 $^{+0.12}_{-0.09}$	2.30 $^{+0.05}_{-0.15}$	-2.27 $^{+0.06}_{-0.09}$	0.96 $^{+0.03}_{-0.05}$	0.17 $^{+0.02}_{-0.03}$	-1.67 $^{+0.10}_{-0.14}$	-7.77 $^{+4.28}_{-\text{inf}}$	1.00	0.00	171	140
0782	7	1.65 $^{+0.01}_{-0.01}$	0.39 $^{+0.03}_{-0.02}$	0.17 $^{+0.01}_{-0.01}$	1.49 $^{+0.06}_{-0.05}$	2.01 $^{+0.14}_{-0.20}$	2.30 $^{+0.07}_{-0.18}$	-2.31 $^{+0.05}_{-0.11}$	0.98 $^{+0.02}_{-0.04}$	0.17 $^{+0.02}_{-0.02}$	-1.63 $^{+0.14}_{-0.13}$	-3.37 $^{+0.32}_{-\text{inf}}$	1.00	0.00	149	140
0782	8	1.66 $^{+0.02}_{-0.01}$	0.38 $^{+0.03}_{-0.02}$	0.19 $^{+0.01}_{-0.02}$	1.45 $^{+0.03}_{-0.05}$	2.05 $^{+0.14}_{-0.16}$	2.29 $^{+0.05}_{-0.16}$	-2.24 $^{+0.05}_{-0.08}$	0.99 $^{+0.02}_{-0.05}$	0.16 $^{+0.03}_{-0.02}$	-1.62 $^{+0.10}_{-0.13}$	-2.91 $^{+0.15}_{-0.22}$	1.00	0.01	185	140
0782	9	1.67 $^{+0.01}_{-0.01}$	0.34 $^{+0.02}_{-0.02}$	0.23 $^{+0.01}_{-0.01}$	1.32 $^{+0.04}_{-0.05}$	2.04 $^{+0.12}_{-0.05}$	2.28 $^{+0.05}_{-0.13}$	-2.12 $^{+0.05}_{-0.06}$	1.01 $^{+0.01}_{-0.03}$	0.15 $^{+0.03}_{-0.02}$	-1.55 $^{+0.12}_{-0.10}$	-4.73 $^{+1.50}_{-\text{inf}}$	0.99	0.02	124	140
0782	10	1.67 $^{+0.02}_{-0.01}$	0.38 $^{+0.03}_{-0.01}$	0.29 $^{+0.01}_{-0.02}$	1.39 $^{+0.04}_{-0.04}$	2.05 $^{+0.15}_{-0.15}$	2.29 $^{+0.07}_{-0.14}$	-2.04 $^{+0.04}_{-0.07}$	1.02 $^{+0.01}_{-0.01}$	0.15 $^{+0.02}_{-0.01}$	-1.45 $^{+0.12}_{-0.07}$	-3.13 $^{+0.31}_{-\text{inf}}$	0.99	0.02	193	140
0783	1	1.61 $^{+0.01}_{-0.01}$	0.30 $^{+0.01}_{-0.01}$	0.10 $^{+0.00}_{-0.00}$	1.41 $^{+0.07}_{-0.10}$	2.16 $^{+0.17}_{-0.10}$	2.29 $^{+0.08}_{-0.18}$	-2.59 $^{+0.05}_{-0.10}$	1.01 $^{+0.03}_{-0.05}$	0.16 $^{+1.84}_{-0.03}$	-2.34 $^{+0.27}_{-0.21}$	-3.45 $^{+0.21}_{-0.45}$	1.01	0.01	153	140
0783	2	1.62 $^{+0.01}_{-0.01}$	0.34 $^{+0.02}_{-0.02}$	0.11 $^{+0.01}_{-0.01}$	1.48 $^{+0.08}_{-0.07}$	2.19 $^{+0.16}_{-0.15}$	2.29 $^{+0.08}_{-0.14}$	-2.44 $^{+0.05}_{-0.09}$	0.98 $^{+0.03}_{-0.08}$	0.17 $^{+0.03}_{-0.03}$	-2.06 $^{+0.20}_{-0.16}$	-3.35 $^{+0.23}_{-0.48}$	1.00	0.01	178	140
0783	3	1.63 $^{+0.01}_{-0.01}$	0.36 $^{+0.02}_{-0.01}$	0.13 $^{+0.01}_{-0.01}$	1.50 $^{+0.05}_{-0.05}$	2.02 $^{+0.23}_{-0.14}$	2.29 $^{+0.07}_{-0.16}$	-2.55 $^{+0.07}_{-0.11}$	1.00 $^{+0.02}_{-0.04}$	0.13 $^{+0.02}_{-0.02}$	-2.02 $^{+0.15}_{-0.05}$	-3.08 $^{+0.15}_{-0.25}$	1.01	-0.00	183	140
0783	4	1.63 $^{+0.02}_{-0.02}$	0.37 $^{+0.03}_{-0.02}$	0.14 $^{+0.01}_{-0.01}$	1.55 $^{+0.12}_{-0.06}$	1.82 $^{+0.22}_{-0.32}$	2.33 $^{+0.42}_{-0.19}$	-2.46 $^{+0.09}_{-0.18}$	0.98 $^{+0.03}_{-0.10}$	0.15 $^{+0.04}_{-0.03}$	-1.93 $^{+0.26}_{-0.15}$	-3.60 $^{+0.43}_{-\text{inf}}$	1.01	0.00	163	140
0783	5	1.62 $^{+0.02}_{-0.01}$	0.30 $^{+0.03}_{-0.01}$	0.18 $^{+0.01}_{-0.01}$	1.40 $^{+0.03}_{-0.04}$	1.50 $^{+0.28}_{-0.00}$	2.31 $^{+0.10}_{-0.21}$	-2.51 $^{+0.08}_{-0.06}$	1.01 $^{+0.02}_{-0.02}$	0.11 $^{+0.03}_{-0.02}$	-2.06 $^{+0.07}_{-0.06}$	-9.59 $^{+6.10}_{-\text{inf}}$	1.01	0.01	173	140
0783	6	1.66 $^{+0.03}_{-0.02}$	0.36 $^{+0.02}_{-0.02}$	0.17 $^{+0.01}_{-0.01}$	1.44 $^{+0.07}_{-0.05}$	1.97 $^{+0.23}_{-0.31}$	2.30 $^{+0.15}_{-0.26}$	-2.39 $^{+0.06}_{-0.16}$	0.97 $^{+0.03}_{-0.06}$	0.16 $^{+0.03}_{-0.03}$	-1.68 $^{+0.18}_{-0.15}$	-3.04 $^{+0.17}_{-0.33}$	1.01	0.01	163	140
0783	7	1.66 $^{+0.01}_{-0.01}$	0.33 $^{+0.02}_{-0.02}$	0.20 $^{+0.01}_{-0.01}$	1.36 $^{+0.04}_{-0.05}$	1.83 $^{+0.15}_{-0.19}$	2.29 $^{+0.07}_{-0.16}$	-2.24 $^{+0.04}_{-0.09}$	1.00 $^{+0.02}_{-0.03}$	0.15 $^{+0.02}_{-0.02}$	-1.70 $^{+0.12}_{-0.11}$	-4.27 $^{+1.02}_{-\text{inf}}$	1.00	0.02	187	140
0783	8	1.66 $^{+0.02}_{-0.01}$	0.32 $^{+0.02}_{-0.01}$	0.23 $^{+0.01}_{-0.01}$	1.32 $^{+0.03}_{-0.04}$	1.96 $^{+0.15}_{-0.18}$	2.30 $^{+0.04}_{-0.17}$	-2.25 $^{+0.04}_{-0.07}$	1.01 $^{+0.02}_{-0.03}$	0.14 $^{+0.01}_{-0.01}$	-1.72 $^{+0.13}_{-0.10}$	-3.31 $^{+0.32}_{-\text{inf}}$	1.00	0.03	204	140
0783	9	1.67 $^{+0.02}_{-0.01}$	0.38 $^{+0.03}_{-0.02}$	0.24 $^{+0.01}_{-0.02}$	1.45 $^{+0.04}_{-0.04}$	1.92 $^{+0.12}_{-0.12}$	2.28 $^{+0.06}_{-0.18}$	-2.19 $^{+0.07}_{-0.08}$	1.00 $^{+0.02}_{-0.03}$	0.14 $^{+0.03}_{-0.02}$	-1.55 $^{+0.15}_{-0.10}$	-3.12 $^{+0.27}_{-0.90}$	1.00	0.01	208	140
0783	10	1.68 $^{+0.03}_{-0.02}$	0.37 $^{+0.03}_{-0.02}$	0.30 $^{+0.02}_{-0.02}$	1.37 $^{+0.04}_{-0.04}$	2.23 $^{+0.16}_{-0.13}$	2.30 $^{+0.13}_{-0.22}$	-2.00 $^{+0.04}_{-0.12}$	1.01 $^{+0.02}_{-0.03}$	0.16 $^{+0.03}_{-0.02}$	-1.39 $^{+0.12}_{-0.12}$	-3.31 $^{+0.41}_{-\text{inf}}$	0.98	0.04	181	140
1702	1	1.51 $^{+0.03}_{-0.02}$	0.43 $^{+0.02}_{-0.02}$	0.04 $^{+0.00}_{-0.00}$	2.07 $^{+0.08}_{-0.17}$	1.88 $^{+0.50}_{-0.38}$	2.46 $^{+0.31}_{-0.28}$	-3.11 $^{+0.26}_{-0.17}$	-	-	-	-3.24 $^{+0.13}_{-0.21}$	1.01	0.00	142	143
1702	2	1.58 $^{+0.02}_{-0.01}$	0.38 $^{+0.02}_{-0.04}$	0.08 $^{+0.01}_{-0.01}$	1.45 $^{+0.11}_{-0.16}$	2.59 $^{+0.71}_{-0.34}$	2.31 $^{+0.11}_{-0.19}$	-2.61 $^{+0.08}_{-0.21}$	1.03 $^{+0.06}_{-0.07}$	0.20 $^{+0.00}_{-0.06}$	-2.27 $^{+0.14}_{-0.34}$	-3.00 $^{+0.12}_{-0.16}$	1.01	0.00	160	140
1702	3	1.61 $^{+0.02}_{-0.03}$	0.46 $^{+0.02}_{-0.04}$	0.12 $^{+0.01}_{-0.01}$	1.61 $^{+0.14}_{-0.12}$	2.11 $^{+0.18}_{-0.31}$	2.30 $^{+0.16}_{-0.23}$	-2.30 $^{+0.07}_{-0.18}$	0.94 $^{+0.05}_{-0.07}$	0.19 $^{+0.01}_{-0.02}$	-1.73 $^{+0.19}_{-0.19}$	-3.03 $^{+0.19}_{-0.37}$	1.00	0.00	158	140
1886	1	1.65 $^{+0.02}_{-0.01}$	0.45 $^{+0.03}_{-0.10}$	0.17 $^{+0.03}_{-0.03}$	1.81 $^{+0.25}_{-0.23}$	1.59 $^{+0.25}_{-0.09}$	3.17 $^{+0.05}_{-0.05}$	-1.73 $^{+0.05}_{-0.06}$	0.89 $^{+0.04}_{-0.01}$	0.20 $^{+0.00}_{-0.02}$	-0.85 $^{+0.04}_{-0.15}$	-3.15 $^{+0.38}_{-\text{inf}}$	0.99	0.03	188	140
1886	2	1.63 $^{+0.02}_{-0.01}$	0.34 $^{+0.05}_{-0.07}$	0.26 $^{+0.05}_{-0.05}$	1.63 $^{+0.24}_{-0.15}$	1.50 $^{+0.27}_{-0.00}$	3.19 $^{+0.05}_{-0.05}$	-1.58 $^{+0.05}_{-0.06}$	0.93 $^{+0.04}_{-0.04}$	0.18 $^{+0.02}_{-0.03}$	-0.89 $^{+0.13}_{-0.15}$	-2.88 $^{+0.30}_{-2.44}$	0.97	0.05	208	140
1886	3	1.63 $^{+0.02}_{-0.02}$	0.40 $^{+0.09}_{-0.12}$	0.25 $^{+0.04}_{-0.04}$	1.80 $^{+0.22}_{-0.19}$	1.50 $^{+0.18}_{-0.00}$	3.20 $^{+0.04}_{-0.02}$	-1.47 $^{+0.05}_{-0.05}$	0.94 $^{+0.04}_{-0.03}$	0.19 $^{+0.01}_{-0.02}$	-0.78 $^{+0.06}_{-0.14}$	-2.89 $^{+0.22}_{-\text{inf}}$	0.97	0.04	223	140
1886	4	1.63 $^{+0.01}_{-0.02}$	0.40 $^{+0.04}_{-0.08}$	0.27 $^{+0.05}_{-0.05}$	1.74 $^{+0.20}_{-0.15}$	1.50 $^{+0.14}_{-0.00}$	3.21 $^{+0.01}_{-0.01}$	-1.34 $^{+0.04}_{-0.05}$	0.94 $^{+0.02}_{-0.01}$	0.18 $^{+0.01}_{-0.02}$	-0.68 $^{+0.04}_{-0.19}$	-3.87 $^{+1.19}_{-\text{inf}}$	0.97	0.05	206	140

Table B.1: The count-rate sliced EPIC pn-camera TIMING mode parameter table for GX 339–4, with errors calculated at the 90% confidence level. The *XMM-Newton* revolution and the spectral slice number are given in columns 1 & 2; columns 3-13 give the model values; 14 & 15 give the gain corrections, and 16 & 17 giving the fit statistics.

## B.2 Count-rate sliced rev-0782 spectra

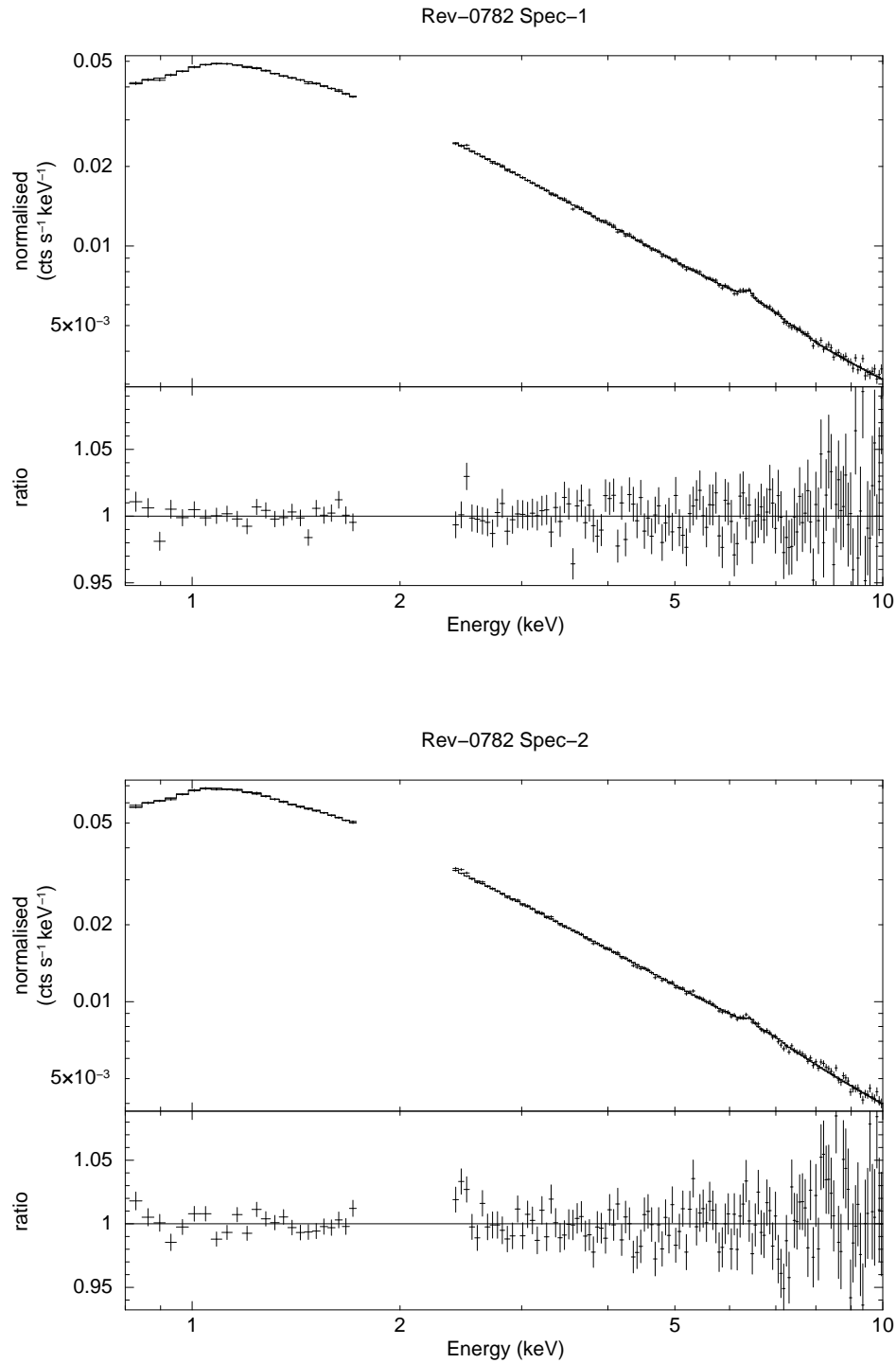


Figure B.1: The folded model and spectra, along with the fit ratio for the 1st and 2nd count rate bins of observation rev-0782.

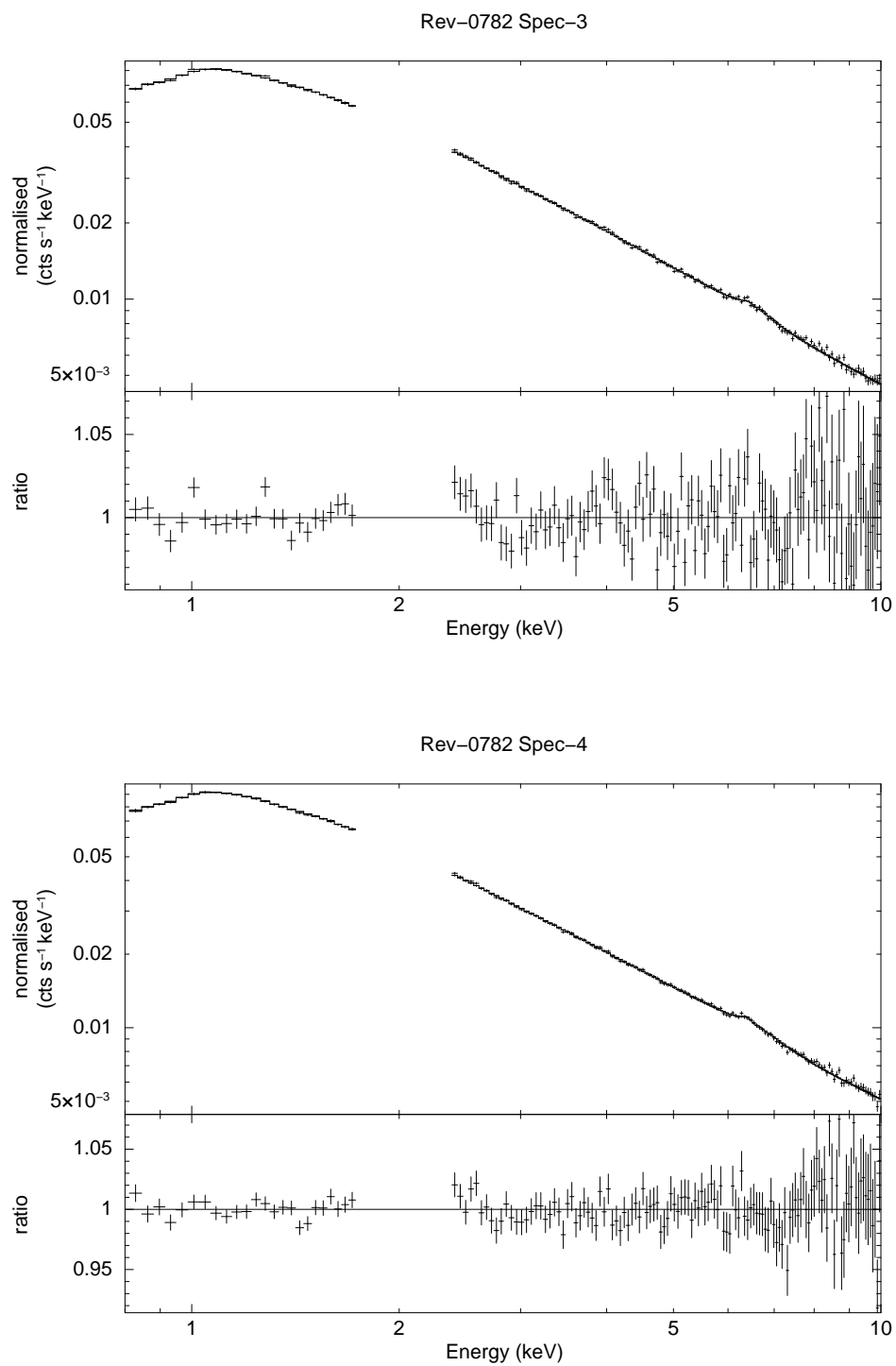


Figure B.2: The folded model and spectra, along with the fit ratio for the 3rd and 4th count rate bins of observation rev-0782.

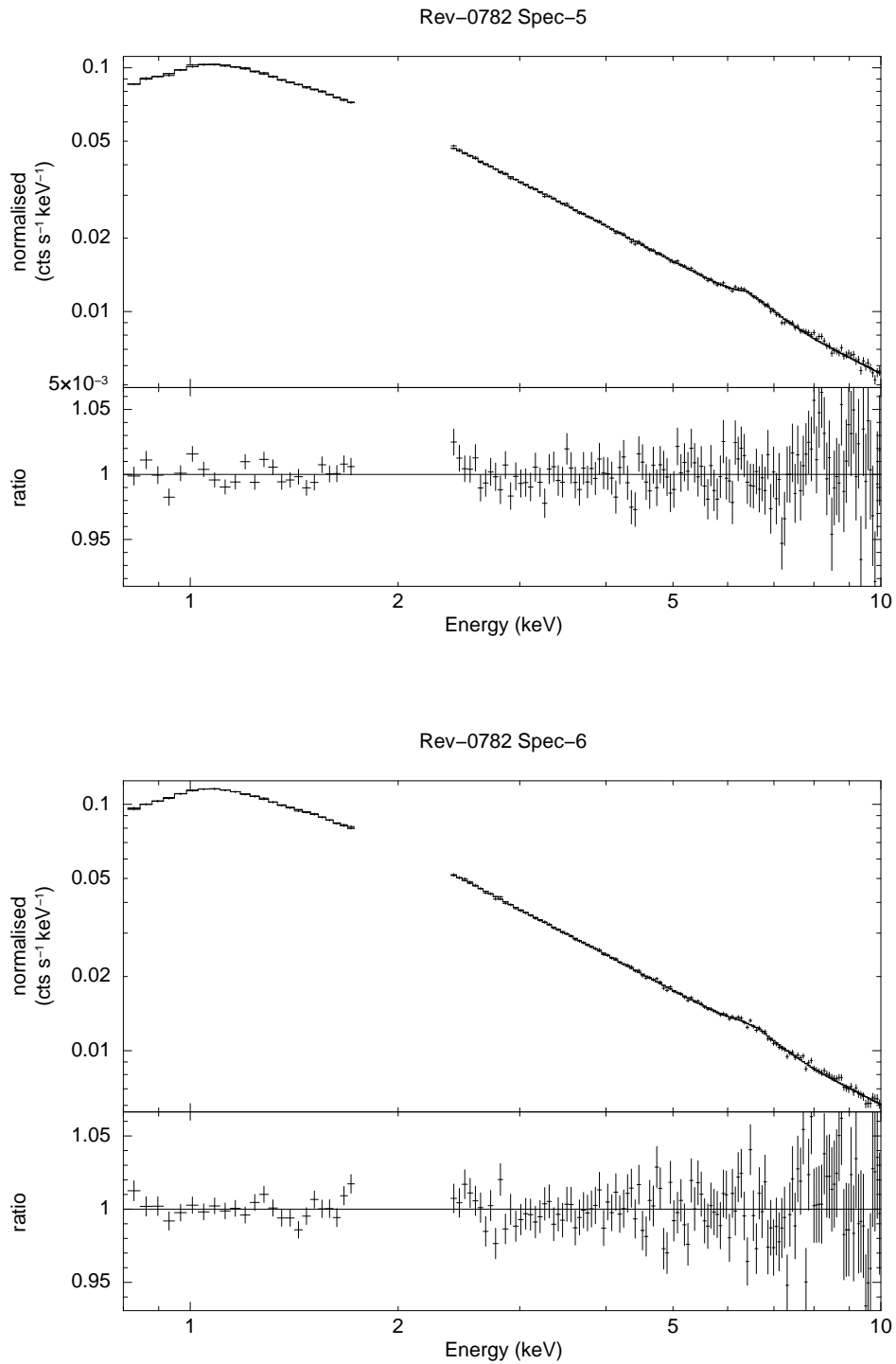


Figure B.3: The folded model and spectra, along with the fit ratio for the 5th and 6th count rate bins of observation rev-0782.

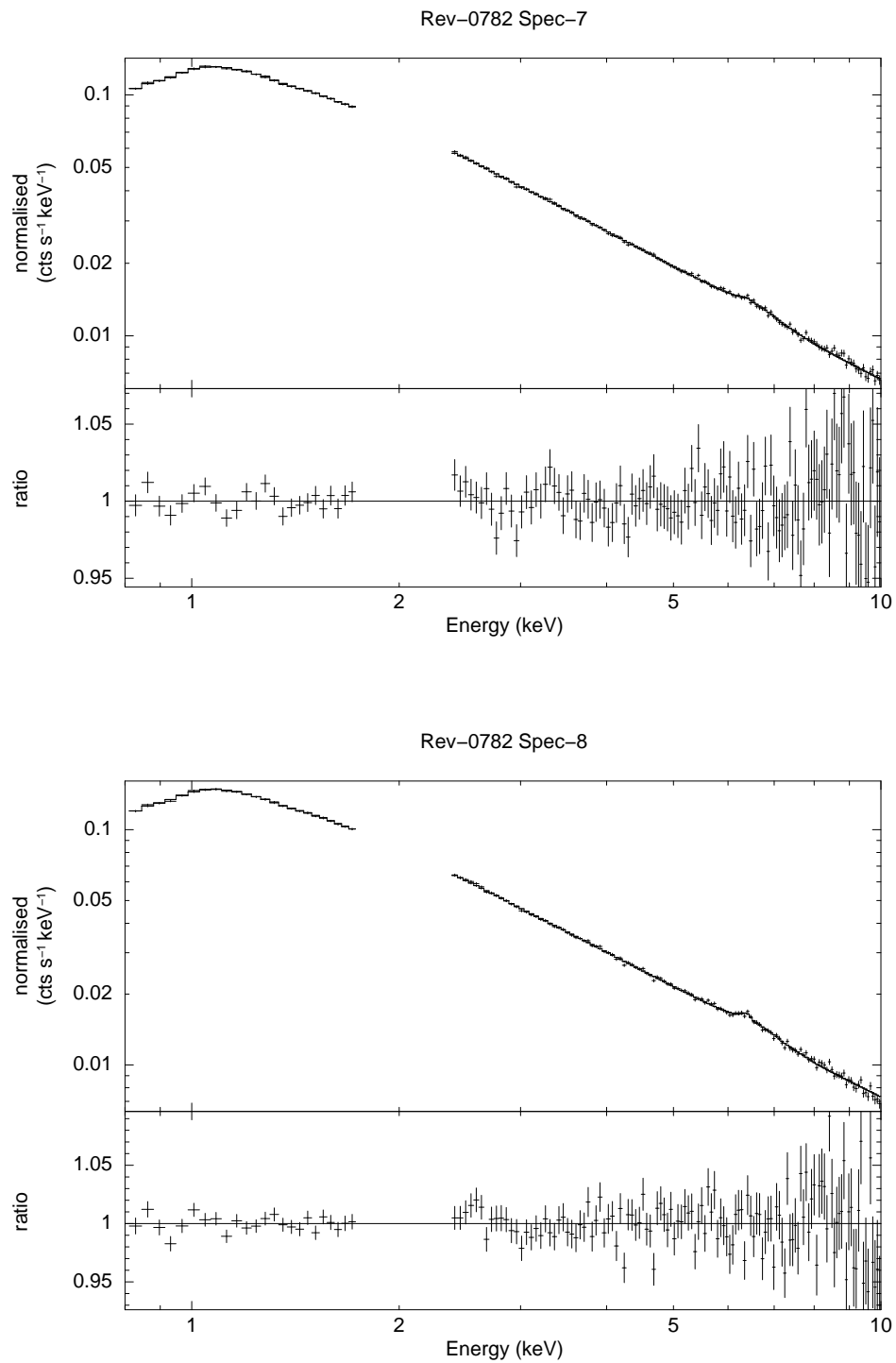


Figure B.4: The folded model and spectra, along with the fit ratio for the 7th and 8th count rate bins of observation rev-0782.

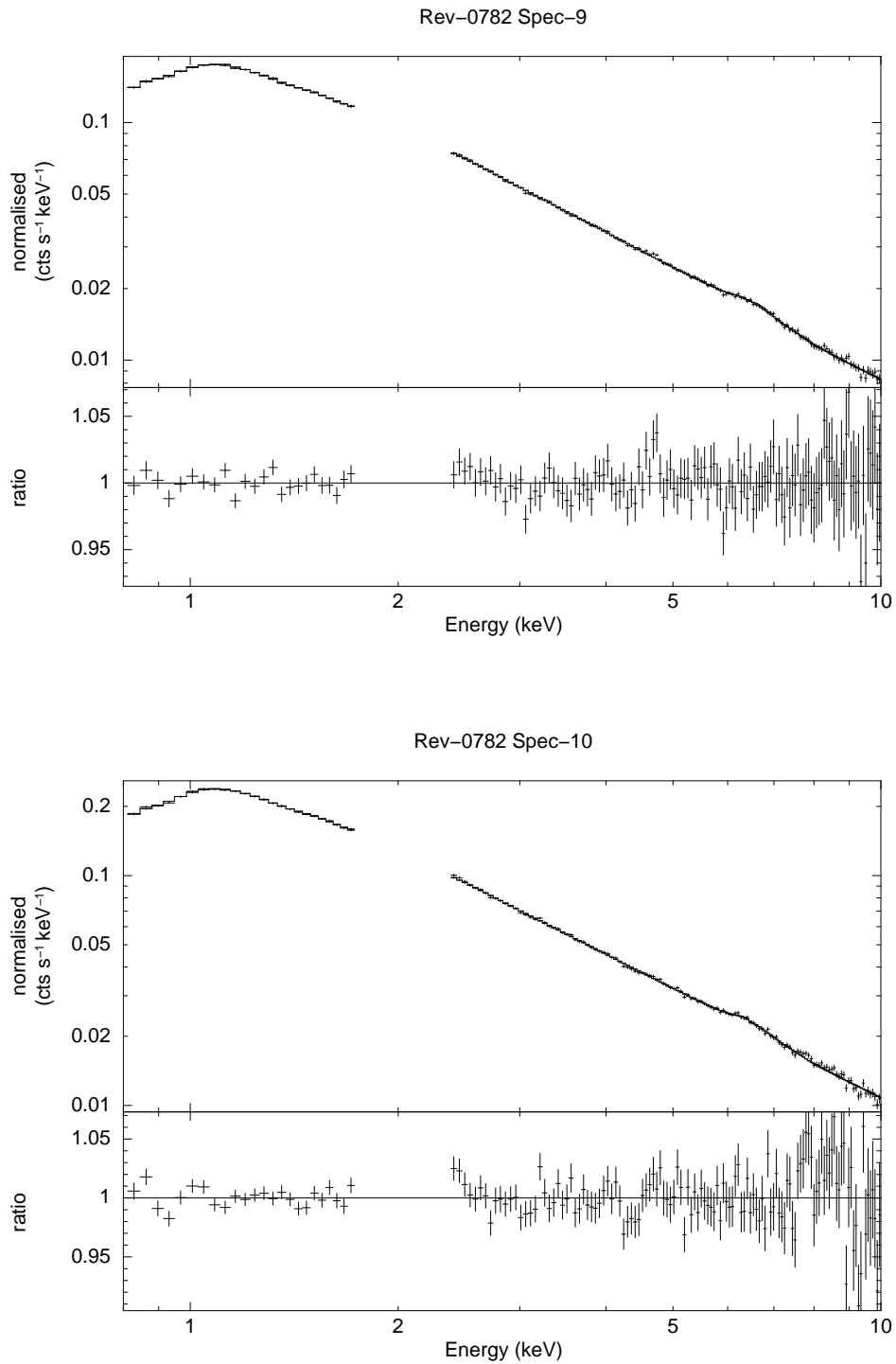


Figure B.5: The folded model and spectra, along with the fit ratio for the 9th and 10th count rate bins of observation rev-0782.

### B.3 Count-rate sliced rev-0783 spectra

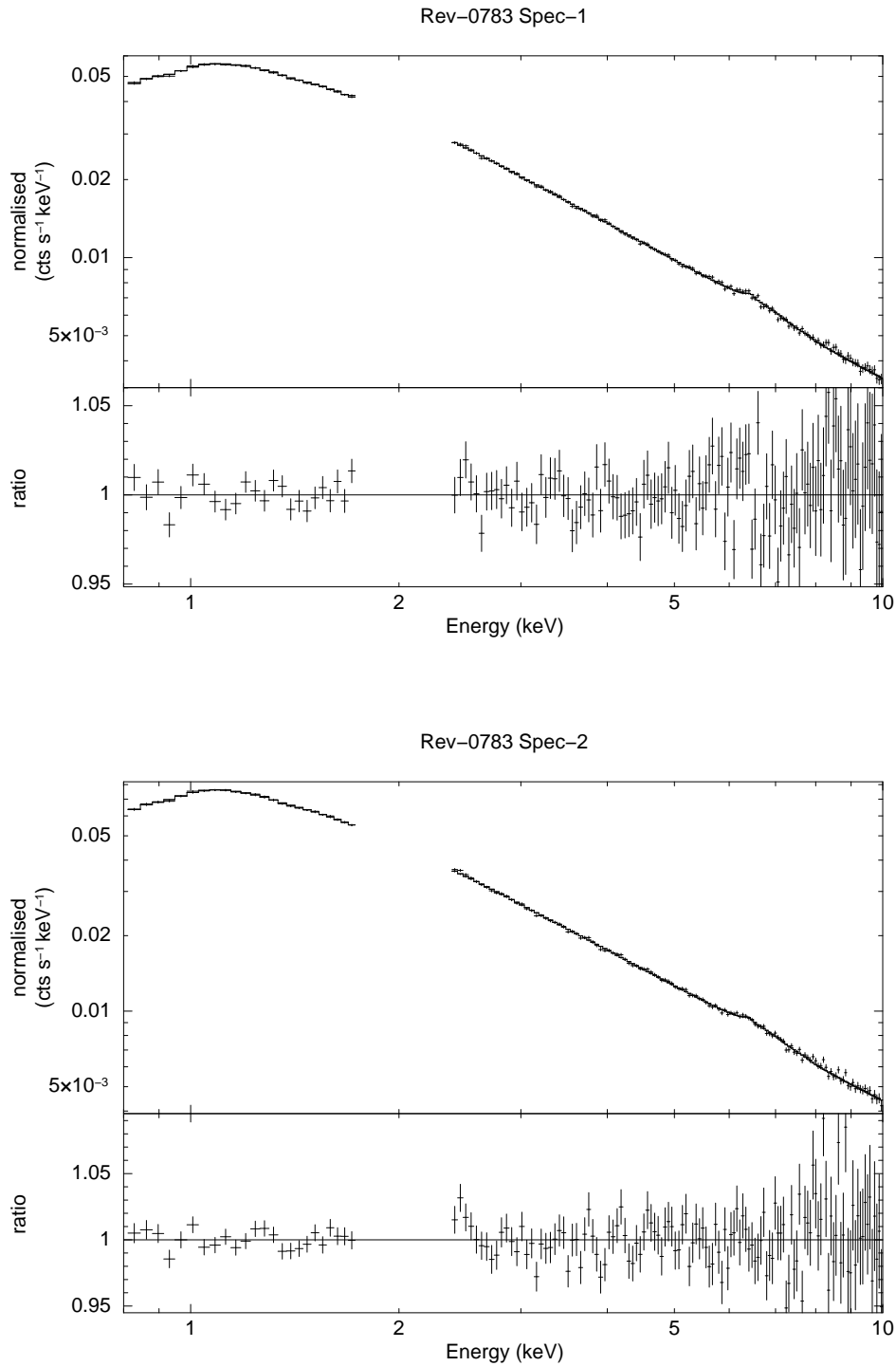


Figure B.6: The folded model and spectra, along with the fit ratio for the 1st and 2nd count rate bins of observation rev-0783.

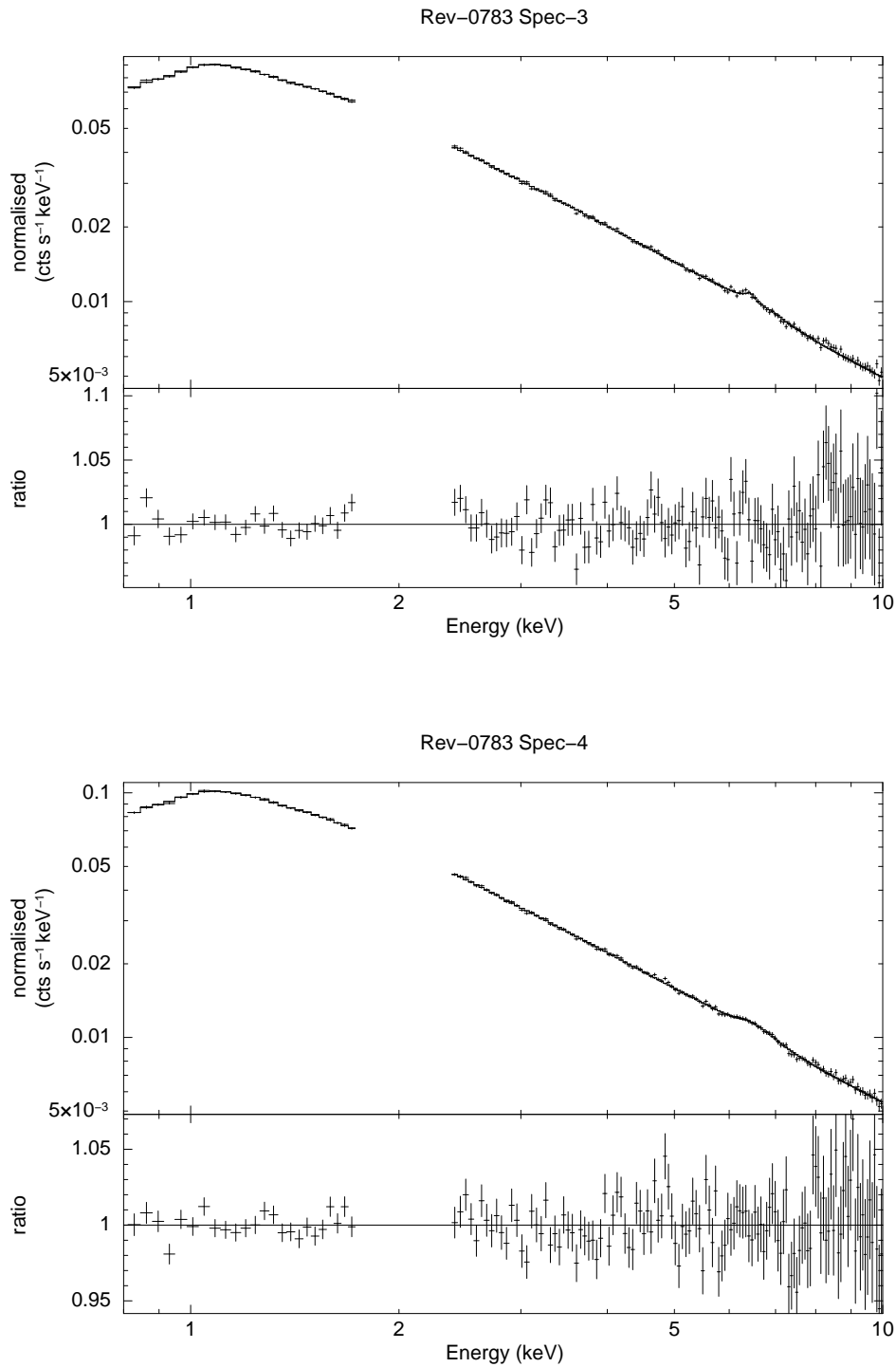


Figure B.7: The folded model and spectra, along with the fit ratio for the 3rd and 4th count rate bins of observation rev-0783.

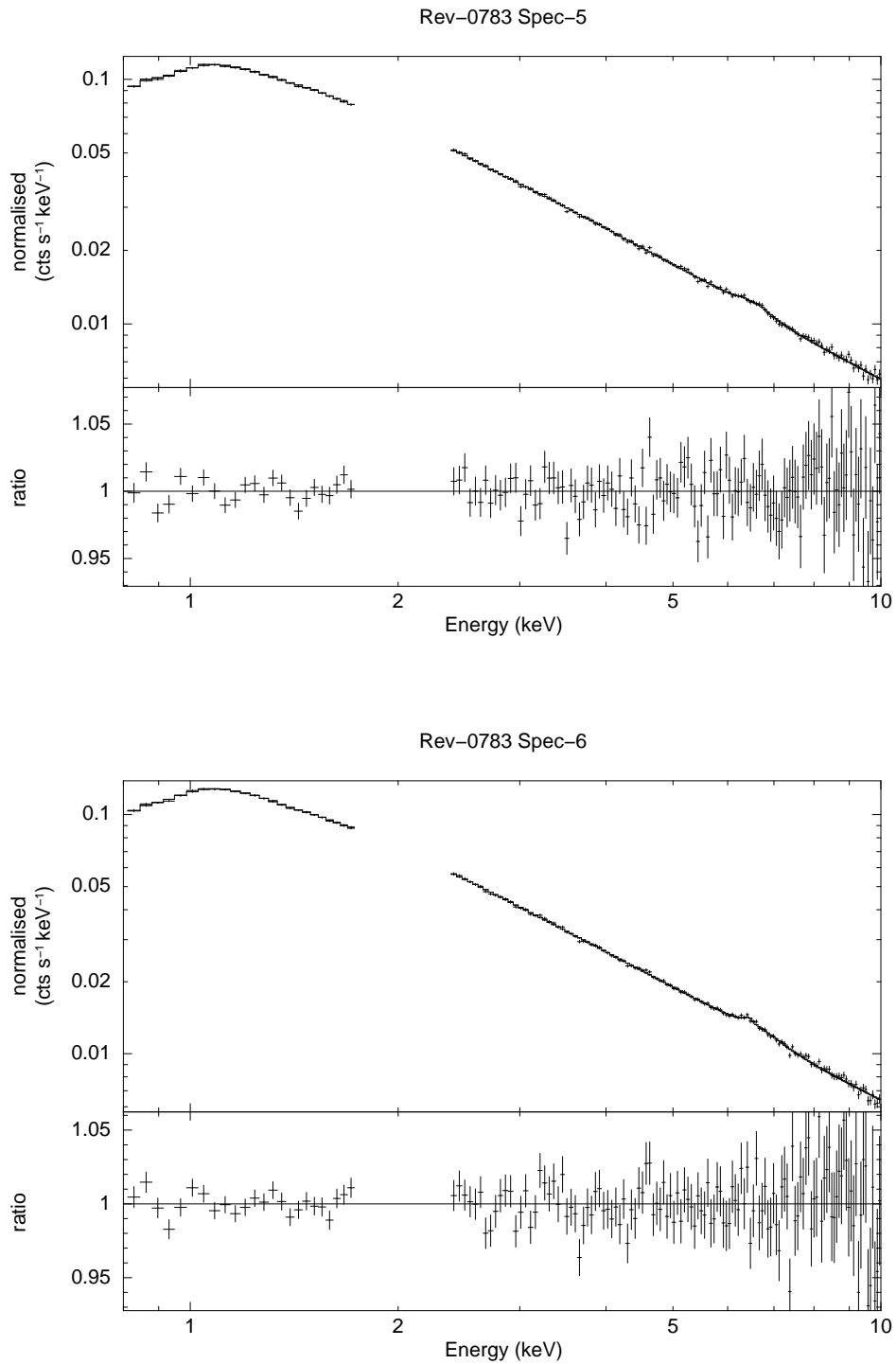


Figure B.8: The folded model and spectra, along with the fit ratio for the 5th and 6th count rate bins of observation rev-0783.

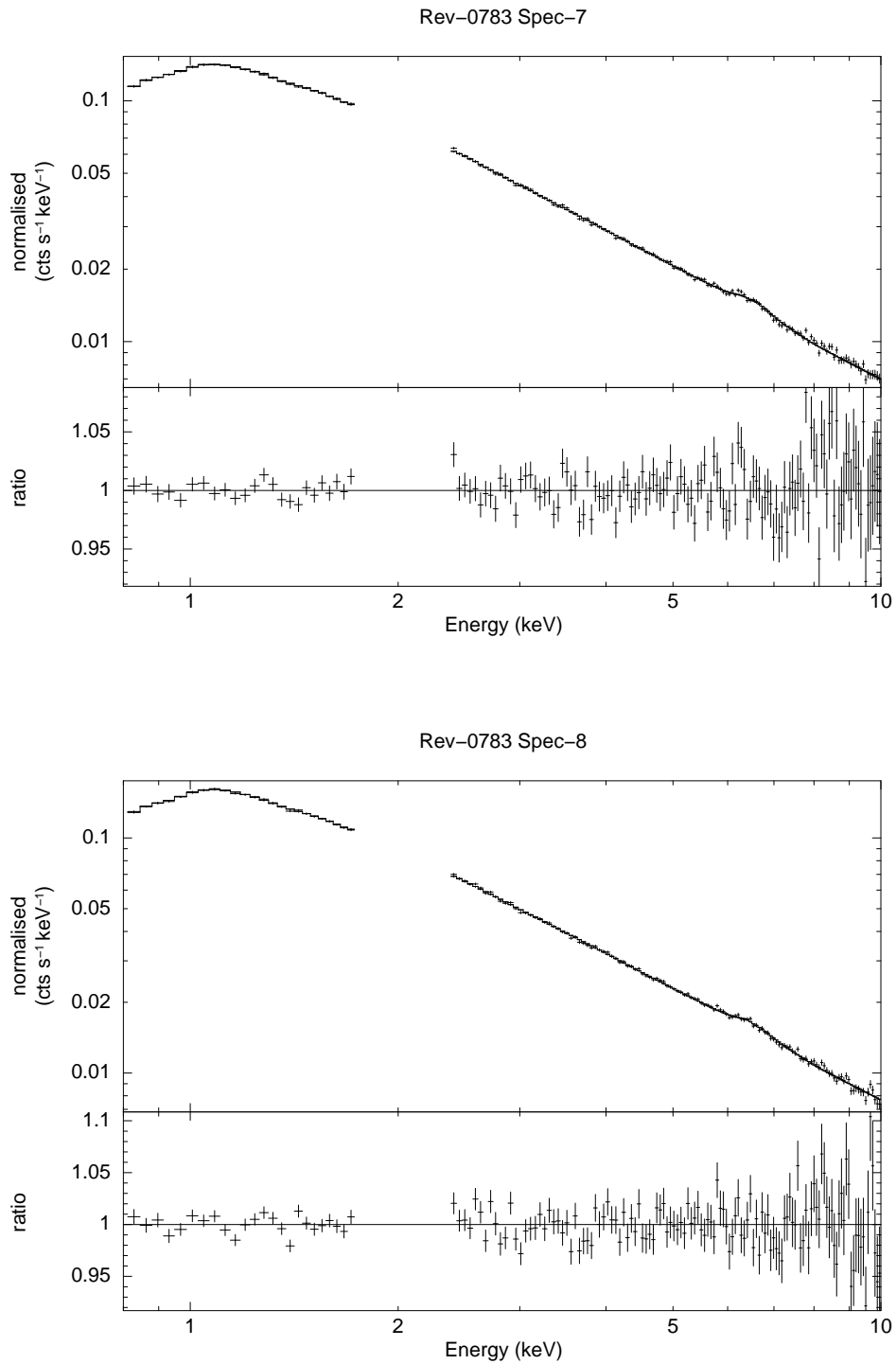


Figure B.9: The folded model and spectra, along with the fit ratio for the 7th and 8th count rate bins of observation rev-0783.

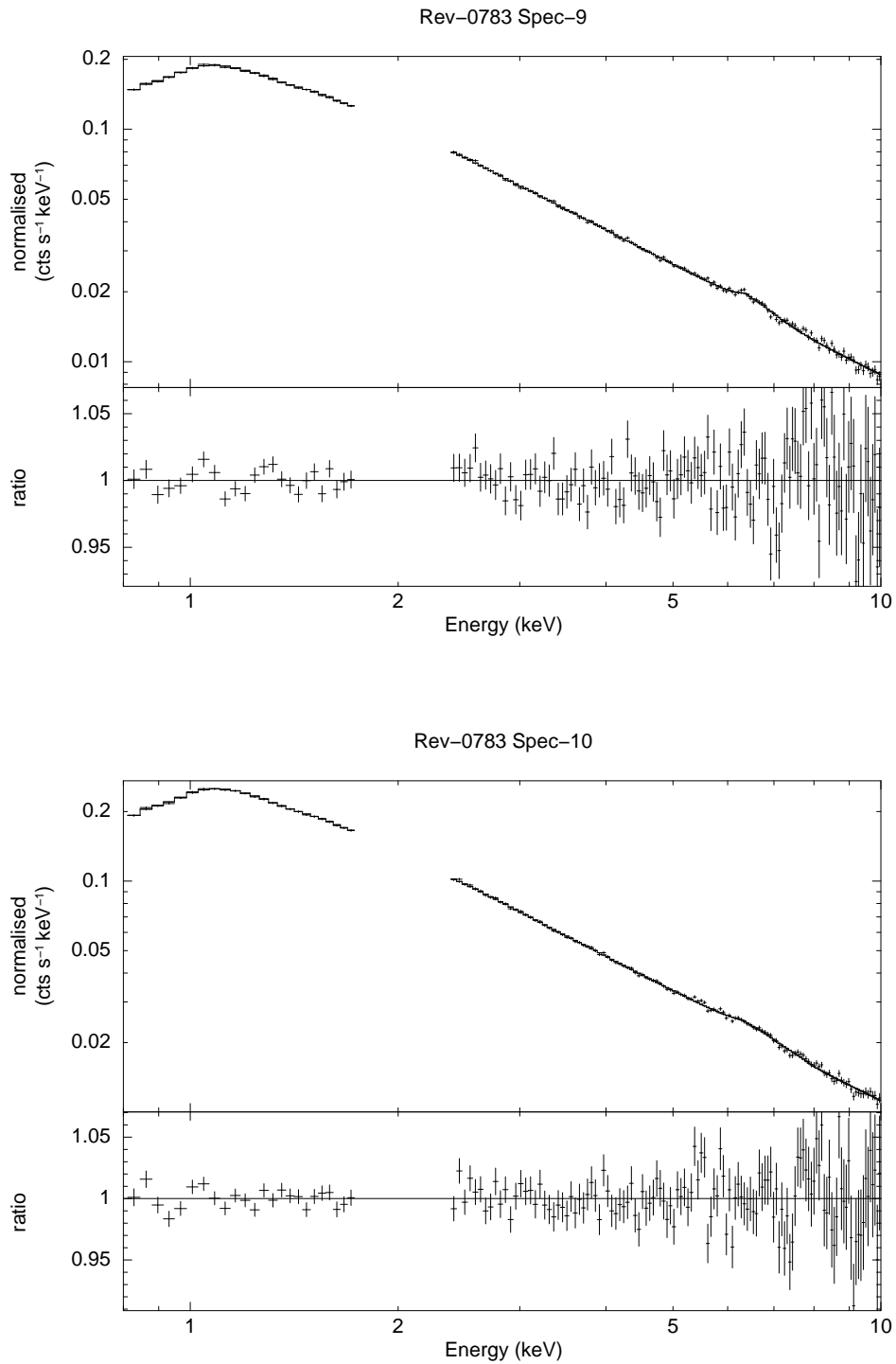


Figure B.10: The folded model and spectra, along with the fit ratio for the 9th and 10th count rate bins of observation rev-0783.

## B.4 Count-rate sliced rev-1702 spectra

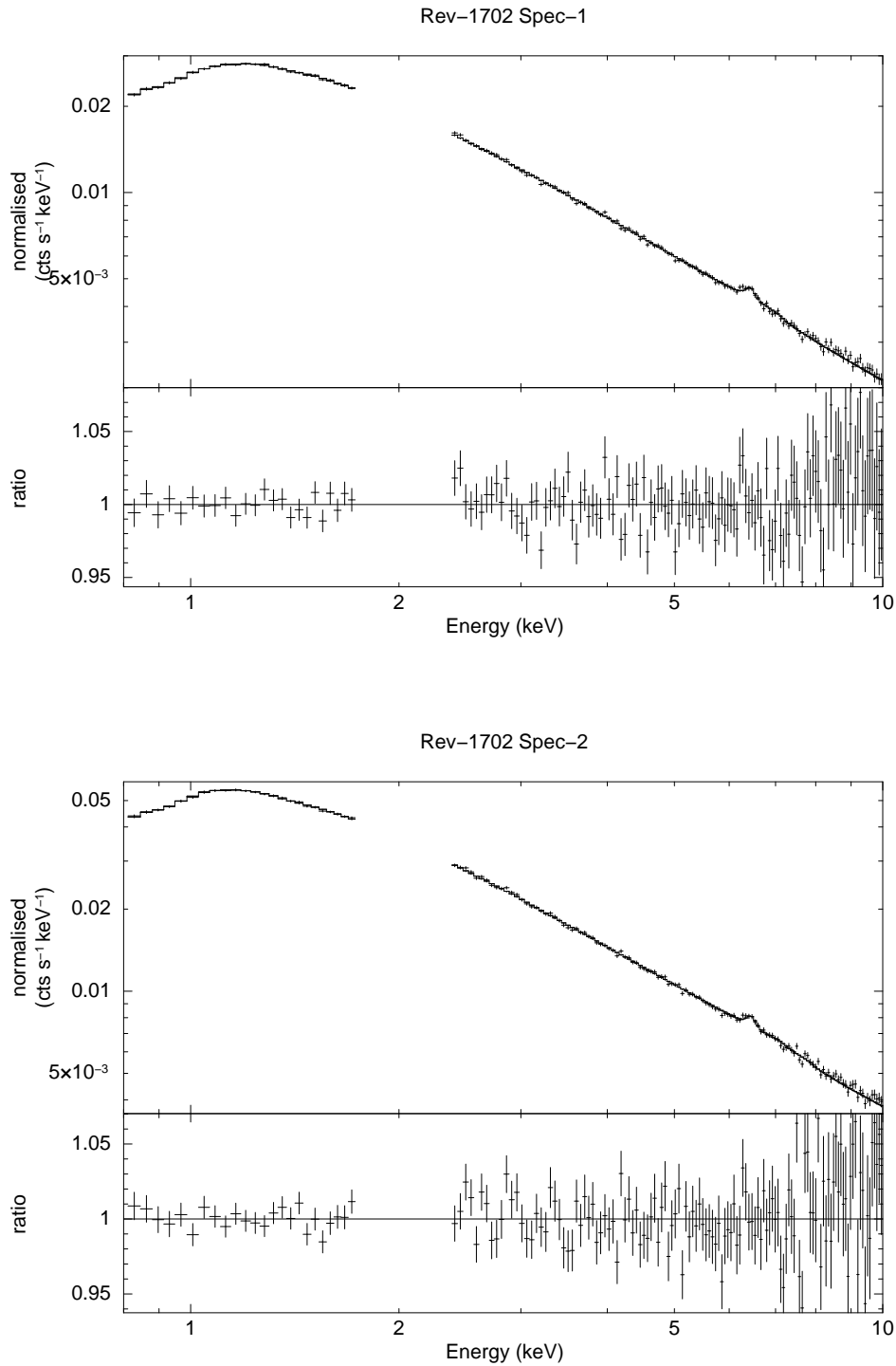


Figure B.11: The folded model and spectra, along with the fit ratio for the 1st and 2nd count rate bins of observation rev-1702.

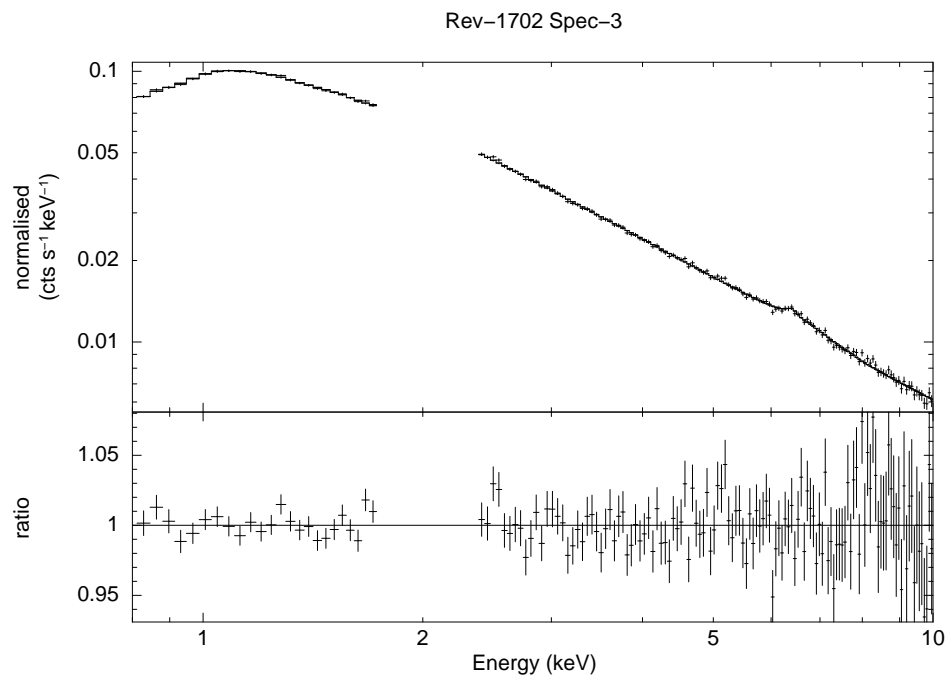


Figure B.12: The folded model and spectra, along with the fit ratio for the 3rd count rate bin of observation rev-1702.

## B.5 Count-rate sliced rev-1886 spectra

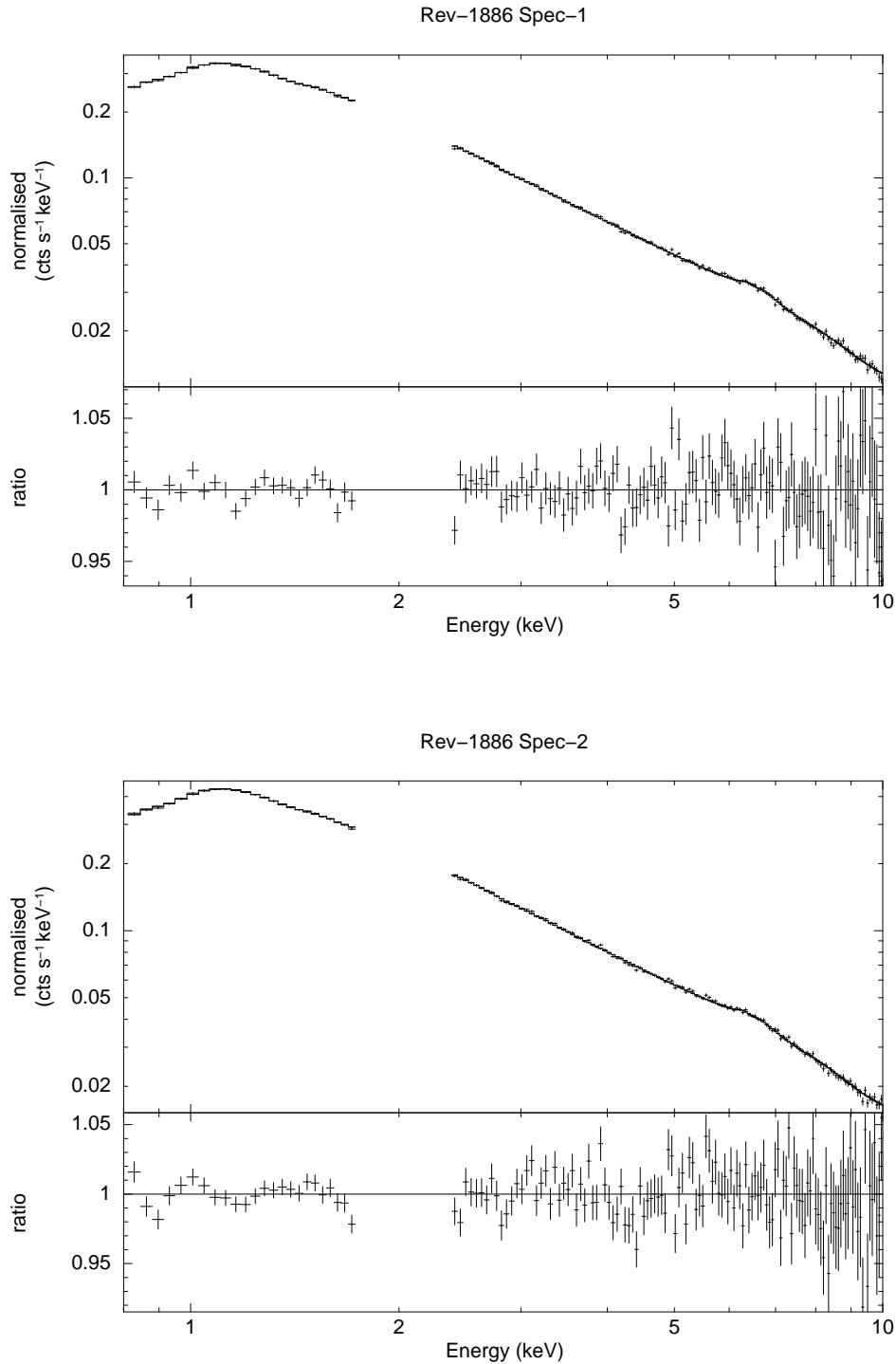


Figure B.13: The folded model and spectra, along with the fit ratio for the 1st and 2nd count rate bins of observation rev-1886.

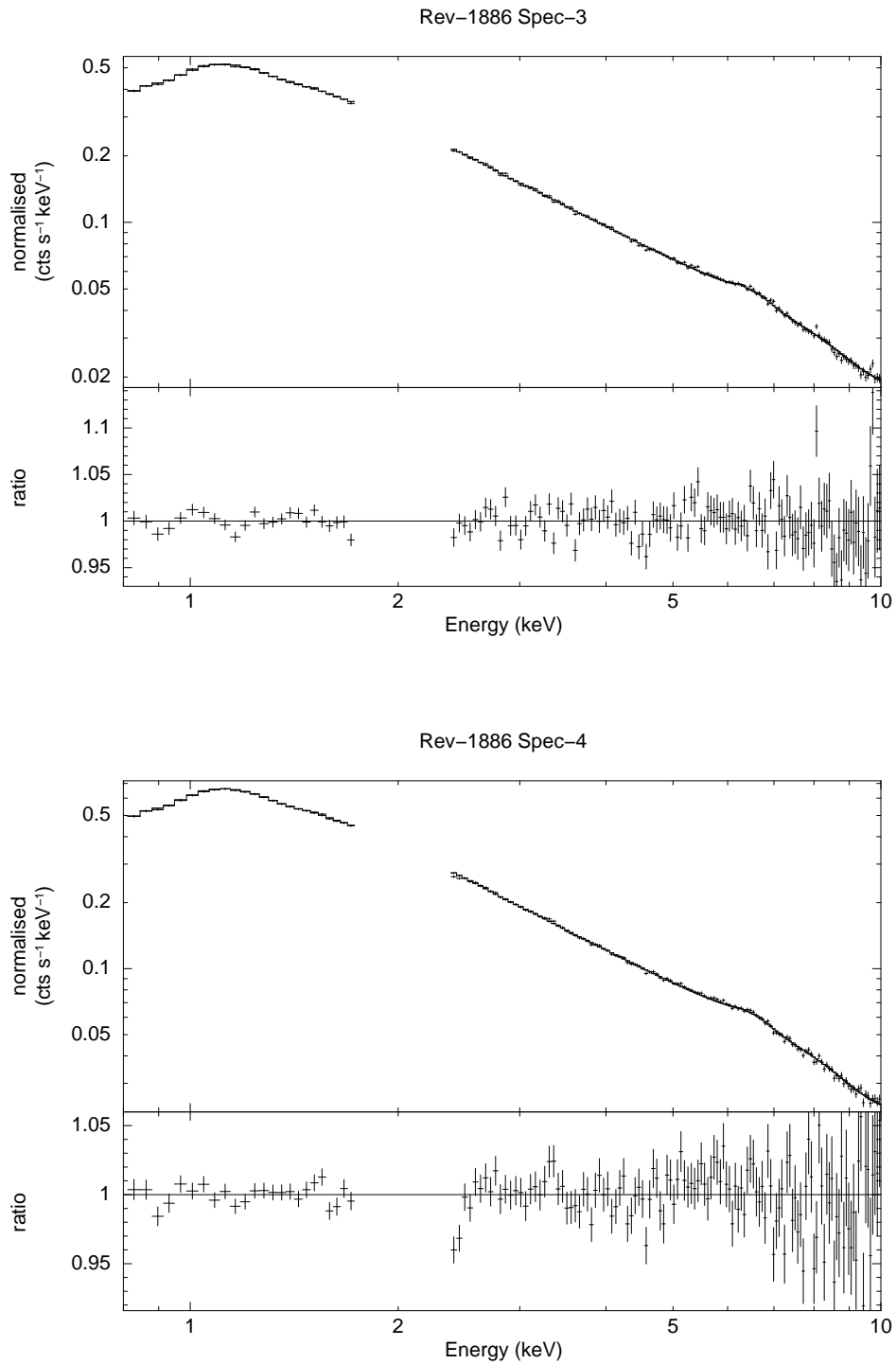


Figure B.14: The folded model and spectra, along with the fit ratio for the 3rd and 4th count rate bins of observation rev-1886.

# C

## The vertical disc structure

This appendix contains the equations for the vertical disc structure. Solving these equations for thermal dynamic equilibrium  $Q_+ = Q_-$  at a fixed radius produces the standard S-curve.

## C.1 Solving for thermal dynamic equilibrium

The vertical structure of an accretion disc can be solved in the same manner as the 1D treatment used for stellar interiors (Paczynski, 1969; Smak, 1984). The only difference is that viscous energy is generated through out the vertical structure of the disc and the tidal gravitational component increases with height (Hameury et al., 1998).

$$\frac{dP}{dz} = \rho g_z, \quad (\text{C.1})$$

$$\frac{dP}{d\rho} = c_s^2, \quad (\text{C.2})$$

$$\frac{d\zeta}{dz} = 2\rho, \quad (\text{C.3})$$

$$\frac{dF_z}{dz} = \frac{3}{2}\alpha\Omega_K P, \quad (\text{C.4})$$

and

$$\frac{d \ln T}{d \ln P} = \nabla. \quad (\text{C.5})$$

Here  $P$  is pressure,  $\rho$  is density,  $g_z$  is the vertical component of gravity,  $c_s$  is the sound speed,  $\zeta$  surface column density,  $F_z$  is the vertical energy flux,  $\alpha$  is the dimensionless viscosity prescription,  $\Omega_K$  is the Keplerian angular velocity,  $T$  is temperature, and  $\nabla$  is the vertical temperature gradient, which is dependant upon the adiabatic gradient  $\nabla_{\text{ad}}$ ,

$$\nabla = \begin{cases} \nabla_{\text{rad}}, & \text{if } \nabla_{\text{rad}} < \nabla_{\text{ad}} \\ \nabla_{\text{conv}}, & \text{if } \nabla_{\text{rad}} > \nabla_{\text{ad}}, \end{cases}$$

where  $\nabla_{\text{rad}}$  is the radiative gradient and  $\nabla_{\text{conv}}$  is the convective gradient. The adiabatic gradient is given as,

$$\nabla_{\text{ad}} = \frac{PQ}{\rho T c_p}, \quad (\text{C.6})$$

where  $c_p$  is the isobaric heat capacity, parameterised by Cannizzo (1993) and  $Q$  is the negative temperature exponent of density,

$$Q = -\left(\frac{\partial \ln \rho}{\partial \ln T}\right)_P = \chi_T / \chi_\rho. \quad (\text{C.7})$$

Here  $\chi_T$  and  $\chi_\rho$  are the density and temperature exponents for total pressure, which have been parameterised by Huré (2000b) (n.b. there is typo in the Huré (2000b) equations<sup>1</sup>). The radiative gradient which generally dominates is given as,

$$\nabla_{\text{rad}} = \frac{\kappa P F_z}{4 P_{\text{rad}} g_z c}, \quad (\text{C.10})$$

where  $P_{\text{rad}}$  is the radiative pressure and  $\kappa$  is the opacity. When the radiative gradient is super adiabatic, the temperature gradient is dominated by convection. Paczyński (1969) solves for the convective gradient using mixing length theory, to find

$$\nabla_{\text{conv}} = \nabla_{\text{ad}} + y(y + V)(\nabla_{\text{rad}} - \nabla_{\text{ad}}), \quad (\text{C.11})$$

where  $y$  is the solution of the cubic equation,

$$\frac{9}{4} \frac{\tau_{\text{ml}}^2}{3 + \tau_{\text{ml}}^2} y^3 + V y^2 + V^2 y - V = 0, \quad (\text{C.12})$$

and  $V$  is defined as,

$$V^{-2} = \left(\frac{3 + \tau_{\text{ml}}^2}{3\tau_{\text{ml}}}\right)^2 \frac{g_z^2 H_{\text{ml}}^2 \rho^2 c_p^2 Q}{512 \sigma^2 T^6 H} (\nabla_{\text{rad}} - \nabla_{\text{ad}}). \quad (\text{C.13})$$

---

<sup>1</sup>These are the corrected equations of Huré (2000b) for B.4 and B.5.

$$\chi_T = \beta + 4(1 - \beta) - \frac{\beta}{\mu \ln(10)} \sum_{i=1,4} \frac{\delta_i}{\Delta_i} \text{sech}^2 \Phi_i, \quad (\text{C.8})$$

and

$$\chi_\rho = \beta - \frac{\beta}{\mu \ln(10)} \sum_{i=1,4} \delta_i \text{sech}^2 \Phi_i \left(\frac{d\Phi_i}{d \log \rho}\right)_T. \quad (\text{C.9})$$

Here  $H_{\text{ml}}$  is the mixing length, defined as  $H_{\text{ml}} = \alpha_{\text{ml}}H$ , where  $H$  is the pressure scale-height and  $\alpha_{\text{ml}}$  is dimensionless mixing constant, which is assumed to be equal to 1.5 (Demarque & Guenther, 1991).  $\tau_{\text{ml}}$  is the optical depth of the mixing eddies, defined as  $\tau_{\text{ml}} = \kappa\rho H_{\text{ml}}$ . A smoother opacity and viscosity prescription is needed from that presented in chapter 5. The Rosseland mean opacity was calculated by interpolation of the solar composition OPAL tables<sup>2</sup> (Iglesias & Rogers, 1996; Grevesse & Noels, 1993; Ferguson et al., 2005). The dimensionless viscosity prescription was adapted from Hameury et al. (1998); with  $\alpha_{\text{cold}} = 0.01$  and  $\alpha_{\text{hot}} = 0.1$  and a smooth temperature dependant transition between the two states,

$$\log(\alpha) = \log(\alpha_{\text{cold}}) + [\log(\alpha_{\text{hot}}) - \log(\alpha_{\text{cold}})] \times \left[ 1 + \frac{2.5 \times 10^4 \text{ K}}{T_c} \right]^{-1}. \quad (\text{C.14})$$

Solving these equations for thermal equilibrium  $Q_+ = Q_-$  at a fixed radius, produces the standard S-curve. The boundary conditions at the disc mid-plane are  $z = 0$ ,  $\zeta = 0$ ,  $F_z = 0$ ,  $T = T_c$  and the boundary conditions at the photosphere are  $F_z = \sigma T_{\text{eff}}$  and  $\zeta = \Sigma$ , where the photosphere is defined as,

$$\kappa P = \frac{2}{3}g_z. \quad (\text{C.15})$$

---

<sup>2</sup>The interpolation was performed using the Fortran subroutines of Dr. Arnold Boothroyd: <https://www.cita.utoronto.ca/~boothroy/kappa.html#download>

# References

- Abbott B. P., Abbott R., Abbott T. D., Abernathy M. R., Acernese F., Ackley K., Adams C., Adams T., Addesso P., Adhikari R. X., et al. 2016, *Physical Review Letters*, 116, 061102
- Abramowicz M. A., Fragile P. C., 2013, *Living Reviews in Relativity*, 16, 1
- Alexander R. D., Wynn G. A., King A. R., Pringle J. E., 2011, *Monthly Notices of the Royal Astronomical Society*, 418, 2576
- Allured R., Tomsick J. A., Kaaret P., Yamaoka K., 2013, *ApJ*, 774, 135
- Balick B., Brown R. L., 1974, *ApJ*, 194, 265
- Ballet J., 2003, *Advances in Space Research*, 32, 2077
- Bardeen J. M., Carter B., Hawking S. W., 1973, *Comm. Math. Phys.*, 31, 161
- Bardeen J. M., Petterson J. A., 1975, *ApJ*, 195, L65
- Bardeen J. M., Press W. H., Teukolsky S. A., 1972, *ApJ*, 178, 347
- Barnard R., 2010, *MNRAS*, 404, 42
- Basak R., Zdziarski A. A., 2016, *MNRAS*, 458, 2199
- Bautista M. A., Kallman T. R., 2001, *ApJS*, 134, 139
- Begelman M. C., Pringle J. E., 2007, *MNRAS*, 375, 1070

- Belloni T., Homan J., Casella P., van der Klis M., Nespoli E., Lewin W. H. G., Miller J. M., Méndez M., 2005, *A&A*, 440, 207
- Boirin L., Méndez M., Díaz Trigo M., Parmar A. N., Kaastra J. S., 2005, *A&A*, 436, 195
- Boirin L., Parmar A. N., Barret D., Paltani S., Grindlay J. E., 2004, *A&A*, 418, 1061
- Bowyer S., Byram E. T., Chubb T. A., Friedman H., 1965, *Science*, 147, 394
- Brocksopp C., Tarasov A. E., Lyuty V. M., Roche P., 1999, *A&A*, 343, 861
- Buxton M., Vennes S., 2003, *MNRAS*, 342, 105
- Cabanac C., Fender R. P., Dunn R. J. H., Körding E. G., 2009a, *MNRAS*, 396, 1415
- Cabanac C., Fender R. P., Dunn R. J. H., Körding E. G., 2009b, *MNRAS*, 396, 1415
- Cambier H. J., Smith D. M., 2013, *ApJ*, 767, 46
- Cannizzo J. K., 1993, *ApJ*, 419, 318
- Carter B., 1971, *Phys. Rev. Lett.*, 26, 331
- Cash W., 1979, *ApJ*, 228, 939
- Chen X., Abramowicz M. A., Lasota J.-P., Narayan R., Yi I., 1995, *ApJL*, 443, L61
- Coleman M. S. B., Kotko I., Blaes O., Lasota J.-P., Hirose S., 2016, *MNRAS*, 462, 3710
- Coriat M., Fender R. P., Dubus G., 2012a, *MNRAS*, 424, 1991
- Coriat M., Fender R. P., Dubus G., 2012b, *MNRAS*, 424, 1991
- Cowley A. P., Crampton D., Hutchings J. B., Remillard R., Penfold J. E., 1983, *The Astrophysical Journal*, 272, 118
- Cowley A. P., Schmidtke P. C., Ebisawa K., Makino F., Remillard R. A., Crampton D., Hutchings J. B., Kitamoto S., Treves A., 1991, *ApJ*, 381, 526

- Cowley A. P., Schmidtke P. C., Hutchings J. B., Crampton D., 2002, *AJ*, 123, 1741
- Dauser T., Garcia J., Wilms J., Böck M., Brenneman L. W., Falanga M., Fukumura K., Reynolds C. S., 2013, *MNRAS*, 430, 1694
- Dauser T., Wilms J., Reynolds C. S., Brenneman L. W., 2010, *MNRAS*, 409, 1534
- Davis S. W., Blaes O. M., Hubeny I., Turner N. J., 2005, *ApJ*, 621, 372
- Davis S. W., Hubeny I., 2006, *ApJS*, 164, 530
- Demarque P., Guenther D. B., 1991, *Post-main-sequence solar evolution..* pp 1186–1223
- den Herder J. W., Brinkman A. C., Kahn S. M., Branduardi-Raymont G., Thomsen K., Aarts H., Audard M., Bixler J. V., den Boggende A. J., Cottam J., et al. 2001, *A&A*, 365, L7
- Díaz Trigo M., Parmar A. N., Boirin L., Méndez M., Kaastra J. S., 2006, *A&A*, 445, 179
- Díaz Trigo M., Parmar A. N., Boirin L., Motch C., Talavera A., Balman S., 2009, *A&A*, 493, 145
- Done C., Diaz Trigo M., 2010a, *MNRAS*, submitted, arXiv:0911.3243
- Done C., Diaz Trigo M., 2010b, *MNRAS*, 407, 2287
- Done C., Gierliński M., Kubota A., 2007, *A&A Rev.*, 15, 1
- Dubus G., Lasota J.-P., Hameury J.-M., Charles P., 1999, *MNRAS*, 303, 139
- Dunn R. J. H., Fender R. P., Körding E. G., Belloni T., Merloni A., 2011, *MNRAS*, 411, 337
- Eggleton P. P., 1983, *ApJ*, 268, 368
- Egron E., Di Salvo T., Motta S., Burderi L., Papitto A., Duro R., D’Ai A., Riggio A., Belloni T., Iaria R., Robba N. R., Piraino S., Santangelo A., 2013, *A&A*, 550, A5

- Einstein A., 1916, Sitzungsberichte der Königlich Preussischen Akademie der Wissenschaften, Berlin, pp 778–786
- Esin A. A., McClintock J. E., Drake J. J., Garcia M. R., Haswell C. A., Hynes R. I., Munro M. P., 2001, *ApJ*, 555, 483
- Esin A. A., McClintock J. E., Narayan R., 1997, *ApJ*, 489, 865
- Esin A. A., Narayan R., Cui W., Grove J. E., Zhang S.-N., 1998, *ApJ*, 505, 854
- Fabian A. C., Iwasawa K., Reynolds C. S., Young A. J., 2000, *PASP*, 112, 1145
- Farrell S. A., Webb N. A., Barret D., Godet O., Rodrigues J. M., 2009, *Nature*, 460, 73
- Ferguson J. W., Alexander D. R., Allard F., Barman T., Bodnarik J. G., Hauschildt P. H., Heffner-Wong A., Tamanai A., 2005, *ApJ*, 623, 585
- Finkelstein D., 1958, *Phys. Rev.*, 110, 965
- Foulkes S. B., Haswell C. A., Murray J. R., 2010, *MNRAS*, 401, 1275
- Fragile P. C., 2009, *ApJ*, 706, L246
- Fragile P. C., Blaes O. M., 2008, *ApJ*, 687, 757
- Frank J., King A., Raine D. J., 2002a, *Accretion Power in Astrophysics: Third Edition*
- Frank J., King A., Raine D. J., 2002b, *Accretion Power in Astrophysics: Third Edition*
- Fürst F., Nowak M. A., Tomsick J. A., Miller J. M., Corbel S., Bachetti M., Boggs S. E., Christensen F. E., Craig W. W., Fabian A. C., et al. 2015, *ApJ*, 808, 122
- Gallo E., Corbel S., Fender R. P., Maccarone T. J., Tzioumis A. K., 2004, *MNRAS*, 347, L52
- Gallo E., Miller-Jones J. C. A., Russell D. M., Jonker P. G., Homan J., Plotkin R. M., Markoff S., Miller B. P., Corbel S., Fender R. P., 2014, *MNRAS*, 445, 290

- García J., Dauser T., Lohfink A., Kallman T. R., Steiner J. F., McClintock J. E., Brenneman L., Wilms J., Eikmann W., Reynolds C. S., Tombesi F., 2014, *ApJ*, 782, 76
- García J., Dauser T., Reynolds C. S., Kallman T. R., McClintock J. E., Wilms J., Eikmann W., 2013a, *ApJ*, 768, 146
- García J., Dauser T., Reynolds C. S., Kallman T. R., McClintock J. E., Wilms J., Eikmann W., 2013b, *ApJ*, 768, 146
- García J., Kallman T. R., 2010, *ApJ*, 718, 695
- García J. A., Steiner J. F., McClintock J. E., Remillard R. A., Grinberg V., Dauser T., 2015, *ApJ*, 813, 84
- Gatuzz E., García J., Kallman T. R., Mendoza C., Gorczyca T. W., 2015, *ApJ*, 800, 29
- Gatuzz E., García J. A., Kallman T. R., Mendoza C., 2016, *A&A*, 588, A111
- Ghez A. M., Salim S., Hornstein S. D., Tanner A., Lu J. R., Morris M., Becklin E. E., Duchêne G., 2005, *ApJ*, 620, 744
- Giacconi R., 2002, in *Nobel Lecture: The dawn of x-ray astronomy*. Nobel Foundation, Stockholm
- Giacconi R., Gursky H., Paolini F. R., Rossi B. B., 1962, *Physical Review Letters*, 9, 439
- Gierliński M., Done C., 2004, *MNRAS*, 347, 885
- Gierliński M., Done C., Page K., 2009, *MNRAS*, 392, 1106
- Gierliński M., Newton J., 2006, *MNRAS*, 370, 837
- Gierliński M., Zdziarski A. A., Poutanen J., Coppi P. S., Ebisawa K., Johnson W. N., 1999, *MNRAS*, 309, 496

- Gillessen S., Eisenhauer F., Trippe S., Alexander T., Genzel R., Martins F., Ott T., 2009, *ApJ*, 692, 1075
- Gold T., 1968, *Nature*, 218, 731
- Goss W. M., Brown R. L., Lo K. Y., 2003, *Astronomische Nachrichten Supplement*, 324, 497
- Grevesse N., Noels A., 1993, *Origin and evolution of the elements: proceedings of a symposium in honour of H. Reeves, held in Paris, June 22-25, 1992*, ed. N. Prantzos, E. Vangioni-Flam, & M. Casse (England, Cambridge: Cambridge University Press), 14
- Grevesse N., Sauval A. J., 1998, *SSR*, 85, 161
- Guainazzi M., Kirsch M., Haberl F., de Juan Ovelar M., Rodríguez-Pascual P., Smith M., S. C., 2014, XMM-SOC-CAL-TN-0083. Available at: <http://xmm.vilspa.esa.es/docs/documents/CAL-TN-0083.pdf>
- Hameury J.-M., Menou K., Dubus G., Lasota J.-P., Hure J.-M., 1998, *MNRAS*, 298, 1048
- Hawking S. W., 1995, *A Brief History of Time*. Bantam Books, London
- Hessman F. V., Gänsicke B. T., Mattei J. A., 2000, *A&A*, 361, 952
- Hewish A., Bell S. J., Pilkington J. D. H., Scott P. F., Collins R. A., 1968, *Nature*, 217, 709
- Hiemstra B., Méndez M., Done C., Díaz Trigo M., Altamirano D., Casella P., 2011, *MNRAS*, 411, 137
- Hirose S., Blaes O., Krolik J. H., Coleman M. S. B., Sano T., 2014, *ApJ*, 787, 1
- Hirose S., Krolik J. H., Blaes O., 2009, *ApJ*, 691, 16
- Hubeny I., 1990, *ApJ*, 351, 632
- Hubeny I., Lanz T., 1995, *ApJ*, 439, 875

- Huré J.-M., 2000a, *A&A*, 358, 378
- Huré J. M., 2000b, *A&A*, 358, 378
- Huré J.-M., Richard D., Zahn J.-P., 2001, *A&A*, 367, 1087
- Hynes R. I., Steeghs D., Casares J., Charles P., O'Brien K., 2004, *Astrophys.J.*, 609, 317
- Hynes R. I., Steeghs D., Casares J., Charles P. A., O'Brien K., 2003, *ApJL*, 583, L95
- Iglesias C. A., Rogers F. J., 1996, *ApJ*, 464, 943
- Israel W., 1967, *Physical Review*, 164, 1776
- Jansen F., Lumb D., Altieri B., Clavel J., Ehle M., Erd C., Gabriel C., Guainazzi M., Gondoin P., Much R., Munoz R., Santos M., Schartel N., Texier D., Vacanti G., 2001, *A&A*, 365, L1
- Jiang Y.-F., Stone J. M., Davis S. W., 2013, *ApJ*, 778, 65
- Johnson B. M., Gammie C. F., 2003, *ApJ*, 597, 131
- Kallman T., Bautista M., 2001, *ApJS*, 133, 221
- Kerr R. P., 1963, *Physical Review Letters*, 11, 237
- King A., Lasota J.-P., 2014, *MNRAS*, 444, L30
- King A. R., 1988, *QJRAS*, 29, 1
- King A. R., Ritter H., 1998, *MNRAS*, 293, L42
- Kolehmainen M., Done C., 2010, *MNRAS*, 406, 2206
- Kolehmainen M., Done C., Díaz Trigo M., 2011, *MNRAS*, 416, 311
- Kolehmainen M., Done C., Díaz Trigo M., 2014, *MNRAS*, 437, 316

- Koliopanos F., Vasilopoulos G., Godet O., Bachetti M., Webb N. A., Barret D., 2017, *A&A*, 608, A47
- Kubota A., Done C., 2004, *MNRAS*, 353, 980
- Kubota A., Tanaka Y., Makishima K., Ueda Y., Dotani T., Inoue H., Yamaoka K., 1998, *PASJ*, 50, 667
- Kumar S., Pringle J. E., 1985, *MNRAS*, 213, 435
- Laplace P. S., 1808, *Exposition du système du Monde*, 3 edn. Courcier, Paris
- Larwood J., 1998, *MNRAS*, 299, L32
- Lasota J.-P., 2001, *New Astronomy Review*, 45, 449
- Lasota J.-P., 2001a, *NAR*, 45, 449
- Lasota J.-P., 2001b, *NAR*, 45, 449
- Lasota J.-P., 2016, in Bambi C., ed., *Astrophysics of Black Holes: From Fundamental Aspects to Latest Developments* Vol. 440 of *Astrophysics and Space Science Library*, Black Hole Accretion Discs. p. 1
- Lasota J.-P., Dubus G., Kruk K., 2008, *A&A*, 486, 523
- Lasota J.-P., Dubus G., Kruk K., 2008, *Astronomy and Astrophysics*, 486, 523
- Leong C., Kellogg E., Gursky H., Tananbaum H., Giacconi R., 1971, *The Astrophysical Journal Letters*, 170, L67
- Li L.-X., Zimmerman E. R., Narayan R., McClintock J. E., 2005, *ApJS*, 157, 335
- Lightman A. P., Eardley D. M., 1974, *ApJL*, 187, L1
- Lin D. N. C., Papaloizou J., 1986, *ApJ*, 309, 846
- Liu B. F., Taam R. E., Meyer-Hofmeister E., Meyer F., 2007, *ApJ*, 671, 695
- Lodato G., Nayakshin S., King A. R., Pringle J. E., 2009, *MNRAS*, 398, 1392

- Lynden-Bell D., 1969, *Nature*, 223, 690
- Lynden-Bell D., Pringle J. E., 1974, *MNRAS*, 168, 603
- Lynden-Bell D., Rees M. J., 1971, *MNRAS*, 152, 461
- Maccarone T. J., 2003, *A&A*, 409, 697
- Magdziarz P., Zdziarski A. A., 1995, *MNRAS*, 273, 837
- Markert T. H., Canizares C. R., Clark G. W., Lewin W. H. G., Schnopper H. W., Sprott G. F., 1973, *ApJL*, 184, L67
- Mayer M., Pringle J. E., 2007a, *MNRAS*, 376, 435
- Mayer M., Pringle J. E., 2007b, *MNRAS*, 376, 435
- McClintock J. E., Haswell C. A., Garcia M. R., Drake J. J., Hynes R. I., Marshall H. L., Munro M. P., Chaty S., Garnavich P. M., Groot P. J., Lewin W. H. G., Mauche C. W., Miller J. M., Pooley G. G., Shrader C. R., Vrtilik S. D., 2001, *ApJ*, 555, 477
- McClintock J. E., Shafee R., Narayan R., Remillard R. A., Davis S. W., Li L.-X., 2006, *ApJ*, 652, 518
- Meier D. L., 2001, *ApJL*, 548, L9
- Menou K., Hameury J.-M., Stehle R., 1999, *MNRAS*, 305, 79
- Merloni A., Fabian A. C., Ross R. R., 2000, *MNRAS*, 313, 193
- Meyer F., Liu B. F., Meyer-Hofmeister E., 2007, *A&A*, 463, 1
- Meyer F., Meyer-Hofmeister E., 1981, *A&A*, 104, L10
- Michell J., 1784, *Royal Society of London Philosophical Transactions Series I*, 74, 35
- Miller J. M., D’Ai A., Bautz M. W., Bhattacharyya S., Burrows D. N., Cackett E. M., Fabian A. C., Freyberg M. J., Haberl F., Kennea J., Nowak M. A., Reis R. C., Strohmayer T. E., Tsujimoto M., 2010, *ApJ*, 724, 1441

- Miller J. M., Fabian A. C., Reynolds C. S., Nowak M. A., Homan J., Freyberg M. J., Ehle M., Belloni T., Wijnands R., van der Klis M., Charles P. A., Lewin W. H. G., 2004, *ApJL*, 606, L131
- Miller J. M., Homan J., Steeghs D., Rupen M., Hunstead R. W., Wijnands R., Charles P. A., Fabian A. C., 2006, *ApJ*, 653, 525
- Miller J. M., Reynolds C. S., Fabian A. C., Cackett E. M., Miniutti G., Raymond J., Steeghs D., Reis R., Homan J., 2008, *ApJL*, 679, L113
- Miller J. M., Reynolds C. S., Fabian A. C., Cackett E. M., Miniutti G., Raymond J., Steeghs D., Reis R., Homan J., 2008, *The Astrophysical Journal Letters*, 679, L113
- Miniutti G., Fabian A. C., 2004, *MNRAS*, 349, 1435
- Mitsuda K., Inoue H., Koyama K., Makishima K., Matsuoka M., Ogawara Y., Suzuki K., Tanaka Y., Shibasaki N., Hirano T., 1984, *PASJ*, 36, 741
- Montgomery M. M., Martin E. L., 2010, *ApJ*, 722, 989
- Morrison R., McCammon D., 1983, *ApJ*, 270, 119
- Muñoz-Darias T., Casares J., Martínez-Pais I. G., 2005, *ApJ*, 635, 502
- Muñoz-Darias T., Casares J., Martínez-Pais I. G., 2008, *MNRAS*, 385, 2205
- Narayan R., McClintock J. E., 2008, *NAR*, 51, 733
- Narayan R., Yi I., 1994, *ApJL*, 428, L13
- Narayan R., Yi I., 1995, *ApJ*, 452, 710
- Narayan R., Zhu Y., Psaltis D., Sądowski A., 2016, *MNRAS*, 457, 608
- Nayakshin S., Kallman T. R., 2001, *ApJ*, 546, 406
- Nayakshin S., Kazanas D., Kallman T. R., 2000, *ApJ*, 537, 833

- Novikov I. D., Thorne K. S., 1973, in Dewitt C., Dewitt B. S., eds, *Black Holes (Les Astres Occlus) Astrophysics of black holes..* pp 343–450
- Nowak M. A., 1995, *PASP*, 107, 1207
- Nowak M. A., Wilms J., Heindl W. A., Pottschmidt K., Dove J. B., Begelman M. C., 2001, *Monthly Notices of the Royal Astronomical Society*, 320, 316
- Ogilvie G. I., Dubus G., 2001, *MNRAS*, 320, 485
- Orosz J. A., McClintock J. E., Aufdenberg J. P., Remillard R. A., Reid M. J., Narayan R., Gou L., 2011, *ApJ*, 742, 84
- Orosz J. A., Steeghs D., McClintock J. E., Torres M. A. P., Bochkov I., Gou L., Narayan R., Blaschak M., Levine A. M., Remillard R. A., Bailyn C. D., Dwyer M. M., Buxton M., 2009, *ApJ*, 697, 573
- Pacini F., 1967, *Nature*, 216, 567
- Paczyński B., 1969, *ACTAA*, 19, 1
- Paczyński B., 1977, *ApJ*, 216, 822
- Paczyński B., 1977, *The Astrophysical Journal*, 216, 822
- Papitto A., D’Ai A., Di Salvo T., Egron E., Bozzo E., Burderi L., Iaria R., Riggio A., Menna M. T., 2013, *MNRAS*, 429, 3411
- Pinto C., Kaastra J. S., Costantini E., de Vries C., 2013, *A&A*, 551, A25
- Plant D. S., Fender R. P., Ponti G., Muñoz-Darias T., Coriat M., 2014, *MNRAS*, 442, 1767
- Plant D. S., Fender R. P., Ponti G., Muñoz-Darias T., Coriat M., 2015, *A&A*, 573, A120
- Plant D. S., O’Brien K., Fender R. P., 2014a, *ArXiv e-prints*
- Plant D. S., O’Brien K., Fender R. P., 2014b, *arXiv e-prints*, p. arXiv:1411.7411

- Ponti G., Fender R. P., Begelman M. C., Dunn R. J. H., Neilsen J., Coriat M., 2012, MNRAS, 422, 11
- Pounds K., 2014, in SSR Vol. 183, Searching for Black Holes in Space. The Key Role of X-Ray Observations. pp 5–19
- Poutanen J., Krolik J. H., Ryde F., 1997, MNRAS, 292, L21
- Powell C. R., Haswell C. A., Falanga M., 2007, MNRAS, 374, 466
- Pringle J. E., 1981, Ann. Rev. A&A, 19, 137
- Pringle J. E., Rees M. J., 1972, A&A, 21, 1
- Rappaport S., Verbunt F., Joss P. C., 1983, ApJ, 275, 713
- Reis R. C., Fabian A. C., Miller J. M., 2010, MNRAS, 402, 836
- Reis R. C., Fabian A. C., Ross R. R., Miniutti G., Miller J. M., Reynolds C., 2008, MNRAS, 387, 1489
- Remillard R. A., McClintock J. E., 2006, Ann. Rev. A&A, 44, 49
- Robinson D. C., 1975, Physical Review Letters, 34, 905
- Ross R. R., Fabian A. C., 2005, MNRAS, 358, 211
- Ross R. R., Fabian A. C., 2007, MNRAS, 381, 1697
- Salpeter E. E., 1964, ApJ, 140, 796
- Salvesen G., Miller J. M., Reis R. C., Begelman M. C., 2013, MNRAS, 431, 3510
- Salvo T. D., Done C., Å»ycki P. T., Burderi L., Robba N. R., 2001, The Astrophysical Journal, 547, 1024
- Schandl S., 1996, A&A, 307, 95
- Schartel N., Santos-Lleo M., Parmar A., Clavel J., , 2010, ESA Bulletin: 10 Years of Discovery, URL: <http://esamultimedia.esa.int/multimedia/publications/ESA-Bulletin-141/pageflip.html>

- Schödel R., Ott T., Genzel R., Hofmann R., Lehnert M., Eckart A., Mouawad N., Alexander T., Reid M. J., Lenzen R., et al. 2002, *Nature*, 419, 694
- Schwarzschild K., 1916, *Abh. Konigl. Preuss. Akad. Wissenschaften Jahre 1906,92*, Berlin,1907,. pp 189–196
- Shahbaz T., Charles P. A., King A. R., 1998, *MNRAS*, 301, 382
- Shakura N. I., Sunyaev R. A., 1973, *A&A*, 24, 337
- Shields G. A., McKee C. F., Lin D. N. C., Begelman M. C., 1986, *ApJ*, 306, 90
- Shimura T., Takahara F., 1995, *ApJ*, 445, 780
- Smak J., 1984, *ACTAA*, 34, 161
- Smith I. A., Liang E. P., Lin D., Böttcher M., Moss M., Crider A., Filippenko A. V., Leonard D. C., Fender R. P., Durouchoux P., Corbel S., Sood R., 1999, *Astrophysical Letters and Communications*, 38, 265
- Soltan A., 1982, *MNRAS*, 200, 115
- Soria R., 2013, *MNRAS*, 428, 1944
- Soria R., Wu K., Page M. J., Sakelliou I., 2001, *A&A*, 365, L273
- Spruit H. C., Ritter H., 1983, *A&A*, 124, 267
- Steiner J. F., García J. A., Eikmann W., McClintock J. E., Brenneman L. W., Dauser T., Fabian A. C., 2017, *ApJ*, 836, 119
- Steiner J. F., McClintock J. E., Remillard R. A., Gou L., Yamada S., Narayan R., 2010, *ApJL*, 718, L117
- Steiner J. F., Narayan R., McClintock J. E., Ebisawa K., 2009, *PASP*, 121, 1279
- Strüder L., Briel U., Dennerl K., Hartmann R., Kendziorra E., Meidinger N., Pfeffermann E., Reppin C., et al. 2001, *A&A*, 365, L18
- Thorne K. S., 1974, *ApJ*, 191, 507

- Thorne K. S., 2003, in Gibbons G. W., Shellard E. P. S., Rankin S. J., eds, 1, Vol. 1, The future of Theoretical Physics and Cosmology, 1 edn, Cambridge University Press, Cambridge, Chapt. 5, pp 74–103
- Tomsick J. A., Kalemci E., Kaaret P., Markoff S., Corbel S., Migliari S., Fender R., Bailyn C. D., Buxton M. M., 2008, *ApJ*, 680, 593
- Turner M. J. L., Abbey A., Arnaud M., Balasini M., Barbera M., Belsole E., Bennie P. J., Bernard J. P., Bignami G. F., Boer M., et al. 2001, *A&A*, 365, L27
- Turner N. J., 2004, *ApJL*, 605, L45
- van der Klis M., Tjemkes S., van Paradijs J., 1983, *A&A*, 126, 265
- Verner D. A., Yakovlev D. G., 1995, *A&AS*, 109, 125
- Webster B. L., Murdin P., 1972, *Nature*, 235, 37
- White N. E., Marshall F. E., 1984, *ApJ*, 281, 354
- Wilkins D. R., Fabian A. C., 2012, *MNRAS*, 424, 1284
- Wilms J., Allen A., McCray R., 2000, *ApJ*, 542, 914
- Wilms J., Nowak M. A., Pottschmidt K., Heindl W. A., Dove J. B., Begelman M. C., 2001, *Monthly Notices of the Royal Astronomical Society*, 320, 327
- Wootton D., 2015, *The invention of Science*. Allen Lane, Milton Keynes
- Yoneyama T., Hayashida K., Nakajima H., Inoue S., Tsunemi H., 2017, *PASJ*, 69, 50
- Yuan F., Narayan R., 2014, *Ann. Rev. A&A*, 52, 529
- Zdziarski A. A., Gierliński M., Mikołajewska J., Wardziński G., Smith D. M., Harmon B. A., Kitamoto S., 2004, *MNRAS*, 351, 791
- Zel'dovich Y. B., Novikov I. D., 1964, *Doklady Akad. Nauk. SSSR*, 155, 1033

Zhu Z., Hartmann L., Calvet N., Hernandez J., Muzerolle J., Tannirkulam A.-K.,  
2007, ApJ, 669, 483

Zimmerman E. R., Narayan R., McClintock J. E., Miller J. M., 2005, ApJ, 618, 832